Thermography of Semiconductor Lasers

From Thermal Emission of Semiconductors towards a Novel Analytical Tool for Optoelectronic Devices

DISSERTATION

zur Erlangung des akademischen Grades
doctor rerum naturalium
(Dr. rer. nat.)
im Fach Physik

eingereicht an der
Mathematisch-Naturwissenschaftlichen Fakultät I
Humboldt-Universität zu Berlin

von
Herr Dipl.-Phys. Mathias Ziegler
geboren am 16.11.1977 in Berlin

Präsident der Humboldt-Universität zu Berlin:
Prof. Dr. Dr. h.c. Christoph Markschies

Dekan der Mathematisch-Naturwissenschaftlichen Fakultät I:
Prof. Dr. Lutz-Helmut Schön

Gutachter:

1. Prof. Dr. Thomas Elsässer
2. Prof. Dr. W. Ted Masselink
3. Prof. Dr. Joachim Wagner

eingereicht am: 24.02.2009
Tag der mündlichen Prüfung: 19.06.2009

Abstract

Semiconductor lasers are unequaled efficient light sources, reaching efficiencies of more than 70%. Nevertheless, thermal limits govern their reliable application, in particular in the field of high power densities. The analysis of thermal properties and degradation processes in such devices contributes essentially to the understanding of these limits. This work exploits thermography as an innovative analytical technique for such purpose. Starting from measurements of the thermal emission from semiconductor laser structures, the thermographic methodology is discussed, taking into account the physical properties of the semiconductor materials. Basing on these considerations, experimental studies on thermal characterization of high-power laser diodes are presented.

Planck's law allows for a radiometric detection of temperatures. In this work, the important physical parameter emissivity is measured spectrally resolved for both semiconductors and semiconductor laser structures and is related to fundamental physical properties. Based on that, methodological aspects are discussed, which are affected on the one hand by the omnipresent thermal radiation and on the other hand by the partial transparency of the semiconductor materials. The resulting analytical capacities allow, for instance, for the determination of the thermal properties of complex high-power lasers of a wide range of different designs in a spatio-temporally resolved fashion. Furthermore, does the knowledge of the involved thermal time constants allow for an extraction of localized peaks of the infrared emission that is analyzed for its relationship with device degradation. The output power of high-power devices is fundamentally limited by the catastrophic optical damage, an abrupt degradation process that is induced significantly by reabsorption of laser radiation at the front facet. This process is analyzed spatio-temporally resolved with help of a combined thermography and optical near-field technique. Extending the detection range down to shorter wavelengths allows for imaging of radiative transitions that are related to defect centers. Such additional luminescence components are characterized and interpreted as radiative signatures of gradual device degradation processes.

Keywords:
Thermography, Semiconductor Lasers, High-Power Laser Diodes, Infrared Spectroscopy, Emissivity, Reliability, Catastrophic Optical Mirror Damage, Degradation

Zusammenfassung

Halbleiterlaser stellen mit über 70% Wirkungsgrad einzigartig effiziente Lichtquellen dar. Dennoch ist ihre zuverlässige Nutzung, insbesondere im Bereich hoher Leistungsdichten, von thermischen Limitierungen geprägt. Einen grundlegenden Beitrag zu deren physikalischen Verständnis leistet die Analyse der thermischen Eigenschaften und Degradationsprozesse solcher Bauelemente. In dieser Arbeit wird hierzu die Thermographie als innovative Analysemethode untersucht. Ausgehend von Messungen der thermischen Emission von Halbleiterlaserstrukturen wird die Methodik der Thermographie unter Berücksichtigung der physikalischen Eigenschaften der Halbleitermaterialien diskutiert. Darauf aufbauend werden experimentelle Studien zur thermischen Charakterisierung von Hochleistungslaserdioden vorgestellt.

Das Plancksche Strahlungsgesetz erlaubt die radiometrische Ermittlung der Temperatur. Die wichtige physikalische Kenngröße Emissivität wird in dieser Arbeit für Halbleiter und Halbleiterlaserstrukturen spektral aufgelöst gemessen und auf fundamentale physikalische Eigenschaften zurückgeführt. Auf dieser Grundlage werden methodische Aspekte der Thermographie diskutiert, welche einerseits durch die omnipräsente thermische Strahlung und andererseits durch die teilweise Transparenz der Halbleitermaterialien geprägt sind. Die daraus folgenden analytischen Fähigkeiten erlauben unter anderem die orts- und zeitaufgelöste Bestimmung der thermischen Eigenschaften von komplexen Hochleistungslasern unterschiedlichster Bauart. Darüber hinaus ermöglicht die Kenntnis der beteiligten thermischen Zeitkonstanten die Extraktion von lokalen Überhöhungen in der Infrarotemission, deren Zusammenhang zur Degradation der Bauelemente untersucht wird. Eine grundsätzliche Begrenzung der Ausgangsleistung ist durch einen abrupten Degradationsprozess gegeben, welcher maßgeblich durch eine Reabsorption der Laserstrahlung an der Frontfacette verursacht wird. Mithilfe einer kombinierten Thermographie-Nahfeld-Messung wird dieser Prozess orts- und zeitaufgelöst analysiert. Die Erweiterung des Messfensters zu kürzeren Wellenlängen hin erlaubt die Detektion strahlender Übergänge unter Einbeziehung von Defektzentren. Diese zusätzlichen Lumineszenzbeiträge werden charakterisiert und mithin wird gezeigt, daß sie als strahlende Signaturen von graduellen Degradationsprozessen aufzufassen sind.

Schlagwörter:
Thermographie, Halbleiterlaser, Hochleistungslaserdioden,
Infrarot-Spektroskopie, Emissivität, Zuverlässigkeit, COMD, Degradation

Contents

1 Introduction 1

2 Basic Concepts and Methods 5
- 2.1 Quantum-Well Laser Basics . . . 5
- 2.2 Thermal Effects in Semiconductor Lasers . . . 10
- 2.3 High-Power Semiconductor Lasers . . . 14
- 2.4 Physical Aspects of Semiconductor Laser Degradation . . . 18
- 2.5 Description of the Laser Samples . . . 24
- 2.6 Thermal Radiation . . . 26
- 2.7 Spectroscopic Techniques . . . 30

3 Thermal Emission from Semiconductor Lasers 37
- 3.1 Determination of the Emittance of Semiconductors . . . 37
- 3.2 Emittance Enhancement due to the Laser Cavity . . . 47

4 Thermography of Semiconductor Lasers: Methodology 55
- 4.1 Measurement Strategy . . . 55
- 4.2 Setup and Acquisition Modes . . . 63
- 4.3 Light Propagation Effects and Resolution Constraints . . . 67

5 Thermography of Semiconductor Lasers: Applications 77
- 5.1 Transient Thermal Behavior of High-Power Laser Diodes . . . 77
- 5.2 Thermography as Analytical Tool in Reliability Studies . . . 87
- 5.3 Real-Time Imaging of the Catastrophic Optical Damage . . . 95
- 5.4 Infrared Emission from Laser Substrates . . . 102
- 5.5 Infrared Emission as Degradation Probe . . . 109

6 Conclusions 117

Bibliography 120

Appendix **143**
- A. Emittance of Semiconductors 143
- B. Quantitative Lock-In Correlation 146
- C. Lumped Capacitance Method 147
- D. Correlation of Hot-Spots with Facet Damages 148
- E. Spatial Model for IR Substrate Emission 152
- F. Abbreviations and Symbols 153

Publications **156**

Acknowledgement - Danksagung **162**

Selbständigkeitserklärung **164**

Chapter 1

Introduction

Semiconductor lasers have made their way to everyday life and serve as indispensable, efficient, compact, and reliable light sources in numerous applications. A novel class of these lasers aims at boosting the available output power towards the kilowatt range. The successful development of such high-power laser sources will lead to novel applications in terms of a wider penetration of photonic technologies into the society. Currently, high-power laser diodes serve as the pump source for solid state lasers or are applied directly with increasing importance. Application is found, e.g., in material processing, medicine, display, and printing systems.[1–4]

The huge electrical and optical power densities that are turned over in these devices lead to a substantial heating. Since the crystal lattice temperature is a key parameter in all optoelectronic devices, all materials parameters and processes in semiconductor lasers depend on it. Consequently, heating directly influences the spectral properties and the efficiency of the device; and the ability to control it eventually decides about the applicability of the device.

Although high-power laser diodes already show impressive output-power levels up to 1 kW from one single monolithic laser device,[5–8] and electrical-to-optical power conversion efficiencies of better than 70%,[9–11] one key issue in further market penetration is reliability. Only until a long enough lifetime (e.g., $> 2 \times 10^4$ h, [12]) is guaranteed some industrial applications will be implemented. Large consortia worldwide deal with reliability issues of laser diodes, e.g., BRIOLAS in Germany,[12, 13], WWW.BRIGHTER.EU in the EU,[14], and SHEDS in the USA,[15]. There, reliability improvement is seen as the primary task, even more important than a further output-power increase. Also to this end the thermal performance becomes increasingly important, owing to the high power densities.

Consequently, techniques for the determination of temperature distributions in semiconductor lasers are required for the design and quality assessment of high-power devices. A convenient and non-invasive way to probe temperature distributions, in particular in extended devices such as laser arrays and stacks of arrays, is analyzing the emitted thermal radiation with a thermography system. Although thermography has a rich application range,[16–19] thermography of semiconductor lasers is still a novelty, with only a few rather qualitative tracks in literature.[20–31] The strength of the thermography concept originates from the universality of Planck's law for an ideal blackbody.[32–34] For a real laser device, however, such radiometric temperature measurements are challenging because of the physical properties of the semiconductor materials the laser consists of. Most importantly, the semiconductor materials are semitransparent for the probed thermal radiation, an issue that has been largely ignored so far.

The motivation for this thesis is to explore the applicability of thermography as novel analytical tool for semiconductor lasers, in particular for high-power laser diodes and laser arrays and to provide the first comprehensive study of this novel tool regarding its fundamental physical and technical prerequisites, the difficulties that arise from the physical properties of the semiconductor device, and to give distinct original examples for applications.

The outline of this thesis is as follows:

Chapter 2 introduces basic concepts and methods which are relevant for the subsequent work on thermography of semiconductor lasers. Consequently, first, basic principles of quantum-well semiconductor lasers are introduced and the analyzed high-power laser samples are described. This introduction involves thermal effects in semiconductor lasers, peculiarities of high-power semiconductor lasers, and physical aspects about the degradation of such devices. Thermal radiation mediates the temperature information from the laser sample toward the detecting camera system, hence basic principles of the thermal radiation emitted from a blackbody and the modifications in case of real materials are introduced. To complete this chapter, the important spectroscopic techniques applied in this work are discussed for their basic properties.

Chapter 3 provides experimental data about the thermal emission from semiconductor lasers. A spectrally resolved measurement of the important parameter emittance, together with transmittance and reflectance, of laser bars and bulk GaAs reference samples is performed and their characteristics are related to the properties of the semiconductor materials and the laser device structure.

Chapter 4 provides the necessary information for thermography of semiconductor lasers. This chapter on methodology involves the description of the thermography setup and of an appropriate procedure for the extraction of temperature distributions taking into account the findings from Chapter 3. A rigorous analysis of thermal images from semiconductor lasers needs to account for the semitransparent nature of the laser diode for the thermal radiation. For the case of highly spatially resolved thermography the thermal radiation propagation inside the laser and effects from diffraction limited imaging are discussed.

Chapter 5 explores the applicability of thermography as a novel analytical tool for high-power semiconductor lasers, in particular for the important aspect of laser reliability. Five original case studies are presented. As a typical application, transient thermography of high-power laser bars, focused on the influence of the heat-sink scheme, is presented. In extending the applicable range of thermography for the analysis of transient thermal phenomena in laser diodes, synchronous undersampling lock-in thermography is introduced. In a second case study, a thermographic method is developed that can, in particular, detect temperature hot-spots in high-power cm-bars. Statistical results from a large number of experiments provide a basis for the correlation of such hot-spots with defects. A third case study deals with the catastrophic optical damage (COD) of high-power laser diodes. A novel approach is developed that applies thermography for spatio-temporally-resolved monitoring of the catastrophic process. Further, the extension of the usable spectral range of the thermographic camera towards shorter wavelengths (i.e., $\lambda < 3\ \mu$m) allows for detection of an additional infrared emission from the substrate of GaAs-based semiconductor lasers. In the last two case studies this extra emission is analyzed for its physical origin and an application using it as a probe for laser degradation is demonstrated.

Chapter 6 concludes this thesis and gives an overview of the major findings and achievements.

Chapter 2

Basic Concepts and Methods

This chapter introduces concepts and methods relevant for the subsequent chapters on thermography results of high-power semiconductor lasers. The first sections provide an overview of important concepts and principles in *semiconductor lasers*: photon generation in quantum-well lasers, thermal effects arising from imperfect electrical-to-optical power conversion, peculiarities in high-power devices, physical aspects of the degradation of laser diodes. The laser-diode samples used in this thesis are described as well. In the second section the basic concept behind *thermal radiation* and its spectral distribution are introduced. The generality of Planck's formula, derived within the framework of the blackbody concept, is modified for real materials. The third section reviews the major *spectroscopic techniques* applied in this thesis. Thermography is introduced as a powerful technique for temperature determination of nearly arbitrary materials and competing alternative techniques are reviewed. Additional spectroscopic methods are applied in the present work, such as Fourier-transform infrared spectroscopy, photoelectrical spectroscopy, and near-field optical microscopy which are introduced for their very basic concepts.

2.1 Quantum-Well Laser Basics

In this thesis, in-plane or edge-emitting laser diodes are discussed and denoted by the term *semiconductor laser*, having in mind that later on more specifically high-power broad-area laser diodes or arrays of such laser diodes are analyzed. Nevertheless, most of the basic relations also apply to other resonator geometries. On the other hand, other concepts such as the quantum cascade laser that relies on radiative intersubband transitions are not considered in the following.[35]

The advent of highly precise growth techniques (molecular-beam epitaxy, metalorganic vapor-phase epitaxy) enabled the utilization of quantum-well (QW) structures for the active region of laser diodes.[36] These are known for a number of advantages, for instance, a low threshold current density, high efficiency, and narrow gain spectrum. Following, some of the basic principles are given, mainly in accordance with Refs. 37–44.

2.1.1 Photon Generation in Quantum Wells

Quantum effects come into play when the electron can be spatially confined to a region (e.g., a QW) L_y smaller than its de Broglie wavelength.

The QW in a laser diode is usually built from an undoped (intrinsic) direct-band-gap semiconductor of a thickness around 10 nm with band gap energy E_g similar to the desired photon energy $h\nu$, surrounded by materials with higher band gap energy. In order to have a confining one-dimensional potential (in y) for both electrons and holes the band edge discontinuity must be of type I, that is positive conduction band (CB) and valence band (VB) offsets between well and barrier.

Electrons in such a QW are treated as a two-dimensional (2D) electron gas forming subbands with quantized energetic states $E_y(j)$ (j - main quantum number) in the direction of confinement (in y-direction) and otherwise (in xz-plane) free dispersion. In the so-called effective mass or envelope function approximation the single-particle electronic wave functions $\Psi(r) = e^{\mathrm{i}\mathrm{k}r} u_{jk}(r)$ that satisfy the Schrödinger equation in a periodic bulk potential can be separated into the envelope functions ψ and the lattice-periodic Bloch functions u yielding

$$\Psi(r) = \psi_j(y) e^{\mathrm{i}\mathrm{k}_x x} e^{\mathrm{i}\mathrm{k}_z z} u_{j(\mathrm{k}=0)}(r)\,. \tag{2.1}$$

Here, r is the spatial coordinate, and k is the wave vector. The ψ (length scale $\sim$ QW thickness $\sim$ 10 nm) are considered to be slowly varying against the u (length scale $\sim$ lattice constant $\sim$ 5 Å). The k-dispersion then has the following form

$$E_{cj}(\mathrm{k}) = E_c^0 + E_y(j) + \frac{\hbar^2 \mathrm{k}_{xz}^2}{2m_c^*} \sim E_c^0 + \frac{\hbar^2}{2m_c^*}\left(\frac{j\pi}{L_y}\right)^2 + \frac{\hbar^2 \mathrm{k}_{xz}^2}{2m_c^*}\,, \tag{2.2}$$

where for the latter approximation infinitely high barriers are assumed. E_c^0 is the CB edge and m_c^* the electron effective mass. For the holes in the individual VBs[1] similar relations hold. The photon energy $h\nu = E_{cj} - E_{vi}$ of an optical transition between the j-th CB subband E_{cj} and the i-th VB

---

[1] Of immediate interest in laser diodes are only the heavy and the light hole bands.

subband E_{vi} is thus given by the band gap energy of the QW ($E_\mathrm{g} = E_c^0 - E_v^0$) plus the confinement energies of the electrons and holes in the CB and VB. This treatment works appropriate for most heterostructure-related problems in the vicinity of the Γ-point. Further away the energy dependence of the effective mass $m_c^*(E)$ needs to be accounted for by introducing nonparabolicity corrections (cf. section 3.2.2).

The density of states of each CB subband is a constant, resembling a step-like shape

$$D_c(E) = \frac{m_c^* j}{\pi \hbar^2 L_y}\,, \quad \text{for} \quad E_{cj}(\mathrm{k}=0) \leq E \leq E_{c(j+1)}(\mathrm{k}=0)\,, \quad \text{else} \quad 0\,. \tag{2.3}$$

For the VB an analogous expression for $D_v(E)$ and m_v^* holds. The joint density of states (JDOS) that combines both bands for optical transitions is again a step function and is given by $D_r^{-1} = D_c^{-1} + D_v^{-1}$, with a reduced effective mass $(m_r^*)^{-1} = (m_c^*)^{-1} + (m_v^*)^{-1}$.

In a laser diode the QW is sandwiched in a heavily doped *pn*-junction, and under forward bias condition quasi thermal equilibria of both the CB and the VB subbands can be assumed since intraband thermalization is much faster than interband relaxation ($\sim$ 100 fs versus $\sim$ 1 ns), described by the Fermi distributions[2]

$$f_c(E) = \frac{1}{\exp\left(\frac{E-F_\mathrm{e}}{kT}\right)+1} \quad \text{and} \quad f_v(E) = \frac{1}{\exp\left(\frac{F_\mathrm{h}-E}{kT}\right)+1} \tag{2.4}$$

with the quasi Fermi energies for electrons F_e and holes F_h, the Boltzmann constant k, and the temperature T.

The gain for such transitions with photon energy $h\nu = E_{ij} = E_{cj} - E_{vi}$ is given by

$$g_{ij}(h\nu) = \frac{e^2 h}{2 m_\mathrm{e}^2 \varepsilon_0 n c}\frac{|M(E_{ij})|^2}{h\nu} D_r(h\nu)(f_{cj} - f_{vi}) = g_\mathrm{max}(E_{ij})(f_{cj} - f_{vi})\,, \tag{2.5}$$

where $f_{cj} = f_c(E_{cj})$, $f_{vi} = f_v(E_{vi})$, and the constants are: e - elementary charge, ε_0 - vacuum permittivity, n - refractive index, c - speed of light in vacuum, m_e - electron mass. The relation for the gain can be divided into a material-related maximum material gain g_max and the Fermi inversion factor $(f_{cj} - f_{vi})$, which depends on the strength of (electrical) pumping and thus increases with current-injection level.

The two ingredients in g_max are the JDOS and the transition matrix element $|M(E_{ij})|^2 = |\langle cj|\mathcal{P}|vi\rangle|^2$ between the two subbands. Where the interaction of the incident electromagnetic wave with the electron is given by

---

[2] k, the Boltzmann constant must not confused with the wave vector k.

an Hamiltonian of form $\mathcal{H}_{int} = -(e/m)\,\mathcal{A}\cdot\mathcal{P}$ constituting of the vector potential $\mathcal{A}$ und the momentum operator $\mathcal{P}$. The dominant transitions that are induced are the electronic dipole transitions, such that a usual approximation of $\mathcal{H}_{int} = -\mathcal{D}\cdot\mathcal{E}$ is given by a dipole interaction between the electrical field $\mathcal{E}$ and the electronic dipole moment $\mathcal{D} = e\mathcal{R}$. The calculation of $|M(E_{ij})|^2$ for a QW is involved owing to the complicated VB structure. In the case of bulk materials, the interband matrix element can be approximated by $|M_{cv}|^2 \approx E_P m_\mathrm{e}/6$, with the Kane energy E_P, which is almost a constant of 20-30 eV for most III-V compounds.

In order to achieve a net optical gain for transitions between the subbands with energies E_{cj} and E_{vi}, a sufficient condition is given by

$$F_\mathrm{e} - F_\mathrm{h} > E_{cj} - E_{vi} = h\nu\,. \tag{2.6}$$

This condition, formulated by Bernard and Durrafourg, is understandable from the fact that in order to have $g_{ij}(h\nu) > 0$ the Fermi inversion factor needs to be positive, i.e., $f_{cj} > f_{vi}$. The total gain $g(h\nu)$ for a certain energy $h\nu$ is a sum over all subband combinations with $E_{cj}(\mathrm{k}=0) - E_{vi}(\mathrm{k}=0) < h\nu$. The dipole selection rules allow only $j = i$ transitions, where the strongest is usually the $i = j = 1$ one. Besides, Eq. (2.6) sets a lower limit for the diode forward bias to $U > h\nu/e$.

The net rate of stimulated emission (i.e., the generation rate of stimulated photons per unit time) is related to the total gain spectrum (i.e., the generation rate of stimulated photons per unit length) by

$$R_\mathrm{stim}(h\nu) = g(h\nu)N_\gamma(h\nu)c/n\,, \tag{2.7}$$

with the photon density $N_\gamma(h\nu)$. Without population inversion (i.e., $F_\mathrm{e} - F_\mathrm{h} < h\nu$) net absorbtion occurs, leading to the usual expression for the absorption coefficient as negative gain (and vice versa) $\alpha(h\nu) = -g(h\nu)$.

2.1.2 Laser Threshold for Fabry-Pérot Lasers

The advantage of using a QW in the active region becomes clear directly from Eq. (2.5). The reduced dimensionality in the JDOS assures, in combination with the Fermi factor, a much narrower gain spectrum than in the bulk-materials case with, ideally, a step-like onset at $h\nu = E_{cj}(\mathrm{k}=0) - E_{vi}(\mathrm{k}=0)$. As a result, the threshold current, that is the amount of carrier injection to achieve population inversion, can be drastically reduced. This is one of the reasons for the application of quantum-wire and quantum-dot (QD) gain materials with even further enhanced electronic confinement.

The beneficial effect of incorporating a (biaxial) strain on the band structure through strained growth of the QW layers has lead to a further decrease of the laser threshold.[45, 46] The main effect is the reduction of the VB effective mass, at best under a compressive strain, which reduces the quasi Fermi level of the electrons, given a constant separation of the quasi Fermi levels according to Eq. (2.6).

The relation between gain and electrical injection current I and with the carrier density N can be approximated by

$$g = g_0 \ln\left(\frac{I}{I_{\mathrm{tr}}}\right) = g_0 \ln\left(\frac{N}{N_{\mathrm{tr}}}\right) , \tag{2.8}$$

where the parameters I_{tr} and N_{tr} relate to the values at transparency of the active medium.

The gain medium amplifies radiation under injection of carriers. In order to form a laser (oscillator), optical feedback is necessary. The solution used for the present devices is the Fabry-Pérot resonator (in the z-direction), which is provided from cleaving the semiconductor structure perpendicular to the layer plane. Additional coating of the such formed facets (cf. section 2.3) to reflectivities of R_1 and R_2 provides optimized outcoupling performance. The condition for lasing threshold gain is given from the requirement of unit photon gain after one roundtrip in the resonator of length L

$$1 = \exp\left[\left(\Gamma g_{\mathrm{th}} - \alpha_{\mathrm{i}} - \alpha_{\mathrm{m}}\right) 2L\right] , \tag{2.9}$$

which is satisfied at a modal gain that compensates for all the losses occurring from internal optical absorption in the resonator α_{i} and from imperfect reflection at the mirrors α_{m}

$$\Gamma g_{\mathrm{th}} = \alpha_{\mathrm{i}} + \alpha_{\mathrm{m}} = \alpha_{\mathrm{i}} + \frac{1}{2L} \ln\left(\frac{1}{R_1 R_2}\right) . \tag{2.10}$$

The confinement factor Γ is the ratio between the volume of the gain medium and the volume of the optical mode. Its numerical value (in high-power broad-area lasers typically on the order of 1%) is defined by how tight the optical mode in such a resonator is guided relative to the volume of the QW (or of multiple QWs) fed with minority carriers. The optical confinement in the directions perpendicular to the resonator axis (i.e., in x- and y-directions) can be provided by surrounding layers of lower refractive index than the QW. In growth direction, for instance, the QW and additional high-index waveguide layers are sandwiched between low-index cladding layers.

2.2 Thermal Effects in Semiconductor Lasers

2.2.1 Heat Sources and Losses

Heat is created in semiconductor lasers due to partial energy transfer from the carriers to the crystal lattice. Heating leads to an increase in the lattice temperature and eventually to a degradation in device performance because the heat generating processes are themselves temperature dependent leading to more heat at higher temperature. The most important heat generation processes and losses are given in the following.[37, 39, 47]

Joule heat: The finite resistivity of the semiconductor materials leads to heating in all semiconductor layers via inelastic carrier scattering with the lattice.

Excess bias heat: An excess in the externally applied forward bias above laser transition energy allows for cooling of the carriers via the emission of phonons. Condition (2.6) requires the quasi Fermi-level separation to be larger than the laser-transition energy and, consequently, the applied bias to be larger than that. Since the laser diode consists of a heterostructure with various band gap energies and CB and VB offsets, a proper band alignment requires a further increase in the externally applied potential. The finite resistivity of the layers around the active region leads to a small potential drop as well.

Nonradiative recombination heat: The nonradiative recombination of electron-hole pairs via defects, via states at semiconductor interfaces and surfaces, and Auger recombination release phonons. The carriers are either electrically injected or photoexcited and predominantly recombine at the pn-junction, or leak out into adjacent layers where they recombine afterwards.

Optical absorption heat: Interband absorption of spontaneous radiation and, above lasing threshold, additionally of stimulated radiation, leads to carrier-pair generation and to heating via subsequent nonradiative recombination. This process dominates in layers of band gap energy smaller than the photon energy, e.g., in the QW and the substrate (via transmission through waveguide and cladding). In the gain, waveguide, and cladding regions free carrier absorption of spontaneous and stimulated radiation occurs, with subsequent cooling of the hot carriers.

Surface heat sources: In addition to the heat generated in the bulk of the laser structure, a fraction is generated at the front and rear facets. These surfaces are in contact with the surrounding air and are a discontinuity of the crystal lattice, which leads, among other effects, to surface states that predominantly serve as nonradiative traps. Optical absorption at the facets, consisting of a semiconductor-coating interface with additional surface contaminants such as oxides or pollutants, leads to additional heating.

Radiative losses: Beside the nonradiative losses that lead to heating, also radiative losses lower the efficiency of a semiconductor laser. Most importantly, the spontaneous emission generated in the QW pumps the stimulated emission. Furthermore radiative recombination (interband or via radiative recombination centers) either through electrically or optically injected minority carriers (see section 5.4 for an example) is possible.

2.2.2 Heat Propagation and Thermal Properties

The above mentioned processes heat the semiconductor laser and the heat spreads throughout the device leading to a temperature distribution. Any temperature probing technique measures either a transient or a stationary temperature distribution. In solid-state, heat transfer is mediated by conduction and the transient heat conduction flux equation is given by [39]

$$\nabla \cdot (\lambda_\mathrm{T} \nabla T) = \frac{\lambda_\mathrm{T}}{\chi}\frac{\partial T}{\partial t} - g_\mathrm{T}\,, \tag{2.11}$$

where T is the temperature, t is the time, λ_T is the thermal conductivity, χ is the thermal diffusivity, and g_T is the power density of the heat sources. The two material parameters λ_T and χ are related by

$$\chi = \frac{\lambda_\mathrm{T}}{C\rho}\,, \tag{2.12}$$

where C is the specific heat and ρ the density.

The quantities λ_T, χ, and g_T are temperature dependent, which makes Eq. (2.11) non-linear. The temperature dependence of λ_T can be approximated by a power law in a wide range around room temperature [39, 48]

$$\lambda_\mathrm{T}(T) = \lambda_{\mathrm{T},0}(T/K)^\mathrm{n}\,, \tag{2.13}$$

where the exponent for many III-V binaries is $-1.6 \leq \mathrm{n} \leq -1.2$ and $\lambda_{\mathrm{T},0}$ is a constant. Consequently, the heat removal from the heat sources falls off nearly inversely with increasing temperature. An additional temperature dependence of χ is given by that of C. For a wide temperature range above room temperature it can be linearly approximated for most III-V binaries [39, 48]

$$C(T) = C_0 + \Delta C \cdot (T/K)\,, \tag{2.14}$$

where $\Delta C/C_0 \sim (1-4)\times 10^{-4}$ and C_0 is a constant, i.e., an almost negligible increase for the temperature rises experienced during laser operation.

Furthermore λ_T depends on the semiconductor alloy and exhibits a pronounced nonlinear behavior (i.e., bowing). Ternaries, for example, have a much lower thermal conductivity than the related binary alloys. The reason is alloy scattering which makes quaternaries particularly bad thermal conductors.[37, 39, 48]

Solutions for the differential equation (2.11) or its stationary counterpart are usually implemented for specific devices by the finite element method (FEM). In cooperation with expert external groups such simulations are used for comparison of the experimental results of this thesis, e.g., in Refs. 49 and 50 and in sections 4.3.1 and 5.1.

In many practical situations, if knowledge about the temperature distribution is not needed and only the temperature at the active region is important, the heat propagation can be characterized by the phenomenological parameter thermal resistance R_th. The temperature increase that corresponds to a certain heat power P_heat is given by

$$\Delta T = R_\mathrm{th}P_\mathrm{heat} = R_\mathrm{th}(UI - P_\mathrm{out})\,. \tag{2.15}$$

This relation allows for the approximate determination of the active region temperature relative to that of the heat sink by the single parameter R_th, provided the electro-optical characteristics (P_out - optical output power, U - forward voltage, I - injection current) are known. In section 5.1 this approach is used for the characterization of the transient thermal behavior of high-power diode laser bars mounted on different heat sinks.

2.2.3 Laser Performance Considerations

The main part of the heat is created within the active region (i.e., at the *pn*-junction) because both electrons and holes are electrically injected into it and since the photon density is highest there. All losses sum up and the overall wall-plug efficiency (WPE) is nowadays in the best case slightly better than 70%,[9–11] but usually it is closer to $50-60\%$, which results in a large amount of excess heat. Output powers of up to 1 kW from a single 1-cm-wide and 100-μm-high facet have been reported, although typical values are rather around 100 W.[5–8] For devices with such typical (or maximal, respectively) output powers from 1 mm (5 mm) long cavities this results in excess heat densities of 10^4 Wcm^{-3} (2×10^5 Wcm^{-3}) for WPE=0.5. The extremely high heat density that needs to be dissipated via a heat sink of footprint 0.1 cm^2 (2×0.5 cm^2) is about 1 kWcm^{-2} in both cases.[3]

---

[3] The devices with maximal power are cooled from both top and bottom.

Consequently, a big effort is directed towards increasing the WPE and optimizing the cooling of the device (cf. section 2.3.1). A reduction from, say 40% to 20% excess heat (i.e., WPE=0.6 to 0.8) would mean for a 10^2 W (10^3 W) output-power device a reduction of cooling need from 67 W (670 W) to 25 W (250 W). Such improvement would result in an even more widespread application of high-power devices, even in mobile devices.

All mentioned heating processes/losses increase with rising temperature and even the thermal resistance (inverse of the thermal conductivity) does. Such an increase in temperature is provided by self-heating (i.e., due to the losses) of the laser diode during regular operation. Regarding the large number of loss processes, an exact microscopic treatment of the temperature dependent P_{out} is extremely difficult, even more since those processes are interdependent and each of them follows different temperature dependencies.

A phenomenological treatment of the output power of a laser diode above lasing threshold involves the two phenomenological parameters threshold current I_{th} and differential quantum efficiency η_{d} [37, 39, 42]

$$P_{\mathrm{out}}(I,T) = \eta_{\mathrm{d}}(T)\frac{h\nu}{e}\left[I - I_{\mathrm{th}}(T)\right] . \tag{2.16}$$

The threshold current is a measure for all losses at threshold, whereas η_{d} describes the number of outcoupled stimulated photons of energy $h\nu$ per injected electron of charge e, both of which can be determined directly from the measured P_{out}-I-curve. The temperature dependence of the threshold current is usually approximated by

$$I_{\mathrm{th}}(T) = I_0 \exp\left(T/T_0\right) , \tag{2.17}$$

where T_0 is taken as constant near room temperature, and values close to 300 K indicate a good temperature stability. For η_{d} a similar relation can be given, however, with a much larger negative T_0 as for the I_{th} relation.[42]

The maximal I_{th} can be derived from inserting Eq. (2.17) into Eq. (2.15) [51]

$$I_{\mathrm{th,max}}(T_0, R_{\mathrm{th}}) = \frac{T_0}{R_{\mathrm{th}}U} , \tag{2.18}$$

which demonstrates that a high T_0 and a low R_{th} (cf. section 2.3.1) are vital prerequisites for achieving a low I_{th}, in particular for such high-power devices mentioned above. Equation (2.17) only holds for a limited temperature range since $T_0(T)$ is decreasing with temperature, because, in particular at elevated temperature, the mentioned losses increase nonlinear. Thus, self-heating at high injection currents increases I_{th} which leads to the so-called thermal rollover where P_{out} falls off with increasing I, and, if $I_{\mathrm{th}} > I_{\mathrm{th,max}}(T_0, R_{\mathrm{th}})$, lasing becomes impossible at all.

2.3 High-Power Semiconductor Lasers

2.3.1 Major Fabrication Steps and Techniques

The fabrication of high-power semiconductor laser diodes involves three major steps from epitaxy until final application. Figure 2.1 illustrates the device geometry of a typical cm-bar and serves for reference in this section.

Materials system and epitaxy: The vast majority of high-power laser diodes in the visible to near-infrared spectral region are implemented on GaAs or InP substrates, where GaAs-based devices, of exclusive concern in this thesis, cover wavelengths between 630 and 1060 nm.[52] The epitaxial layer structures employ binary, ternary, and quaternary alloys of the (AlGaIn)-(AsP) III-V compound family[4]. In order to avoid detrimental misfit dislocations, the thick waveguide and cladding layers need to be lattice matched to the (100)-oriented GaAs substrate, in contrast to the QW which is commonly strained to facilitate a higher wavelength agility and for reasons of threshold reduction.

Epitaxial growth of modern high-power laser diodes demands, amongst others, for accurate thickness control on the nm-scale because of the employed QW-gain region. On the other hand, a high throughput is necessary for economical reasons. Both boundary conditions are fulfilled by molecular-beam epitaxy and metalorganic vapor-phase epitaxy (MOVPE) which facilitate growth rates of up to $1-2$ μm/h.[52, 53]

Processing: Optical waveguiding in the layer plane is usually provided either by gain guiding or by index guiding.[39, 53, 54] Gain guiding for the planar stripes used in this work is facilitated by restricting the injection current to a narrow window via metallization of the stripe region and passivation of the outer regions by electrically insulating layers (e.g., SiN_x, SiO_2) or by ion implantation (e.g., by He^+ ions).

The next step is metallization of the top and bottom sides.[53, 54] Depending on the semiconductor material and the doping several different metals are regularly evaporated or sputtered on the highly-doped semiconductor contact layers. Ohmic contacts for efficient current injection are formed by thermal alloying.

If lateral arrays (i.e., bars) are produced, the individual emitters are electrically (though still connected through the substrate and *n*-contact metal)

---

[4] Throughout the thesis abbreviations for the semiconductor alloys are used according to Appendix F and Ref. 43. The main reason for that is nondisclosure of the manufacturers which does not allow for citing exact compositions and layer thicknesses.

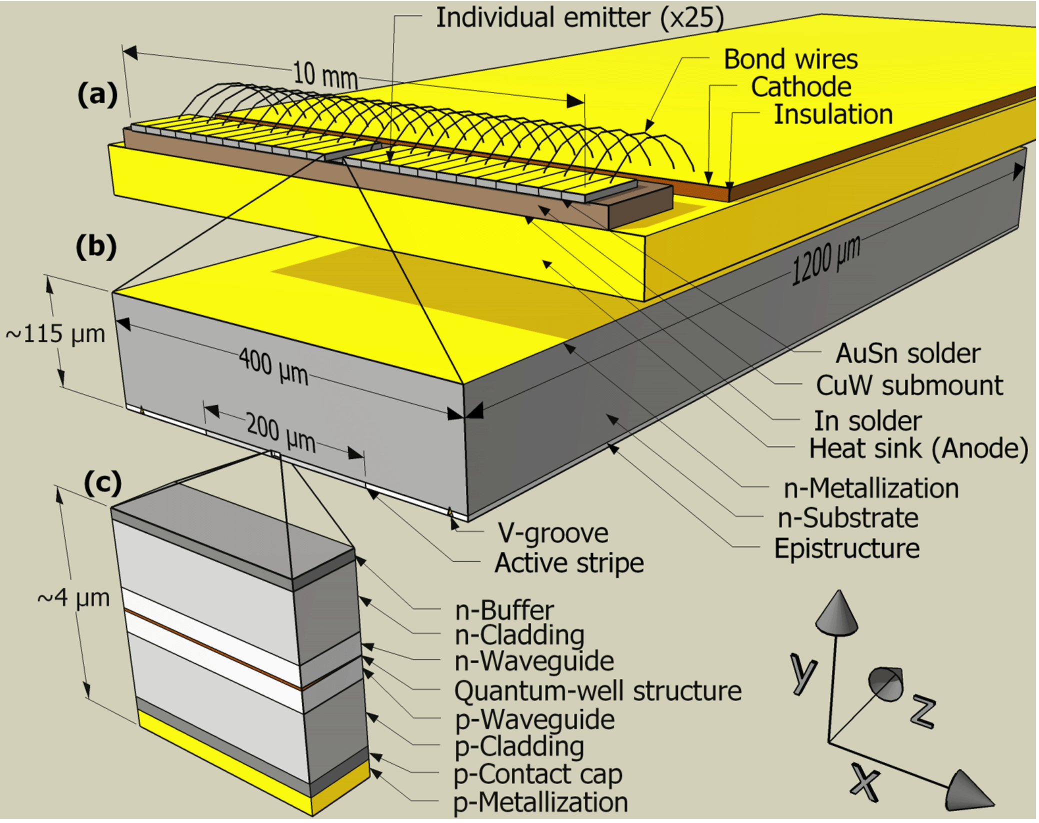

Figure 2.1: **(a)** Schematic of a typical high-power cm-bar device with 25 emitters as used for sample **QW-808-1-bar**. The bar is soldered with AuSn onto a CuW heat sink that is soldered with In onto a thin micro-channel heat sink. **(b)** Schematic of a single individual emitter of the bar. The active stripe is 200 μm wide. The geometry is p-side down. **(c)** Schematic of the epistructure with p-metallization. The standard coordinate system of this thesis is indicated.

and optically separated by deeply etched grooves, which also prevent lasing perpendicular to the designed resonator axis.

From cleaving mostly perfect and parallel mirrors are formed at the front and rear facet. The subsequent facet processing serves for protection purposes and reflectivity control. The most severe limitation regarding the facets is due to COD (cf. section 5.3). Several different proprietary techniques for facet passivation, including cleaning and coating, exist that all aim at a reduction of additional facet heat sources. Since after cleaving the laser facets exhibit (normal-incidence) reflectivities of $\sim 30\%$, additional high-reflection (HR) at the rear facet and anti-reflection (AR) coating at the front facet support reflectivities of $\gtrsim 90\%$ and $\sim 3-20\%$, respectively, in order to direct the laser beam out of the front facet only.

Packaging and cooling: The high power densities achieved during operation of high-power laser diodes and, in particular, of laser arrays demand for highly efficient cooling.[55] Usually, a high-power laser diode is soldered p-side down onto a rigid heat sink which simultaneously acts as the anode. The cathode is either provided by wire bonding or soldering of metal sheets onto the top n-contact metallization.

The thermal resistance of the assembly represents an important key figure in packaging. With regard to Eqs. (2.15) and (2.18) the lowest possible values are vital for high-power operation. The heat is dissipated either by a conductive heat sink, usually made from copper, mounted on a thermoelectric cooler, or by a convective heat sink, where the (copper) block contains several micro channels. The coolant that is usually water flows with a constant rate only some 100 μm below the semiconductor chip. Optimized heat sinks with micro-channel widths on the order of 100 μm outperform conductive heat sinks by almost an order of magnitude and reach numerical values significantly smaller than 1 K/W.[55, 56] In section 5.1 a comparison of the transient thermal behavior of the two heat-sink types is discussed.

Since the mismatch of the coefficient of thermal expansion (CTE) between the semiconductor chip and the heat sink introduces a strain in the thin semiconductor chip during soldering, much attention is drawn towards CTE-matched heat sink concepts (cf. sections 2.4, 5.2). This is the main reason why for extended devices such as laser arrays the standard Cu heat-sink, where the semiconductor chip is soldered on with In, is nowadays about to be replaced by CTE-matched heat-sink materials like CuW. Besides this issue, a CTE-matched heat sink allows for a stiff solder like AuSn which shows long-term reliability superior to In.[56]

2.3.2 Output Power Scaling

Since there is an ever-growing demand for reliable high output powers, certain power scaling techniques can be explored. Even for highly efficient devices such scaling needs to take into account several issues that limit the available parameter space. Among others, thermal power management is one of the key issues that makes a tool like thermography for thermal analysis necessary.

Stripe width scaling: Widening of the stripe directly scales the achievable output power but at the price of a reduced beam quality. Lasers with wide stripes ($\sim 50 - 200$ μm) are called broad area (BA) lasers and allow, in contrast to single-mode lasers with narrow stripes, multiple spatial modes. Lateral mode instabilities and filamentation can result, leading to a higher risk for COD failure (cf. section 5.3). The total dissipated thermal power that can be removed by heat conduction limits the stripe width to about 200 μm.[54]

Resonator-length scaling: Longer resonators allow lower threshold current densities due to reduced mirror losses.[57] The main effect at high powers is, however, the lower thermal resistance for longer devices,[5, 7, 8] which leads to a later thermal roll-over.[5–8] Common values for the resonator length are around 1 mm and reach up to 5 mm for ultra-high output powers.[5–8] On the down-side, the facet area stays constant during power scaling, being principally limited by COD.

Lateral array formation: Alignment of the stripes into an array with passive regions in between scales the output power.[54] However, the individual beams need to be coupled and the strain that is induced due to CTE mismatch between semiconductor and heat-sink materials can enhance power-degradation (c.f. sections 2.4, 5.5). A typical width for high-power devices is 1 cm (i.e., *cm-bar*) containing 19-100 individual emitters. The thermal power-density limitation also limits this power scaling technique to filling fractions significantly below 1.

Vertical array stacking: A further output-power increase to the kW-range is achieved by vertical staking of arrays.[4]. This uncouples the (lateral) arrays thermally, but also optically. Hence, even more involved as for the lateral arrays, collimating optics for beam combination is necessary.

2.4 Physical Aspects of Semiconductor Laser Degradation

2.4.1 Defects in Semiconductors

Degradation of semiconductor optoelectronic devices is intimately related to the presence of defects. The crystalline long-range periodicity is interrupted by the emergence of defects leading to distortions in the electronic band structure and to the generation of additional localized electronic states. Those cause additional electron and photon scattering, absorption, and emission, and may behave as acceptors or donors at various energetic positions within the band gap. The presence of defect states lowers the nonradiative lifetime because defect sites often serve as nonradiative recombination centers (traps), in this way directly lowering the internal quantum efficiency.

The classification of crystal defects is traditionally inspired by their dimensionality. [58, 59] Point defects are zero-dimensional. Native or intrinsic point defects can consist of anti-sites, vacancies, and interstitial. Extrinsic point defects are divided into substitutional and interstitial ones. The size of point defects varies from single atoms to clusters and large complexes of them. One-dimensional defects are dislocation lines. Two-dimensional defects are, e.g., dislocation loops and stacking faults. Three-dimensional defects are, e.g., precipitates, inclusions, voids, and stacking faults.

Another classification of defects is given by their energetic configuration. Two principal classes need to be distinguished. First, defects that effectively behave like hydrogen atoms within the host crystal have an electronic structure that can be approximately described by an effective mass. They are called hydrogenic impurities or shallow impurities with very small binding energies (< 100 meV) compared to the band-gap energy, and are easily ionized at room temperature. The second class, so-called deep-level defects (DL defects) or deep centers, does not obey a hydrogenic character. Their tightly spatially localized nature makes them difficult to treat by simple symmetry arguments. Furthermore, the interaction with the lattice makes their microscopic treatment even more difficult. In general, these DL defects are mostly responsible for the degradation in semiconductor lasers. Consequently, device degradation is almost always restricted to a phenomenological analysis. Since modern epitaxial growth of GaAs-based laser diodes is practically free of other than point defects[5], only these DL point defects should be of concern in the following.[62]

---

[5] Due to thermodynamic reasons there will be always point defects in a crystal lattice at finite temperature, even in thermal equilibrium.[60, 61]

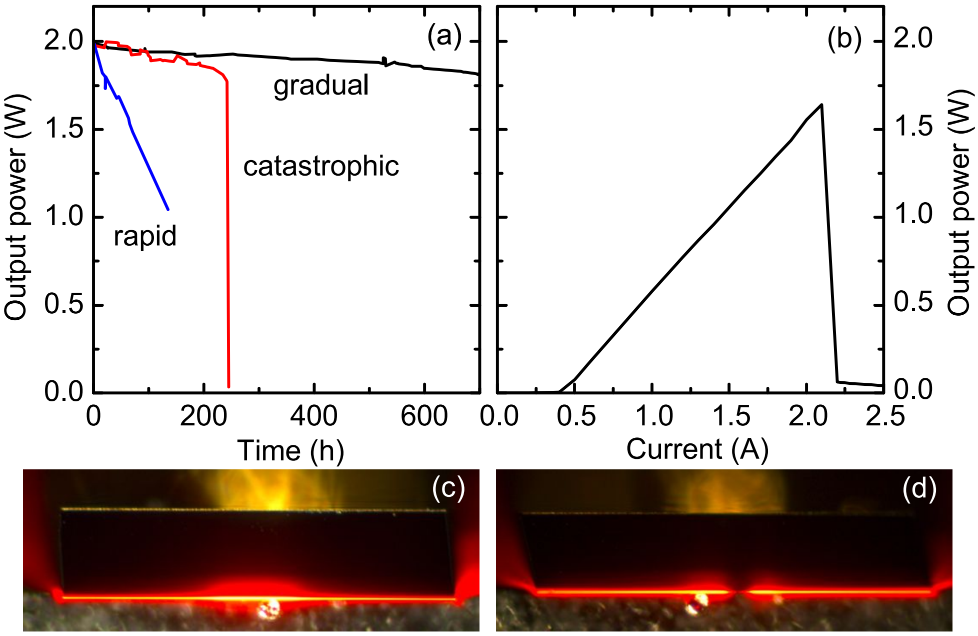

Figure 2.2: **(a)** Optical output-power degradation of laser diodes driven at constant injection current vs operation time, divided into gradual, rapid, and catastrophic degradation. **(b)** Output power of a BA red-emitting high-power laser vs injection current. Around 2 A COD occurs along with a sharp drop in output power. **(c,d)** Micrographs of laser diodes such as in (b) showing red electroluminescence at low injection currents of 10 mA, **(c)** before, and **(d)** after COD.

2.4.2 Degradation of Semiconductor Lasers

Degradation of semiconductor lasers means a reduction in output power with time. Figure 2.2(a) provides the usual phenomenological classification into three different degradation modes [58, 63–65]:

Gradual degradation is related to a progressive decrease of the output power during regular operation, mainly associated with a decrease in quantum efficiency due to an increase in the (point) defect density. Gradual degradation usually defines the lifetime of the device. In general, from this mode the accumulative nature of degradation becomes most clear.

Rapid degradation is a rapid decrease of the output power, typically within the first 100 hours of operation. This mode points to very severe causes, often to the presence of dislocations that are elongated during operation or that move through the crystal. In luminescence experiments often dark lines or spots of drastically reduced luminescence are observed which extend along the device.

Catastrophic degradation exhibits a very pronounced drop in the output power, resulting in an inoperable device, or, in case of extended laser diodes, to a device with failed parts. The origin for catastrophic degradation may lie inside the device or at the facets. The most important case in state-of-the-art devices is due to damage starting at the outcoupling facet, called catastrophic optical (mirror) damage (COD). Usually this mode limits the maximal output power of a laser device and, consequently, is observed predominantly at high injection currents.

Package-related degradation is, in particular for high-power devices, a major issue. Mainly two scenarios can be distinguished. In the first scenario, degradation of the solder or the contact is possible due to several reasons: thermo- and electro-migration of the solder [66–70]; interdiffusion of the semiconductor contact layers with the contact or solder metals leading to clusters or whiskers; interaction of different contact and solder metals creates intermetallics.[71] All those processes introduce inhomogeneities in thermal and electrical conductivity. In the second scenario the heat sink degrades. In case of active cooling, e.g., erosion and corrosion lead to an effective dissolution of the metallic micro-channel structure.[56]

Driving forces of laser degradation

The driving forces of laser degradation deliver the energy necessary to generate, migrate, and accumulate defects. In particular under high-power regime, it seems very likely that all of them couple or even build up positive feedback loops.[58, 62–65, 72–74]:

Mechanical strain is introduced by various mechanisms during processing. As a result, large-scale and localized strain fields and gradients may occur which influence the defect generation rate and their migration. Furthermore, always if strain is present, it can be thought of mechanisms to relief it by introduction of defects such as dislocations. Inside strain fields interstitials or vacancies can migrate, eventually accumulating to larger complexes. On the other hand, the utilization of strained epitaxial layers in modern lasers is not necessarily enhancing degradation, provided that the critical thickness limitation for dislocation-free growth is preserved.[75] A relation between strain introduced during device packaging and enhanced point-defect concentrations has been demonstrated repeatedly (see, e.g., section 5.5 and Refs. 76–78).

Heat generated in the bulk or at the facets is principally found to accelerate degradation. The thermal activation of power degradation from a level P_0 with time t can be described by $P = P_0 \exp(-\beta t)$ with the degradation rate $\beta = \beta_0 \exp(-E_\mathrm{a}/kT)$. β_0 is a constant and E_a the corresponding activation energy. Often gradual degradation is described in this way with $E_\mathrm{a} \sim 0.6 - 1.0$ eV for GaAs-based lasers and LEDs. The average temperature increase of the active region of laser diodes operating at room temperature is usually in the range of 20-50 K, which corresponds to a thermal energy of ~ 30 meV. Such a low value makes thermally activated degradation very slow unless there is a way to increase the temperature locally and/or temporally to much higher values like in the process described in the next point. An indirect effect of heat is due to thermal expansion leading to additional strain.

Nonradiative recombinations are responsible for the so-called recombination enhanced defect reaction which is a process for the generation, propagation, and the reaction of defects. The excess energy from nonradiative recombination at an existing DL defect can be released as vibrational energy, concentrated at the point defect. Such amount of energy ($\sim 0.6 - 1.0$ eV in GaAs-based devices), given by the energetic position of mid-gap DL defects, is within the range of activation energy for the creation of a new point defect or the migration of an existing one. This process is found responsible for the elongation of dislocations and extension of point defect complexes. The necessary minority carriers are generated from electrical current injection or from reabsorption of radiation.

Photons can provide vibrational/thermal energy if absorbed in the bulk or at the facets and if the photoexcited carriers recombine nonradiatively, e.g., as in the above mentioned process. If this process happens at or near the facets, the facets are heated. The high photon density at the low-reflective front facet is mainly responsible for the COD degradation mode.

Existing defects such as dislocations and point defects are precursors for further defect accumulation, for instance by recombination enhanced defect reaction. Even if the as-grown laser die has a low defect density, during processing further defects can be introduced, which, e.g., can attract further point defects. In any case, the presence of defects enhances degradation.

2.4.3 Catastrophic Optical Damage

The COD of laser diodes is certainly the most spectacular degradation mode. The first time-resolved thermography study of the COD in laser diodes is presented in section 5.3, and here some physical aspects will be discussed.

COD mechanism: The COD process is commonly explained by a thermal runaway process.[73, 79, 80] Reabsorption of laser light leads to strong local heating, eventually reaching a critical temperature level where the feedback loop of thermally induced band gap shrinkage and reabsorption enhancement cannot be balanced anymore by the thermal conductance of the semiconductor materials.[81] As a result, the semiconductor materials start to melt locally.[79, 82] The melt front propagates along the resonator as long as enough heat is provided by further absorption. After successive re-crystallization a network of defects is left behind, which leads to a vastly increased nonradiative recombination rate, eventually shifting the lasing threshold to higher values or even makes lasing impossible at all. The damage can be recognized as dark regions in the electroluminescence pattern; see Fig. 2.2(c,d).

Spatial extension of the defect network: The spatial extension of the resulting defect region is found to be confined to approximately 50-200 nm in vertical direction, i.e., to the QW and part of the waveguide.[82–86] In lateral directions, the widths vary widely between values on the order of $1 - 10$ μm at the front facet.[82, 84, 86, 87] While this region extends along the resonator up to a high fraction of its total length, a spreading into many branches is possible, reaching lateral extensions of up to a high fraction of the total stripe width, i.e., of many 10 μm for high-power BA lasers.[82, 84] The explanation for this behavior is related to the pumping geometry and the composition of the materials. The optical pumping extends along the lateral dimension to the stripe width, it is modulated by filamentation, and can be characterized by measuring the optical near-field. In the vertical dimension the optical mode profile (with a width similar to the waveguide) determines the amount of optical facet load. In the case of GaAs-based lasers, barrier layers such as the waveguide and cladding usually contain a high mol-fraction of Al. Hence the melting point of these layers is much higher than that of the QW materials, e.g., for GaAs it is $\sim$ 1500 K whereas for AlAs it is $\sim$ 2000 K.[88] Consequently, it is more likely for the QW to melt before the surrounding materials reach their melting points. Also it is possible that a change in the III-V stoichiometry (e.g., by diffusion of group-V atoms out of the lattice) may occur at considerably lower temperatures of a few 100°C.[83, 89] However, not all aspects of the microscopic processes have been uncovered yet, partly due to a lack of sufficient spatio-temporally resolved studies. That renders one of the motivations for the case study described in section 5.3.

Paths toward COD: Different paths toward COD are known; it can be induced, e.g., by operating the laser diode at a high injection level for a longer time or by increasing the injection current beyond the COD threshold; see Fig. 2.2(a,b). The destructive process, however, shows always the same or at least very similar characteristics. The difference between both paths mainly lies in how the laser diodes reach their critical temperature at the front facet. Three main processes can be identified that lead to the detrimental facet heating: (i) Nonradiative recombination of carriers from reabsorption (e.g., interband absorption) of laser light at the front facet or optical absorption at non-semiconductor materials, i.e., at the facet coating or at oxides and pollutants (short: reabsorption heating); (ii) Nonradiative recombination of carriers at surface states injected from the *pn*-junction (short: surface-recombination heating); and (iii) Heating of the bulk materials always offsets any heating at the front facet (short: bulk heating). The two recombination heating mechanisms are obviously subject to the quality of the facet. If the quality is poor, e.g., if it contains a high density of surface states, facet heating increases. It is known that operation of the device leads to alteration of the facet or even the bulk materials near the surface, thereby experiencing chemical processes such as oxidation, which increase the defect density or the absorption strength.[62, 64, 89–92]

Improvements against COD: The most promising techniques to improve the laser diodes against COD are given by optimization of the laser facets. Proper passivation of the facets against oxidation lowers the heating due to optical absorption of the laser light and lowers surface-recombination heating.[11, 73, 92–95] Another technique is to increase the band gap energy near the facet by QW intermixing (nonabsorbing mirror) in order to reduce reabsorption heating and carrier diffusion toward the facet.[73, 96–98] Another way of increasing the maximal output power is to decrease the optical power density at the facet by way of a broad waveguide with a low optical-confinement factor.[99]

2.5 Description of the Laser Samples

The high-power laser diodes that are analyzed in this thesis are designed for wavelengths of 650, 808, and 980 nm, each with different epitaxial design and device structure. All QW laser structures are grown by MOVPE on *n*-type GaAs substrates, and the QD laser by molecular beam epitaxy. Due to reasons of nondisclosure by the manufacturers exact compositions and layer thicknesses cannot be given in the following.

QW-808-1-bar The first 808 nm design is used in **sections 3.1**, **3.2**, **5.1**, and **5.2**. The epitaxial structure consists of an undoped compressively strained AlGaInAs single QW, surrounded by *n* and *p*-type $\mathrm{Al_{0.4}Ga_{0.6}As}$ waveguide and $\mathrm{Al_{0.6}Ga_{0.4}As}$ cladding layers.

The laser-diode arrays (cm-bars) consist of 25 large optical cavity emitters with a stripe width of 200 μm and a pitch of 400 μm. The outer chip dimensions are 1.2 mm × 10 mm × 115 μm (length×width×height). The facets are passivated with standard dielectric HR and AR mirror coatings. Threshold currents are about 13 A with slope efficiencies of about 1.15 W/A. Optical output powers are in the range of 50-80 W. Mounting on different heat sinks is described in section 5.2. More detailed information on the laser bar can be found in Refs. 100, 101.

QW-808-2-BA The second 808 nm design is used in **sections 4.1.2**, **4.3**, **4.2.3**, and **5.4**. The epitaxial structure consists of an undoped tensile strained GaAsP single QW, surrounded by asymmetric waveguide layers, namely *n*-type GaInP and *p*-type AlGaAs. The cladding layers consist of *n* and *p*-type AlGaAs.

The BA lasers are designed for high-temperature (i.e., 50°C heat-sink temperature) purposes. The chip dimensions are $1500 \times 500 \times 115$ $\mu\mathrm{m}^3$ (length×width×height) and the active stripe width is 130 μm. Standard cleaning, passivation, and coating processes are applied to both facets. The devices are hard-soldered with AuSn *p*-side down onto 300-μm-thick CuW heat spreaders that are attached to copper C-mounts. Threshold currents are 0.6 A and typical output-power levels are at about 4 W at 5 A, with a maximum output power of up to $\sim$ 10 W at 13.5 A. More details on the structure is given in Ref. 102.

QW-650-1-BA This 650 nm design is used in **sections 5.3** and **5.4**. The epitaxial structure consists of an undoped GaInP single QW, surrounded by *n* and *p*-type AlGaInP waveguide and cladding layers with Te and Mg as

n and p dopants, respectively. The BA lasers are grown by MOVPE on a (100), 6° towards $(1\bar{1}\bar{1})$ off-oriented n-GaAs substrate.

The front and rear facets are asymmetrically coated with Al_2O_3 and Al_2O_3/Si, for low ($R = 0.18$) and high reflectance ($R = 0.95$) respectively. The chip dimensions are $1200 \times 500 \times 115$ μm^3 (length×width×height) and the planar active stripe width is 100 μm, which is defined by 10 μm-wide trenches etched into the GaAs cap layer and by passivation outside the stripe with a dielectric. The lasers are mounted with AuSn p-side down via AlN_x submounts on copper C-mount heat sinks. Threshold currents are 0.4 A and slope efficiencies of 0.9-1.0 W/A are observed.

QW-650-2-bar The second 650 nm design is used in **section 5.5**. The epitaxial structure consists of an undoped GaInP compressively strained double QW, surrounded by n-type AlGaInP and p-type AlGaAs waveguide and cladding layers.

The cm-bars consist of 19 emitter sections with a pitch of 500 μm, each with an active stripe width of 30 μm. The outer chip dimensions are 750 μm× 10 mm × 115 μm (length×width×height). The devices are hard soldered with AuSn p-side down onto CuW submounts which are attached to copper heat sinks.[103] Threshold currents amount to 3.1 A with slope efficiencies of 1.2 W/A. More details on this epitaxial structure can be found in Ref. 104.

QD-950-BA The 950 nm QD design is used in **section 4.3**. The 2.5 μm thick core region is based on $Al_{0.3}Ga_{0.7}As$ and contains three layers of highly strained $In_{0.53}Ga_{0.47}As$ QDs spaced within 30 nm of GaAs spacer layers.

The BA lasers were fabricated using TiPtAu as the p-side contact metallization and AuGeNi as the n-contact metallization. The SiO_2 isolated stripes are 50 μm wide. The chip dimensions are $1500 \times 500 \times 115$ μm^3 (length×width×height). The devices are p-side down packaged with In onto copper C-mounts. Threshold currents amount to 0.45 A at a slope efficiency of 0.72 W/A. More details on such QD structures can be found in Ref. 105.

2.6 Thermal Radiation

2.6.1 Planck's Blackbody Radiation

In 1900 *Max Planck* found the spectral distribution of the energy of thermal radiation.[32–34] The law which has been named after him can be written in a form to describe the spectral radiance of a blackbody

$$L_{\nu,\mathrm{BB}}(\nu,T) = \frac{2h\nu^3}{c^2\left(e^{\frac{h\nu}{kT}}-1\right)}\,, \tag{2.19}$$

that is the power radiated from a source per solid angle $d\Omega$, frequency interval $d\nu$ and area dF at frequency ν and absolute temperature T. The only parameter is the temperature which makes this formula universal.

In the derivation Planck assumed a cavity filled with electrically charged linear harmonic oscillators that exchange energy with an electromagnetic field, all in thermal equilibrium with each other. The modal density for such a (three-dimensional) cavity $M(\nu) = 8\pi\nu^2/c^3$ was known from classical electromagnetic theory. On the other hand, the average energy per mode must not be a constant $\overline{E}(T) = kT$, which would be in accordance with the law of equipartition of energy in classical statistical mechanics, but rather proportional to ν, the frequency of the oscillator: $\overline{E}(\nu,T) = h\nu/[\exp(h\nu/kT)-1]$. With the spectral energy density $u(\nu,T) = M(\nu)\overline{E}(\nu,T)$ the spectral radiance in Eq. (2.19) is then given by $L_{\nu,\mathrm{BB}}(\nu,T) = u(\nu,T)c/(4\pi)$. The ansatz for $\overline{E}(\nu,T)$ that assumed integer multiples of $h\nu$ as the allowed energies for the oscillators and that lead to the correct description of the blackbody spectrum, is seen as the birth of quantum theory.[38, 106, 107]

Differentiation of Eq. (2.19) in the wavelength formulation with respect to λ gives the wavelength for which the thermal radiation spectrum of a blackbody has maximal intensity [108]

$$\lambda_{\mathrm{max}}(T) = \frac{2897.8\ \mu\mathrm{m}}{T/K}\,. \tag{2.20}$$

This is *Wien's displacement law* (dotted line in Fig. 2.3) which demonstrates that the thermal radiation for room-temperature has its maximum at $\lambda_{\mathrm{max}}(300\ \mathrm{K}) \approx 9.7\ \mu\mathrm{m}$, whereas the visible spectrum (grey shaded area) is given by the surface temperature of the sun ($\sim$ 5800 K). The thermography as studied here probes at slightly shorter wavelength (light grey shaded area, $3.4 - 6.0\ \mu\mathrm{m}$) as compared to the maximal emitted power from operating laser diodes of temperatures around $300 - 350$ K.

Integration of Eq. (2.19) over the hemisphere Ω, the radiating area F, and all photon frequencies yields the total radiant power emitted from a

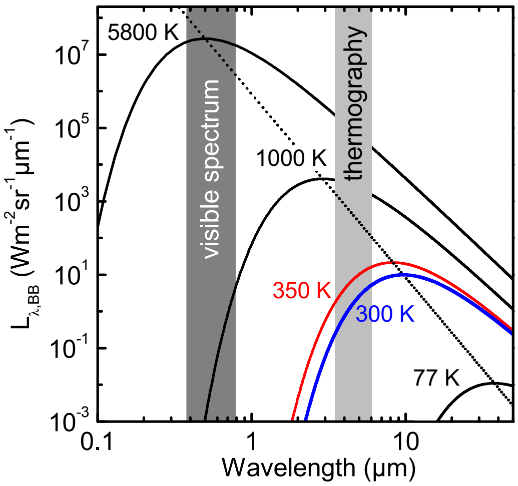

Figure 2.3: spectral radiance of a blackbody in wavelength formulation $L_{\lambda,\mathrm{BB}}(\lambda,T) = \frac{2hc^2}{\lambda^5}\left[\exp\left(\frac{hc}{\lambda kT}\right)-1\right]^{-1}$ at temperatures between that of liquid nitrogen (77 K) and the sun surface (5800 K). The latter defines the visible spectral range, whereas thermography as studied here probes at wavelengths between 3.4 and 6.0 μm. Temperatures between 300 and 350 K mark the relevant range of temperatures of operating laser diodes. The locus of the maxima is given as dotted line.

blackbody at temperature T as

$$P_{\mathrm{BB}}(T) = \int_{\Omega}\int_{0}^{\infty}\int_{F} L_{\nu,\mathrm{BB}}(\nu,T)\cos\theta\, d\Omega\, d\nu\, dF = \sigma T^4 F\,. \tag{2.21}$$

This is the *Stefan-Boltzmann law* with the Stefan-Boltzmann constant $\sigma = \pi^2 k^4/(60\hbar^3 c^2) = 5.6704\times 10^{-8}\ \mathrm{W\,m^{-2}\,K^{-4}}$.

2.6.2 Thermal Radiation from Real Materials

Hitherto the term blackbody is still lacking definition. The definition *Kirchhoff* (1859-60) gave relates to an object that is a perfect absorber of all incident radiation and, at the same time, a perfect emitter of it.[108]

The proportionality factor between a blackbody and a real body is called emissivity. The directional-spectral emissivity $\epsilon_\nu(\nu,T,\theta,\varphi)$ of radiating real materials, a dimensionless quantity, is defined as the ratio of the spectral radiance of this object from the direction (θ,φ) to the spectral radiance of a blackbody at the same temperature

$$\epsilon_\nu(\nu,T,\theta,\varphi) = \frac{L_\nu(\nu,T,\theta,\varphi)}{L_{\nu,\mathrm{BB}}(\nu,T)}\,. \tag{2.22}$$

Kirchhoff's law states that for thermodynamic equilibrium the directional-spectral absorptivity is equal the directional-spectral[6] emissivity [108]

$$\epsilon_\nu(\nu,T,\theta,\varphi) = \tilde{a}_\nu(\nu,T,\theta,\varphi)\,. \tag{2.23}$$

---

[6] In principle, the equality only holds for each component of polarization, however, for a blackbody both components are equal.

Consequently, according to energy conservation, the directional-spectral emissivity is related to the directional-spectral reflectance and directional-spectral transmittance by

$$\epsilon_\nu(\nu, T, \theta, \varphi) = 1 - \tilde{\varrho}_\nu(\nu, T, \theta, \varphi) - \tilde{\tau}_\nu(\nu, T, \theta, \varphi)\,. \tag{2.24}$$

Emittance of real materials

Note, the term *emissivity* denotes the physical quantity and is also used for the description of general material properties. The emissivity of a specific sample is usually referred to as *emittance*. In the following, the term *emittance* is always used for the description of the experiments and theoretical considerations.

Emittances of real materials differ considerably from the spectrally flat behavior of black or grey bodies, where the latter are characterized by a constant less than 1. For radiometric temperature measurements like thermography, special coatings have been developed for nearly grey characteristics (cf. section 3.1). The emittance of solid state and semiconductor materials depends on material, surface treatment, and geometry. The lack of exact knowledge of the parameters poses the cardinal problem of a radiometric determination of temperature as will be discussed in great detail in the following chapters.

For most III-V compound semiconductors the range of minimal optical absorption overlaps with the spectral probing range of typical thermographic systems ($\sim 3 - 6\ \mu$m). This effectively changes the situation from an opaque material to a transparent or semitransparent material. The issues arising from this property are discussed throughout the thesis as well.

Kirchhoff's law for nonequilibrium systems

The derivations of Planck's and Kirchhoff's laws are based on a theoretical construct stating (global) thermodynamic equilibrium of the ideal blackbody with its surrounding radiation field in an perfectly absorbing enclosure. Later, Einstein who recognized the quantization principle behind Planck's formula, [109–111] introduced a two-state atomic system in equilibrium with the surrounding radiation field and deduced the famous relation between spontaneous emission and stimulated absorption (or emission).[112]

For practical applications these assumptions need to be relaxed further. For instance, thermography of operating laser diodes cannot support such a global thermodynamic equilibrium allowing no net heat transfer. Also the carriers (electron-hole pairs) of the inverted laser diode (i.e., with positive gain) are not in thermodynamic equilibrium with the radiation field, simply because stimulated emission additionally depends on the photon density and not on the electronic system and temperature alone. At laser emission wavelength, the emitted power is by far exceeding that of a blackbody at the same temperature. However, this luminescence radiation is created nonthermally and such the above laws do not hold for this part of radiation.

Nevertheless, often the restriction to global thermodynamic equilibrium can be relaxed, to a very close approximation, in favor of local thermodynamic equilibrium. The extension of Kirchhoff's law to such commonly met nonequilibrium systems is given by the (experimentally evidenced) assumption that in most cases the emission and absorption properties are independent on the surrounding radiation.[108] It has been shown that Kirchhoff's law remains valid for a freely radiating body whose atomic states are in equilibrium, independent on the radiation field.[113–115]

Further analysis[7] lead to the conclusions that it stays valid in a nonequilibrium environment and even for nonequilibrium electron distributions as for instance in a laser diode. Then local equilibrium distributions needs to be defined instead.[114, 116–118] Such local equilibrium distributions exist in laser diodes and are described by three parameters, the quasi Fermi levels for electrons F_e and holes F_h, and the lattice temperature T. Except from the case of highly excited systems within very short times, where non-thermalized carriers exist (on the order of $t < 1$ ps) or the carrier distributions are excited to an effective temperature higher than the lattice (hot carriers; on the order of 1 ps $< t <$ 1 ns), the temperature of the electrons and holes equal that of the lattice.

Hence, thermography of non-operating and operating laser diodes is assumed to reflect the true temperature of the lattice and the carriers, and the laws of Planck and Kirchhoff stay valid. In chapter 3 Kirchhoff's law is applied explicitly and throughout this thesis Planck's law is used as well.

---

[7] It is argued that the validity follows from the reversibility of the microscopic equations of motion, that is an outgoing wave at time t is equivalent to an incoming wave at time $-t$.[116, 117]

2.7 Spectroscopic Techniques

2.7.1 Thermography and Competing Techniques

Thermography[8] is the principal characterization technique of this thesis. Due to generality of Planck's law (2.19) it is applicable to a wide class of problems. In principle, if the demand is not for the utmost possible accuracy, only the single parameter emittance (2.22) must be known to straight forward receive a temperature information; a fact that is made use of in pyrometers (or infrared thermometers). Application of detector arrays enables 2D temperature determination. This direct temperature mapping of nearly arbitrary materials is the unique feature of thermography which consequently entered into many fields of application, for instance: night vision for defense applications, thermal analysis of buildings and infrastructure, materials evaluation, process and product monitoring and control, bio-medical imaging, characterization of electronic devices such as power transistors or solar cells.[18, 19, 119]

Thermal radiation is spontaneously emitted from the sample and infrared (IR) optics image its distribution onto a 2D detector array usually made of HgCdTe, InSb, PtSi, or QWIP (QW IR photodetector) for the atmospheric windows around $2-5$ μm and $8-13$ μm with sensitivities up to 10 mK.[19, 120–123] The diffraction limit of ~ 6 μm is reached by application of microscope optics (cf. sections 4.3.2). The temperature of the sample can be calculated from the detected thermal radiation via Planck's law, given a known emittance, or - if unknown - a calibration measurement under controlled conditions can be performed (cf. section 4.1). A detailed description of the used thermographic setup and the methodology follows in chapter 4.

Thermography of semiconductor lasers

Available literature on thermography of semiconductor lasers is rare. In 1975 one group reported on temperature analysis of GaAs-AlGaAs double-heterostructure laser diodes obtained through a window at the n-side.[20–22] In 1995 another Bell Labs group reported on rather qualitative results for modeling purposes obtained again through a n-side window and from the side of high-power QW lasers.[23, 24]. Only recently (2002) new activity started on thermography of LEDs [25] and on qualitative inspection of the solder quality of high-power arrays by imaging the n-contact.[26] Also vertical stacks of high-power laser bars have been thermographically inspected

---

[8] In order to avoid ambiguities, the term thermography is used in this thesis exclusively to denote the described technique. Other denotations that appear in literature are, e.g., infrared thermography, thermal imaging, and infrared microscopy.

with very low spatial resolution from the front facet.[27] Thermography of high-power devices started in 2004 at the Max-Born-Institut and lead to the ability to image the front facet of single stripe lasers and to detect hot-spots (i.e., localized sites of increased signal magnitude).[28] Later, arrays were inspected and an additional short-wavelength non-thermal spectral component was found (for discussion see section 5.4)[29] that indicated a correlation with degradation behavior of single-stripe lasers.[30]

This work is continued in the present thesis, exploiting a wider range of applications adopted to the special advantages of the thermography technique, which are in particular its fast and spatially resolved imaging capabilities for a number of different materials. Furthermore, physical principles relating to the semiconductor materials are thoroughly analyzed and used to provide a more profound basis for thermography of semiconductor lasers.

Alternative techniques for temperature determination

Alternative techniques make use of the temperature dependence of particular physical processes in semiconductor lasers. Since the laser is operating at high output power, contact techniques or techniques that use (micro-) probes close to the laser output facet are ruled out,[124, 125] as well as covering of the laser facet with paints or temperature sensitive materials.

Through their temperature dependence the P_{out}-U-I characteristics may serve as temperature probes, provided, however, that earlier made calibrations of the studied device against temperature exist. Either the dissipated power [via Eq. (2.15)], the forward voltage across the pn-junction[9],or the threshold current [via Eq. (2.17)] can be exploited.[126, 127]

Analysis of the emission wavelength shift: The standard method is the spectroscopic determination of the emission wavelength shift, in particular, since the emission spectrum is usually determined anyway. The basic process behind is the temperature dependence of the fundamental band gap that decreases with temperature, approximated by the empirical Varshni-formula $E_{\mathrm{g}}(T) - E_{\mathrm{g}}(T = 0) = -\alpha T^2/(T + \beta)$, with $\alpha = 0.5405$ meV/K and $\beta = 204$ K in the case of the direct gap at the Γ-point of bulk GaAs $E_{\mathrm{g}}(300\ \mathrm{K}) = 1.4225$ eV.[43, 88, 128] At room temperature the emission spectrum experiences a red-shift of $dE_{\mathrm{g}}/dT \approx -0.45$ meVK^{-1}, i.e., the relative wavelength change is $(d\lambda/dT)/\lambda \approx 3 \cdot 10^{-4}$ K^{-1}. Provided a calibration

---

[9] The basic relations are in this case Shockley's diode equation $I = I_0[\exp{(\frac{eU}{\eta kT})} - 1]$ and $I_0 \propto \exp{(-\frac{E_{\mathrm{g}}}{kT})}$, with ideality factor $\eta \sim 2$.[41]

against heat-sink temperature, this technique delivers an average value for the gain material along the resonator.

A more critical review of this technique reveals a number of physical processes that alter this simple approach. To a lesser extend (by 1-2 orders), the wavelength of the longitudinal modes red-shift with thermal expansion of the laser resonator $(d\lambda/dT)/\lambda = (dL/dT)/L \sim 5 \cdot 10^{-6}$ K^{-1} and the refractive-index change $(d\lambda/dT)/\lambda = (dn/dT)/n \sim 5 \cdot 10^{-5}$ K^{-1} (for GaAs [88]). Furthermore, the strain that is introduced during device fabrication and packaging leads to a distortion of the electronic band structure. In extended devices this strain (with various symmetries) is non-equally distributed, typically compresses the device center by up to $(1-2)10^{-3}$ which gives rise to blue-shifts as large as 2-5 meV,[63, 129, 130] and, if it relaxes during heating, it can increase the usual temperature tuning by up to 20%.[131] Such effects can, in principle, be accounted for by a calibration where the laser is operated with short pulses and the heat-sink temperature is tuned. Other processes are related to the population of the electronic states, consequently change with injection current, and cannot be accounted for by temperature calibration. Most prominent, many-body effects lead to band gap renormalization (red-shift) and band filling (Burstein-Moss shift, blue-shift) for increasing carrier concentration. Typically, band filling dominates,[37, 132] and blue-shifts of $(d\lambda/dN)/10^{18}\mathrm{cm}^{-3} \sim -(10^{-4}-10^{-2})$ are found from $g(N)$ (blue-shift of peak gain frequency) and $n(N)$ (carrier-induced index reduction) in dependence of the laser design (e.g., well width, materials, etc.).[48, 132–135] Such effect is further modified by the nonequally distributed $N(z, I)$ along the resonator (higher N at the HR rear facet) which is also current dependent [i.e., through $g(N)$ and $n(N)$].[24, 136–138] At threshold N is typically on the order of $10^{18}\mathrm{cm}^{-3}$, and $N(z, I)$ can change during operation by similar values. Such blue-shifts, thus, can markedly interfere temperature determination. Since $N(z, I)$ is not accessible by easy means (in standard industrial environment), a principal systematic error of this technique is to be admitted.

Nevertheless, since this technique is the established one, a cross-check of thermography measurements is performed in section 5.1. Thermography extends such probing of the active region temperature towards the entire semiconductor chip and the heat sink, and even more it allows to probe novel gain media such as, e.g., quantum cascade lasers or quantum dot lasers, which exhibit only a weak spectral tuning with temperature.

Surface-probing techniques: The following techniques apply external excitation with short-wavelength lasers to probe the temperature of a surface-near volume and, thus, deliver complementary information as compared to the two bulk-probing techniques mentioned before.

Raman spectroscopy is the most frequently applied technique among the three.[59, 80, 93, 139–141] A good measure of the crystal lattice temperature is given by the intensity ratio of the Stokes and anti-Stokes lines or by their spectral shift relative to the incident light. Accuracies of about $\delta T \sim 10$ K are given with spatial resolution depending on the excitation laser spot size and can be below $\delta x \sim 1$ μm.

Thermoreflectance spectroscopy measures the change in reflectance of the laser facet upon a periodic modulation of its temperature, induced by a modulation of the injection current.[59, 140–142] The relative change in reflectance upon modulation is very weak on the order of $\Delta R/R \sim 10^{-4}$, which makes lock-in amplification an essential prerequisite to this technique. $\delta T \sim 1$ K and $\delta x \lesssim 1$ μm can be achieved.

Photoluminescence spectroscopy detects photoluminescence (PL) from layers around the QW and waveguide.[90, 143, 144] The restriction to the passive layers is given from the requirement that the photoexcited minority carrier concentration should exceed the electrically injected one. Since leakage currents are predicted in the waveguide,[145, 146] considerable pump levels would be necessary, leading to a detrimental excess facet heating. $\delta T \lesssim 1$ K is possible and δx is limited by the carrier diffusion length and can be as small as ~ 1 μm.

Careful calibration measurements for each individual device are of utmost importance for all three techniques. Especially in the case of Raman and thermoreflectance spectroscopy, the probing depth is so shallow[10] that fluctuations of the surface morphology can lead to false signals. Moreover, the reflectance is determined by the properties of the bulk semiconductor, the coating, and any pollution or oxide on it.[59] Finally, all techniques use a laser beam for probing, which can heat the probed regions up to a few Kelvin.[90, 143, 149]

2.7.2 Fourier-Transform Infrared Spectroscopy

Fourier-transform infrared (FTIR) spectroscopy is a commonly applied spectroscopic technique,[150, 151] used for the following applications.

The thermal emission spectra presented in section 3.1 were recorded with a NICOLET 5DXB FTIR spectrometer equipped with a temperature-stabilized DTGS (deuterated tri-glycine sulfate) detector working in the

---

[10] The penetration depth of the excitation laser can be approximated as $1/\alpha \sim 1/(10^4 - 3 \times 10^5)$ cm ~ 30 nm $- 1$ μm, given by the absorption coefficient α for GaAs at photon energies between 1.5 and 2.8 eV.[147, 148] In the case of PL, the carrier diffusion length limits the probing depth.

wavelength range from 4 to 40 μm with a spectral resolution of 8 cm^{-1}. The thermal radiation was imaged by a 90° off-axis parabolic mirror with a focal length of 350 mm into the internal beam path of the spectrometer.

The integral IR-emission spectra from laser diodes presented in section 5.4 were recorded with a BRUKER IFS 66 FTIR spectrometer, equipped with a liquid Nitrogen-cooled HgCdTe detector. A BRUKER external PL modul with collimating off-axis mirrors was used to focus the IR emission of the laser diodes into the measurement port of the spectrometer. A spectral resolution of 2 cm^{-1} was used in the wavelength range from 0.4 to 10 μm.

For the determination of filter transmittances, the source was a blackbody radiator (tungsten halogen lamp or Globar) and the sample was positioned between interferometer and detector. In reflection configuration, the beam was reflected out of its normal path onto the sample, re-collected afterwards, and sent to the detector. For both measurements the BRUKER FTIR spectrometer was equipped either with the HgCdTe or with DTGS detector.

2.7.3 Photoelectrical Spectroscopy

Photoelectrical spectroscopy such as photocurrent spectroscopy (PCS) and laser-beam-induced current (LBIC) provides valuable information on the defect status of laser diodes. An overview of the techniques (also for strain measurement) is given in Ref. 63. The discussion in the following is confined to the mechanisms that support the LBIC measurements presented in section 5.5. Several physical processes are involved in signal generation and the most important ones are sketched in Fig. 2.4.

The front facet of an unbiased laser diode is illuminated with light of photon energy $h\nu \gtrsim E_{\mathrm{e1}} - E_{\mathrm{hh1}}$ (e1, hh1 - first electron, heavy-hole subbands in the QW) thereby generating excess electron-hole pairs. For photocurrent generation (measured externally by closing the circuit by an Ampere meter) real-space charge separation in growth direction is necessary, which effectively means that the localized electrons (or holes) need to be transferred out of the QW layer into the waveguide where they can drift away within the electrical field of the *pn*-junction. This transfer process is usually described as thermionic emission.[41, 152–155] Consequently, the measured photocurrent is proportional to the concentration of photoexcited carriers in the QW. The lifetime of these carriers is reduced by the presence of defect states that offer additional recombination channels. It has been shown by numerous examples (e.g., Refs. 63, 78, 79, 156) that device degradation is related to an increase in the defect concentration. As a result, photocurrent measurements can detect variations in the defect concentration through their effect on the nonequilibrium carrier lifetime, either with location (spatial scan) or with

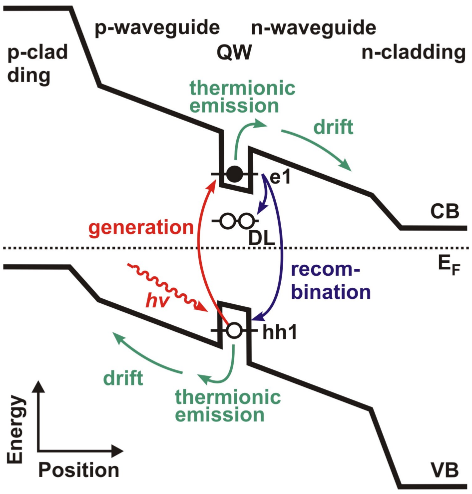

Figure 2.4: Schematic for the photocurrent generation in an unbiased laser diode with (resonant) photoexcitation of the hh1-e1 QW interband transition. The Fermi energy E_{F}, conduction band edge CB, and valence band edge VB are indicated. A donor-like defect level (DL) is considered, but acceptor-like ones work analogously. Photoexcited electrons are given as filled circles, and holes as open circles.

operation time.[63]

LBIC scanning, applied in section 5.5, uses a HeNe laser ($h\nu = 1.96$ eV) that is focused by a cylindrical lens onto the front facet of a cm-bar, resulting in a narrow line perpendicular to the epilayer plane. The laser sample is mounted on a step-motor-controlled translation stage and scanned along the whole width of the bar. A step-width of 2 μm is chosen according to the spatial extension of the beam waist in scanning direction. The photocurrent is measured by a lock-in amplifier that is triggered by a mechanical chopper for modulation of the excitation laser beam.

2.7.4 Near-Field Scanning Optical Microscopy

The Rayleigh criterion states that the smallest resolvable distance for a microscope operating at wavelength λ that uses diffractive optics with a numerical aperture N.A. is restricted to $\delta x = 0.61\lambda/\mathrm{N.A.}$[157] Near-field scanning optical microscopy (NSOM) overcomes this limitation by using the near-field of the radiation source and not its far-field,[158, 159] and is thus able to characterize electromagnetic fields on a nm-scale.[160–163] The spatial characteristic of a monochromatic plane wave is given by $\exp(ikr)$, i.e., it propagates (in vacuum) with a phase factor into the far-field. For the evanescent part of the electromagnetic field the wave vector k takes complex values so that its amplitude decays strongly with growing distance r from the surface as $\exp(-\mathrm{k}r) = \exp(-2\pi r/\lambda)$. But for distances $\ll \lambda$ the evanescent field dominates over the propagating field and may locally vary with $\ll \lambda$, in stark contrast to the propagated far-fields that obey Rayleigh's criterion.

In aperture NSOM working in the collection-mode, the near-field is coupled into an extremely sharp tip (diameter $\ll \lambda$) of a tapered optical fibre.

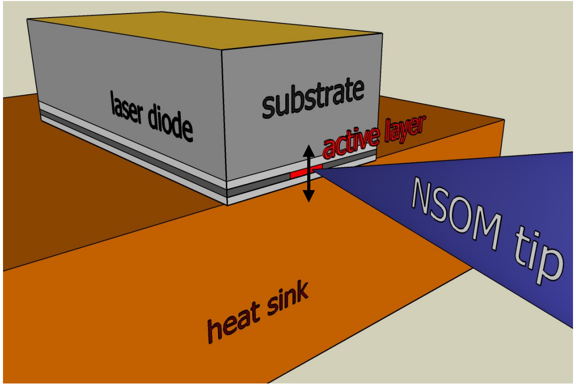

Figure 2.5: Schematic of the geometry for an NSOM measurement of the emission from a laser diode. The principal scanning direction normal to the epilayer in front of the laser facet is indicated by a black double-headed arrow.

Such perturbation leads to a scattered propagating field which is guided within the fiber towards a detector. An image forms up from scanning the object with the fiber, similar as, e.g., in scanning tunneling microscopy.[160, 164] The achievable spatial resolution is well below the used wavelength, limited by the tip aperture, and can be as good as $\sim 10 - 30$ nm.[165]

For the highly spatially resolved analysis of the IR emission that is coming from the front facet of laser diodes in section 5.4 a home built[11] NSOM in the collection-mode with spatial resolution of $\sim$ 200 nm is applied (Fig. 2.5). The distance between chemically etched, single mode, uncoated fiber tip and sample surface ($\sim$ 10 nm,[166]) is controlled by shear-force feedback using an oscillating tuning fork.[167, 168] At each step during scanning a spectrum is recorded, yielding spatio-spectral information about the operating laser diode, in extension of measuring the optical mode intensity only.[169, 170]

During emission scans, pulsed-current operation was necessary to avoid overheating of the tip.[170] Two measurement regimes were applied: 5×5 μm^2 near-field maps of the epilayers with a step size of 0.1 μm and active shear-force control, using a deep depletion Si CCD camera, and 60 μm line scans of the epilayers and half of the substrate, with a step size of 1 μm, the tip held $\sim$ 4 μm above the sample, measured with a nitrogen-cooled InGaAs CCD camera. The cameras were mounted behind a grating-spectrograph with focal lengths of 0.5 and 0.3 m, and at each pixel integration times of 0.1 and 5 s were used for the maps and the line scans, respectively. In addition, from photoexcitation of the devices by a HeNe laser and collection of the PL through the same tip, maps of the PL are measured as well.[167, 168]

---

[11] The NSOM has been constructed and operated by C. Lienau, R. Pomraenke *et al.*, formerly with the Max-Born-Institut and now with the Institut für Physik, Carl von Ossietzky Universität, 26111 Oldenburg, Germany.

Chapter 3

Thermal Emission from Semiconductor Lasers

In the previous chapter, fundamental aspects of thermal radiation from a blackbody and the alterations in the case of real materials were discussed. In this chapter, a spectrally resolved measurement of the thermal emission from a stack of laser bars together with bulk GaAs reference samples and a calibrated blackbody is performed. A formalism for the evaluation of the measured raw data is derived, which takes into account all components contributing to a thermal radiation signal in the detection unit. As a result, the emittance, transmittance, and reflectance are determined simultaneously. The thermal emission properties of the semiconductor lasers relate to underlying materials properties and the fact that the laser device is assembled from multiple components, in particular, pronounced deviations are found for the laser sample as compared to the bulk reference samples.

3.1 Determination of the Emittance of Semiconductors

3.1.1 Sample Description

For the measurements commercial cm-bars **QW-808-1-bar** (cf. section 2.5) are used. These bars are 1 cm wide, have a resonator length of 1.2 mm and an overall thickness of ≈ 115 μm. (Fig. 3.2). In the emittance measurements a spatial average of the whole bar is probed. The epistructure with a thickness < 4 μm, containing gradually p- and n-doped layers around the QW, contributes less than four percent to the overall thermal emission of the non-operating device compared to the thick n-GaAs substrate. Additionally, the

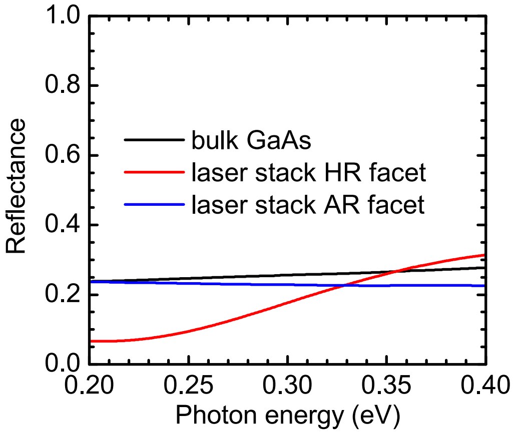

Figure 3.1: Reflectance of the AR (blue line) and HR coated (red line) facets of the laser diode samples and of the (averaged) bulk GaAs reference samples (black line), as determined from additional FTIR measurements for photon energies from 0.2 to 0.4 eV.

metallization on the top and bottom faces are together less than 1 μm thick. Nevertheless, the p-doped semiconductor and the metal layers influence the thermal emission behavior notably as will be quantified in section 3.2.

The AR facet coating has a negligible influence in the region of maximal thermal emission ($h\nu < 0.4$ eV), whereas the reflectance of the HR coating is slightly below that of the bulk material; see Fig. 3.1. One estimates a reduction of emittance of $\lesssim 1-2\,\%$ compared to the situation of GaAs bulk material. In view of the later on discussed enhancement, such reduction serves as a further support.

In order to enhance the available signal level, a vertical stack is built from 82 cm-bars (Fig. 3.2). Two bulk n-doped GaAs wafers with thicknesses close to the laser resonator length are chosen for comparison (cf. Table 3.1). The wafers originate from the same vendor (Freiberger Compound Materials GmbH, Freiberg, Germany), the doping concentrations are in the same range, and the degree of compensation is expected to be very similar as for the laser-diode substrates.

3.1.2 Setup Description

The calibrated setup for quantitative measurements of spectrally resolved emittances is constructed and operated at the PTB[1] and is schematically depicted in Fig. 3.3.[171]

The thermal emission spectra are recorded with a NICOLET 5DXB FTIR spectrometer described in section 2.7.2.

The semiconductor samples are kept in a rectangular sample holder made of Cu [Fig. 3.3(c)]. Round apertures on each side of the sample holder limit

---

[1] Physikalisch-Technische Bundesanstalt (German national metrology institute), Abbestrasse 2-12, 10587 Berlin, Germany

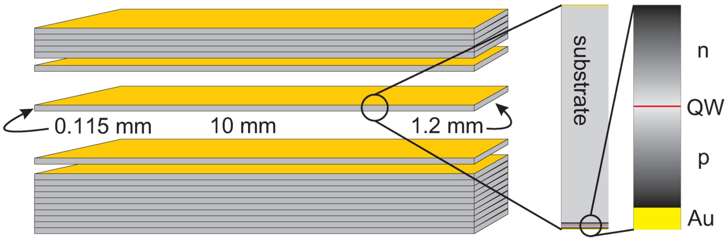

Figure 3.2: Schematic of the laser diode stack. The stack consists of 82 cm-bars, resulting in a total front facet emission area of 1 cm^2. The exploded region shows the dimensions of a single cm-bar and magnified views show the proportions of its constituents: GaAs substrate, epilayers consisting of gradually n- and p-doped regions and the QW, and Au contacts on top and bottom.

the emitting area to 9 mm in diameter. The sample holder is either in good thermal contact with a Cu mounting plate or thermally insulated from the plate, depending on the type of measurement. The sample holder is mounted on a heating plate made of INCONEL 600 and heated by a bifilar-wounded THERMOCOAX resistive heater. The temperature of the heating plate is regulated by an EUROTHERM 2704 PID controller. In order to shield the sample against the environmental thermal background it is placed inside a hemispherical enclosure with a diameter of 250 mm, made of Cu with a helical heat exchanger soldered on its outer surface. The temperature of the enclosure is stabilized by a water thermostat. Its inner surface is grooved and covered with the infrared black paint NEXTEL 811-21,[172] providing an emittance of 0.97.[173]

In order to quantify the thermal emission from the sample, the sample in its holder is mounted on a translation stage in front of the spectrometer together with a blackbody-reference radiator. In a series of measurements, they are subsequently moved in front of the spectrometer. The blackbody has been constructed and manufactured at the PTB and consists of a cylindrical cavity (diameter 64 mm, length 180 mm) with a 60° conical bottom and a 34 mm emission aperture. The cavity is completely grooved and painted with NEX-

No.	Sample	Carrier conc.	Thickness
S	Stack	$1.16 \times 10^{18}\text{cm}^{-3}$	1.20 mm
R1	GaAs:Si	$1.01 \times 10^{18}\text{cm}^{-3}$	1.16 mm
R3	GaAs:Si	$2.97 \times 10^{18}\text{cm}^{-3}$	1.23 mm

Table 3.1: Sample parameters. Carrier concentrations of the reference samples were determined by the wafer manufacturer and the value for the stack sample is derived in section 3.2.2.

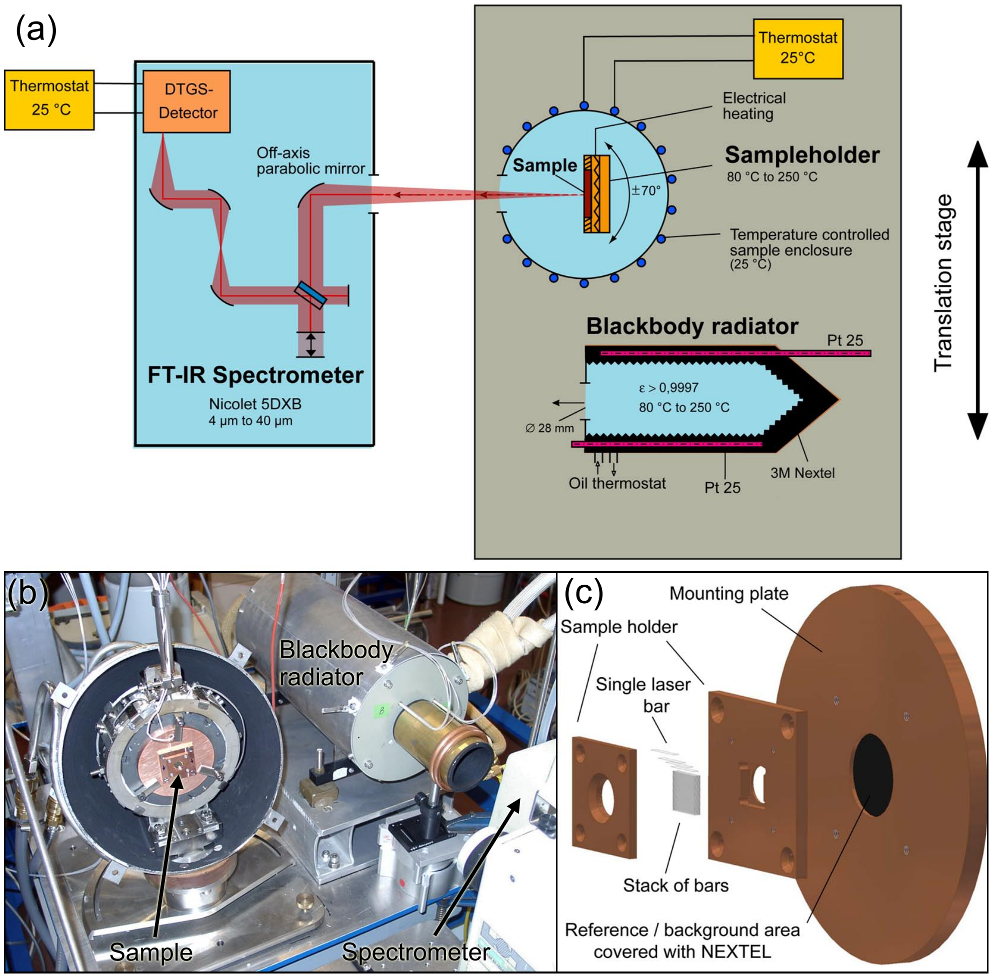

Figure 3.3: **(a)** Schematic of the setup for emittance and transmittance measurements. The three main parts are a FTIR spectrometer with DTGS detector, a sample holder with spherical radiation shield and heating plate, and a calibrated reference blackbody radiator. **(b)** Photograph of the sample in the sample holder and the reference blackbody in front of the spectrometer. One hemisphere of the radiation shield is removed for accessing the sample. **(c)** Exploded schematic of the sample holder together with the laser stack and the mounting plate, which is attached to the heating plate and covered with black NEXTEL 811-21 paint.

TEL 811-21. It is temperature-controlled in the range from 60 °C to 250 °C. The blackbody with an emittance of 0.9997 is calibrated against the heat-pipe blackbodies of the low-temperature radiation-scale of the PTB.[174]

The temperatures of the DTGS detector, sample holder, heating plate, and sample enclosure are monitored by PT100 sensors, and that of the blackbody by two PT25 sensors. The sensors are calibrated traceable to the primary standards of the international temperature scale (ITS-90) at the PTB.

3.1.3 Measurement Strategy and Analysis

Experimental challenges and solution strategies

The small size of a laser diode represents a major challenge for the spectrally resolved measurement of its thermal emittance. The emitting front facet area of a rather large cm-bar has a typical value of $\approx 1\ \text{mm}^2$. Such small area leads to a small power of thermal emission, especially if realistic conditions are desired. Typically, laser diodes operated at ambient temperature only exhibit a relatively weak temperature increase of $\sim 20 - 40$ K. In order to discriminate their thermal emission against the environmental thermal background, 82 cm-bars are vertically stacked over each other (Fig. 3.2) and only slightly elevated temperatures from 80 °C to 120 °C are used in the experiment[2]. Although emittance measurements of semitransparent solids have been established already in the 60'ies, [177] semiconductors have mainly been studied at elevated temperatures (mostly a few hundred °C) and at photon energies close to the band gap where the emittance is highest, [178–183] because of such difficulties.

Since the semiconductor samples exhibit both a finite reflectance and a finite transmittance the measured signal consists of different contributions. Experimentally this fact is addressed by embedding the sample in an isothermal hemispherical enclosure of constant spectral emittance and constant temperature (Fig. 3.3) in front of a background of known spectral emittance. Consequently, the total signal consists of thermal radiation emitted:

- directly from the semiconductor sample
- from the sample holder
- from the reference area transmitted through the semiconductor sample
- from the isothermal enclosure reflected from the semiconductor sample
- from the detector/spectrometer

In principle, there is an additional background from other parts of the experimental environment, which is - according to a careful experimental analysis of the setup - very small and thus neglected in the following.

Individual variation of the mentioned contributions allows for their separation from the measured total signal. Measurements with the sample at constant temperature and the reference surface behind the sample at different

---

[2] In case of laser diodes built for high-temperature operation, as e.g., for 50 °C described in Ref. 102 that have been studied in this thesis, [94, 175, 176] the temperature range of operation is exactly met.

temperatures allow for a separation of the emitted and transmitted fractions of thermal radiation. Measurements of the sample in front of the reference area and of the reference area alone allow the determination of setup related contributions. In particular, the expected signal from the sample in the sample holder is composed of a contribution from the sample and a contribution related to the sample holder as the area probed by the detector is slightly larger than the sample area itself.

Formalism for the analysis of experimental data

The spectrometer detects the spectral radiant power Φ_ν in the frequency interval $\Delta\nu$, which is the spectral radiance L_ν [compare Eqs. (2.19) and (2.22)] integrated over the area F of the sample and the detection cone of the spectrometer Ω

$$\Phi_\nu(\nu, T, \theta)\Delta\nu = \int\limits_\Omega \int\limits_F L_\nu(\nu, T, \theta) d\Omega dF \Delta\nu. \tag{3.1}$$

In a good approximation, the angular dependence of $L_\nu(\nu, T, \theta)$ within the cone of observation can be neglected and the integral can be approximated by a product. For detection in nearly normal incidence ($\cos\theta \approx 1$) this results in

$$\Phi_\nu(\nu, T)\Delta\nu = L_\nu(\nu, T, \theta = 0)\Omega F \Delta\nu. \tag{3.2}$$

The directional spectral emissivity (2.22) is defined as the spectral radiance of a sample normalized to that of a blackbody. Because of the proportionality in Eq. (3.2) this is equivalent to a measurement of the spectral radiant power of a sample with respect to that of a blackbody-reference radiator at the same temperature.

The FTIR signal measured for the sample in the sample holder is given by the following expression

$$\begin{aligned} S_\mathrm{S}(\nu, T_\mathrm{S}, T_\mathrm{H}, T_\mathrm{N}, T_\mathrm{E}, T_\mathrm{D}) = s_\mathrm{D}(\nu)\Omega F \Big[& A\epsilon_\mathrm{S}(\nu) L_\mathrm{BB}(\nu, T_\mathrm{S}) \\ & + (1 - A)\epsilon_\mathrm{H}(\nu) L_\mathrm{BB}(\nu, T_\mathrm{H}) \\ & + A\widetilde{\tau}_\mathrm{S}(\nu)\epsilon_\mathrm{N}(\nu) L_\mathrm{BB}(\nu, T_\mathrm{N}) \\ & + \{A\widetilde{\varrho}_\mathrm{S}(\nu) + (1 - A)\widetilde{\varrho}_\mathrm{H}(\nu)\}\epsilon_\mathrm{E} L_\mathrm{BB}(\nu, T_\mathrm{E}) \\ & - \epsilon_\mathrm{D} L_\mathrm{BB}(\nu, T_\mathrm{D})\Big]. \end{aligned} \tag{3.3}$$

The subscripts S, H, N, E, and D denote contributions from the sample, the sample holder, the reference area behind the sample[3], the enclosure, and the

---

[3] This area has been painted by NEXTEL 811-21 black infrared paint with an emittance above 0.95 in the investigated wavelength range.[172]

detector, respectively. $s_\mathrm{D}(\nu)$ is the spectral responsivity of the spectrometer and $A \approx 0.9$ is the sample-related fraction of the total area seen by the detector (cf. next section). $\widetilde{\tau}$ denotes the transmittance and $\widetilde{\varrho}$ the reflectances of the samples.

The exact derivation via a variation of the individual contributions is outlined in detail in the Appendix A. Here, only the result for the emittance of the sample is given as

$$\begin{aligned}\epsilon_\mathrm{S}(\nu) = {} & \frac{\epsilon_\mathrm{N}(\nu)}{L_\mathrm{BB}(\nu, T_\mathrm{S}) - L_\mathrm{BB}(\nu, T_\mathrm{E})} \\ & \times \left\{ \frac{S_\mathrm{S}(\nu, T_\mathrm{S}, T_\mathrm{H}, T_\mathrm{N}) - S_\mathrm{H}(\nu, T_\mathrm{H}, T_\mathrm{N})}{S_\mathrm{H}(\nu, T_\mathrm{H}, T_\mathrm{N}) - S_\mathrm{H}(\nu, T_\mathrm{H}, T'_\mathrm{N})} \left[L_\mathrm{BB}(\nu, T_\mathrm{N}) - L_\mathrm{BB}(\nu, T'_\mathrm{N})\right] \right. \\ & \left. - L_\mathrm{BB}(\nu, T_\mathrm{N})[\widetilde{\tau}_\mathrm{S}(\nu) - 1] - L_\mathrm{BB}(\nu, T_\mathrm{E}) \left[1 - \frac{\widetilde{\tau}_\mathrm{S}(\nu)}{\epsilon_\mathrm{N}(\nu)}\right] \right\}, \end{aligned} \tag{3.4}$$

where the transmittance of the sample is

$$\widetilde{\tau}_\mathrm{S}(\nu) = \frac{S_\mathrm{S}(\nu, T_\mathrm{S}, T_\mathrm{H}, T_\mathrm{N}) - S_\mathrm{S}(\nu, T_\mathrm{S}, T_\mathrm{H}, T'_\mathrm{N})}{S_\mathrm{H}(\nu, T_\mathrm{H}, T_\mathrm{N}) - S_\mathrm{H}(\nu, T_\mathrm{H}, T'_\mathrm{N})}. \tag{3.5}$$

These two equations consist of quotients of measured signals S, quotients of blackbody radiances L_BB, and the separately measured emittance of the reference area $\epsilon_\mathrm{N}(\nu)$ only, leaving no free parameter.

Calibration of the emittance measurements

Numerical values for the measured temperatures are given in Table 3.2. Also, the ambient temperature in the laboratory was stabilized with an accuracy of ±1 °C. To rule out changes of the detector responsivity $s_\mathrm{D}(\nu)$ - a prefactor of the radiance terms - each set of measurements was complemented by a spectrum of the reference blackbody and normalized to it. Each individual measurement was repeated several (≥ 4) times.

The thermal radiation detected in the FTIR spectrometer consists of the fraction A originating from the sample and the fraction $(1 - A)$ from the sample holder. Its extraction from spectrally resolved measurements with and without the sample is derived in Appendix A. In Fig. 3.4(b), its numerical values are plotted as a function of photon energy exhibiting values close to 0.9 (i.e., 90 percent of the detected signal originate from the sample). Besides, A is useful in evaluating the quality of the measurement. Since the ratio of the two areas is fixed, also $A(h\nu)$ should be a constant. This essentially is the case with fluctuations strongly increasing at photon energies beyond

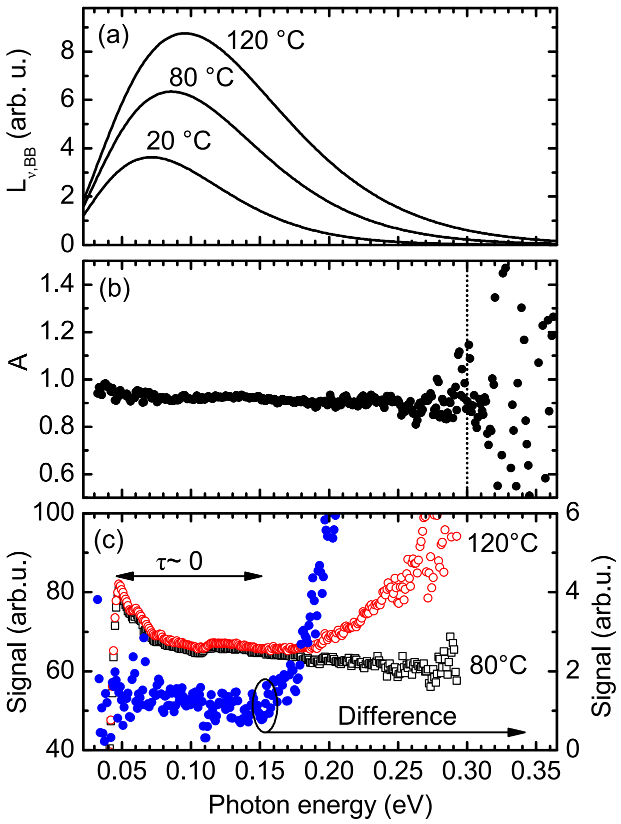

Figure 3.4: **(a)** Spectral radiance of a blackbody at 20, 80, and 120 °C. **(b)** Fraction A of the probed area related to the semiconductor samples. The dotted vertical line at 0.30 eV indicates the upper limit up to which the measured data are reliable for further analysis. Beyond this line the scatter in the data points exceeds three times the standard deviation of the interval below 0.25 eV. **(c)** Measured raw emission signals from reference sample R1 for background temperatures of 80 and 120 °C, and the difference of it (blue dots, displayed at tenfold magnification). The region with almost zero transmission ($<$ 0.15 eV) was used for offset correction.

0.30 eV, because the absolute intensity of thermal radiation gets very small there [Fig. 3.4(a)]. Consequently, only data for $h\nu < 0.30$ eV are used in the following.

According to the separation approach, the sample was measured in front of the background reference area at different temperatures T_{N} and T'_{N}. As expected, a higher signal is found with the background area at higher temperature [Fig. 3.4(c)]. For $h\nu < 0.15$ eV the sample R1 is fully absorbing and, consequently, the signals for different background temperatures should be identical. The data display, however, a small almost constant offset of $1-2\%$ in this range, which originates from different contributions, including the so-called size-of-source effect[4] and a small fraction of emission from the heated background plate[5] that is reflected from the sample into the detec-

---

[4] The size-of-source effect is known to cause deviations in radiometric measurements in dependence on the size of the source, in spite of the usage of apertures between the source and the detector, and is typically explained by diffraction.[184–187].

[5] The emitting area of the heating plate (diameter = 12 cm) is much larger than that of the sample (diameter = 0.9 cm) including the sample holder (side length = 4 cm); see Figs. 3.3(b) and 3.3(c). Therefore its indirect contribution, e.g., via reflection from the

Part	Symbol	Value in °C
Semiconductor samples	T_S	80.0 ± 0.1
Sample holder	T_H	80.0 ± 0.1
Reference background	T_N	80.67 ± 0.03
Reference background	T'_N	123.0 ± 0.9
Enclosure	T_E	23.04 ± 0.09
Detector	T_D	23.08 ± 0.03
Reference blackbody	T_B	80.01 ± 0.01

Table 3.2: Measured temperatures of the samples and the individual parts of the setup.

tor via the enclosure. In the data sets as presented here, a constant offset signal derived from the difference in the non-transparent region [blue dots for $h\nu < 0.15$ eV in Fig. 3.4(c)] was subtracted from the values measured with increased background temperature. The described procedure leads to zero transmittance in the far infrared, as expected for thick semiconductor samples; see Fig. 3.5(b).

3.1.4 Experimental Spectra

The calibration of the measurement data along with the earlier described variation approach leads with Eqs. (3.4) and (3.5) as well as $\widetilde{\varrho} = 1 - \epsilon - \widetilde{\tau}$ to numerical values. The spectrally resolved emittance ϵ, transmittance $\widetilde{\tau}$, and reflectance $\widetilde{\varrho}$ of the samples are displayed in Fig. 3.5.

The transmittance spectra allow for a straight-forward interpretation. Two major spectral regions are encountered: for $h\nu < 0.18$ eV, the transmittance spectrum is flat with absolute values close to zero for all semiconductor samples. This demonstrates complete absorption of all infrared radiation originating from the reference area behind. At higher photon energies, the absorption of the 1.2 mm samples is not sufficient for a complete extinction of the radiation from the reference area, a fact that poses a challenge in an exact radiometric temperature determination with thermography with its detection range peaking close to 0.25 eV (cf. section 4.1.1).

The emittance spectra of the semiconductor samples that all exhibit similar high numerical values of nearly 0.7 over the $0.1 - 0.18$ eV spectral range, start to depart from each other in the range of semitransparency. The GaAs sample with the lowest doping (R1, green triangles) falls off most strongly, followed by the stack sample (S, blue dots) and the heavily doped GaAs sample (R3, red squares). In the following section this fact will be related to the increasing absorption due to free carriers.

---

enclosure, to the detected radiation is not completely screened.

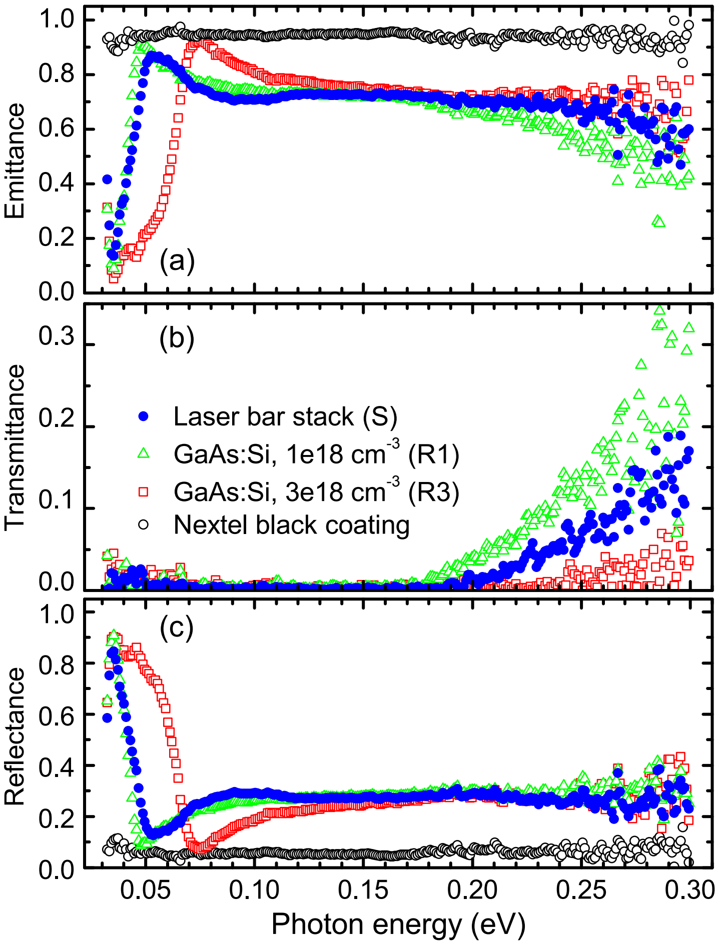

Figure 3.5: Spectrally resolved **(a)** emittances ϵ, **(b)** transmittances $\widetilde{\tau}$, and **(c)** reflectances $\widetilde{\varrho}$ for the stack of laser bars (S), the reference samples (R1, R3), and for the background reference areas covered with NEXTEL. ϵ, $\widetilde{\tau}$, and $\widetilde{\varrho}$ are calculated from Eqs. (3.4) and (3.5), and $\widetilde{\varrho} = 1 - \epsilon - \widetilde{\tau}$.

For $h\nu < 0.18$ eV the transmittance is almost zero for all semiconductor samples and the spectra of emittance and reflectance are complementary to each other because of energy conservation. Consequently, the additional increase and subsequent sharp drop of the emittance at small photon energies < 0.1 eV is caused by a drop and subsequent sharp rise in the reflectance. These features are inherent characteristics to semiconductor materials and originate from the interaction of the radiation with free electrons on the one hand and with the crystal lattice on the other hand. In the following section, such spectral characteristics are used to relate the emission and absorption properties to basic physical properties and analyze to what extent such properties are different for bulk semiconductor materials and laser devices.

The NEXTEL background reference area behaves almost grey (i.e., flat spectral characteristics) with an emittance around 0.95 and a residual reflectance around 0.05.

3.2 Emittance Enhancement due to the Laser Cavity

3.2.1 Free Carrier Absorption

For the semitransparent semiconductor samples, the measured quantities $\tilde{\tau}$, $\tilde{\varrho}$, and ϵ are determined by the material-specific reflection coefficient ϱ and absorption coefficient α. The transmissivity is given by $\tau = \exp(-\alpha d)$, where d is the thickness of the absorbing sample. In good approximation, identical ϱ at both facets are assumed. For multiple (incoherent) reflections under normal incidence at the interfaces, the Fresnel formulae are simplified and a geometrical series of the form $\sum_{n=0}^{\infty} ax^n = a/(1-x)$, $|x| < 1$ leads to the following expressions

$$\begin{aligned}
\tilde{\tau} &= \tau(1-\varrho)^2(1+\varrho^2\tau^2+\varrho^4\tau^4+\dots) = \frac{\tau(1-\varrho)^2}{1-\varrho^2\tau^2} \\
\tilde{\varrho} &= \varrho\left[1+\tau^2(1-\varrho)^2\left(1+\varrho^2\tau^2+\varrho^4\tau^4+\dots\right)\right] = \varrho\left[1+\frac{\tau^2(1-\varrho)^2}{1-\varrho^2\tau^2}\right] \\
\epsilon &= (1-\varrho)(1-\tau)(1+\varrho\tau+\varrho^2\tau^2+\dots) = \frac{(1-\varrho)(1-\tau)}{1-\varrho\tau}\,. \qquad (3.6)
\end{aligned}$$

The last line relies on the equality of emittance and absorbance given by Kirchhoff's law (2.23). The absorption coefficient is thus determined by solving this equation system for the first and last line

$$\alpha = -\frac{\ln(\tau)}{d} = -\frac{1}{d}\ln\left[-\epsilon-\frac{\epsilon^2}{2\tilde{\tau}}+\left(\epsilon^2+\frac{\epsilon^3}{\tilde{\tau}}+\frac{\epsilon^4}{4\tilde{\tau}^2}+1\right)^{1/2}\right]. \qquad (3.7)$$

In Fig. 3.6(b) corresponding spectra of $\alpha(h\nu)$ for the laser structure are plotted together with that for the two GaAs reference samples. The data display is restricted to the range of sufficient transmittance ($h\nu > 0.2$ eV).

The absorption behavior of semiconductor materials is governed by various physical processes, some of which are depicted in Fig. 3.6(a). In the analyzed case of photon energies well below the fundamental band gap, the absorption behavior of most of the semiconductor layers in the laser structure and of the GaAs reference structures is governed by the absorption due to intraband transitions of electrons.[48, 189–192] Beside such free carrier absorption (FCA), for the thin ($\lesssim 2$ μm) p-doped layer of the laser structure inter-VB absorption of holes is the predominant absorption mechanism.[193–195] For the displayed photon energies between 0.2 and 0.3 eV, the absorption spectra in Fig. 3.6(b) feature a monotonous decrease of absorption. This behavior fits with the power law $\alpha_{\text{FCA}} \propto (h\nu)^{-p}$ with $2 < p < 3$. The value of p

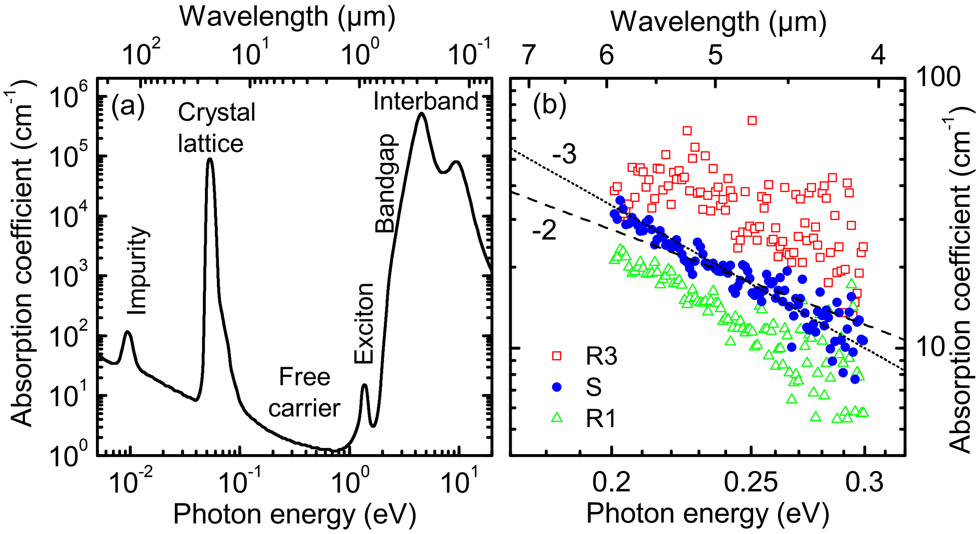

Figure 3.6: **(a)** Typical absorption spectrum of a semiconductor indicating major absorption processes (reproduced from Ref. 188). The thermography-relevant spectral region of free carrier absorption is close to the absolute minimum. **(b)** Absorption coefficient spectra $\alpha(h\nu)$ for the samples S, R1, and R3 in double logarithmic scale, derived from applying Eq. (3.7) to $\epsilon(h\nu)$ and $\widetilde{\tau}(h\nu)$ of Fig. 3.5. The display is restricted to the spectral region of recognizable transmittance $h\nu > 0.2$ eV. Dotted and dashed lines indicate $\alpha \propto (h\nu)^{-p}$ with p equal to 3 and 2.

originates from the interaction of the electron with either acoustic phonons ($p \approx 1.5$), optical phonons ($p \approx 2.5$), or impurities ($p \approx 3.5$).[48, 189–192] In contrast, from the Drude model of the free electron an exponent of $p = 2$ is expected on account of scattering times independent on the photon energy.[59]

For laser structures high electron concentrations in the range of $N \sim 10^{18}$ cm^{-3} are necessary, which leads to a highly degenerate electron gas with a quasi-Fermi level of $F_e(N = 10^{18}\ \text{cm}^{-3}) \approx 65\,\text{meV}$. Under such conditions, FCA leaves the range of almost linear dependence on N and starts to become superlinear.[48, 189–192] In bulk GaAs crystals, values of $\alpha_{\text{FCA}} \approx 20$ cm^{-1} have been reported for a photon energy of 0.2 eV and an electron density of $N = 1.1 \times 10^{18}$ cm^{-3}.[191] This compares well with the values displayed in Fig. 3.6(b). The absorption cross section per free electron calculates as $\sigma_{\text{FCA}}(h\nu = 0.2\ \text{eV}) = \alpha_{\text{FCA}}/N \approx 1.8 \times 10^{-17}$ cm^2.

For p-doped GaAs, on the other hand, inter-VB absorption of free holes from the heavy-hole into the light-hole band is the dominating absorption mechanism for temperatures $T > 300$ K and photon energies below 0.3 eV. [193–196] The absorption spectrum shows a monotonous decrease by a factor of 3.5 without any spectral substructure for photon energies from 0.2 to 0.3 eV. The absorption cross section per free hole has a value of $\sigma_{\mathrm{IV}}(h\nu = 0.2\text{ eV}) \approx 1.5 \times 10^{-16}\,\mathrm{cm}^2$, i.e., roughly 10 times higher than for the intraband absorption of an electron in n-type GaAs with similar free carrier concentration.

3.2.2 Reflectance and Plasma Resonance

The free carrier concentrations of the substrates used in the laser stack are initially unknown. The specification[6] of the manufacturer about the doping of standard production-type wafers for laser diodes is always subject to fluctuations inherent to the bulk crystals growth, in terms of both variations from wafer to wafer and spatial variations across individual wafers. A determination of the average free carrier concentration of the entire laser stack is possible via the plasma resonance in the reflectance spectrum given by $\widetilde{\varrho} = 1 - \widetilde{\tau} - \epsilon$. The reflectance spectra (under normal incidence conditions) are shown in Fig. 3.7 for the samples in the range of their plasma edges. On the other hand, the normal-incidence reflectance is given by

$$\widetilde{\varrho} = \left|\frac{1-\mathcal{N}}{1+\mathcal{N}}\right|^2 = \left|\frac{1-\sqrt{\varepsilon}}{1+\sqrt{\varepsilon}}\right|^2 , \tag{3.8}$$

with the complex refractive index

$$\mathcal{N} = n - \mathrm{i}k = \sqrt{\varepsilon} = \sqrt{\varepsilon_1 - \mathrm{i}\varepsilon_2}\,. \tag{3.9}$$

In this expression, n is the real refractive index, k the extinction coefficient, and ε the complex dielectric function with its real and imaginary parts ε_1 and ε_2. In the spectral region that is relevant here (reststrahlen region) the IR light interacts with the lattice vibrations, which can be described by an harmonic-oscillator model, and, if free carriers are present, plasma contributions to the dielectric function need to be taken into account. The dielectric function reads as

$$\varepsilon(\omega) = \varepsilon_\infty \left(1 + \frac{\omega_{\mathrm{LO}}^2 - \omega_{\mathrm{TO}}^2}{\omega_{\mathrm{TO}}^2 - \omega^2 - i\omega\Gamma} - \frac{\omega_{\mathrm{p}}^2}{\omega^2 + i\omega\Gamma_{\mathrm{p}}}\right) , \tag{3.10}$$

where ω_{LO} and ω_{TO} are the LO and TO phonon frequencies in the long-wavelength limit, and Γ is the phonon damping constant.[48] The intraband

---

[6] The reference bulk GaAs wafers are standard production-type wafers as well, but they were selected and measured for their (room-temperature) free carrier concentrations by the manufacturer for testing purposes at the Max-Born-Institut.

Figure 3.7: Reflectance spectra of samples R3, S and R1 (the two upper plots are shifted 0.5 up each for better visibility). Data points are taken from Fig. 3.5(c), are expanded around the plasma resonance. Least-squares fits according to Eqs. (3.8) and (3.10) result in solid lines and parameters given in Table 3.3.

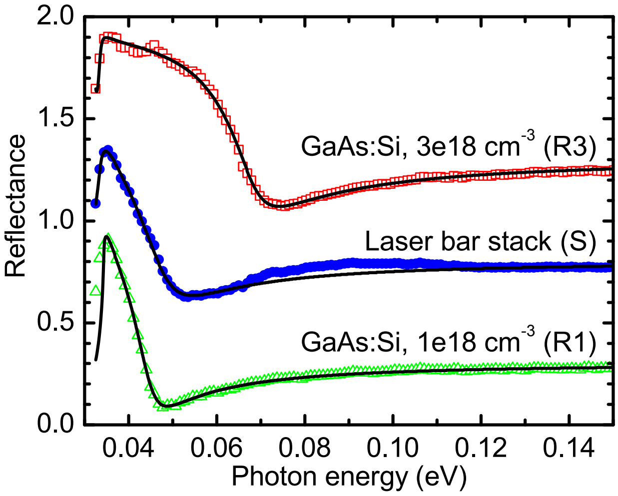

contribution (FCA) to the refractive index of the n-doped layers is negative, resulting in the observed plasma edge of far-IR reflectivity. This is the last term in Eq. (3.10) with the plasma frequency

$$\omega_{\mathrm{p}}^2 = \frac{Ne^2}{m_c^* \varepsilon_\infty \varepsilon_0} \tag{3.11}$$

and the plasmon damping constant Γ_{p}. The effective mass of the conduction band electrons is m_c^*. The contribution of free holes to the plasma edge is negligible.[195]

A nonlinear least-squares fit (solid lines in Fig. 3.7) of the measured sample reflectance (symbols) according to Eqs. (3.8) and (3.10) determines ω_{p} and the other sample parameters (Table 3.3). There is apparently a very good agreement of the fit and the experimental data points and of the parameter values with the literature.[48]

For the stack sample, the plasma resonance between 50 and 60 meV is broader than for the reference samples (cf. Γ_{p} in Table 3.3) and a small deviation of the fit from the experimental data occurs between 60 and 110 meV. Such peculiarities may arise from the spread of the doping levels of the 82 individual laser bars within the stack, originating from different epitaxial runs and wafers.

Equation (3.11) gives the relation between the electron concentration and the plasma frequency. A modification to this is caused by the high electron concentrations relevant here. For the resulting degenerate electron gas, electron states lying high in the CB are populated. There the parabolic band approximation around the CB minima is insufficient in describing the electron k-dispersion. The nonparabolicity can be accounted for by introducing

No.	$\hbar\omega_p$	Γ_p	$\hbar\omega_{LO}$	$\hbar\omega_{TO}$	Γ	ε_∞	m_c^*/m_{e}
R3	67.3	11.2	35.6	33.4	0.8	11.62	0.0778
S	44.0	18.9	37.6	33.5	1.2	11.58	0.0711
R1	41.3	10.7	36.5	33.3	0.2	11.57	0.0706

Table 3.3: Parameters obtained from fitting the data from Fig. 3.7 to (3.8) and (3.10). All parameters are given in meV except for ε_∞ and m_c^*. agreement with literature values is achieved.[48]

higher order correction terms to the constant effective electron mass, i.e., by making it energy dependent $m_c^*(E)$. The N-dependence is introduced through the Fermi energy, because the effective mass probed in the experiments is known as the optical mass at the Fermi energy, that is $m_c^*(F_{\mathrm{e}}(N))$. For $N \approx 10^{18}\mathrm{cm}^{-3}$, a linear relation has been found with a small quadratic correction term on the order of 0.6%.[197] Thus, a linear interpolation is used here

$$\frac{m_c^*(N)}{m_{\mathrm{e}}} = \frac{A_{\mathrm{p}} N}{\varepsilon_\infty \hbar^2 \omega_{\mathrm{p}}^2(N)} = m_0^* + aN = 0.06683 + \frac{3.70\,N}{10^{21}\ \mathrm{cm}^3}\,. \tag{3.12}$$

Here, $A_{\mathrm{p}} = \alpha\hbar^3 c 4\pi m_{\mathrm{e}}^{-1} = 1.3788422 \times 10^{-21}\,\mathrm{eV}^2\mathrm{cm}^3$ is a constant (α - fine-structure constant). The numerical values for m_0^* and a were derived with the plasma frequencies and dielectric constants from Table 3.3. From the known electron concentrations of the reference samples, their effective masses are calculated and given in Table 3.3. The values found in this way are in good agreement with other measurements.[48, 191, 197, 198]

3.2.3 Emittance Enhancement for Laser Structures

The spectral structure of the reflectance data yields the average plasma frequency of the stack. The determination of the FCA coefficients, on the other hand, utilizes not the spectral information but the magnitudes of the transmittance and emittance data. Both parameters $\omega_{\mathrm{p}}(N)$ and $\alpha(N)$ relate to the free carrier concentration N.

The ratio of electron concentrations in two different samples can, with help of Eq. (3.12), be written as

$$\frac{N_1}{N_2} = \frac{\left(\varepsilon_{\infty,2}\hbar^2\omega_{\mathrm{p},2}^2\right)^{-1} - \frac{a}{A_{\mathrm{p}}}}{\left(\varepsilon_{\infty,1}\hbar^2\omega_{\mathrm{p},1}^2\right)^{-1} - \frac{a}{A_{\mathrm{p}}}} = \frac{\left(\varepsilon_{\infty,2}\hbar^2\omega_{\mathrm{p},2}^2\right)^{-1} - 2.6834\,\mathrm{eV}^{-2}}{\left(\varepsilon_{\infty,1}\hbar^2\omega_{\mathrm{p},1}^2\right)^{-1} - 2.6834\,\mathrm{eV}^{-2}}\,. \tag{3.13}$$

Table 3.4: Ratios of electron concentrations N and absorption coefficients α for the samples S, R1, R3, and REF. $\alpha(h\nu)$ of REF is taken from Ref. 191 ($N = 1.12 \times 10^{18}\,\mathrm{cm}^{-3}$).

No.	N_1/N_2	α_1/α_2	$f_\alpha = \frac{\alpha_1/\alpha_2}{N_1/N_2}$
S/R1	1.144	1.453	1.27
S/R3	0.389	0.508	1.30
S/REF	1.026	1.610	1.57
R3/R1	2.941	3.171	0.93

This expression eventually yields a numerical value for the electron concentration of the laser sample of $N = 1.16 \times 10^{18}\mathrm{cm}^{-3}$ that is very close to that of sample R1 (cf. Table 3.1).

In case of $\alpha(N)$, usually a linear relationship on N is assumed that becomes superlinear in case of degeneracy.[48, 189–192] But, due to close proximity of carrier concentrations of stack and reference sample R1, the assumption of a linear relationship is still justified in the analyzed case.

The slopes of the absorption spectra for 0.2 eV $\leq h\nu \leq$ 0.3 eV of the stack and of the reference samples are very similar [Fig. 3.6(b)], resulting in constant ratios of the absorption coefficients. Such ratios are given together with the ratios of the electron concentration in Table 3.4 for the stack, the reference bulk GaAs samples, and for a sample (REF), taken from Ref. 191 (sample No. 5 with $N = 1.12 \times 10^{18}$ cm^{-3}).

Evidently, the absorption of the laser stack is enhanced by a factor that is substantially larger than the ratio of the electron concentrations, numerically expressed by the absorption enhancement factor f_α. For the stack and the very similarly doped reference sample R1 a value of $f_\alpha(\mathrm{S/R1}) = 1.27$ follows. The value derived with the spectrum of sample R3, on the other hand, is much less accurate because of the large uncertainty of the absolute values of $\alpha(\mathrm{R3})$. Nevertheless, also such ratio points to an enhancement of absorption in the device structure, as well as the large ratio with the literature reference REF does. The ratio for the reference samples of $f_\alpha(\mathrm{R3/R1}) = 0.93$ is, as expected, close to unity, although the slightly too low value points to the influence of the superlinearity on N in $\alpha(N)$.

According to Kirchhoff's law, the enhancement of absorption is connected with an enhancement of emission. The emission enhancement factor f_ϵ is derived from the absorption enhancement factor f_α using Eqs. (3.6) and (3.7) as

$$f_\epsilon = \frac{\epsilon}{\epsilon_0} = \frac{1-\tau}{1-\tau_0} \cdot \frac{1-\varrho\tau_0}{1-\varrho\tau} = \frac{1-\mathrm{e}^{-\alpha d}}{1-\mathrm{e}^{-\alpha/f_\alpha d}} \cdot \frac{1-\varrho\mathrm{e}^{-\alpha/f_\alpha d}}{1-\varrho\mathrm{e}^{-\alpha d}}\,, \tag{3.14}$$

where the subscript 0 indicates the expected bulk values in case of no en-

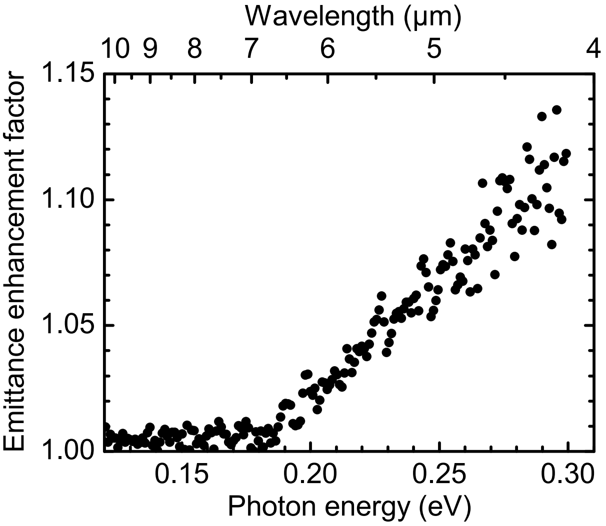

Figure 3.8: Spectral dependence of the emittance enhancement factor f_ϵ as derived from Eq. (3.14) for an absorption enhancement of $f_\alpha = 1.27$. This factor illustrates the spectral dependence of the experimentally observed emittance enhancement of the semiconductor laser sample over the bulk GaAs samples.

hancement. The reflection coefficient used follows from solving Eqs. (3.6)

$$\varrho = \frac{-1-\tau^2+\left(1+2\tau^2+\tau^4-8\tilde{\varrho}\tau^2+4\tilde{\varrho}^2\tau^2\right)^{1/2}}{2(\tilde{\varrho}\tau^2-2\tau^2)} . \tag{3.15}$$

The magnitude of the emittance enhancement factor f_ϵ is calculated in this way for $f_\alpha = 1.27$ and plotted in Fig. 3.8. Apparently there is a linear increase in $f_\epsilon(h\nu)$ for photon energies larger than about 0.18 eV which corresponds to the onset of transparency of the stack sample [cf. Fig. 3.5(b)]. For smaller photon energies the sample is opaque, limiting the emittance to $\epsilon = 1 - \varrho$, independent of the absorption strength, as is easily seen from setting $\tau = 0$ in Eqs. (3.6). At wavelengths as short as 4 μm, the emittance of the laser diodes is up to 10 % – 15 % higher than in the comparable bulk crystal sample.

Enhancement mechanisms

The observed enhancement of absorption and emission of thermal radiation is mainly caused by two mechanisms, the imperfect reflection of thermal radiation from the metal layers in the device structure and the absorption of thermal radiation in the p-doped layers. Both mechanisms are unique to the laser devices and are not present in n-doped bulk crystals.

In the case of the experiments with the laser stack, about 150 metal-semiconductor interfaces are probed. The setup records thermal radiation with an angle of divergence of ±3°, corresponding to very shallow angles of ±1° with the metal-semiconductor interfaces inside the laser devices. Structural imperfections of these interfaces lead to a partly diffuse reflection of thermal radiation, in particular for such small angles of incidence.[108] Another potential source of losses in such a grazing incidence geometry is due to the excitation of surface plasmons on the metal layers.

A related experiment on a series of undoped GaAs bars with different lengths (0.6-6 mm) demonstrated that their emittance is considerably increasing with the cavity length only in case of metallizations on top and bottom.[199] For the bare GaAs bars, on the other hand, no noticeable increase in emittance was seen because of the very low absorption coefficient of the nominally undoped GaAs.

In addition to the metallization, a laser diode structure contains highly p-doped layers. There, at ambient temperatures and in case of photon energies between 0.2 and 0.3 eV the absorption spectrum is dominated by inter-VB transitions of heavy holes into the light hole band.[193–196] The average hole concentration in the p-doped layers is close to the average electron concentration in the n-doped layers but their total thickness is $\lesssim 2\,\%$ of the total thickness of the n-doped material. Nevertheless, since the absorption cross section per hole is typically up to 10 to 50 times higher than for the indirect intraband transitions of electrons, their absorption is expected to make an appreciable contribution to the overall absorption.

3.2.4 Chapter Conclusions

In this chapter, a direct experimental verification of the thermal emission properties of GaAs-based semiconductor lasers was provided. This was accomplished with help of a calibrated setup for quantitative measurements of spectrally resolved emittances. Thermal emission spectra, measured against a calibrated blackbody radiator, from a stack of high-power laser bars and from bulk GaAs reference samples were compared. The thermal radiation measurements were analyzed with a formalism providing the directional spectral emittance, transmittance, and reflectance under normal incidence. This allowed to relate the thermal emission properties of the devices to the underlying materials properties absorption coefficient and carrier concentration. The analysis revealed a pronounced enhancement of the thermal emission from the laser as compared to the bulk reference samples. Laser specific components, namely the metallic contacts and the heavily p-doped semiconductor layers were identified as the origin of this enhancement.

Chapter 4

Thermography of Semiconductor Lasers: Methodology

In this chapter, the methodology for the extraction of temperature information from thermography of semiconductor lasers is described, including the measurement strategy for the composite thermal radiation signal, the temperature calibration procedures, the materials property issues, the thermography setup, and the acquisition modes. The implications due to the semitransparent nature of the laser diode for the thermal IR radiation are analyzed for the case of highly spatially resolved thermography and related to the effects from diffraction limited imaging.

4.1 Measurement Strategy

4.1.1 Signal Contributions

A successful thermographic measurement accounts for the fact that thermal radiation is inherent to all objects with finite temperature. Thus the measured signal in the camera detector is, in any case, a composite of different contributions. For laser diodes the overall signal S can be expressed by

$$S = S_\epsilon + S_\varrho + S_\tau + S_{\mathrm{Bg}}\,, \tag{4.1}$$

which is given by the thermal radiation originating from the laser diode and being proportional to the laser's emittance (subscript ϵ), thermal radiation of the environment that is reflected from the laser and being proportional to the laser's reflectance (subscript ϱ), thermal radiation that is transmitted

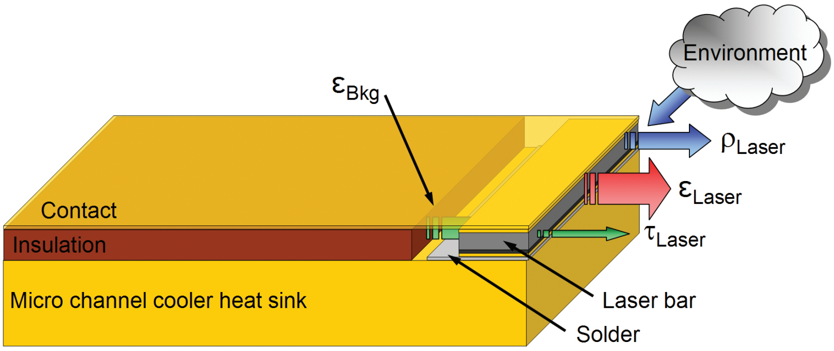

Figure 4.1: Schematic of the typical assembly of a high-power device together with the main radiation sources giving rise to the composite signal in case of a thermographic analysis of the front facet.

through the laser and being proportional to the laser's transmittance (subscript τ), and an offset due to the background intensity (subscript Bg); see Fig. 4.1.

The straight-forward way would be, in analogy to section 3.1.3, to vary S_ϱ, S_τ, and S_{Bg} and, thus, to separate S_ϵ. Such experiments are difficult for high-power bars because they would demand for destructive access to the bar background. But, since in almost all cases the interest is in the operating device, the strategy is to take, beside the image of the operating device (*on image*), an image including all mentioned contributions but with the device not operating (*off image*). In practice, first the device is kept at or close to room temperature - the usual operating point - and a reference image is acquired. Then the device is turned on and another image is acquired. The resulting difference image contains only one non-vanishing term, namely the difference of both S_ϵ contributions:

$$S(\mathrm{on}) - S(\mathrm{off}) = S_\epsilon(\mathrm{on}) - S_\epsilon(\mathrm{off})\,. \tag{4.2}$$

Such approach results in temperature differences and addition of the homogeneously warm device in the reference image (e.g., 25°C) leads to absolute temperatures.

4.1.2 Temperature Calibration Procedure

By virtue of the generality of Planck's formula (2.19) the measured signal $S(T)$ versus object temperature T can be calculated. The spectral blackbody radiant power from the area F_p, corresponding to one pixel of the detector array (including magnification), emitted into a solid cone Ω with half-opening

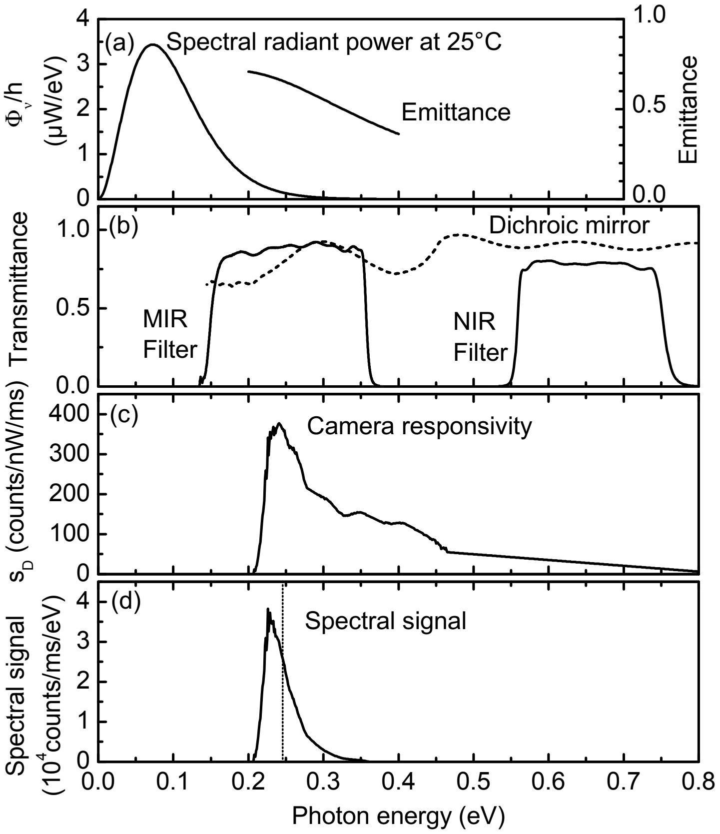

Figure 4.2: Overview of spectra leading to the camera signal for a laser diode: **(a)** spectral radiant power of a blackbody at 25°C into a cone of 30° [cf. Eq. (4.3)] and typical emittance of a laser diode (fit from chapter 3); **(b)** transmittance of optical filter elements; **(c)** camera responsivity; **(d)** spectral camera signal after multiplication according to the integrand in Eq. (4.5). Area dependent parameters are given for the equivalent of one pixel (60 μm)^2.

angle θ is given by the following expression

$$\Phi_{\nu,\mathrm{BB}}(h\nu, T, \theta, F_\mathrm{p})\frac{dh\nu}{h} = \int\limits_{\Omega}\int\limits_{F_\mathrm{p}} L_{\nu,\mathrm{BB}}(\nu, T)\cos\theta\, d\Omega\, dF\,\frac{dh\nu}{h} \tag{4.3}$$

$$= F_\mathrm{p}\pi\sin^2\theta\frac{2h\nu^3}{c^2}\left[\exp\left(\frac{h\nu}{kT}\right)-1\right]^{-1}\frac{dh\nu}{h}\,. \tag{4.4}$$

In Fig. 4.2(a) this is displayed in units of μW/eV for $F_\mathrm{p} = (60\ \mu\mathrm{m})^2$, $\theta = 30°$, and a temperature of 25°C.

Together with the emittance $\epsilon(h\nu)$ of a typical laser diode [derived from a fit of the experimental data of chapter 3 and displayed in Fig. 4.2(a)] and the transmittances of the optical filters $\widetilde{\tau}_\mathrm{Filter}(h\nu)$ [in Fig. 4.2(b) the dichroic mirror and two spectral filters are displayed, cf. Section 4.2.1], the spectral radiant power from a laser diode reaching the thermographic camera can be calculated. For the applied MIR filter an integration over the photon energy range $\Delta h\nu$ from 0.2 eV to 0.4 eV leads, with the earlier determined (see Ref. 200) responsivity $s_\mathrm{D}(h\nu)$ of the thermographic camera [Fig. 4.2(c)], to

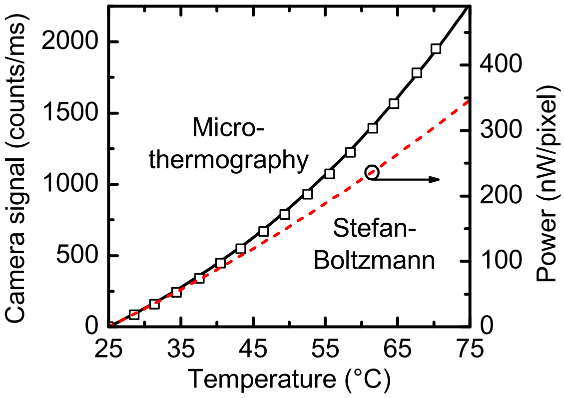

Figure 4.3: The solid black line marks the theoretical calibration curve [camera signal vs temperature; cf. Eq. (4.5)] for a laser diode. The experimental calibration curve (black squares) is replotted from Fig. 4.4(b). The power law according to the Stefan-Boltzmann law (4.6) is given as dashed red line for the same angle and area as in Fig. 4.2.

the camera signal in units of counts/ms

$$S(T,\theta,F_\mathrm{p}) = \int\limits_{\Delta h\nu} s_\mathrm{D}(h\nu)\,\varPhi_{\nu,\mathrm{BB}}(h\nu,T,\theta,F_\mathrm{p})\epsilon(h\nu)\tilde{\tau}_\mathrm{Filter}(h\nu)\,\frac{dh\nu}{h}\,. \tag{4.5}$$

The spectral signal in the integral is shown in Fig. 4.2(d) together with the weighted average (dotted line) resulting in a central wavelength of 5.0 μm, i.e., a photon energy of 0.246 eV.

In Fig. 4.3 the theoretical calibration curve for a laser diode (solid black line) together with the experimental data of Fig. 4.4(b) (black squares) are presented, both relative to 25°C. The theoretical curve is obtained from Eq. (4.5) multiplied with 0.4855 to account for the different objective lenses in experimental calibration and $s_\mathrm{D}(h\nu)$ determination. A clear agreement of the two approaches is visible.

In contrast, a simplified approach with the Stefan-Boltzmann law (2.21) for the same solid angle and pixel area, given by

$$\varPhi_\mathrm{BB}(T,\theta,F_\mathrm{p}) = \int_0^\infty \varPhi_{\nu,\mathrm{BB}}(T,\theta,F_\mathrm{p})\,d\nu = \sigma T^4 F_\mathrm{p}\sin^2\theta \tag{4.6}$$

and displayed relative to 25°C as dashed red line, fails because of the small spectral region $\Delta h\nu$.

Experimental calibration procedure

Nevertheless, the parameter emittance is usually not well defined. It is strongly dependent on the material and the surface of the object. In case of complete devices, the emittance is thus spatially varying which requires individual calibration procedures for each type of device. With a measurement like the one outlined in Chapter 3 a determination is of course possible but involves a lot of effort. A more convenient way to perform a calibration is

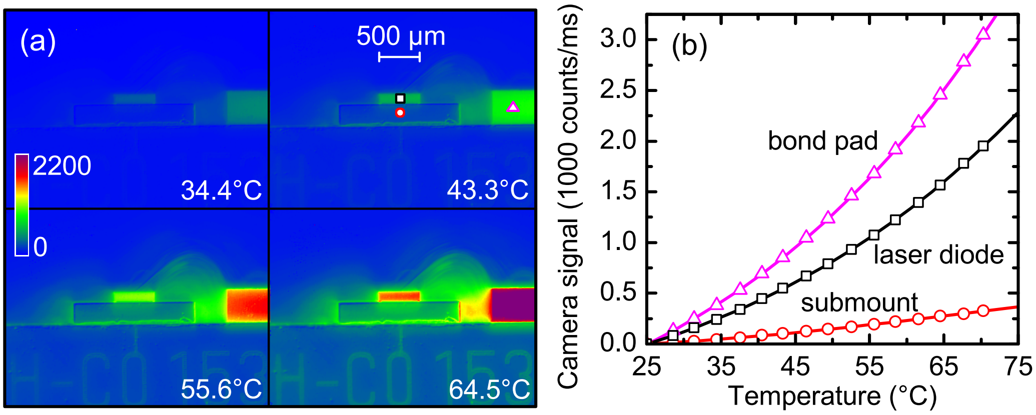

Figure 4.4: Experimental calibration of a 500 μm-wide high-power laser mounted on a CuW submount sitting on a Cu heat sink. **(a)** Raw thermal difference images at different indicated heat-sink temperatures given in counts/ms. The reference image has been recorded at a heat-sink temperature of 25.0°C. **(b)** Camera-signal-vs-temperature curves for the laser diode, the submount, and the bond pad as indicated by the symbols in (a). The data points have been averaged over several raw image pixels and fitted by third order polynomials (full lines).

provided by the heat sink of the device. It can be used to heat the device in a calibration measurement where the response of the thermographic camera is monitored simultaneously.

In Fig. 4.4 selected thermal images of such a calibration measurement are shown together with camera-signal-vs-temperature curves for the laser diode, the submount, and the bond pad. The different slopes correspond to different emittances: ~ 0.7 for the laser diode, ~ 0.1 for the CuW submount, and ~ 0.9 for the ceramic bond pad. The camera signal response $S(T, x, y)$ can be approximated by a n-th order polynomial

$$S(T, x, y) = \sum_{0 \leq \mathrm{i} \leq \mathrm{n}} p_{\mathrm{i}}(x, y) \times T^{\mathrm{i}}(x, y)\,. \tag{4.7}$$

Usually, n=3 yields sufficient accuracy[1] for object temperatures of $20°\mathrm{C} \leq T \leq 100°\mathrm{C}$. Application to raw thermal images of the operating device yields absolute temperature distributions like those presented in Fig. 4.5 for injection currents of 1.0 and 2.5 A. Well visible is the heated laser diode and the temperature distribution therein. The bond pad, on the other hand, that gave rise to a strong signal in Fig. 4.4(a) obviously is a bad thermal conductor and stays cool during operation.

---

[1] The built-in camera software allows for a linear interpolation only, sometimes referred to as *emissivity correction*, leading to underestimated temperatures.

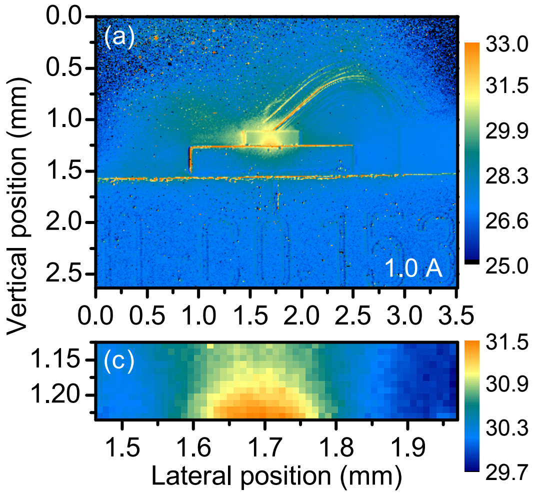

Figure 4.5: Temperature distribution (given in °C) after calibration with the raw images displayed in Fig. 4.4(a) for an operating laser diode at a heat-sink temperature of 25.0°C at an injection current of **(a,c)** 1.0 A and of **(b,d)** 2.5 A. Panels **(c,d)** show the data of the laser diode chip on an expanded scale.

4.1.3 Semiconductor Materials Issues

The parameters emittance (ϵ) and transmittance ($\tilde{\tau}$) depend on the laser cavity length and the carrier concentration N, plotted in Fig. 4.6. The experimental values measured in chapter 3 for the laser stack with 1.2 mm cavity length and $N = 1.16 \times 10^{18}$ cm^{-3} (open circles) are extended to the technologically relevant range of $10^{18}\text{cm}^{-3} \leq N \leq 3 \times 10^{18}\text{cm}^{-3}$ by linearly scaling α of the laser sample with N (solid lines), in this way somewhat underestimating α at high N values. In all cases, ϵ saturates at a constant value of 0.74 with increasing cavity length, becoming effectively reflectance-limited ($\epsilon = 1 - \tilde{\varrho}$), whereas $\tilde{\tau}$ approaches zero.

A high ϵ value is advantageous for thermographic applications because it results in a large signal S_ϵ, enabling high thermal resolution and good discrimination against the ambient thermal background. Second, a low $\tilde{\tau}$ results in a small signal S_τ originating from other sources. Thus, a long cavity and a high doping level are preferable prerequisites for precise thermography. The environment signal S_ϱ that is reflected into the camera does not follow such a dependence on cavity length and neither the ambient background S_{Bg} does. Such signal contribution can be accounted for by keeping the environment stable during the measurement.

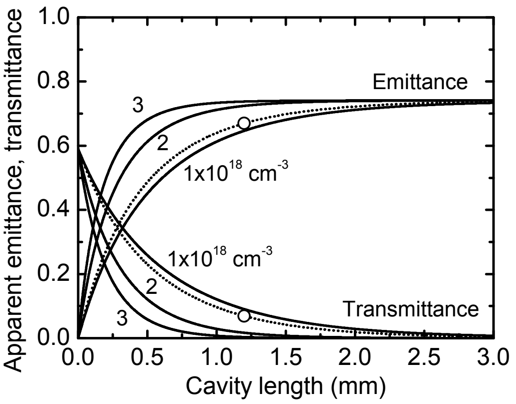

Figure 4.6: Apparent emittance and transmittance for the present thermography system, plotted vs the laser cavity length for substrate dopings N of 1, 2, and 3×10^{18} cm^{-3}. Circles represent experimental values for the actual laser sample and dotted lines are calculated from Eqs. (3.6) and (3.7). Full lines are derived from linear interpolation of $\alpha(N)$ of the laser sample in chapter 3.

Transparency issues

The laser devices of chapter 3 show average values of $\epsilon = 0.67$ and $\widetilde{\tau} = 0.07$. In the worst case of a blackbody source behind the laser sample, of same temperature as the sample, the total thermal radiation would give rise to a camera signal corresponding to an apparent $\epsilon = 0.67 + 0.07 = 0.74$ instead. In the case of free-standing single emitters, this effect is well controllable by means of the mentioned reference subtraction. But for complex packaging schemes like in high-power bars, the contribution of the background assembly is accessible only by disassembling the device. In such cases the impact on the temperature determination is defined via the experimental calibration where the entire device, that is laser diode plus background assembly, is homogeneously heated. During operation, on the other hand, the background assembly is at a lower temperature than the laser and even smaller than the heat-sink temperature directly below the laser. Measurements and calculations (cf. Refs. 49, 201) provide values for the latter of around 60% the temperature increase of the active region. Consequently, and in accordance with section 4.3.1, the effect is mostly a diffuse flat offset leading to an underestimation of the temperature of laser bars by at most $\sim 4\%$.

Temperature stability

The outlined strategy relies on the stability of ϵ, $\widetilde{\tau}$, and $\widetilde{\varrho}$, which are indeed very slowly varying for temperature differences of typically ≤ 20 K experienced during laser operation. For laser diodes like those studied in chapter 3 the temperature dependence of the relevant parameters can be linearly approximated for temperatures around 300 K (probing wavelength 5 μm): $(d\widetilde{\varrho}/dT)\widetilde{\varrho} \sim 8\cdot10^{-5}\mathrm{K}^{-1}$, $(d\alpha/dT)/\alpha \sim 4\cdot10^{-3}\mathrm{K}^{-1}$, $(d\widetilde{\tau}/dT)/\widetilde{\tau} \sim -8\cdot10^{-3}\mathrm{K}^{-1}$, $(d\epsilon/dT)/\epsilon \sim 8\cdot10^{-4}\mathrm{K}^{-1}$.[48, 88, 192] Such slight shifts are compensated by an experimental calibration.

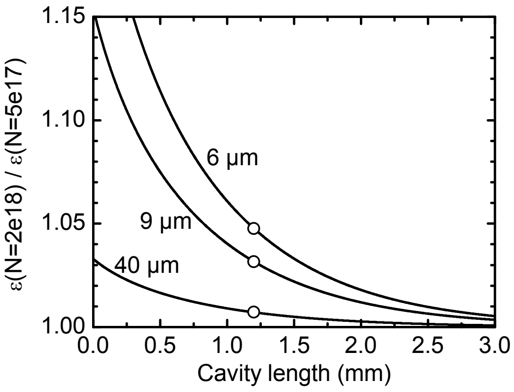

Figure 4.7: Effect of carrier injection into the active region for spatial resolutions of $6, 9, 40$ μm/pixel, plotted vs laser cavity length (circles at 1.2 mm). Ratio of ϵ averaged over one pixel containing the 1-μm-wide active region with $N = 5 \times 10^{17}$ cm^{-3} and ϵ with $N = 2 \times 10^{18}$ cm^{-3} during operation. $\epsilon(N)$ is derived as in Fig. 4.6.

Materials homogeneity

From the dependence $\epsilon(N)$ a fundamental restriction on the achievable accuracy of thermography follows. The nominal thermal resolution of most recent infrared detector arrays is on the order of $\delta T \approx 20$ mK (at 300 K), giving rise to $\delta T \approx 30$ mK for semiconductor lasers with $\epsilon = 0.67$.[120–123] This corresponds to a relative difference in N of about 0.6% in laser structures doped to $N = 10^{18}$ cm^{-3}. In spatially resolved imaging, this high sensitivity is, however, reached only for small spatial fluctuations of $\delta N/N \approx 10^{-3}$. Such extraordinary high homogeneities are commonly not achievable on large scales. In case of production-type GaAs wafers, typical fluctuations of up to $\delta N/N \sim 1 - 10\%$ are encountered across single wafers,[202] resulting in detectable temperature differences with an accuracy of $50 - 500$ mK. However, a spatially resolved calibration can compensates such effects.

Dependence on the injected carrier concentration

During calibration (no injection) and during operation N is different. Nevertheless, thermography is intrinsically robust against the effect of $\epsilon(N)$, because of the long laser cavities and because the signal is built up from thermal radiation coming from active and passive regions. In contrast, laser-spectrum measurements for temperature determination (cf. section 2.7.1) are much more affected by the N dependence of E_{g}, g, and n. Assuming a 1.2-mm-long resonator, a 1-μm-wide QW plus waveguide region with average $N = 5 \times 10^{17}$ cm^{-3} without injection, and, under high injection conditions with $N = 2 \times 10^{18}$ cm^{-3}, the thermographic temperature is by only 3% overestimated for a spatial resolution of 9 μm/pixel. For longer cavities and lower resolutions this value gets even smaller (Fig. 4.7). Since these considerations base on experimental data (chapter 3) they already include the N dependent parameters $\alpha(N)$ and $n(N)$.

4.2 Setup and Acquisition Modes

4.2.1 Thermography Setup

The thermography setup is sketched in Fig. 4.8 with all its major components.

The HgCdTe focal plane array [384×288 pixels, pixel area $(20\ \mu\text{m})^2$; pixel pitch 24 μm] thermographic camera system (THERMOSENSORIK CMT 384M) images the front facet of the laser diode. It has a responsivity range of $1.5-6.0\ \mu$m [see Fig. 4.2(c)] at integration times of 40 $\mu\text{s} - 3$ ms. Frame rates between ≤ 150 Hz for full frame and ~ 5 kHz for sub-frame imaging are possible with NETD[2] (blackbody at 300 K, 2 ms integration time) of $\lesssim 20$ mK. Different IR objective lenses together with different extension tubes ($1-13$ cm) provide variable magnifications between 0.4× (imaging of complete cm-bars) and 6× (imaging of single emitters), corresponding to spatial resolutions of nominally 60 and 4 μm/pixel with N.A.≈ 0.5.

The measurement strategy outlined in section 4.1 relies on the stability of the temperature of all relevant objects else than the laser device. This is provided by the shielding compartment that is temperature stabilized by the laboratory air conditioning. Furthermore, in order to protect the objective lens and to avoid an additional thermal signal from the otherwise heated lens, a dichroic mirror based on a Si wafer with HR coating for fundamental laser emission (reflectance of $R \geq 0.99$ for $0.8\ \mu\text{m} \leq \lambda \leq 1\mu\text{m}$) and AR coating for thermal emission ($R < 0.1$ for $3\ \mu\text{m} \leq \lambda \leq 6\ \mu\text{m}$) is mounted in between the camera and the laser diode. The AR coating assures low losses for the desired thermal IR and suppresses reflection of ambient thermal radiation via the mirror into the camera lens. The mirror is tilted by $30-45°$ to avoid back-reflection of the intense laser radiation.

Interchangeable band-pass and long-wave-pass filters [see transmission spectra in Fig. 4.2(b)] are applied, resulting in two spectral channels, called mid-IR (MIR: $3.4-6.0\ \mu$m, with weighted average at 5.0 μm) and near-IR (NIR: $1.6-2.2\ \mu$m, centered around 1.9 μm).

4.2.2 Free-Run and Sampling Thermography Mode

Three modes of operation are distinguished. In the *free-run mode* the camera records images according to its frame rate, uncorrelated to the laser diode. This mode is used for lasers in continuous wave (cw) operation where a number (~ 100) of images is averaged for noise reduction. For time-dependent measurements of identical thermal pulses, for instance in sections 5.1 and

---

[2] Noise Equivalent Temperature Difference

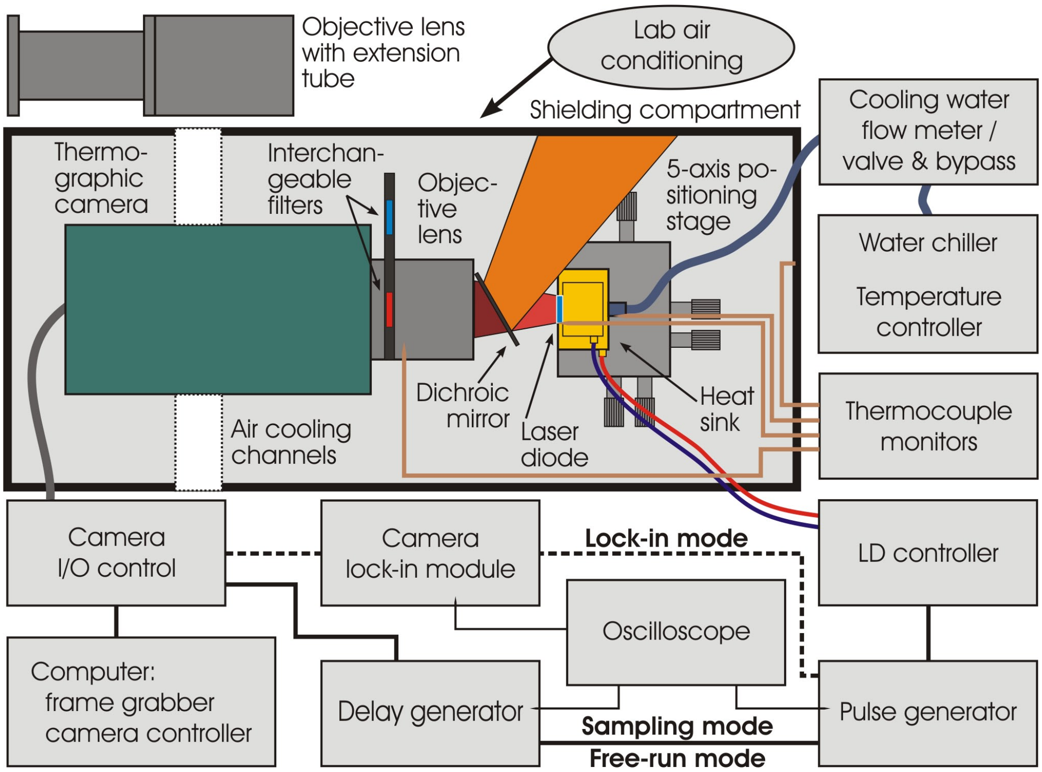

Figure 4.8: Schematic of the thermography setup. Inside of the shielding compartment the thermographic camera (green) together with the laser diode (light blue) in the heat sink (yellow) mounted on the 5-axis positioning stage are given. The laser beam (red and orange) is split at the dichroic mirror. An interchangeable objective lens with extension tube is given for comparison. The laser diode cooling and temperature controlling devices are sketched at the right part of the image. At the bottom the two electronic circuits for the lock-in mode (dotted lines) and the sampling/free-run modes (solid lines) are given.

5.2, the *sampling mode* is applied. There the camera and the pulsed laser excitation are triggered by a delay generator (STANFORD DG535). The data acquisition can be subsequently delayed in the camera I/O control, in this way sweeping the gate, as defined by the integration time, over the thermal transient.

In all cases, the devices are mounted on thermo-electrically cooled heat sinks or mounted on top of water cooled stages [water flux typically $\sim (20 \pm 1)$ l/h at temperature of typically $\sim 25°$C] and are aligned with the camera detector by a 5-axis positioning stage. For single emitters a HP 8114A pulse-generator delivers cw and pulsed currents up to 2 A and for bars laser diode controllers (LDC 3060, OSTECH) deliver currents up to 80 A.

4.2.3 Time-Resolved Lock-In Thermography

Although high-power laser diodes dissipate large amounts of heat during operation, initial stages during turn-on are characterized by a much smaller temperature rise. For the present thermographic camera with spatial resolution on the order of 10 μm the maximal thermal resolution for a semiconductor laser is about 40 mK for 1 ms integration time [cf. calibration curve in Fig. 4.4(b)]. If one increases the temporal resolution, i.e., by decreasing the integration time, by one order of magnitude to 100 μs, the thermal resolution concomitantly decreases with the square root to about 100 mK. Consequently, only temperature distributions showing values larger than that are resolvable.

To this end, lock-in techniques[3] offer, thanks to their phase-locked detection, a higher signal-to-noise ratio which increases with the square root of the measurement time. Since laser diodes can be modulated via the injection current they are well suited for lock-in detection. In the *lock-in mode* every pixel in the thermal image is phase-locked to the pulsed excitation by a combination of hardware (excitation is triggered by the camera lock-in module) and software (correlation for every pixel).

Standard and synchronous undersampling lock-in concept

In standard lock-in techniques, the temporal resolution is restricted to half the frame rate which is commonly below a few 100 Hz, even for state-of-the-art cameras.[120–123] Higher time resolution is attained by advanced methods such as the so-called *synchronous undersampling lock-in thermography.* Here, lock-in frequencies higher than the frame rate are applied and the camera frames necessary for correlation are sampled at different times, each separated by n periods. The highest temporal resolution is achieved by correlation of a minimal number of camera frames. The camera software allows down to four images and a simple rectangular correlation function.

For operation of a laser diode at 50% duty cycle the time resolution is given by the pulse width of the injection current

$$\tau_{\mathrm{PW}} = \frac{\tau_{\mathrm{frame}}}{2(\mathrm{n}+1/4)}\,. \tag{4.8}$$

The period between two camera frames τ_{frame} is a function of the integration time and the image size. For full frame images (384 × 288 pixel) a maximal frame rate of $1/\tau_{\mathrm{frame}} \approx 150$ Hz can be achieved for the used camera system. In Fig. 4.9 the timing scheme is outlined. There n=0 refers to the standard

---

[3] An introduction into lock-in thermography is given in Ref. 18.

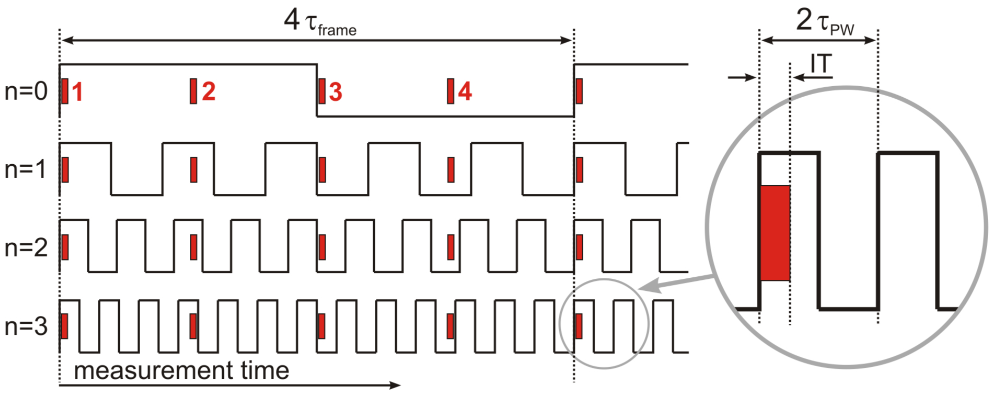

Figure 4.9: Scheme of the lock-in timings. Black pulses mark both the laser injection current and the correlation function. Red squares represent the camera frames. Four of them are required by the camera software for one lock-in correlation. The pulse train at the top represents the situation of standard lock-in (temporal resolution limited to the frame rate τ_{frame}), whereas the three pulse trains below illustrate the synchronous undersampling lock-in concept. The magnified view at the right represents the situation of highest attainable temporal resolution ($2\,\mathrm{IT} = \tau_{\mathrm{PW}}$).

lock-in technique. In the case of n>0, the time resolution is limited by the integration time IT of the IR camera and the phase stability of the lock-in setup and experiment. If the latter is provided the current pulse width can be as short as 2 IT (inset in Fig. 4.9).

In the experiments presented in section 5.1.2, $\mathrm{N} = (5 - 50) \times 10^3$ lock-in periods, each consisting of four camera frames and 4n+1 current pulses, are sampled. The duration of such measurement is about 0.5-5.5 minutes. The accumulated camera image is given by

$$S(x,y) = \frac{1}{4\mathrm{N}} \sum_{\mathrm{i}=1}^{N} \sum_{\mathrm{j}=1}^{4} K_{\mathrm{j}} S_{\mathrm{i,j}}(x,y)\,, \quad K_{\mathrm{j}} = \begin{cases} +2 & \text{for } \mathrm{j} = 1,2 \\ -2 & \text{for } \mathrm{j} = 3,4 \end{cases}, \tag{4.9}$$

with the individual camera frames $S_{\mathrm{i,j}}(x,y)$ and the correlation function K_{j}. By such summation for all pixels (x,y) of the detector, the thermal sensitivity for detection of a laser diode in pulsed operation can be improved to below 10 mK.

4.3 Light Propagation Effects and Resolution Constraints

4.3.1 Thermal Radiation Propagation in a Semiconductor Laser Cavity

The small absorption coefficient in the relevant IR spectral region enables the redistribution of thermal radiation inside the laser cavity, eventually influencing the thermal radiation distribution detected with thermography from the front facet. This issue has been met in thermography of semiconductor transistors and laser diodes but has not been resolved since.[28, 119] In the following, this effect is treated in terms of geometrical optics with raytracing. From comparison with modeled and experimental data it follows that on a micrometer scale the thermal radiation propagation inside semiconductor lasers leads to a broadening of the thermographically detected temperature distribution that is sufficiently modeled by raytracing.

Thermography experiments and samples

In order to perform a reliable comparison between experimental data sets and simulation results two different laser devices are used, measured with different thermographic methods and modeled with independent thermal FEM models. Both laser designs, a QD laser **QD-950-BA** and a QW laser **QW-808-2-BA** are described in section 2.5, where the QD device has its 50-μm-wide active stripe asymmetrically placed $\approx$ 185 μm from the left side and the 130-μm-wide active stripe of the QW device is centered.

For the QD laser, operated in cw, standard thermography was used for different operating points, and for the QW laser, operated with pulsed currents, synchronous undersampling lock-in thermography was applied, which allows, via variation of the electrical pulse width, for recording quite different transient thermal situations. The situation 15 μs after turn-on represents a narrow temperature distribution with only a limited heat spread away from the active layer, whereas at 11 ms after turn-on almost the steady-state situation with heat spread across most of the device is found. Corresponding experimental data is presented in section 4.2.3 and the extraction of the given times is discussed in Appendix B.

Thermal FEM modeling

At least three facts make computer simulations of the temperature distribution in laser diodes indispensable: first, so far there is no standard experimental techniques able to probe the bulk temperature of the entire device that could serve for comparison with thermography, second, for prediction of the thermal behavior of novel devices, and third, experimental equipment is much more expensive than commercial software.

FEM is a numerical technique for finding approximate solutions of partial differential equations. For solving the heat conduction equation it assumes heat-sources of which the major ones have been discussed in section 2.2. Usually, a broad and established source for reliable materials parameters is necessary and great care must be spend on the definition of an appropriate discretization mesh which needs to adequately address the large differences in the spatial dimensions of the device (e.g., QW vs substrate thickness). Thus, an experimental technique like thermography for testing FEM results is required.

Both laser designs have been numerically simulated with independent 2D FEM models, neglecting a temperature variation along the laser axis. The QD laser was modeled by J. Mukherjee *et al.*[4] with a steady-state electrothermal FEM model as outlined in Ref. 47. For the QW laser a transient 2D FEM simulation is performed by R. Sarzała, W. Nakwaski *et al.*[5] in accordance with Refs. 50, 74, 203–205.

Raytracing approach

The laser device geometry as presented in Fig. 4.10 is approximated by two parts, the substrate and the epilayer structure. The materials properties of the latter are averaged over its entire width since each of its individual thin layers has a thickness small compared to the thermal radiation wavelength of 5.0 μm. The metallic contacts on top and bottom are approximated by setting the reflectivity of the corresponding surfaces to a fixed value R.

In raytracing[6] typically $10^7 - 10^8$ rays with an intensity given by the thermal FEM simulation and a random polarization start from random source points in space into random directions (i.e., thermal radiation with unpolarized isotropic intensity). They are traced until they reach the detector array which is placed outside the laser device directly in front of the front facet or until they are damped to 10^{-3}.

The objects that the rays travel in and the approximation of geometrical optics govern both the power and the trajectory of the rays.[38] Raytracing is

---

[4] J. Mukherjee is with the Optoelectronics Group, Department of Physics/ Tyndall Institute, University College Cork, National University of Ireland, Cork, Ireland

[5] R. Sarzała and W. Nakwaski are with the Laboratory of Computer Physics, Institute of Physics, Technical University of Łódź, ul. Wólczańska 219, 93-005 Łódź, Poland

[6] Here ZEMAX (ZEMAX Development Corporation, www.zemax.com) is used.

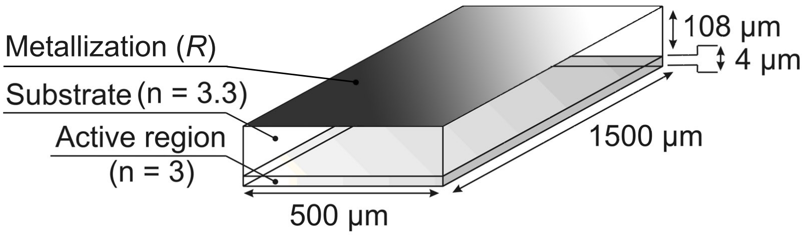

Figure 4.10: Schematic of the device geometry used in raytracing of the QW laser. The observer is facing the front facet and the detector (thermographic camera or software detector array) sits in front of it (not shown).

implemented with monochromatic rays with photon energy of $h\nu = 0.246$ eV ($\lambda = 5.0$ μm) averaged over the camera detection window (compare section 4.1), which limits the number of semiconductor materials parameters to the refractive index n and the linear absorption coefficient α, and the specular reflectivity R of the opaque metallic surfaces. Including a useful range, the materials parameters are chosen accordingly: $\alpha = (18 \pm 6)$ cm^{-1} [according to $N = (1.16 \pm 0.39) \times 10^{18}$ cm^{-3}], calculated from the absorption spectrum in Fig. 3.6; for n two different values are used: 3.3 for the GaAs substrate and 3.0 for the epitaxial structure; for the metallic contacts $R = 1$ is assumed.

The FEM-simulated 2D bulk temperature distributions are spatially averaged to resolutions either meeting the spatial resolution of the thermographic camera or to yield a decent signal-to-noise ratio with the maximal number of allowed rays ($\sim 10^8$) and are extended along the entire cavity length, effectively defining an array of homogeneous cuboids. Transformation into IR light sources is performed via application of an experimental calibration as described in section 4.1.2.

To account for internal attenuation, the ratio between a homogeneous light source distribution and the according homogeneous response distribution in the detector array is determined as $(7.1 \pm 0.3) \times 10^{-3}$. Such small outcoupling ratios are caused by the small exit cone due to the large refractive index jump from semiconductor to air [$2\pi\,(1-\cos\theta_{\text{crit}})\,/2\pi \approx 4.7\times10^{-2}$, with the critical angle for total internal reflection $\theta_{\text{crit}} = \arcsin\,(1/n)$], by internal absorption (~ 0.5; cf. Fig. 4.15), and by internal reflection at the front facet (~ 0.3).

Quantitative comparison of simulation and experiment

Figures 4.11 provide an overview of representative results from FEM simulation (a,b,e,f), raytracing of these maps (c,g), and thermography (d,h) of

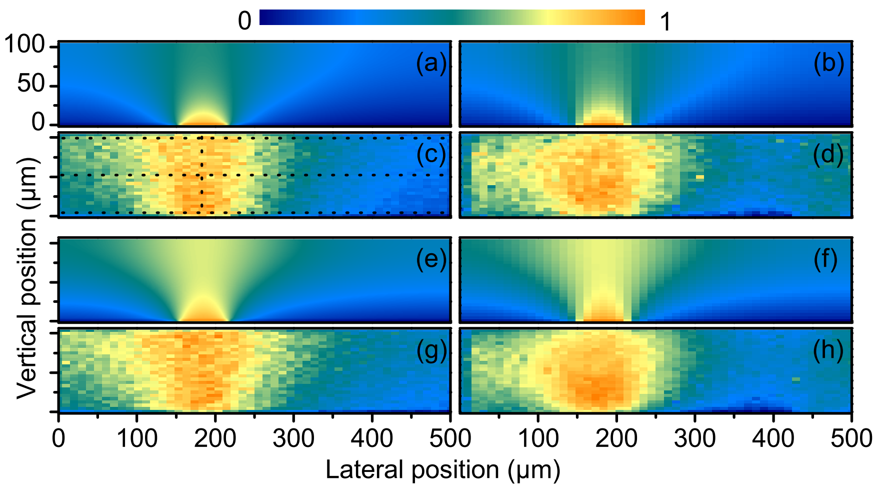

Figure 4.11: Modeled and measured normalized thermographic images from a QD laser operated **(a-d)** at 0.9 A ($2I_{\text{th}}$) and **(e-h)** at 1.8 A ($4I_{\text{th}}$). **(a,e)** temperature distributions obtained from a 2D-FEM thermal simulation for $1 \times 1\ \mu\text{m}^2$ spatial resolution; **(b,f)** FEM data spatially averaged to 26×50 pixel with a pixel size of $4\ \mu\text{m} \times 10\ \mu\text{m}$ (vertical × lateral) as input data for raytracing; **(c,g)** raytracing result; **(d,h)** thermography result spatially averaged to $4\ \mu\text{m} \times 10\ \mu\text{m}$. Dotted lines represent the cuts used for comparison.

the QD laser at two operating points (2 and 4 I_{th}). From these calibrated and normalized temperature maps a distinct broadening is clearly visible. In addition to the originally sharp temperature distribution around the active layer a considerable amount of thermal radiation is detected, appearing to come from the entire height of the substrate. Raytracing obviously explains such apparent disagreement in temperature distribution very well.

Lateral and vertical cuts through the maps are displayed in Fig. 4.12 (QD laser at 2 and $4I_{\text{th}}$) providing absolute values for the temperature. In Fig. 4.13 the analogous comparison is presented for the QW laser 15 μs (a,b) and 11 ms (c,d) after turn on in terms of normalized temperature profiles. In all cases, there is an exceptionally good agreement between the experimental and raytracing results of the FEM inputs.

The only adjustable parameter in the QD laser comparison is the heat-sink temperature. The FEM model assumes a fixed temperature of 25.0°C at the device heat-sink interface, whereas in the experiment the heat-sink was controlled to (25.0 ± 0.2)°C approximately 4 mm away, which could result in a small temperature difference. In order to nearly perfectly match model and experiment, heat-sink temperatures of 26.1°C [Fig. 4.12(a-d)] and 25.0°C [Fig. 4.12(e-h)] are assumed.

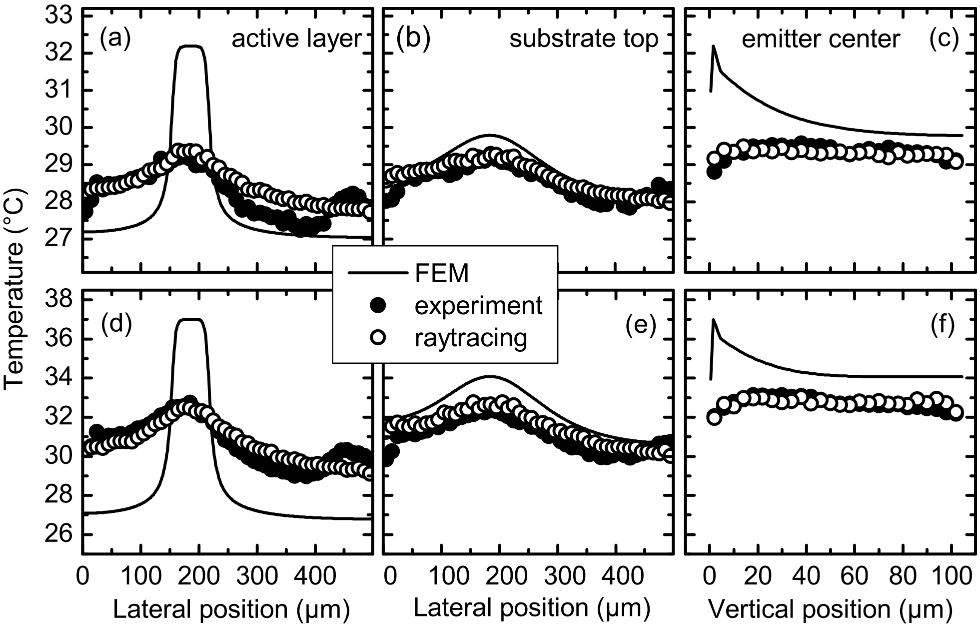

Figure 4.12: Absolute temperature profiles from a QD laser operated **(a-c)** at 0.9 A [cuts from Fig. 4.11(a-d)] and **(d-f)** at 1.8 A [cuts from Fig. 4.11(e-h)]. Lateral profiles **(a,d)** around the active layer, **(b,e)** at the top of the substrate, and **(c,f)** vertical profiles at the stripe center. All profiles are averaged from three pixel rows or columns for noise reduction.

Parameter variation and geometrical treatment

In order to evaluate the degree of agreement between experimental thermographic images and intensity distributions derived from raytracing of temperature distributions (from FEM), the impact of the governing parameters is studied. The parameters α, n, and R are varied individually and the resulting profiles of the active layer region are displayed in Fig. 4.14.

An increase in α or n and a decrease in R lower the absolute intensities on the detector in front of the front facet. The shape (i.e., the normalized intensity), on the other hand, is only barely affected for the n variation and does only depend at its outer wings on a strong α variation.

The observed tendencies can be phenomenologically explained with help of Figs. 4.14(e) and 4.15. In Fig. 4.14(e) source distributions as in Fig. 4.13(a) but with a length of only a quarter of the total cavity length are used. Such distributions are placed into the first to fourth quarter of the cavity while keeping the original geometry. The shapes of the resulting thermal radiation signature exhibit pronounced deviations in dependence of the distance of the sources from the front facet. They effectively change from profiles very simi-

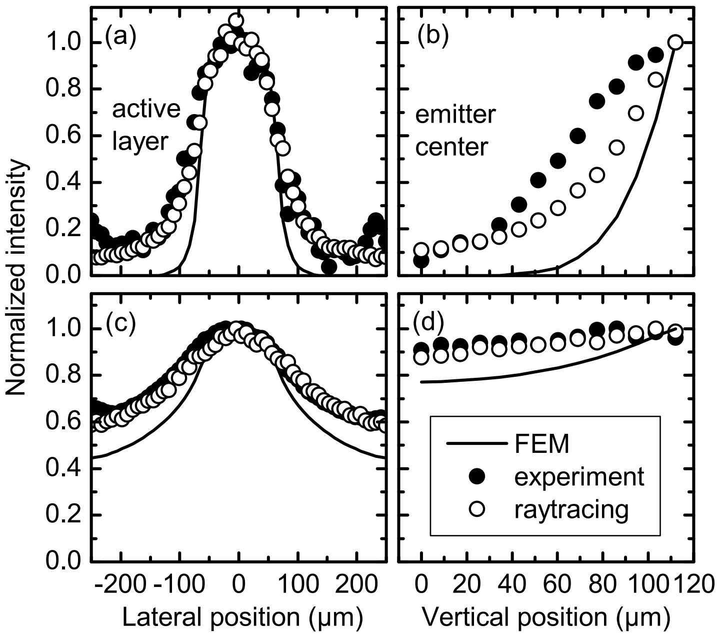

Figure 4.13: Normalized temperature profiles from a QW laser operated at pulsed currents of 1 A. Solid lines represent the FEM results, open circles the raytracing results, and closed circles the results from thermography. **(a)** lateral profiles of the active layer, and **(b)** vertical profiles of the emitter center of a transient thermal situation 15 μs after turn-on. **(c)** and **(d)** are analogous profiles after 11 ms. For lateral cuts 2 rows and for vertical cuts 5 columns are averaged in the corresponding 14×58 data matrices.

lar to the raytracing input towards a low-intensity homogeneous background without any structure. The intensity profile that is measured with thermography is the sum of these contributions from different depths. Consequently, an increase of α would change the relative contributions from different cavity depths in favor of the regions closest to the front facet.

In Fig. 4.15 the relative intensities outside the front facet in terms of the number of experienced reflections on top and bottom metallizations are given for a simplified 2D geometrical model assuming a radiation source placed exclusively in the active region. Total internal reflection for $n = 3.3$ allows for only a limited cone ($\approx 18°$ with respect to the surface normal) of thermal radiation starting at each cavity point to exit the front facet. Accordingly, every 352 μm along the cavity length another reflection becomes possible adding up to four reflections for rays coming from deeper than 1408 μm. The impact of reflections[7] is a redistribution of the radiation in the detector

---

[7] It is known that metals can exhibit a partly diffuse reflection, especially if the surface is

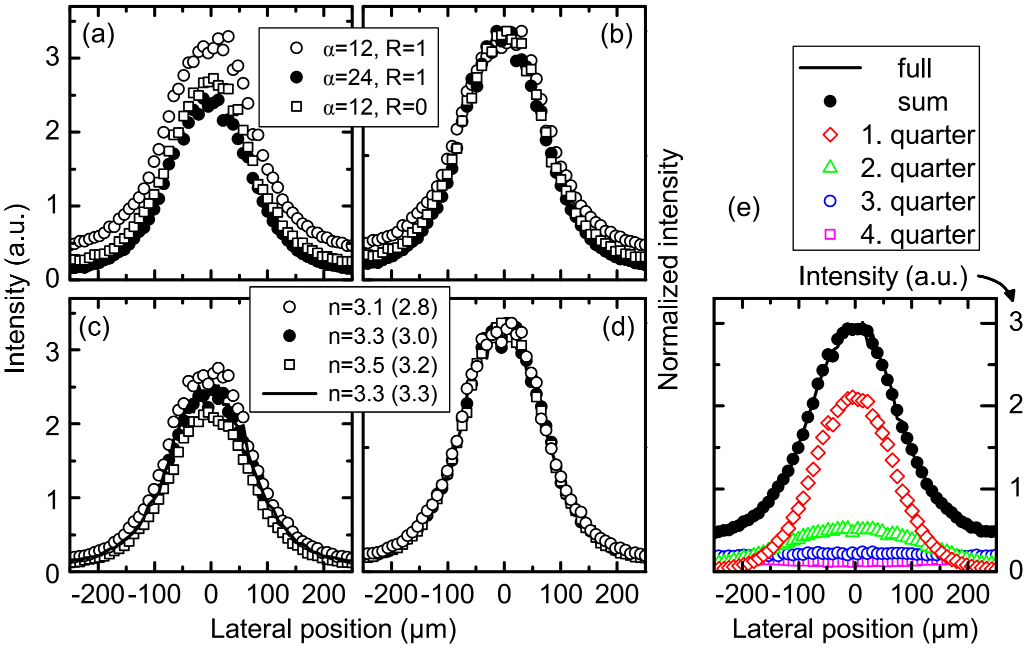

Figure 4.14: **(a)** absolute and **(b)** normalized profiles of IR light intensity along the active layer of a QW laser obtained from raytracing [as in Fig. 4.13(a)]. Open symbols result from $\alpha = 12\ \text{cm}^{-1}$, closed symbols from $\alpha = 24\ \text{cm}^{-1}$, circles from $R = 1$, and squares from $R = 0$. **(c,d)** corresponding profiles for varying n (given in the graphs) of the substrate and of the epilayer region (given in parentheses). Full circles mark the standard situation. **(e)** Open symbols mark results from individual raytracing simulations with source distributions placed in the first to fourth quarter of the device only and closed circles their sum which perfectly agrees with a reference simulation of the full cavity given as full line.

plane as compared to the direct contribution.

In conclusion, direct light coming through a small angle, mainly from the first few hundreds of microns of the laser cavity, is responsible for the shape of the thermal image and the contribution from further inside the cavity is, to a large extend, composed of reflected light giving rise to an additional flat background. It follows that high α or low R values increase the relative amount of direct light (cf. Fig. 4.14) and that a realistic increase in n only results in a slightly smaller exit cone and consequently lower intensities.

---

rough.[108] This would lead to a further diffuse redistribution of thermal radiation inside the laser cavity. Such an effect is, however, difficult to measure and consequently not implemented in the raytracing approach.

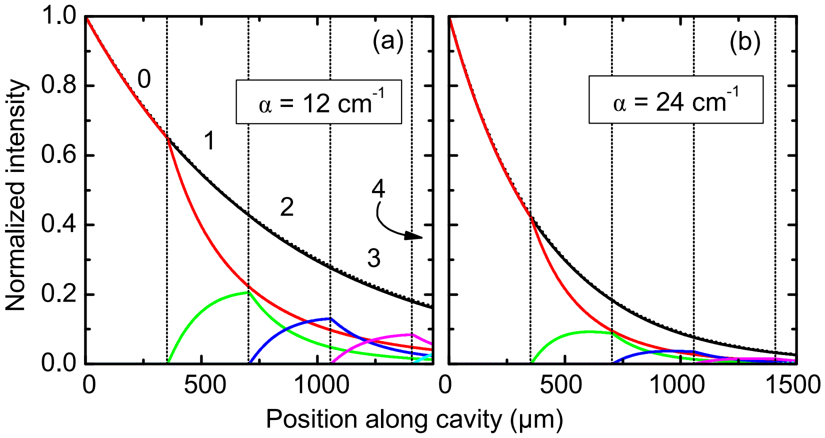

Figure 4.15: IR light intensity directly in front of the front facet, normalized to the allowed exit cone for a 2D model, plotted vs source position along the laser cavity (y). Vertical dotted lines mark allowed regions of 0-4 reflections on top and bottom metallizations. Colored lines represent average values of the relative ray intensities exiting the front facet, full black lines are the sum of these. Dotted black lines follow the $\exp(-\alpha \cdot y)$ dependence for direct light; **(a)** for absorption coefficients of $\alpha = 12\ \text{cm}^{-1}$ and **(b)** of $\alpha = 24\ \text{cm}^{-1}$

4.3.2 Thermography at the Diffraction Limit

Since the maximum of the blackbody emission is at room temperature close to a wavelength of 10 μm, a thermographic detection of such temperatures should take place around this wavelength as well. The Rayleigh criterion, however, allows discrimination of point-sources with a microscope down to a distance close to their emission wavelength only. Thus the use of a detection system with high responsivity at relatively short wavelengths is essential for thermography of semiconductor lasers with typical dimension in the micrometer range. In this work, the detection wavelength is centered around 5 μm with N.A.$\approx$ 0.5, thus enabling a maximal spatial resolution of approximately $0.61 \cdot 5\ \mu\text{m}/0.5 \approx 6\ \mu\text{m}$. In view of the spatial dimensions of some of the major heat-sources, typically around 1 μm, a basic constrain in the thermographic approach becomes evident. As a result, at least vertical (in epitaxial growth direction) temperature profiles measured by thermography are intrinsically affected and always represent a spatial average of the real situation.

In Fig. 4.16(a) the contrast function measured with an alternating line pattern (standard USAF1951 resolution pattern) and with the MIR and NIR filters at a 6× magnification (nominal resolution: 4 μm/pixel) is plotted against the pattern line width. In this situation, the MIR spectral range used

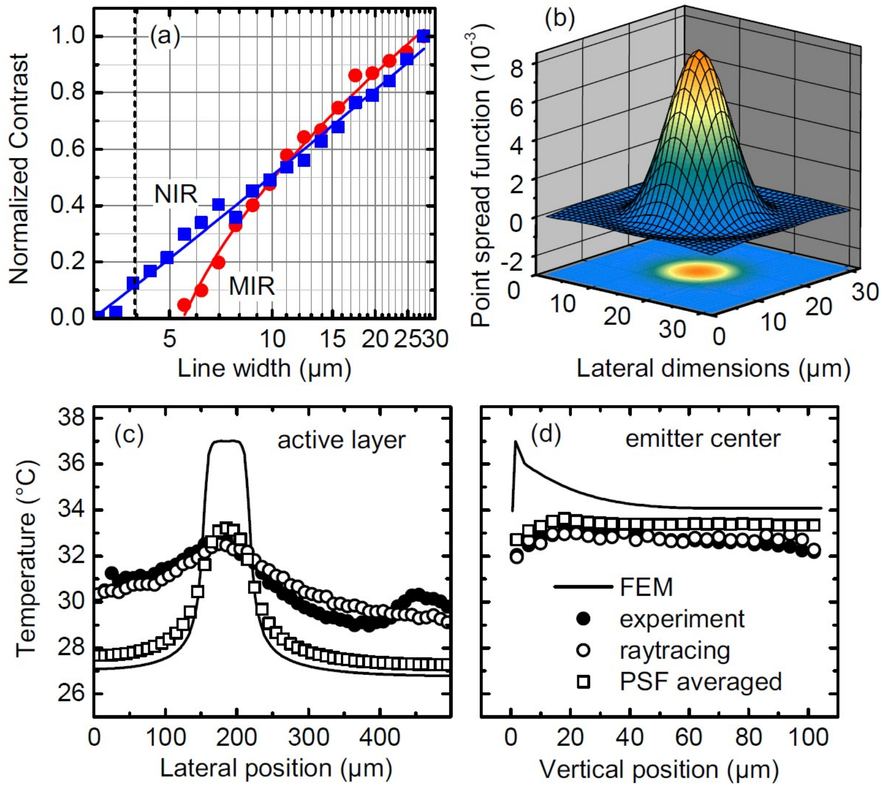

Figure 4.16: **(a)** Contrast function for the thermographic system with filters for the 3.4 – 6.0 μm (MIR, red circles) and 1.62 – 2.24 μm (NIR, blue squares) wavelength ranges and a microscopic lens for 6× magnification (nominal resolution of 4 μm marked by dotted vertical line). **(b)** Symmetrized in-plane PSF for the MIR range. **(c,d)** Temperature profiles for a QD laser operated at 1.8 A ($4I_{\mathrm{th}}$). The cuts are taken from Fig. 4.12(e,h) and the square symbols are derived from averaging the FEM distributions (solid lines) with the PSF of (b).

for thermography is clearly diffraction limited to about 6 μm at a contrast of about 10% while for the NIR range the magnification of the lens is still suitable. The point spread function [PSF, see Fig. 4.16(b)] is the Fourier transform of the modulation transfer function which relates to the contrast function in Fig. 4.16(a), and which specifies the response of a radiating point source on the imaging detector.[17] The full width at half maximum is about 9.8 μm, which means that it cannot be expected to fully discriminate two radiating sources closer than such distances. Consequently a smearing of steep temperature gradients in vicinity of the active layer is expected.

For illustration [Fig. 4.16(c,d)] on an undisturbed distribution of radiation sources, the PSF is applied as a linear filter to the FEM-modeled temperature distributions of the QD laser. The impact due to the diffraction limited optics is less pronounced than the propagation effect, but of similar strength for lateral positions directly above the active stripe. And, second, the propagation effect treated by raytracing alone is able to reproduce the right distribution of the thermal IR radiation in good approximation also apart from the active stripe. For other situations (i.e., for $1 - 5I_{\mathrm{th}}$) equivalent results are found. Consequently, an additional convolution of the raytracing result with the PSF is not necessary.

4.3.3 Chapter Conclusions

In this chapter, basic steps were provided that lead to a temperature information from a semiconductor laser. The setup arranged around an IR camera allows for thermography with spatial resolution as small as 6 μm. The omnipresent thermal radiation background makes it necessary to determine temperature differences, which allows for quantification of absolute temperatures via calibration measurements.

In addition to such basic considerations, the fact that the semiconductors are semitransparent for the thermal radiation has an effect on the image formation. Its propagation leads to broadened thermographic images in case of high spatial resolutions on a 10 μm-scale as demonstrated by raytracing of FEM-modeled temperature distributions and comparison with experimental data for QD and QW lasers. For QD lasers this is particularly important because for this type of laser devices the use of the emission wavelength as a thermal probe widely fails. The presented approach enables the verification of thermal simulations such as obtained by FEM for complete semiconductor laser devices without restriction to the active region only.

The considerations on diffraction-limited thermography lead to a very important approximation. If temperatures along the stripe are discussed, it is often sufficient to evaluate the thermographic results in the same way as if they were purely resolution-limited. Outside the stripe, however, only an inclusion of the thermal radiation propagation leads to the exact temperature values. When applying thermography on a more macroscopic scale such as in case of extended laser arrays, the achievable spatial resolution (~ 40 μm) sets a more rigid limitation than the propagating thermal radiation. Such situation is encountered in section 5.1 where a cross calibration with thermal wavelength shifts has been performed.

Chapter 5

Thermography of Semiconductor Lasers: Applications

In this chapter, five different case studies are presented. In addition to the temperature determination shown earlier, such case studies illustrate how the thermographic approach can extend the established analytical methods for semiconductor lasers. First, time-resolved thermography is used to analyze the transient thermal behavior of high-power laser diodes. Following, thermography is applied to detect temperature distributions and hot-spots in high-power cm-bars and it is discussed how they relate to defects. In a third case study, the catastrophic optical damage of high-power laser diodes is monitored spatio-temporally-resolved with a setup combining the thermal and the near-field characteristics during the catastrophic process. The last two studies deal with the analysis of additional IR emission from GaAs-based semiconductor lasers and with application of such spectral component as a probe for laser degradation.

5.1 Transient Thermal Behavior of High-Power Laser Diodes

The transient thermal behavior of high-power laser diodes is accessible with time-resolved thermography. Application of the free-run and sampling modes (cf. section 4.2.2) allows for characterization of the complete device, including the heat sink, in the ms-time scale. The behavior of the semiconductor chip itself is not accessed by the present thermography setup, because the heat spreading within the chip typically takes place on a μs-time scale ($\sim$

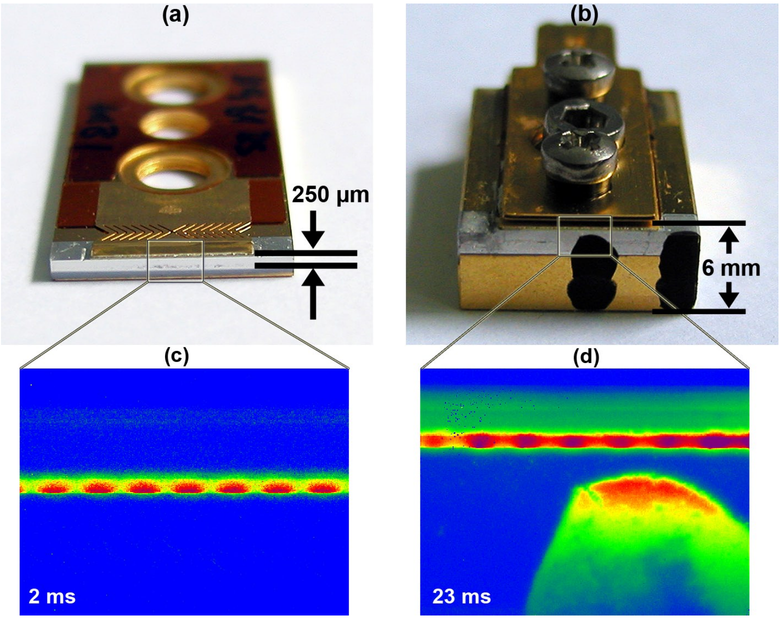

Figure 5.1: Photographs and raw thermographic images (2 and 23 ms after turn-on) of **(a,c)** an actively cooled and **(b,d)** a passively cooled laser bar. The distances between laser diode chip and microchannel cooler or thermoelectric cooler are indicated. The heat sink of the passively cooled device is partly covered with NEXTEL black paint (cf. chapter 3) to enhance the thermal emission.

$10 - 100$ μs).[206–208] One possibility to access this temporal regime even with the present setup is represented by synchronous undersampling lock-in thermography (cf. section 4.2.3); a technique which allows for visualization of the heat flows within the semiconductor chip for times < 1 ms.

5.1.1 Thermal Time Constants of High-Power Laser Bars

Samples and methods

The two principal heat-sink schemes for high-power laser bars, namely active and passive cooling, are implemented in commercial cm-bars **QW-808-1-bar** (cf. section 2.5) and used for comparison of their transient thermal behavior. The actively cooled device [Fig. 5.1(a)] involves microchannels, which allow for direct access of cooling water (temperature 25°C, flow rate 80 l/h) into the Cu heat sink, separated from the semiconductor bar by about 0.25 mm only. In contrast, the passively cooled device [Fig. 5.1(b)] relies on heat conduction through a 6 mm thick copper heat sink, tightly attached to

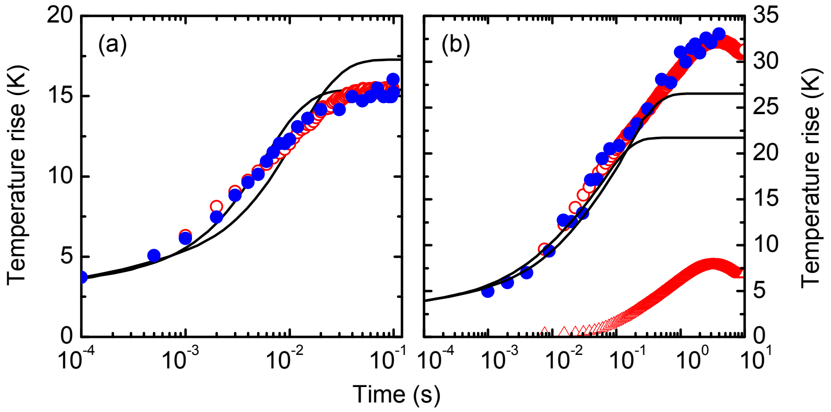

Figure 5.2: Temperature rise determined from FEM calculations (lines), thermography (open circles), and wavelength tuning (full circles) at the active region of the central emitter vs turn-on time relative to 25°C for an injection current of 30 A for **(a)** the actively cooled device and **(b)** the passively cooled device. Triangles mark the thermographically determined temperature rise at the bottom of the passive heat sink (5.9 mm below the position for the circles).

an external thermoelectric cooler (temperature 25°C).

Time-resolved thermography with integration times of 1 ms and sampling rates of 1 and 0.13 kHz was used for the actively and passively cooled devices, respectively. A spatial resolution of 9 μm/pixel [cf. Fig. 5.1(c,d)] was chosen to study the central emitters of both devices and, additionally, a spatial resolution of 34 μm/pixel enabled imaging of the complete front of the passively cooled device.

For comparison with thermography, the thermally induced shift of the emission spectrum was determined with a setup as described in Refs. 206 and 207. The laser bars were mounted parallel to the entrance slit of a grating monochromator and the emission spectra of the individual emitters were measured in parallel with a charge-coupled device (CCD) camera. The wavelength of the central emitter was determined from the weighted average of its emission spectra and the temperature was calibrated with a short-pulse generator (~ 100 ns pulse width and low duty cycle) by recording the wavelength tuning versus the heat-sink temperature as 0.27 nm/K.

Beside the experimental methods, transient thermal 2D FEM simulations were performed by R. Sarzała, W. Nakwaski *et al.* in accordance with Refs. 49, 74, 203–205. In order to exploit the degree of freedom in the FEM simulations, a realistic variation of the heat capacities of the heat sinks was introduced resulting in two thermal transients for each device type.

Experimental results

The temperature rise of the central emitter $\Delta T(t)$ above heat-sink temperature for pulsed injection currents of 30 A ($\sim 2I_{\mathrm{th}}$) are displayed together with the simulation results in Fig. 5.2.

If normalized, the experimental data from both experimental techniques show an excellent agreement. The absolute values as determined after temperature calibration of the thermography experiments are lower than the results from spectral tuning experiments by a factor of ~ 1.3 (applied in Fig. 5.2) because of the spatial averaging and thermal radiation propagation issues discussed in section 4.3.

The time evolutions for the two device types are markedly different. The actively cooled device [Fig. 5.2(a)] reaches the thermal equilibrium after approximately 40 ms and the temperature rises by about 15 K above the initial situation. Comparison with FEM data at the central emitter shows good agreement for this device. The passively cooled device, on the other hand, reaches its maximal temperature rise of about 32 K approximately 2 s after turn-on and saturates close to 31 K after about 10 s. The FEM data shows in this case a much larger deviation, because it assumes a fixed temperature at the interface between heat-sink and thermoelectric-cooler. Instead, thermography of this location [triangles in Fig. 5.2(b)] shows a pronounced increase of about 7 to 8 K that is markedly delayed compared to the transient of the emitter. Obviously, the cooler heats up with a large time constant and also introduces the slight decrease in the temperature in the 2-10 s range. Subtraction of this heat-sink transient from the emitter transient leads to a good agreement of the emitter steady-state temperatures of ~ 24 K and $\sim 22-27$ K, respectively, for experiment and FEM data-sets.

One-dimensional heat conduction model

As an extension of the simplest case of a transient heat transfer problem, that is the lumped capacitance method,[209] the entire laser device is approximated by a linear chain of n such capacitances of mass m_{i} and specific heat C_{i}, each coupled by a thermal resistance $R_{\mathrm{th,i}\to\mathrm{i+1}}$. The overall energy balance of the n stages - from the heat source around the active region P_{gen} down to the bottom of the heat sink at fixed temperature T_{n} - determines their time-dependent temperature $T_{\mathrm{i}}(t)$ as

$$P_{\mathrm{i}}(t) = m_{\mathrm{i}}C_{\mathrm{i}}\frac{\partial T_{\mathrm{i}}(t)}{\partial t} = P_{\mathrm{i-1}\to\mathrm{i}}(t) - P_{\mathrm{i}\to\mathrm{i+1}}(t) = P_{\mathrm{i-1}\to\mathrm{i}}(t) - \frac{T_{\mathrm{i}}(t) - T_{\mathrm{i+1}}(t)}{R_{\mathrm{th,i}\to\mathrm{i+1}}}\,. \tag{5.1}$$

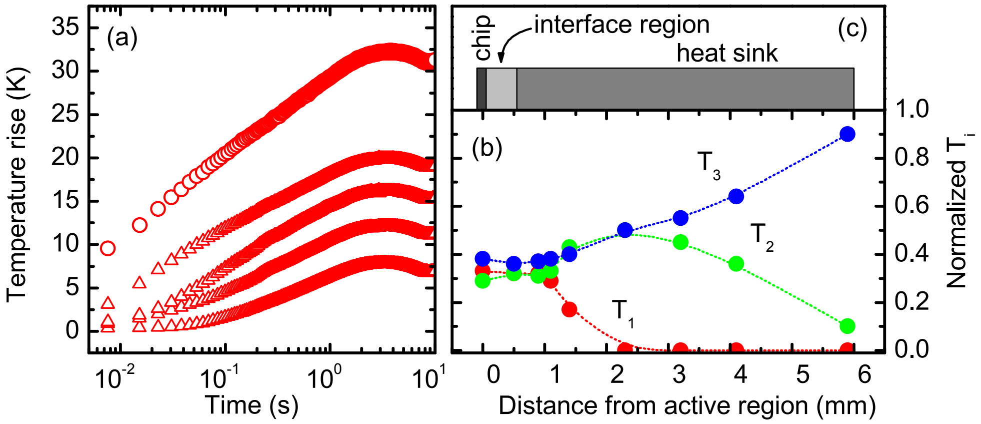

Figure 5.3: **(a)** Transient temperature rise for the passively cooled device [circles from Fig. 5.2(b)] including the heat sink 0.5, 2.3, 4.1, and 5.9 mm below the laser chip (triangles, from top to bottom). **(b)** Normalized thermal amplitudes vs distance from the active region, derived from fits of the thermography transients of (a) according to Eq. (5.3). Dotted lines are guides to the eye only. **(c)** Schematic of the device geometry.

The solution to this expression is derived in Appendix C, which in case of a limited number of sufficiently well separated thermal time constants resembles the following formula for the temperature rise of the first stage

$$\Delta T_1(t) = \sum_{\mathrm{i}=1}^{\mathrm{n}-1} T_{\mathrm{i}}^* \left(1 - e^{-t/\tau_{\mathrm{i}}}\right) \; . \tag{5.2}$$

The 2(n-1) parameters are the thermal amplitudes $T_{\mathrm{i}}^* = P_{\mathrm{gen}} R_{\mathrm{th,i}\to\mathrm{i+1}}$ (in Kelvin) and the time constants $\tau_{\mathrm{i}} = R_{\mathrm{th,i-1}\to\mathrm{i}} m_{\mathrm{i}} C_{\mathrm{i}}$ (in seconds).

Spatially resolved thermal time constants

A total number of three terms in Eq. (5.2) is sufficient to describe the passively cooled device, whereas for the actively cooled device a single term is necessary. The following expression is used for fitting the experimental and simulated results

$$\Delta T(t)/\Delta T_{\mathrm{max}} = T_1\left(1 - e^{-t/\tau_1}\right) + T_2\left(1 - e^{-t/\tau_2}\right) + T_3\left(1 - e^{-t/\tau_3}\right) \; . \tag{5.3}$$

With ΔT_{max} as the maximal temperature rise minus the temperature at 10^{-4} s this results in up to three normalized thermal amplitudes T_1 to T_3 and thermal time constants τ_1 to τ_3.

In addition to the data from the emitters, thermal transients of the passively cooled heat sink are measured [Fig. 5.3(a)]. Numerical fits according

Method	Probed location	τ_1 (ms)	τ_2 (ms)	τ_3 (ms)	T_1	T_2	T_3
Actively cooled bar							
FEM	Emitter	9 ± 3	…	…	1	…	…
TG+WT	Emitter	10 ± 2	…	…	1	…	…
Passively cooled bar							
FEM	Emitter	9 ± 3	110 ± 50	…	0.3	0.7	…
TG+WT	Emitter	10 ± 2	60 ± 10	720 ± 30	0.33	0.29	0.38
TG	HS 0.5 mm	11 ± 3	70 ± 10	670 ± 30	0.32	0.32	0.36
TG	HS 0.9 mm	10 ± 3	70 ± 20	670 ± 20	0.32	0.31	0.37
TG	HS 1.1 mm	10 ± 3	70 ± 20	630 ± 20	0.29	0.33	0.38
TG	HS 1.4 mm	10 ± 3	60 ± 20	630 ± 30	0.17	0.43	0.40
TG	HS 2.3 mm	…	80 ± 20	650 ± 50	…	0.50	0.50
TG	HS 3.2 mm	…	80 ± 20	650 ± 40	…	0.45	0.55
TG	HS 4.1 mm	…	70 ± 20	620 ± 30	…	0.35	0.65
TG	HS 5.9 mm	…	90 ± 30	650 ± 50	…	0.10	0.90

Table 5.1: Exponential time constants and normalized amplitudes obtained from fits according to Eq. (5.3) for actively and passively cooled devices, measured at the central emitter or on the heat sink (HS) 0.5-5.9 mm below the emitter. Methods: FEM = FEM modeling, TG = thermography, WT = emission wavelength tuning.

to Eq. (5.3) are summarized in Table 5.1 and Fig. 5.3(b) versus the vertical distance from the emitter, that is along the direction of heat flow. All three time constants agree to a high degree with average values of $\tau_1 = 10 \pm 2$ ms, $\tau_2 = 70 \pm 20$ ms, and $\tau_3 = 650 \pm 30$ ms.

Such additional spatial information, derived from thermography in a natural way, gives insight into the physical mechanisms behind the thermal time constants. The fastest resolvable component τ_1 characterizes the heat transport from the chip towards the heat sink through the multilayer ~ 0.5-mm-thick interface consisting of the multilayer p-side metallization, the In solder, and the top of the heat sink itself [Fig. 5.3(c)]. Such assignment follows from its presence in both device types and its fast decay with growing distance from the semiconductor bar. The component τ_2 reaches a maximum in the center of the heat sink and can be assigned to the vertical heat conduction through the 6 mm thick heat sink towards the thermoelectric cooler. Finally, the slowest component τ_3 that is increasing along the heat sink is assigned to heat spreading within the heat sink and the cooler until the temperature controller reacts and increases the current in the Peltier element. The latter sets an upper limit on τ_3 and depends much on the particular cooling setup.

5.1.2 Visualizing Heat Flows in Laser Diodes

Time-resolved synchronous undersampling lock-in thermography is implemented as described in section 4.2.3. In this way, a minimal current pulse width of $\sim 110\ \mu$s (IT= 40 μs, $\tau_{\mathrm{frame}} = 6.7$ ms, n=30) at a spatial resolution of $\sim 8.6\ \mu$m/pixel and with a sensitivity on the order of 10 mK is achieved for full frame images. Such images allow for the visualization of heat flows across the device in different planes. Out of a set of measured devices, results from one device at pulsed injection currents of 1 A ($\sim 2\,I_{\mathrm{th}}$), are given in Fig. 5.4.

The QW laser diodes **QW-808-2-BA** (cf. section 2.5), analyzed in section 4.3.1, have an active stripe width of 130 μm and chip dimensions of $1500\times500\times115\ \mu\mathrm{m}^3$ (length×width×height). They are soldered *p*-side down onto CuW heat spreaders that are attached to copper C-mounts, which allow for a good access to the laser from the front *and* the side.

In-plane heat flows

For analysis, cuts through the images [dotted lines in Fig. 5.4(f,l)] are calibrated to temperatures [Fig. 5.5(a,b)]. All figures show that already during the shortest pulse ($\tau_{\mathrm{PW}} = 110\ \mu$s) the heat has spread away from the active region. In lateral direction, the heat reaches the device edges (distance of $\sim 200\ \mu$m) within the 1.1 ms pulses, whereas in vertical direction this process appears to be faster because the distance to the top of the device is only $\sim 100\ \mu$m. The final shape of the temperature distribution is given by the energy balance of device heating and heat-sink cooling which takes place on a tens of milliseconds time scale. Heat flow from the epilayers via the submount and toward the heat sink reduces the initially steep temperature gradients and establishes a steady-state temperature profile on this time scale. The difference between the profiles for 17 and 69 ms long pulses is only marginal. Such time scales have been observed also in surface-sensitive thermo-reflectance studies of laser front facets.[210] The duration of the heat spreading within the GaAs substrate with a characteristic length of $l = 100\ \mu$m can be estimated as $l^2/\chi \sim 300\ \mu$s, where $\chi = 0.31\ \mathrm{cm}^2/s$ is the thermal diffusivity of GaAs.[88, 208] Such numbers meet the observed behavior as well.

Facet-heating observed from the side

The measurements along the laser axis reveal surface and/or near-surface heat sources [Fig. 5.4(right panels) and Fig. 5.5(c,d)]. The temperature rises in a < 100-μm-region around the facets. As for the lateral and vertical heat

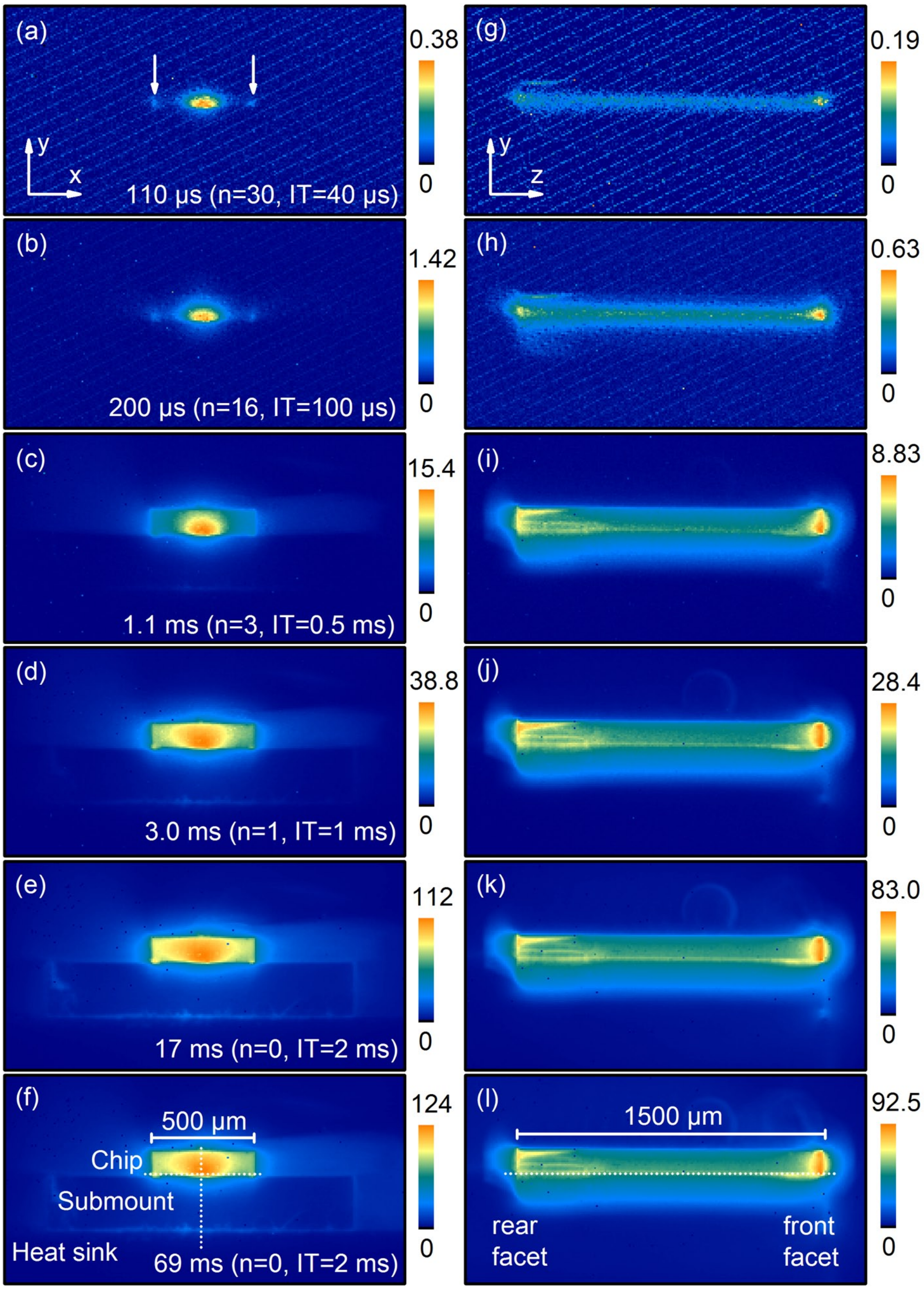

Figure 5.4: Images (in camera counts) from synchronous undersampling lock-in thermography at pulsed currents of 1 A at 50% duty cycle; **(a-f)** of the front facet (x-y-plane); **(g-l)** of the laser side (y-z-plane). Pulse widths, undersampling parameters n, and integration times IT are given. Dotted lines in (f,l) mark the positions for the profiles of Fig. 5.5. Arrows in (a) point to additional hot-spots.

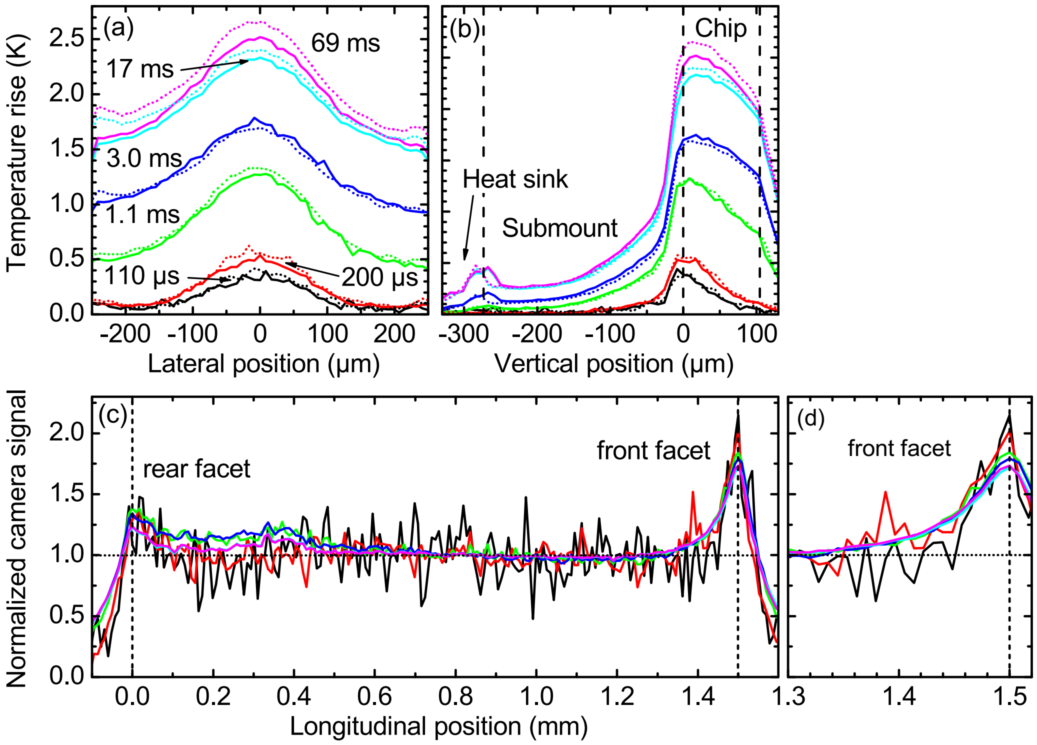

Figure 5.5: Temperature profiles obtained as **(a)** horizontal x-cuts and **(b)** vertical y-cuts trough Fig. 5.4(a-f). Solid and dotted lines represent data from two different devices. **(c)** Normalized (to the average between 0.6 and 1.2 mm) profiles along the laser axis [z-cuts trough Fig. 5.4(g-l)] at the active region **(d)** of the first 200 μm from the front facet. Dashed vertical lines represent the position of the facets. The region between 0.1 and 0.6 mm exhibits enhanced magnitudes because of a poor surface quality due to cleaving.

spreading seen from the front images, also the temperature gradients starting from the facet heat sources become flatter with increasing pulse width. A higher temperature at the facets is caused by the heating mechanisms described in section 2.2 and, in case of the front facet, by a decreased heat removal from mounting against the submount edge, including a slight overhang on the order of ~ 10 μm. Scattered thermal radiation from the device edges into the camera can be ruled out as the main cause, because the front facet exhibits a much higher signal amplitude than the rear facet, while the reflectivities (in this spectral region) of both are not substantially differing from the bulk value. Such finding is in agreement with results from qualitative thermographic studies from the side facet [137] and from electroluminescence collected through a window in the n-side contact,[211] where even the temperature decay length of ~ 100 μm is attested. In general, the excess of temperature at the front facet over that at the rear facet can be explained if the dominant heating process is reabsorption of stimulated emission at the facet (or near to it), because of the higher photon density there.[24, 136–138]

Hot-spots at the edges

In addition to the heat conduction from the heat sources (concentrated at the active region) toward the heat sink, hot-spots at the device edges occur already at the shortest pulses; see arrows in Fig. 5.4(a). Since the heat has not spread there within such times - there are even minima around ±200 μm - these hot-spots are not related to heat conducted from the active stripe. Two alternative possibilities exist. A possible explanation is thermal radiation originating from the active layer, which is guided within the waveguide and reflected or scattered toward the camera. It has been shown in Ref. 212 that such guiding of thermal radiation inside the waveguide is, in principle, possible. But, such an effect is very weak and is expected to be most pronounced shortly after the turn-on when most of the heat still resides inside the waveguide. Alternatively, a weak electrical contact at the device edges may give rise to a shortage that bypasses the electrical insulation layers.

Summary

In summary, the transient thermal behavior of high-power laser bars is found to be strongly dependent on the type of heat sink. In case of passive heat sinking, the device performance is limited by heat conduction in the thick heat sink, characterized by τ_2 - even if the external cooler would be perfect. Such findings are relevant for the design of applications. The imaging capabilities of the thermography method enabled a spatio-temporally resolved analysis in a natural way, including characterization of the heat sink. As an extension, time-resolved synchronous undersampling lock-in thermography demonstrated access to the transient thermal behavior of laser diodes on a sub-ms-time scale for spatial resolutions on a μm-length-scale with high sensitivity on the order of 10 mK. Such an experimental technique delivers information that is relevant for the analysis of the thermal kinetics inside laser diodes. For instance, the heat-spreading inside the laser chip is found to happen on a 100-μs-time scale, whereas the overall thermal equilibrium with the present heat-sink is reached on a 10-ms-time scale.

5.2 Thermography as Analytical Tool in Reliability Studies

In this section, the applicability of thermography as an analytical tool for reliability studies is explored. The thermographic approach is described and selected results from 197 bars are presented that mainly base on statistics over the large number of experiments. Interesting will be if and how such an analytical tool can be used, separately or in combination with other tools, to predict failures.

5.2.1 Thermographic Approach

Sample description

The high-power cm-bars **QW-808-1-bar** are described in section 2.5. They are mounted *p*-side down on actively cooled microchannel heat sinks by two companies and two different technologies. Batches A and B are soldered with In directly on the Cu heat sinks, whereas batches C and D are soldered with AuSn on CuW submounts, (nearly) expansion-matched to GaAs, which are attached to the copper part of the heat sink. The AuSn-on-CuW technology is expected to solve the reliability problems caused by the thermal expansion coefficient mismatch of the In-on-Cu technology,[5, 63, 67, 213–215] and by the unstable In solder that is subject to electro- and/or thermomigration.[66–70] The use of two batches, containing 40-60 bars each, for both technologies helps to discriminate between technology-related and batch-related effects. During operation, the entire device is fixed on a laser carrier with access to cooling water [temperature (25.2±0.2)°C, flow rate (20±2) l/h] and electrical current.

Experimental conditions and data generation

Thermographic screening in terms of temperature profiling and determination of hot-spots is applied to all devices before the burn-in and aging. The thermographic camera is applied with the wide-angle objective lens, allowing for imaging of the whole bar at once at a spatial resolution of $40 - 60$ μm. The MIR filter ($3.4 - 6.0$ μm) detects thermal radiation, whereas the NIR filter ($1.6 - 2.2$ μm) detects IR radiation involving defect states (mainly) inside the substrate (for detailed discussion see section 5.4). The basic idea is to use distinct local increases or decreases of the signal magnitude in both spectral channels, called MIR and NIR hot-spots, as indication for defective or partly damaged emitters.

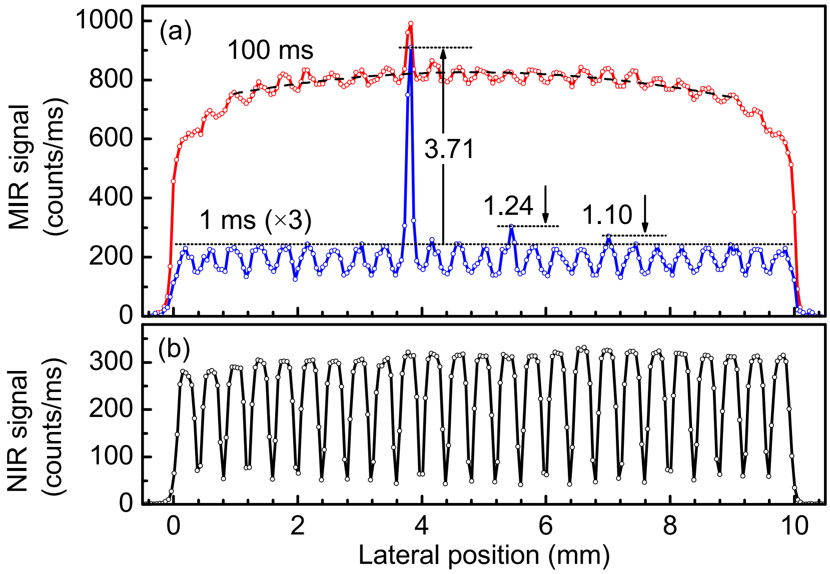

Figure 5.6: **(a)** Vertical profiles through the maximal pixel line of the MIR images (the 1^{st}ms profile was multiplied by 3). Hot-spot determination is indicated by dotted lines and arrows. Determination of the thermal curvature by a second order polynomial fit is indicated by a dashed line. **(b)** Vertical profiles through the maximal pixel line of the NIR image.

For analysis in the MIR channel [Fig. 5.6(a)], the laser bars are driven at an injection current of 60 A ($\sim 4I_{\text{th}}$), with a pulse width of 100 ms and a repetition rate of 0.5 Hz. Since different thermal time constants are involved in heating of a laser bar, thermal images taken at different times after turn-on relate to different dominant time constants (compare section 5.1). Initially, primarily the active region gets warm. Then at later times, heat-conduction establishes a thermal equilibrium with the heat-sink and the environment. Consequently, the detection of hot-spots that relate to emitter-defects is performed with thermal images recorded at early times (here 1 ms is used) after turn-on, and hot-spots are defined as an ≥ 5 % increase over the average signal amplitude of the generic emitters. For the NIR spectral range the hot-spots are filed analogously.

The overall thermal profile [Fig. 5.6(a)], on the other hand, can be acquired from a situation at later times. It was found in section 5.1 that after about 100 ms the measured temperatures in such actively cooled high-power laser bars resemble nearly 95% of the thermal equilibrium situation. As a measure of the curvature (T_2) of the thermal profile a second order polynomial fit $T(x) = T_0 + T_1(x - 5\text{ mm}) + T_2(x - 5\text{ mm})^2$ is performed for local positions $1\text{ mm} \leq x \leq 9\text{ mm}$. The average bar temperature is filed as well.

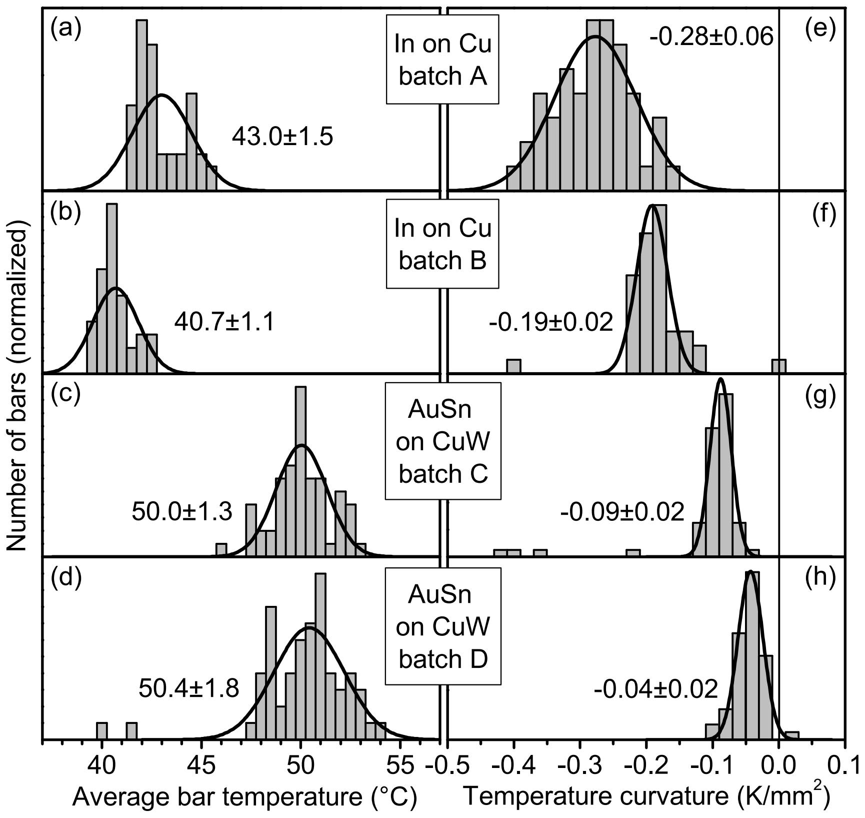

Figure 5.7: Statistics of the average bar temperature for **(a,b)** In-on-Cu technology and **(c,d)** AuSn-on-CuW technology, each for two batches. **(e-h)** statistics of the temperature curvature for the same batches. Mean values and standard deviations are derived from gaussian fits.

5.2.2 Statistical results

Average temperature and temperature curvature

For the average bar temperature [Fig. 5.7(a-d)] there is a clear difference between the two packaging technologies. The AuSn-on-CuW technology causes about 9 K higher numerical values because of the lower thermal conductivity of the CuW material [$\lambda_T(\mathrm{Cu}) \approx 390\ \mathrm{Wm^{-1}K^{-1}}$, $\lambda_T(\mathrm{W}) \approx 170\ \mathrm{Wm^{-1}K^{-1}}$].[63] [1] The data spread of more than 1 K is larger than the uncertainty of the experiment (a standard deviation of 0.2 K was derived from repeated measurements). Most probably this is caused by the spread in the WPE of the devices which affects the output power and the dissipated power.

---

[1] This is one of the reasons for the nearly exclusive application of the In-on-Cu technology for ultra-high-power bars delivering up to 1 kW per cm-bar.[5, 6, 216, 217]

An indication for such assignment is given by the relative spread of the temperature increase above 25°C which amounts to $\sim 5-7\%$, almost equal for all batches. The WPE of the bars is ~ 0.5 and the double[2] of its spread is indeed comparable to the observed relative spread in temperature.[218] Variations of the substrate doping within one batch (originating from one wafer) are less probable since a rather large 10% variation corresponds to 0.5°C only (cf. section 4.1.1).

The thermal curvature parameter [Fig. 5.7(e-h)] is negative in all cases because the center of the device is warmer than the edges. The transition to the AuSn-on-CuW technology lowers the thermal curvature and such enhances the wavelength homogeneity, in the best case from about 0.26 nm (batch A) to 0.05 nm (batch D) along the bar. This is a consequence of the reduced lateral heat-spreading in the CuW submount under the bar, given by both its lower thermal conductivity and its smaller width. In contrast to the bar temperature, for this parameter a clear correlation with the batch is observed. The distribution of batch A shows a much larger width than the other batches. A simple explanation cannot be given to this phenomenon from the available data; maybe larger variations in the heat sink or in the solder interface caused it.

Hot-spots

As the potential signature of either defective emitters or emitters that are expected to fail during operation, hot-spot statistics (Fig. 5.8) are extracted for the MIR and NIR spectral channels. Between both channels there is a difference concerning the transition from the In-on-Cu toward the AuSn-on-CuW packaging technology. For the MIR channel the relative hot-spot frequency is halved from $\sim 1.0\%$ to $\sim 0.5\%$ hot-spots per emitter, whereas for the NIR channel the numerical value staid almost constant at $\sim 0.3\%$.

The shape of the distributions is in all cases very similar; the frequency is lowest in the bar center and increases toward the edges. There are two exceptions: batch A [Fig. 5.8(a)] and, in particular, batch B [Fig. 5.8(b)] exhibit additionally high probabilities for hot-spots across the entire device. Such behavior indicates that for the In-on-Cu technology additional In-solder-related hot-spots occur, which are otherwise absent in the devices packaged with AuSn-on-CuW. The In solder is known as potential source for a number of related problems, for instance solder creeping into the proximity

---

[2] The temperature increase is, via the thermal resistance, proportional to the dissipated heat. For 50% WPE, half of the electrically injected power is dissipated as heat. Consequently, the spread in the temperature is given by the double of the numerical value for the spread in WPE.

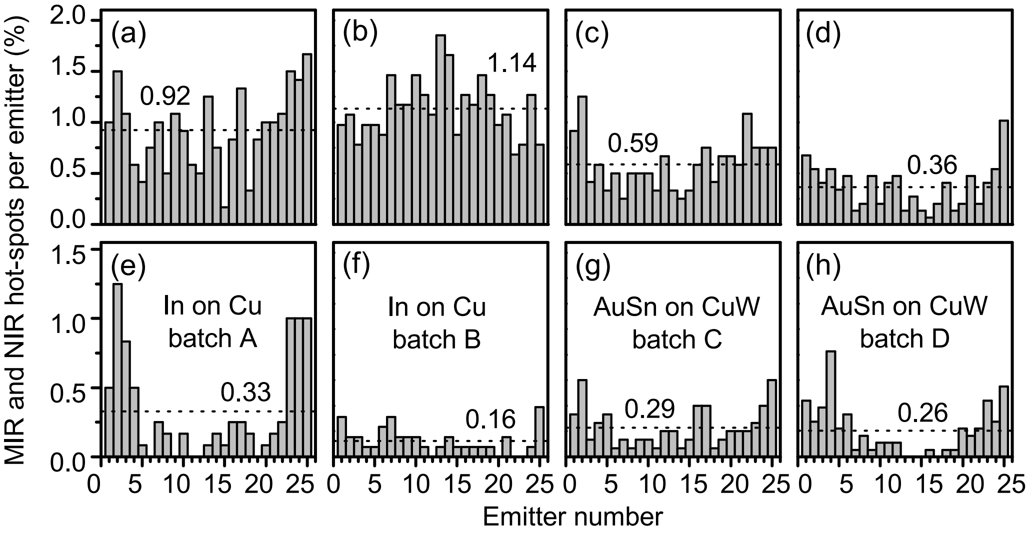

Figure 5.8: Hot-spot statistics, given in percent per emitter, as a function of the emitter number for batches A-D. Dotted horizontal lines indicate the average values given in the graphs.**(a-d)** for the MIR spectral range (i.e., temperature) and **(e-h)** for the NIR spectral range (i.e., defect luminescence).

of the epilayers, solder drops that can be heated by laser light, solder voids leading to local heating, and solder vapors leading to an enhanced absorption at the front facet.[66, 67, 213, 219]

Semiconductor-related origins for hot-spots are, e.g., nonradiative recombination at large defect complexes (dark-spot and dark-line defects) or enhanced absorption of the fundamental laser emission at such defects.[20, 21] The size and amplitude of a detected hot-spot depends on the amplitude of the temperature overshoot and its position. According to section 4.3.1 attenuation and broadening of the thermal radiation emitted from a defect site grow with increasing distance from the front facet. In Ref. 28 such defect sites in the depth of the cavity are observed and for distances smaller than approximately $300 - 500$ μm a hot-spot signature (i.e., a localized overshoot in the signal) can be observed. Consequently, also for the hot-spot statistics reported here it can be expected that only such near-facet defects lead to considerable and localized signal overshoots that are regarded as hot-spots.

In the case of NIR hot-spots, the distribution is to a lesser extend influenced by the packaging technology and bar specific factors seem to be dominant. The nature of the NIR signal and its correlation with degradation is discussed in sections 5.4 and 5.5. NIR hot-spots are likely to be caused by localized concentrations of DL defects. In bars, a hot-spot may even be

Table 5.2: Correlation of MIR and NIR hot-spots with front facet damages or anomalies observed with a microscope. ● means observed, ○ not observed. 97 bars have been analyzed. For details see Appendix D.

Case	Relative probability	MIR hot-spot	NIR hot-spot	Facet damage
1	0.43	○	●	○
2	0.30	●	○	●
3	0.12	●	●	●
4	0.10	●	○	○
5	0.04	●	●	○
6	0.01	○	●	●

present if the corresponding emitter has failed. Then the DL defects are excited by spontaneous radiation coming from other nearby emitters.

5.2.3 Correlation with Complementary Techniques

Microscopy of the front facet

In order to correlate the hot-spots with damages or anomalies at the front facet, emitters that are affected by MIR or NIR hot-spots were inspected with a microscope at 100× magnification. Those are anomalies in the vicinity of the epilayers with a size of at least one micron, e.g., particles, burned-in particles, defects from COD, cracks, solder drops, contaminations from solder vapor, coating defects, and delaminations of the *p*-contact metallization. The correlations and their probabilities relative to the probability of hot-spot occurrence are listed in Table 5.2 (note, the sum for all cases equals one). For cases 1 to 5, profiles in the two spectral channels containing hot-spots together with the corresponding micrographs are given in Appendix D, each for two representative examples.

Several facts follow from this table. First, MIR and NIR hot-spots are only weakly correlated (cases 3 and 5). Second, most of the NIR hot-spots do not occur with a visible front-facet defect (case 1), whereas most of the MIR hot-spots do (case 2). But there are also cases (4 and 5) where a MIR hot-spot occurs without any facet anomaly. However, if for instance solder drops sit nearby the emitter only and not in front of it (i.e., no heating expected), some of the correlations counted for cases 2 and 3 may actually belong to cases 4 and 5. The few observed hot-spots counted as case 6 correspond to locally decreased NIR magnitudes caused by shadowing due to solder drops.

These findings support that most of the MIR and NIR hot-spots have different causes, rather semiconductor-related ones for the NIR hot-spots (cf. sections 5.4, 5.5) and mostly visible facet defects for the MIR hot-spots.

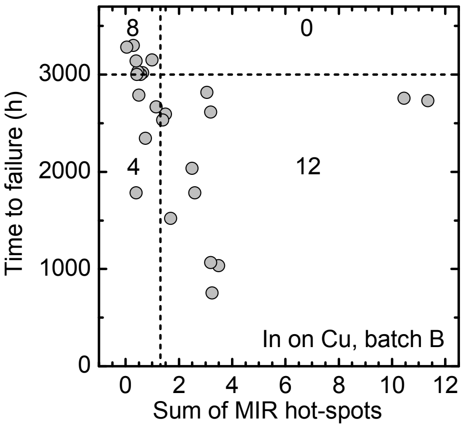

Figure 5.9: Combination of aging data with the sum of MIR hot-spots per bar for 24 bars from batch A (In-on-Cu). The aging experiments were stopped after 3000-3500 h of operation or after device failure (20% output power loss). The dotted vertical line divides the batch into two equal groups of high (hot-spot sum < 1.3) and low MIR homogeneity; the horizontal into survived (≥ 3000 h) and failed devices.

Correlations and discussion

It is important to note that all measurements have been performed on fresh devices before the burn-in. During regular operation it is shown that gradual degradation can be probed by enhanced NIR emission and that a correlation with packaging-induced strain is evident (see section 5.5 and Refs. 76, 77, 220–222). In contrast, for analysis prior to operation the situation is obviously different. Here, the maxima of the hot-spot distributions are at the bar edges (Fig. 5.8), neither related to the temperature profile nor to the profile of the packaging-induced strain[3]. Furthermore, within the framework of the project (cf. Ref. 13) that the thermographic measurements have been measured for, further parameters were determined on a semiconductor wafer level: etch-pit density (i.e., density of crystalline defects), shear stress, integral PL intensity, and particle concentration. It was found that also these parameters are not strongly correlated to MIR or NIR hot-spots. Nevertheless, for some of the bars non-generic NIR profiles are found with long range features such as tilts and gradients. Those may correspond, for example, to gradients of the defect density.

Such observations fit with the idea that semiconductor-related hot-spots should be uniformly distributed across the as-grown bar. As a consequence, the measured hot-spot distributions with a high hot-spot probability at the edge emitters strongly indicate post-growth causes on a bar level. Probably the bar cleaving, the handling during facet coating, or further processing/packaging steps that predominantly stress the bar edges led to microscopic damages. And, since all batches show very similar hot-spot distri-

---

[3] This strain component is caused by the CTE mismatch between semiconductor chip and heat sink. Usually, the device center exhibits the maximal compressive strain of the order of magnitude of 0.1%, falling off to almost no strain towards the edges.[63, 129, 130]

butions, specific packaging-related reasons are less probable. In addition, the MIR hot-spots that strongly correlate to front facet damages lead to a randomly distributed background, in particular for the In-on-Cu packaging technology [Fig. 5.8(a,b)].

Finally, correlation with device degradation can judge the impact of hot-spots. Unfortunately, such data is very heterogeneous because aging has been performed by the manufacturers under different operation conditions and with different termination conditions; see Ref. 214. In general, it was found that there is no clear correlation between the degradation of *individual emitters* and MIR or NIR hot-spots and also not with the above mentioned wafer parameters. Nevertheless, an example for a (partial) correlation on a *bar level* is presented in Fig. 5.9 for devices from batch B (In-on-Cu packaging technology). The time to failure (defined as 20% total output power loss within 3000 h.) is plotted against the sum of all MIR hot-spot relative to the average of each bar. If the 24 bars were divided into two groups of 12 bars each than the group with the more homogeneous MIR profiles (hot-spot sum < 1.3) contains only four failures (33%), whereas all devices of the other group failed (100%). This comparison reveals at least a tendency that such a hot-spot screening could be beneficial for a pre-selection of more reliable from less reliable bars.

Summary

In summary, thermography as a screening tool is able to detect hot-spots in high-power cm-bars, in addition to the temperature determination. It turned out that such hot-spots, extracted from thermal images measured during the first millisecond of operation (at $\sim 4I_{\mathrm{th}}$) and the temperature distributions, correlate with the applied packaging technology. Beside the thermal information, the defect-related NIR emission was detected with a different spectral filter. Hot-spots from both spectral channels were reduced in frequency when replacing the In-solder with the AuSn-solder technology. Comparison with microscopic facet inspection indicates that the NIR hot-spots are rather semiconductor-related, whereas the MIR hot-spots are rather related to visible defects at the front facet. And, surprisingly, the shape of the hot-spot distributions which shows pronounced maxima at the edge emitters, did neither follow the temperature nor the packaging-induced strain distributions. Although comparison with lifetime-data indicated tendencies for higher degradation of bars with many hot-spots, a clear correlation of hot-spots with device failures could not be provided. Such results obtained from fresh devices strongly suggest that a substantial portion of causes for device failure are brought into the device during operation.

5.3 Real-Time Imaging of the Catastrophic Optical Damage

The optical output-power density achievable from high-power laser diodes is limited by the COD threshold. As the high quality of present-day semiconductor laser structures allows for power scaling by, e.g., increasing the resonator length, the properties of the out-coupling facet are of increasing interest. For present near-infrared lasers, COD is mainly encountered during pulsed operation which prevents a thermal rollover. For such cases, the dynamics of facet temperature increase [80, 223] and of melting-induced non-radiative defect propagation [85, 224, 225] were discussed. In this section, the first spatially and temporally resolved analysis of the COD process in red-emitting high-power AlGaInP lasers is presented. The experimental approach for COD monitoring is itself novel.

5.3.1 Samples and Experimental Techniques

The analyzed lasers **QW-650-1-BA** are described in section 2.5. Three such devices with almost identical COD scenarios have been investigated.

The setup for real-time COD imaging [Fig. 5.10(a)] employs the thermographic camera for bulk temperature determination and a Si-CCD camera (spectral range: 300-1100 nm, nominal spatial resolution: 0.77 μm/pixel) to measure the spatial distribution of the laser-light intensity at the front facet, that is the optical near-field (NF). The thermographic camera records with a frequency of $\approx$ 430 Hz (2 ms integration time, 0.3 ms dead time) images of 64×40 pixel (spatial resolution 8.8 μm/pixel) corresponding to $\approx 560 \times 350$ μm^2, that is the whole laser device plus $\sim$ 200 μm submount. The parameters where chosen as a compromise between high temporal resolution (2.3 ms), high thermal contrast ($\approx$ 30 mK) and high probability of catching the COD event (2 ms/2.3 ms $\approx$ 0.87).

The injection current is ramped with a frequency of 0.5 Hz from zero to above the COD level in discrete steps of 20 mA [cf. Fig. 5.10(b)]. The NF camera with an integration time of 0.5 s is synchronized to the center of each current step.

5.3.2 Experimental Results and Discussion

Time evolution of the temperature

Information on the laser bulk temperature *en route* to COD is obtained from imaging the front facet with the thermographic camera. Figures 5.11(a-d)

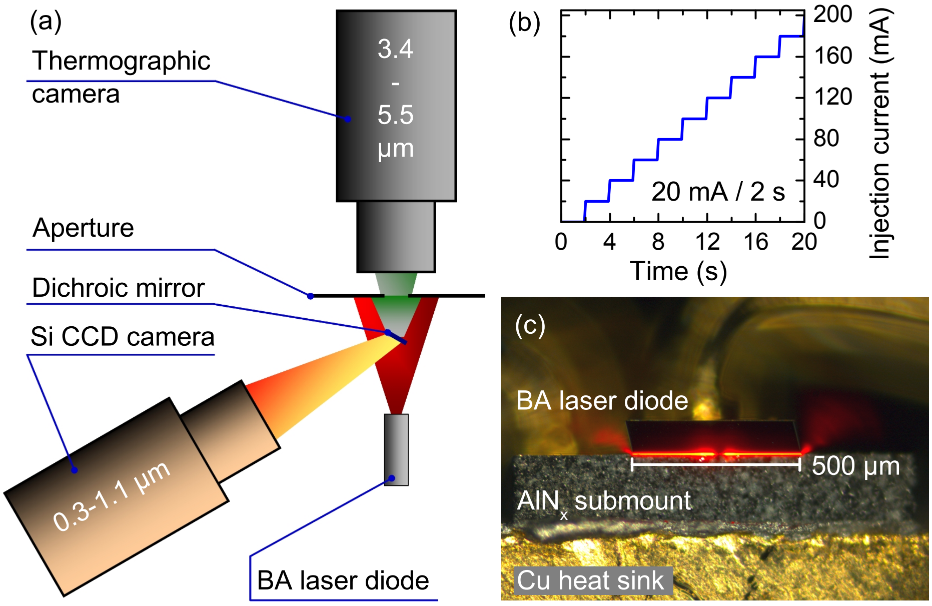

Figure 5.10: **(a)** Schematic of the setup for real-time COD imaging. The BA laser diode is directed toward the thermographic camera (sensitive for wavelength λ of $3.4 - 6.0$ μm). In between both a tilted dichroic mirror transmits for $\lambda >$ 1.1 μm and reflects the fundamental laser emission into a Si CCD camera for NF imaging. In front of the thermographic camera an aperture prevents direct exposure to fundamental laser emission. **(b)** The injection current is ramped by 20 mA steps every 2 s. **(c)** Micrograph of an analyzed laser diode after COD, showing electroluminescence at 10 mA. It is soldered on an AlN$_x$ submount which itself is soldered on a gold-plated Cu heat sink fixed to a thermoelectric cooler.

show thermal images around the occurrence of COD, taken from a series of 1.2×10^5 images. The temperature increases of the region where COD occurred (*COD seed*, red line) and of the entire 100-μm-wide active stripe (black line) are plotted as functions of injection current in Fig. 5.11(e).

Starting at zero current, the bulk temperature of the laser chip rises linearly up to the laser threshold [$I_{\mathrm{th}} \approx 0.48$ A]. Above threshold, the linear slope is reduced due to stimulated emission. At the current step from 2.02 to 2.04 A, the COD takes place and a single pixel [arrow in Fig. 5.11(b)] of the thermal images exhibits an exceptionally short temperature spike [Fig. 5.11(e)] not exceeding one camera frame (≤ 2.3 ms). At the same time a rapid increase of the average bulk temperature of the stripe [Fig. 5.11(c,d)] is observed.

For all three investigated devices the catastrophic process takes place at around 2.0-2.2 A. In order to separate the explicit dependence on the

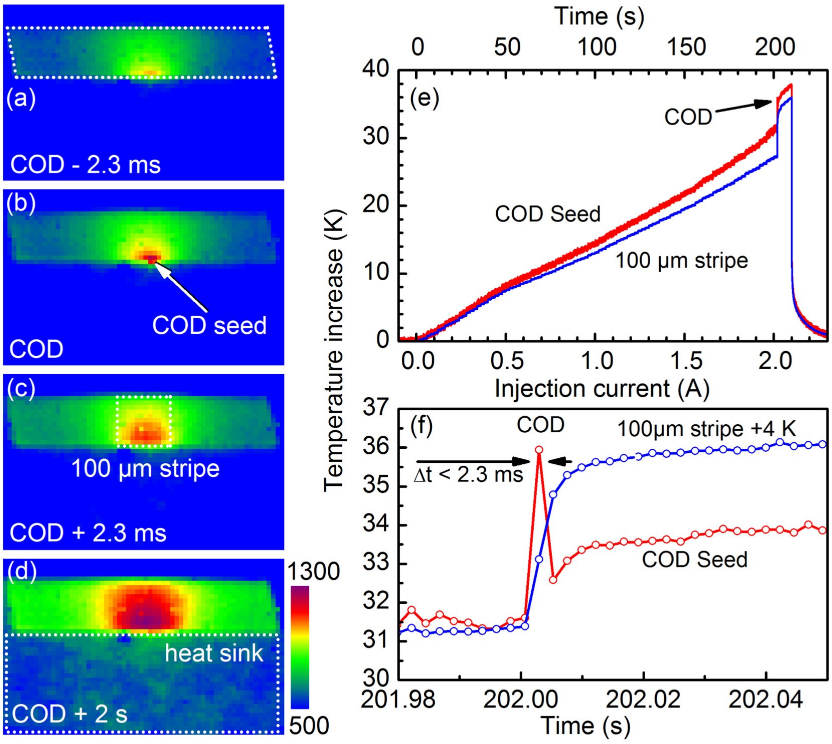

Figure 5.11: **(a-d)** Thermographic images of a laser diode around the COD event: **(a)** 2.3 ms (i.e., one camera frame) before COD (outer device dimensions are marked); **(b)** at COD, exhibiting a single camera pixel (*COD seed*, marked by arrow) with an overshoot in the signal during a single camera frame; **(c)** 2.3 ms after COD; **(d)** 2 s after COD. **(e,f)** Temperature increase vs time and current relative to the situation without current (18.5°C heat-sink temperature). Blue lines and symbols correspond to an average of the 100 μm active stripe shown in (c); red lines and symbols correspond to the COD seed in (b). **(e)** The COD event is marked by an arrow and is displayed on an expanded scale in **(f)**.

particular heat sink, the transients around the COD event are displayed in Fig. 5.12 after subtraction of the submount temperature, which has been thermographically measured in parallel. The temperature spikes for the three unaged devices are approximately 4.0, 1.4, and 1.7 K. The slight difference between the characteristics of the laser diode of Fig. 5.12(a) as compared to that of Fig. 5.12(b,c) is most probably because they originate from two different epitaxial runs with otherwise unchanged epitaxy. Apparently, the thermo-temporal COD characteristic is batch-dependent. This ability to resolve those slight differences can be regarded as a feature of the time-resolved thermography.

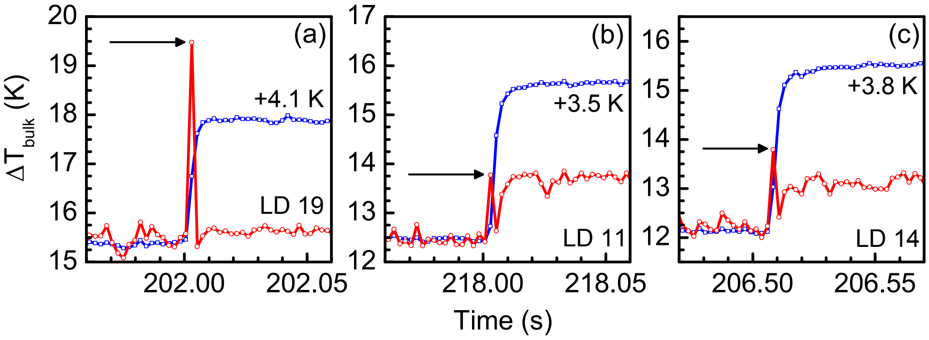

Figure 5.12: Temperature increases of three laser diodes around COD. Symbols and lines mark the same probing areas as in Fig. 5.11(f) but here the temperature increase has additionally been subtracted by the temperature of the heat-sink marked in Fig. 5.11(d). **(a)** Corresponds to the device from Fig. 5.11, **(b)** and **(c)** to two devices of another batch.

Temperature during COD

Due to the restrictions in spatial and temporal resolution, the COD is basically seen as a single pixel ($8.8 \times 8.8\ \mu\mathrm{m}^2$) and single frame (2.3 ms) event. Assuming a thermal runaway process in which the melting point of the InGaP-QW materials is reached, a local temperature increase of ~ 1200 K is required. From pulsed experiments on IR laser diodes a velocity of $2-4$ m/s of the melt-front propagation along the resonator axis is found.[224, 225] Such velocity is $\sim 4-8$ times higher than the present 1.2 mm long cavity divided by the frame duration. The destructive in-depth analyses referred to in section 2.4.2 show COD-driven defect complexes extending in vertical direction (i.e., direction of epitaxial growth) to roughly about 50-200 nm. Consequently, the derived temperature increase during the COD is only an averaged value and the true temperature increase is expected much higher. Extrapolation of the nonlinear camera-response-vs-temperature curve according to the theoretical calibration presented in section 4.1.2 shows compatibility of the measured data with locally melting semiconductor materials at temperatures as high as ~ 1500 K.

Evolution of the optical near-field with injection current

The temperature at the laser facets is higher than in the bulk, mainly because of additional absorption and surface recombination processes.[79, 223] Reabsorption of the fundamental laser emission at the front facet is the most important facet heating mechanism at elevated injection currents and is pro-

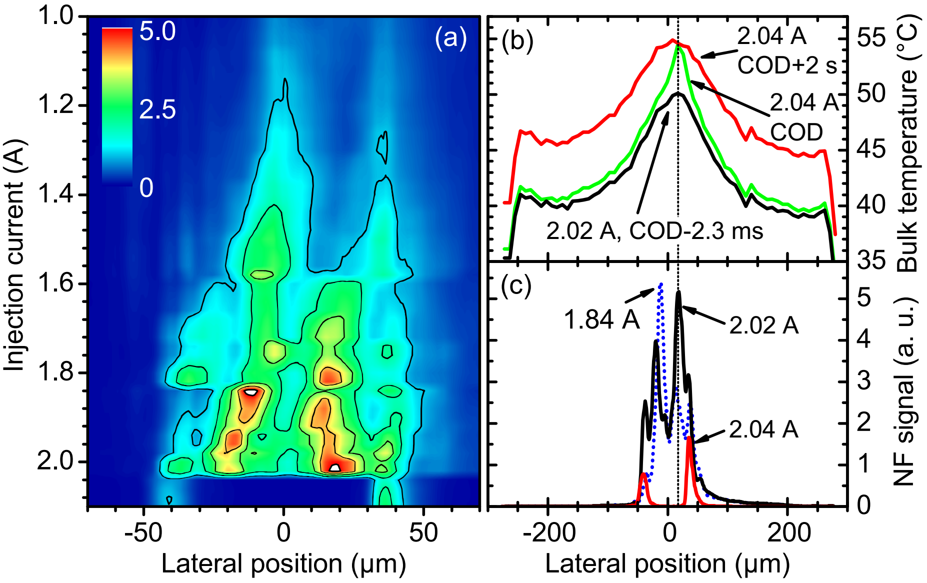

Figure 5.13: **(a)** NF intensity taken from the maximal lines of the Si-CCD camera vs injection current. COD occurred between 2.02 and 2.04 A. Equipotential lines at intensities of 1, 2, 3, 4, and 5 a.u. are given. **(b)** Absolute bulk temperature profiles taken from Fig. 5.11(a) (black line), 5.11(b) (green line), and 5.11(d) (red line) along a line that contains the active region. **(c)** Corresponding NF profiles before and after COD [black and red lines as in (a)]. The dotted blue line represents the highest NF intensity observed at $I = 1.84$ A.

portional to the NF intensity distribution[4]. Two regions at around the center of each half of the device show intense filaments [Fig. 5.13(a)]. There the highest facet temperatures are expected. Comparison [Fig. 5.13(b,c)] between lateral profiles taken from thermal images and the corresponding NF distributions does indeed demonstrate that the temperature spike occurs at the same point in space as the strongest peak of the NF distribution, measured just before COD, and followed by a nearly complete break-down.

Such filamentation which is observed as an inhomogeneous near-field distribution, is thought of to be a result of the coupling of the gain and the refractive index. In particular, the (complex) refractive index depends on the minority carrier concentration, which itself depends on the optical field intensity being a result of the gain (through minority carrier concentration) and the refractive index (through waveguiding). This nonlinear interaction leads to self-focusing of the optical modes thereby enabling simultaneous las-

---

[4] Facet temperatures derived from Raman-spectroscopy scanning of analogous red-emitting devices showed indeed a close, nearly linear relation with the optical NF.[226–228]

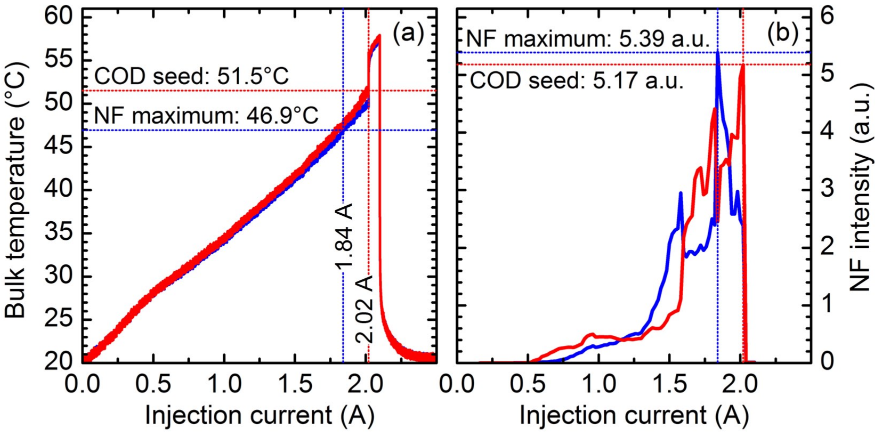

Figure 5.14: **(a)** Absolute bulk temperature T_{bulk} and **(b)** NF intensity I_{NF} vs current I for two points in space at the active region of the laser diode of Figs. 5.11 and 5.13, namely the COD seed at a lateral position around 19 μm (red lines) and the point of highest NF intensity around -12 μm (blue lines). Dotted horizontal and vertical lines mark the two prominent situations: (i) highest ever observed NF intensity at $I = 1.84$ A with $T_{\text{bulk}} = 46.9$°C, $I_{\text{NF}} = 5.39$ a.u., (ii) the situation just before the COD event at $I = 2.02$ A with $T_{\text{bulk}} = 51.5$°C, $I_{\text{NF}} = 5.17$ a.u.

ing of many spatial modes (filaments) in lasers of large stripe widths. The degree of this coupling depends on the materials properties, the heterostructure design, and the device structure.[39, 53, 229, 230]

Combination of thermography and near-field data

The combination of the two imaging methods strongly suggests that the COD process in high-power AlGaInP laser diodes is indeed triggered by a thermal runaway process at the front facet. In this framework, the high optical facet load due to reabsorption of red laser light leads to a local melting of the semiconductor materials along the resonator, which is compatible with the experimentally observed temperature spike. After successive recrystallization a dense network of defects is left behind, leading to a vastly increased nonradiative recombination rate, which experimentally is found as the pronounced jump in the average device temperature.

>From this concerted approach the concept of a COD critical temperature becomes evident as well.[79, 80, 226] A closer inspection of Fig. 5.13(a) shows that the intensity of the NF filament observed at the left device side at 1.84 A was already larger than the one that actually lead to the COD at 2.04 A. A direct comparison of the two parameters bulk temperature and NF intensity in Fig. 5.14 shows that only the combination of a high optical

load at the facet plus a high thermal load in the facet-near bulk materials leads to the COD. Since both processes contribute to the facet heating, a critical facet temperature and a high photon flux can be regarded as the key precondition for the occurrence of COD. Similarly, earlier experiments on analogous devices showed that the injection-current level leading to COD falls with increasing heat-sink temperature.[226–228]

Estimation of the critical facet temperature

Figure 5.14 allows for an estimate of the critical facet temperature. Assuming an additive linear relation $T_{\mathrm{facet}} = T_{\mathrm{bulk}} + a \cdot I_{\mathrm{NF}}$, between facet temperature T_{facet}, bulk temperature T_{bulk}, and NF intensity I_{NF}, the data yield a maximal numerical value for the constant $a \approx 21$ K/a.u. As a result, a maximal facet temperature of about 160°C is reached 2 s before initiation of the COD process. Such number corresponds well with values on the order of $100 - 200$°C derived from Raman spectroscopy measurements.[226–228]

Summary

In this section, the applicability of thermography as an analytical tool for COD experiments was demonstrated. Using cw-operating red-emitting high-power AlGaInP lasers this novel experimental approach has been proven very useful, in particular, since there is a lack of alternative techniques capable of probing temperature distributions in extended devices in a fast sub-second fashion. Although thermography as presented here could not fully resolve the temperature dynamics of the COD process, the achieved results represent the most highly resolved COD study so far. Simultaneously recorded optical near-fields confirmed both the existence of a critical facet temperature of the order of $100 - 200$°C as precondition for COD occurrence and the utmost importance of a proper control of facet reabsorption in order to achieve high output powers. The described methodology is applicable to a wide class of semiconductor laser diodes and not confined to the presented red-emitting lasers.

5.4 Infrared Emission from Laser Substrates

>From initial experiments with the thermographic camera temperatures have been determined that were much higher than expected. It became evident that such overestimated values were caused by a non-thermal IR emission from the laser. Since this luminescence does not extend further than $\sim 2\ \mu$m into the mid-IR, spectral separation with filters solved the problem of proper temperature determination.

Early investigations on GaAs-based laser diodes identified the IR luminescence as coming from the active layer,[231–234] and later first indications for its origin in the substrate and its relation to DL defects have been given.[235–237] Although not completely understood, a direct correspondence between such IR signatures and certain degradation/failure signatures have been observed.[28, 76, 156, 231, 232, 235, 238]

In this section, a more complete and consistent study is presented that applied spectrally and spatially resolving NSOM and FTIR spectroscopy for two completely different laser designs. It is shown that between QW-transition energy (responsible for lasing) and blackbody radiation (responsible for thermography signal) of GaAs-based laser diodes several emission bands are spectrally located, being indicative for different radiative loss mechanisms.

The two epitaxial structures **QW-650-1-BA** for the red ($\lambda = 650$ nm) and **QW-808-2-BA** for the NIR spectral range ($\lambda = 810$ nm) are described in section 2.5. Important for this study is the fact that both high-power BA laser designs base on n-type GaAs substrates and involve different gain materials, i.e., GaAsP-QW with GaInP and AlGaAs waveguide and cladding layers versus GaInP-QW with AlGaInP waveguide and cladding layers.

5.4.1 Experimental Results and Discussion

Integral emission spectra

The FTIR emission spectra of the laser diodes given in Fig. 5.15(a) were recorded with a FTIR spectrometer described in section 2.7.2. The laser lines were attenuated by color filters (see vertical arrows). Energetically below these lines the laser diodes exhibit each a shoulder (B1) and three common features: a distinct peak (B2) around $1.3 - 1.4$ eV, a broad band (B3) at $0.7 - 1.5$ eV centered around ~ 1.1 eV, and the onset of blackbody radiation at ~ 0.4 eV (B4). Immediately, this leads to the conclusion that B1 is connected to the gain medium, whereas the low-energy emissions (B2,B3) are related to the GaAs substrate as this is common to both lasers.

The (B2,B3) emission intensities in dependence of the heat-sink tempera-

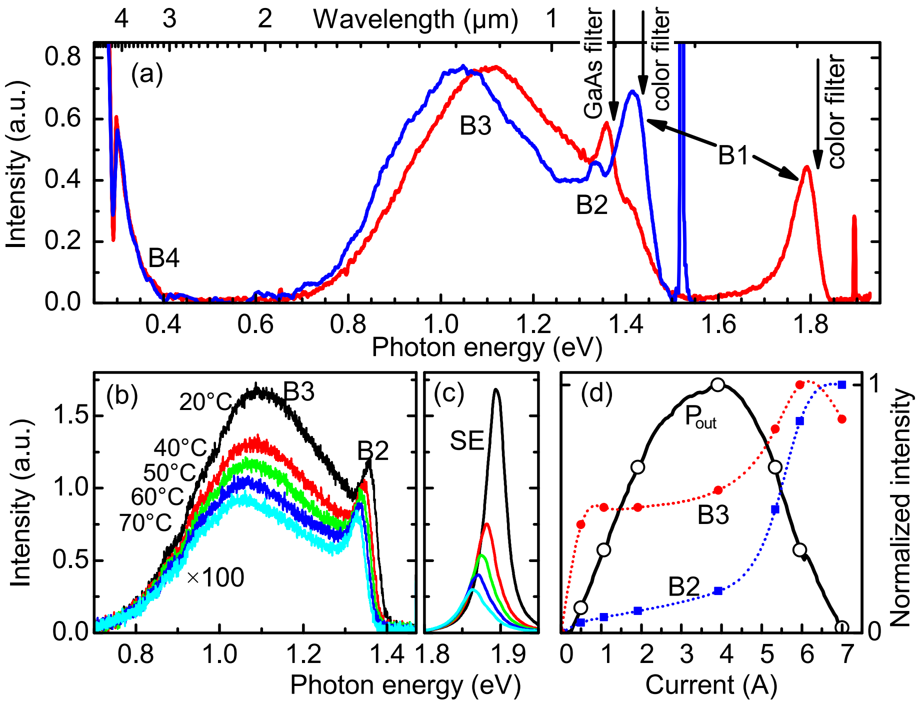

Figure 5.15: **(a)** FTIR emission spectra of a red laser (red line) at an injection current of $I = 0.7$ A (heat-sink temperature $T = 23°$C) and of a NIR laser (blue line) at $I = 1.9$ A ($T = 50°$C). The absorption edges of the long-wave-pass color filters (690 and 850 nm) and of GaAs (used in Fig. 5.16) are indicated by arrows. Four major emission bands B1-B4 below fundamental emission are labeled. **(b)** (B2,B3) emission bands (multiplied by 100) for $T = 20 - 70°$C and $I = 0.7$ mA of a red device measured without spectral filters and **(c)** fundamental spontaneous emission (SE) for same conditions. **(d)** Emission peaks (all normalized) of B2 (full squares) and B3 (full circles), and total front-facet output-power (full line) of a NIR device vs current at $T = 50°$C.

ture and the injection-current are displayed in Fig. 5.15(b,d). In all analyzed devices the (B2,B3) intensities decrease with increasing heat-sink temperature, following the decrease in spontaneous emission strength, which is measured without a color filter in Fig. 5.15(c). The QW spontaneous emission rate is known to clamp or partly clamp at the lasing threshold.[146, 239] In cw operation, however, especially at an elevated heat-sink temperature, device heating leads to a rollover in output power P_{out}, which means a decrease in the stimulated emission rate and a concurrent increase in the spontaneous emission rate. Such behavior of B2 and B3 is seen in all cases [Fig. 5.15(d)], definitely ruling out stimulated emission as a significant excitation source.

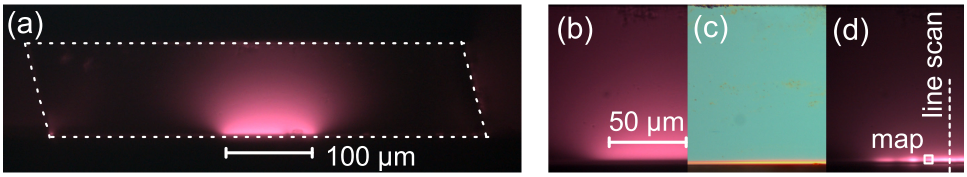

Figure 5.16: Micrographs of the front facet of a red laser diode **(a,b,d)** with and **(c)** without a GaAs filter in the beam path. **(a)** Overview micrograph at $I = 0.1$ A. White dotted lines mark outer device dimensions. The active stripe width is indicated. **(b-d)** Micrographs at higher magnification, each showing the left half of the active stripe, at **(b)** $I = 0.5$ A, **(c)** $I = 20$ mA, and **(d)** $I = 1.5$ A. The scanning experiment regions are marked by a dotted line (line scan) and a square (NSOM map).

Micrographs of the infrared emission

Micrographs (Fig. 5.16) of the laser diodes are recorded with a standard microscope equipped with a Si-CCD camera (sensitive to ≥ 1.1 eV) behind a GaAs filter [see the arrow for the GaAs filter edge in Fig. 5.15(a)]. At currents well below threshold [Fig. 5.16(a,b)] the emission comes from an extended part of the substrate with its maximum shifted a few microns away from the peak of the QW emission position, which is measured with external illumination and without such filters [Fig. 5.16(c)]. At higher currents [~ 1.5 A, Fig. 5.16(d)] an additional contribution appears that is strongly confined to a narrow layer of the substrate only

Spatially resolved emission spectra

In order to unambiguously clarify the association of the low-energy B2 and B3 emission bands with the substrate, emission scans at different currents were performed for a red and a NIR laser diode with a NSOM as described in section 2.7.4. Near-field maps are integrated along the epitaxial plane and are presented in Fig. 5.17, the line scans are presented in Fig. 5.18. Both show the emission bands discovered in the FTIR emission spectra.

The position of the QW (maximal fundamental laser emission) is set to zero in the figures. The position of the GaAs substrate ~ 1 μm away is derived from PL measurements [signal at $\lambda \sim 820 - 900$ nm in panels (c,f) in both figure sets], excited with a 633 nm HeNe-laser trough the collecting fibertip. Thus B1 can be assigned with the QW-gain region and (B2,B3) with the GaAs substrate. And it follows that B2 is the GaAs interband luminescence. In the electrically driven case a major part of this luminescence is reabsorbed in the substrate for distances $\gtrsim 2$ μm, also seen as a narrowed B2 spectrum

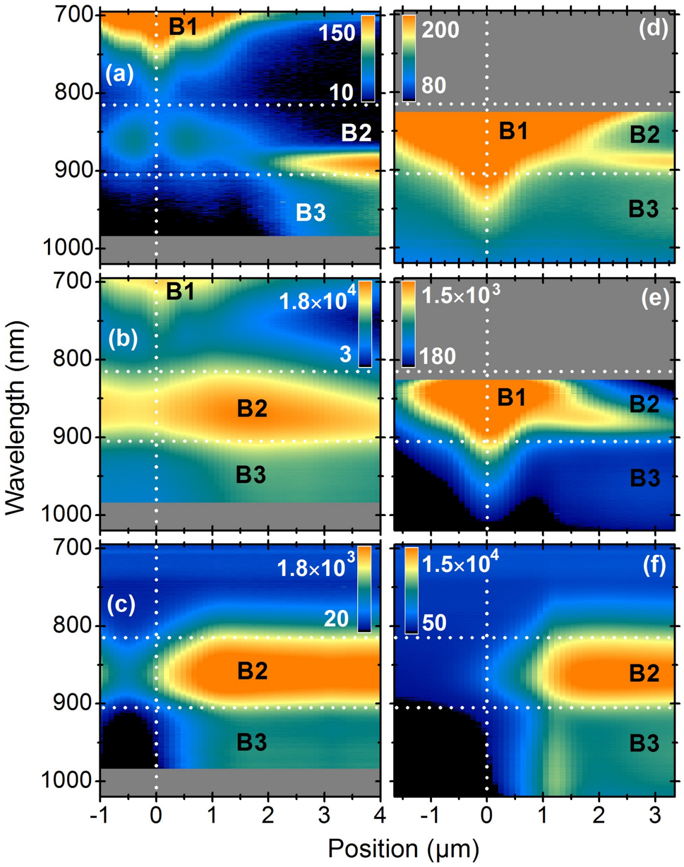

Figure 5.17: Emission maps (NSOM scans, step-width ≈ 0.1 μm) of red (left panels) and NIR (right panels) lasers. Pulsed currents of **(a)** 0.1 A, **(b)** 0.65 A, **(d)** 0.1 A, **(e)** 1.0 A are used. **(c,f)** HeNe-laser-excited PL maps. Dotted horizontal lines indicate emission bands B1-B3, vertical lines indicate the QW position. Data display starts at the color-filter edges (left: 690 nm, right: 825 nm). For comparison, identical wavelength regions are used, no data is indicated by gray color. Logarithmic scale is chosen to enhance the displayable dynamic range.

in the integral FTIR spectra. The PL-data, on the other hand, shows no narrowing because the penetration depth for the HeNe radiation is much smaller than the extinction length for the GaAs interband luminescence[5]. Comparison with the micrographs indicates that a fraction of B2 may also be guided within the wide-band-gap waveguide and cladding region.

5.4.2 Physical Model and Discussion

A band-edge-vs-position model explaining the origin of the observed emission bands is depicted in Fig. 5.19 together with the collection geometry of the emission scanning experiments. In the QW several radiative transition are possible. Beside the fundamental laser transition also various band tail emissions are possible that involve the localized QW states and states

---

[5] Similar effects for GaAs concerning the difference in the integral spectrum for different excitation-collection geometries have been observed in Ref. 240.

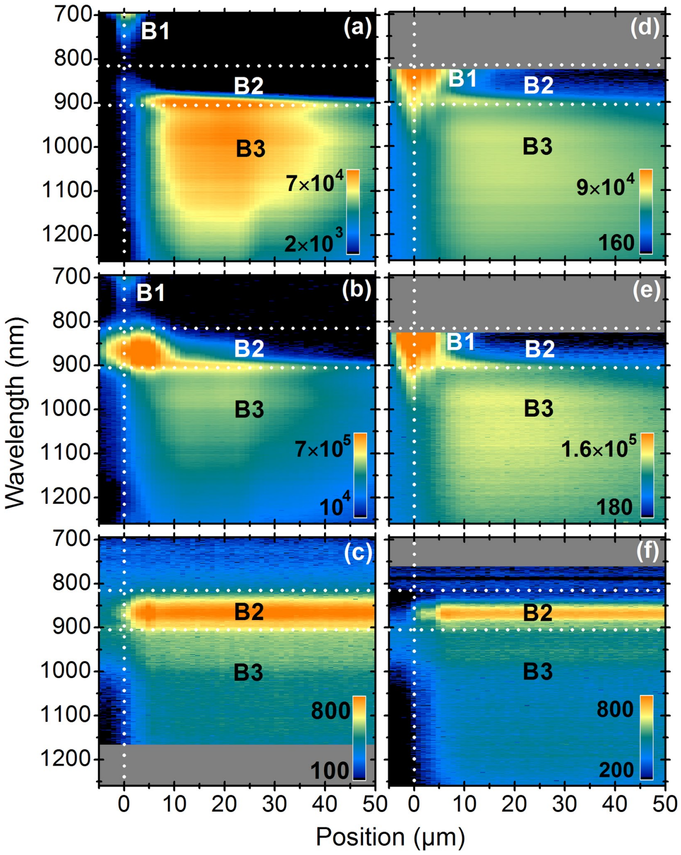

Figure 5.18: Emission maps of a red-emitting (left panels) and a NIR (right panels) laser diode derived from line scans (step-width ≈ 1 μm) across the epilayers and half of the substrate. Pulsed currents of **(a)** 0.2 A, **(b)** 1.0 A, **(d)** 0.2 A, and **(e)** 0.6 A are used and **(c,f)** are HeNe-excited PL maps. Data display is analogous to Fig. 5.17.

related to shallow-impurities and DL defects. This variety forms the shoulder B1 whose signature has been measured and discussed earlier, e.g., in photocurrent studies.[156, 238] The bands (B2,B3), on the other hand, are excited within the GaAs substrate. It is very likely that B2 corresponds to interband transitions and B3 corresponds to transitions involving radiative recombination centers located below the middle of the GaAs band gap.[241–244] Since the substrate is n-type, the radiative recombination leading to B2 is governed by the concentration of minority-holes, whereas their capture into the DLs results in B3.

Such holes may be provided by either reabsorption of spontaneous radiation (stimulated radiation has been ruled out) from the QW with successive electron-hole-pair generation or by a leakage current from the active region. Several reasons do, however, argue against (an appreciably) hole-leakage current that would inject holes into the GaAs after thermionic emission over the cladding layer where they diffuse and/or drift towards the n-side. The hole-diffusion length within the n-substrate is known to be very small, i.e., $\lesssim 1 - 2$ μm.[245] Furthermore, such leakage currents should considerably

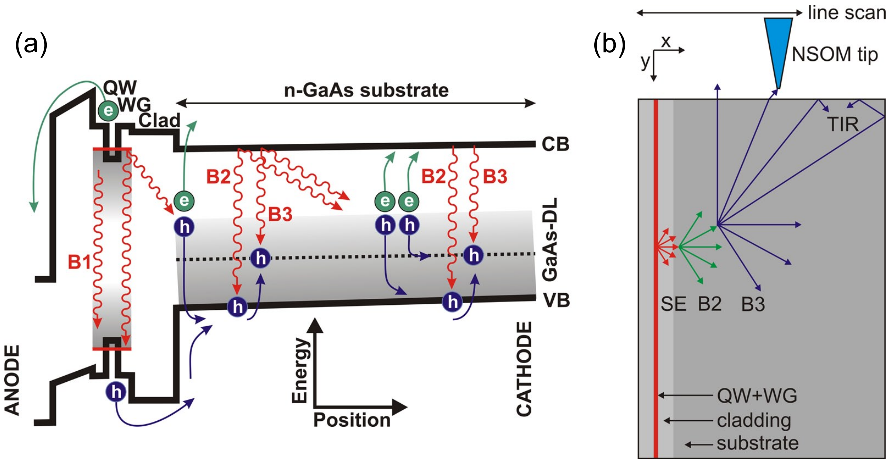

Figure 5.19: **(a)** Schematic model picture with CB and VB band edges (black lines), DL bands (dotted black lines, gray-shaded regions), QW electron and hole levels (red horizontal lines), QW impurity and DL bands (gray-shaded), and the radiative transitions B1-B3 (red wavy arrows) for a red laser diode. Possible electron (e) and hole leakages (h) are sketched, as well as, from left to right, the photon-recycling processes. **(b)** 2D schematic of the line-scan collection geometry along the laser front facet. The two-staged photon-recycling process SE $\rightsquigarrow$ B2 $\rightsquigarrow$ B3 for obtaining the shift in the maximum of Fig. 5.20 is given (SE - spontaneous emission from the QW).

increase with rising temperature,[145, 246] which contrasts the findings in Fig. 5.15(b). However, electron-leakage into the *p*-cladding (i.e., transport into the opposite direction) is considered a significant source of losses in red-emitting lasers and is made responsible for the considerable degradation in efficiency of AlGaInP lasers with emission wavelength below 650 nm.[145, 146]

The maximal intensity of the B3 emission is shifted $\sim$ 20 μm into the substrate [e.g., Figs. 5.18(b) and 5.20(a)]. This effect allows to uncover the energy transfer from the QW spontaneous radiation towards B2. This QW radiation is transmitted through the wide-band-gap waveguide and cladding layers and absorbed in a narrow layer ($\sim$ 1 μm thick) of the substrate adjacent to the cladding [red arrows in Fig. 5.19(b)]. Now, two things are most relevant for the measured spatio-spectral characteristic, namely photon-recycling[6] and light propagation from the depth of the 1.2 mm long device.

---

[6] In this context, photon-recycling describes the reuse of radiation emitted (spontaneously) into directions out of the gain region via absorption, electron-hole pair generation, and radiative recombination. As a result, the internal quantum efficiency, the minority carrier lifetime and diffusion length can be enhanced.[247–249] Photon recycling is possible within the same material (i.e., due to self-absorption) or with transparent regions in between the region of original and recycled photon emission.

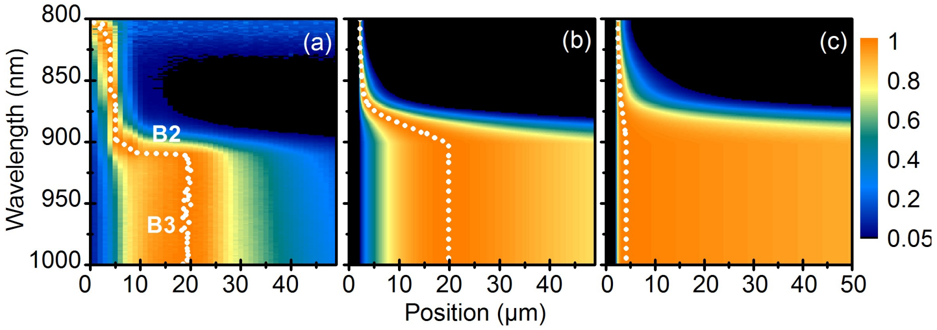

Figure 5.20: Spatio-spectral characteristic of the IR emission, normalized at every wavelength. White dots mark the position of the maximum per wavelength. **(a)** Emission map of the red laser ($I = 0.4$ A); **(b)** modeled emission intensity fed by reabsorption of B2 starting at 2 μm with $\alpha(\nu_{\mathrm{B2}}) = 300\ \mathrm{cm}^{-1}$, and **(c)** only by direct excitation of the QW radiation $\alpha(\nu_{\mathrm{QW}}) = 35000\ \mathrm{cm}^{-1}$. Both are calculated for single pass radiation and Fresnel transmission at the GaAs-air interface for n-type GaAs ($N = 2 \times 10^{18}\ \mathrm{cm}^{-3}$, $n = 3.5$).

The initially excited narrow GaAs layer emits spontaneous Stokes-shifted B2 (green arrows) and B3 radiation (blue arrows) that travels through the substrate until most of B2 is subsequently reabsorbed and partly reemitted as B3. Such a cascaded photon recycling for B3 explains the right magnitude of the maximum shift [Fig. 5.20(b)] if it is modeled as a spatial convolution of the QW excitation, the intermediate interband excitation (B2), and the decay of the DL luminescence (B3). In contrast, a direct excitation of B3 by the QW spontaneous radiation only, i.e., without intermediate reabsorption via B2, shows no significant spatial shift; see Fig. 5.20(c). The corresponding derivation is given in Appendix E.

Summary

In summary, the origin of the non-thermal IR emission, originally observed in early thermographic measurements with an open detector, was studied. It was found that the spontaneously emitted radiation from the gain material (i.e., QW active layer) of GaAs-based high-power laser diodes photoexcites both band-to-band and band-to-DL-defect transitions with different spectral and spatial emission properties inside the GaAs substrate. The obtained experimental data suggested a cascaded photon-recycling process for the energy transfer from QW spontaneous radiation towards substrate-DL luminescence. Very interestingly, the emergence of such IR emission from the substrate is, by definition, not restricted to structures comprising particular gain materials, which was verified from the analysis of different laser diodes.

5.5 Infrared Emission as Degradation Probe

COD of laser diodes is demonstrated in section 5.3 as a very rapid and pronounced process leaving an inoperable device behind. Another regime that describes a reduction in output power and life-time is gradual degradation. In case of extended laser devices such as high-power laser bars, comprising, e.g., 19 individual emitters, the parameters that give rise to the microscopic degradation processes might be spatially non-equally distributed among the individual emitters. For example, the mechanical strain introduced during packaging and mounting on a heat sink and the bulk temperature are repeatedly demonstrated to exhibit higher numerical values at central emitters than at emitters near the device periphery.[28–31, 49, 77, 129, 175, 199, 201, 250–252] In this respect, an experiment with a single bar could be regarded as 19 individual experiments with single emitters having different values for the strain or the temperature.

If operated for a certain time, different spectroscopic techniques detect specific degradation signatures according to the probed physical parameters. In the case study presented in the following, four spectroscopic techniques are applied that identify packaging-induced strain as the physical parameter giving rise to a gradual degradation. Amongst others, the earlier discussed IR DL-luminescence B3, measured with the same thermographic camera as for temperature determination, is demonstrated as a degradation probe.

5.5.1 Samples and Experimental Techniques

The spectroscopic analysis is carried out on a red-emitting (emission wavelength: $\lambda = 650$ nm) cm-bar **QW-650-2-bar** with 19 individual emitters and is described in section 2.5.

Degradation signature I: LBIC scanning

Photo-electrical spectroscopy in terms of LBIC scanning across the width of the device is applied to probe the distribution of defect concentration (cf. section 2.7.3). From photocurrent spectroscopy of fresh, aged, and degraded laser diodes a correspondence between the change in the photocurrent spectrum and the accumulation of defects in the active layer and the waveguide was deduced.[76, 77, 156, 238] The decrease in the QW interband photocurrent ($h\nu \approx 1.90$ eV) was found to be accompanied by an increase of the photocurrent at energies smaller than the QW band gap mediated by DL defects.[76] The latter effect is explained by an effective increase of the DL-absorption coefficient ($\alpha_{\mathrm{DL}} = \sigma_{\mathrm{DL}} N_{\mathrm{DL}}$; DL-absorption cross-section: σ_{DL})

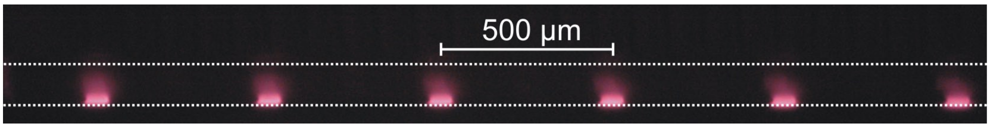

Figure 5.21: Micrograph showing IR emission from the substrate of the first six emitters of a high-power red-emitting laser bar similar to the described devices. The injection current is 2 A, the fundamental laser emission is blocked by a GaAs filter like in Fig. 5.15(b). Dotted white lines mark the bar height.

that is assigned to an increase in the concentration of DL defects (N_{DL}). The decrease in the QW interband photocurrent, on the other hand, is explained by an increased defect concentration as well, because the photocurrent is proportional to the steady-state nonequilibrium lifetime of the photoexcited carriers in the QW, which is reduced due to such increased defect concentration. Spatially resolved LBIC scanning with a 633 nm ($h\nu \approx 1.96$ eV) HeNe laser for excitation is thus able to detect spatial variations in the defect concentration.

Degradation signature II: Thermography of the infrared emission

In continuation of the last section's results the IR emission from the substrate is used as degradation probe. A typical micrograph (Fig. 5.21 with Si-CCD camera behind a GaAs filter) of a red-emitting laser bar shows the IR emission from the substrate. In order to expand the applicability of thermography to this shorter wavelength region, the thermographic camera was applied to detect, beside the thermal IR (with MIR filter, wavelength range: $3.4-6.0$ μm), the non-thermal IR (with NIR filter, wavelength range: $1.6-2.2$ μm). The resulting signal from thermography through the NIR filter is called *NIR signal* in the following.

Similar as in LBIC scanning the NIR images contain information about the defect distribution. A defect accumulation in the QW (as probed by LBIC) leads to an increase of the laser threshold current, resulting in an increase of the spontaneous emission rate. This leads to an increase of the DL-luminescence, similarly as a defect accumulation in the substrate. Consequently, both information is intermixed within the measured NIR signal in a non-trivial way, but the microscopic causes for both processes may eventually be identical, for instance a DL-defect accumulation due to a long-range (several μm) strain-field.

5.5.2 Experimental Results

Degradation signatures

In Fig. 5.22 the data of four scanning and imaging techniques are presented, namely LBIC scanning (a), NIR imaging (b), thermography (c), and micro-PL scanning (c).

The LBIC scans [Fig. 5.22(b)] exhibit a pronounced decrease with operation time in the regions around the emitter stripes (30 μm wide, centered around every 500 μm), whereas the rest of the bar seems to be less affected.

The cuts from the NIR images [Fig. 5.22(b)] demonstrate an increase of the NIR signal with operation time. The spatial resolution of the thermographic camera is limited to 38 μm/pixel in order to image the entire cm-bar at once. Both the stripe width (30 μm) and the width of the IR emission [cf. previous section and Fig. 5.21] are below or around this value. Consequently, the NIR images consist of a series of peaks at the emitters with a full width at half maximum of $60 - 70$ μm.

For comparing data sets before and after aging, their reproducibility needs to be secured. For NIR imaging, hundreds of bars have been measured (cf. section 5.2) and it was found that the reproducibility is within a few percent. For LBIC scanning, on the other hand, absolute values are less reliable, which partly stems from the difficult alignment of the small-aperture exciting laser beam with the laser device. Nevertheless, probing of the regions far away from the emitters, in particular at the outer device edges, is used to align both LBIC data sets (the data after aging is multiplied by 1.15), because these regions are expected to degrade, if at all, to a much lesser extend than the emitters themselves.

Degradation-driving parameters: Temperature and strain

Two prominent parameters being responsible for laser-diode degradation (cf. section 2.4) are the bulk temperature and the packaging-induced strain. Both parameters are quantified in a spatially resolved way.

The bulk-temperature profile is displayed in Fig. 5.22(c) showing a typical temperature distribution with the highest values in the center of the device and nearly perfect symmetry. The temperature profile corresponds to the situation after aging and does not show any clear change with aging.

The incomplete CTE-match between chip and CuW submount gives rise to packaging-induced strain, as well as the even more unmatched Cu heat sink residually impacting through the thin CuW lamella. Such strain is expected to dominantly uniaxially compress the array along its width of 1 cm, that

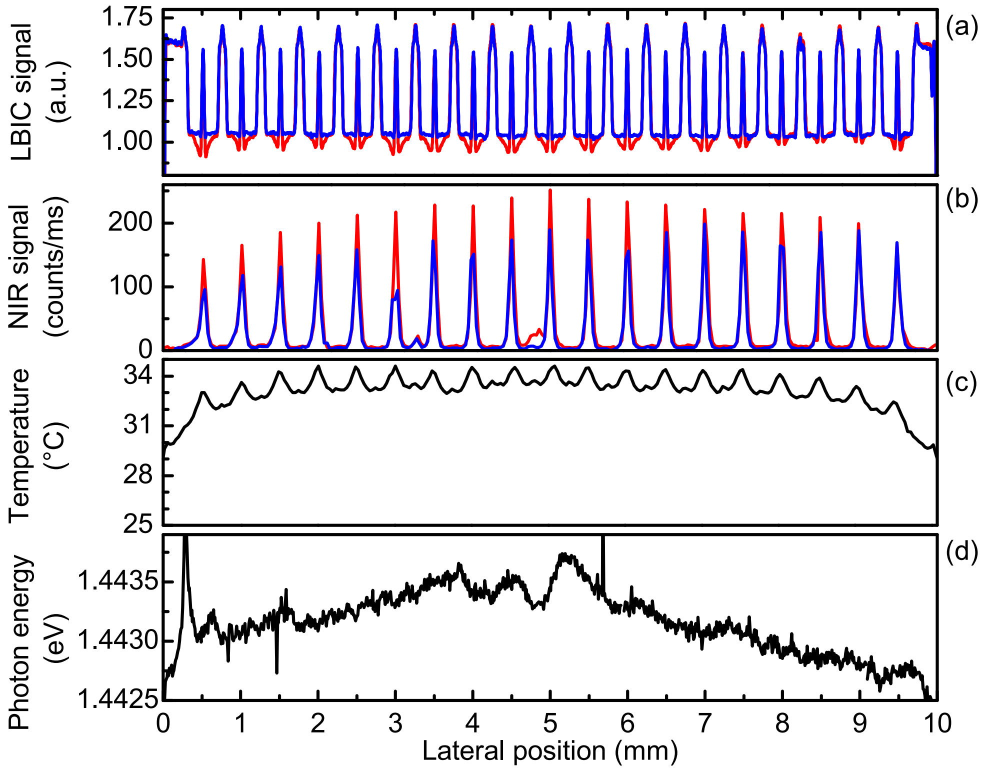

Figure 5.22: **(a)** LBIC scan with HeNe-laser excitation (633 nm), **(b)** NIR profiles (cuts through maxima) at an injection current of $I = 6$ A. Blue lines are measured before aging and red lines after 200 h of operation. **(c)** Temperature profile containing the active region at $I = 6$ A (heat-sink temperature 25°C). **(f)** Micro-PL peak position for a lateral scan across the substrate representing the overall packaging-induced strain.

is along $\langle 110 \rangle$. Its distribution is measured by a micro-PL scan[7] across the front facet, taken in the center of the GaAs substrate [Fig. 5.22(d)]. The energetic shift in the PL-peak position correlates to a change in the direct GaAs band gap induced by a varying strain. A peak energy of 1.4425 eV as reached at the device edges is assumed to be indicative for zero packaging-induced strain and the observed ~ 1 meV blueshift represents an uniaxial compression along $\langle 110 \rangle$ by about 0.05% only.[63] The left side of the device shows a slightly higher compression than the right one.

Before epitaxy, processing, mounting, and operation the GaAs substrate is expected to be of superior quality in terms of both crystalline perfec-

---

[7] The micro-PL scan experiments have been performed by Julien Nagle (Thales Research and Technology, RD128, 91767 Palaiseau Cedex, France), Myriam Oudart (Alcatel Thales III-V Laboratory, RD128, 91767 Palaiseau Cedex, France) *et al.*

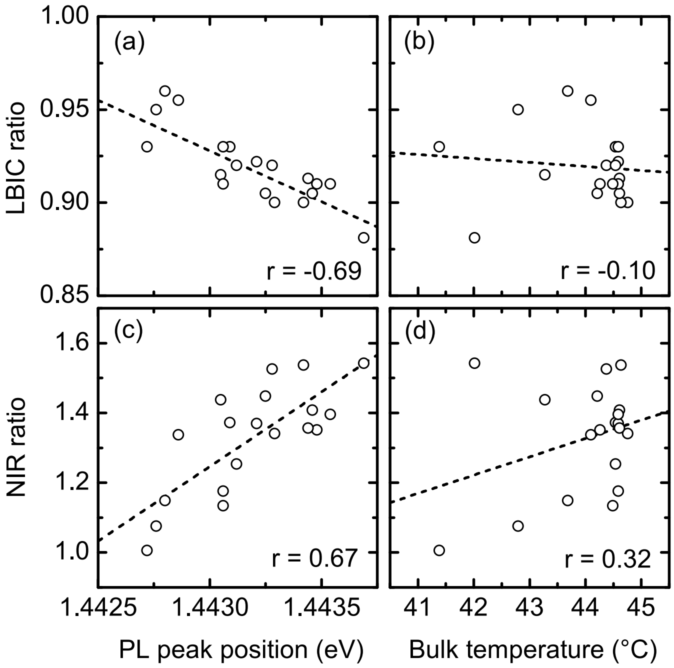

Figure 5.23: Linear correlation figures for the change in the LBIC signal (i.e., the ratio of the magnitudes after aging and before aging) **(a)** vs micro-PL peak position, and **(b)** vs bulk temperature. Accordingly, the change in the NIR signal is plotted **(c)** vs micro-PL peak position, and **(d)** vs bulk temperature. Straight lines indicate the linear fit. The correlation coefficients r are given in the figures.

tion and homogeneity of dopants and intrinsic defects. Its PL-peak shift is assumed to be a reliable measure for the average packaging-induced strain along the bar since measurements before mounting show a flat characteristic. Thus local band structure variations of the active layer, caused, for instance by fluctuation of the epitaxial layer thickness or the composition, do not at all or only marginally interfere the results of such a substrate scan as compared to a scan of the QW-PL.

5.5.3 Correlation of Data Sets and Discussion

The two degradation signatures (LBIC, NIR), the bulk temperature, and the packaging-induced strain have been quantified in a spatially resolved way. Although both degradation-driving parameters act simultaneously and peak at or near the device center, a separation of their impact seems possible. A straight-forward way to display their potential relationship with the degradation signatures is to plot the data sets against each other and to compute the corresponding correlation coefficient. For this the ratios are calculated for the data sets presented in Fig. 5.22(a,b) after and before aging. The locations showing most changes are evaluated for the correlation; for NIR at the emitter sites and for LBIC approximately $40-50$ μm away from the emitter centers; cf. Fig. 5.24.

The linear correlation (Fig. 5.23) of the LBIC and NIR ratios versus

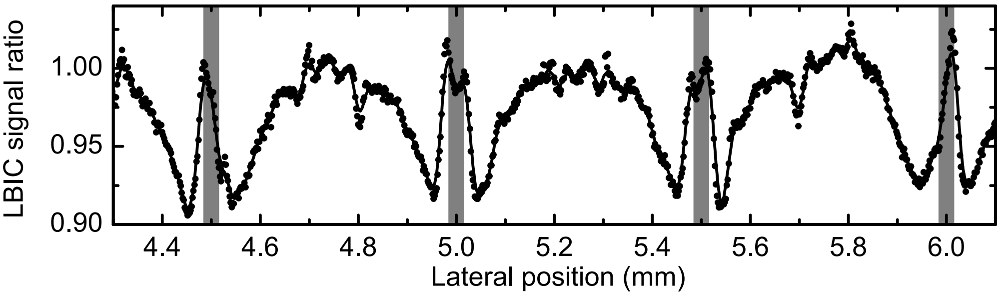

Figure 5.24: Ratio of the LBIC signals for emitters 9 to 12 given as points with 2 μm step-width and as a line for an 11-point average. The metallized 30-μm-wide active stripes are indicated by gray shaded areas centered around each 500 μm.

micro-PL yields correlation coefficients of $r = -0.69$ and $r = 0.67$, and versus bulk temperature of $r = -0.11$ and $r = 0.32$, respectively. The correlation coefficient r (Spearman rank correlation coefficient) is a normalized measure of the strength of the linear relationship between two data sets. Uncorrelated data sets result in $r = 0$ and equivalent ones in $r = 1$. Additionally, the visual comparison of the data suggests a closer relationship between the degradation signatures and micro-PL, because all data show a higher magnitude on the left half than on the right half, whereas the temperature profile is much more symmetric. Such treatment strongly suggests the parameter packaging-induced strain as the principally responsible for the observed degradation. An at least partial influence of the inhomogeneous temperature distribution can, however, not excluded completely with such an analysis.

Discussion

The presented concerted approach suggests the following aging scenario. First, the LBIC degradation signature (Fig. 5.24) strongly indicates the edges of the metallized emitter stripes, at which the signal-reduction is maximal, as starting point of the observed degradation. At these sites the QW starts to degrade, effectively resulting in a reduction of the nonequilibrium carrier lifetime. Second, the established correlation of (average) packaging-induced strain and both degradation signatures identified this strain as a major trigger for aging.

Now, since such local degradation signature at the edges of the metallized emitter stripes have not been observed in similar single emitter devices, [156] it is likely to assume a bar-specific effect causing the observed signatures. The signatures around the emitters (Fig. 5.24) are probably caused by local strain fields which are produced by the metallization. Similar strain distributions have been seen already at metallizations on semiconductors,[253] and at emitter edges.[254] Those strain fields peak a few ten microns outside the metallized regions and extend on the order of hundreds of microns away from the stripe edge.[253] This is similar to the LBIC signature where the maximal signal reduction is seen $\sim 40 - 50\ \mu$m away from the emitter centers. If the distance of the emitter stripes is less than the typical spatial extension of the strain fields they may overlap and lead to a higher strain. Similarly, it renders likely that the observed degradation signatures are caused by the interplay of the two strain contributions, bar-inherent spatially extended packaging-induced strain and localized strain at the metallization edges.

On the other hand, the determined aging rate was very low, only $1.5 \times 10^{-5}\ \text{h}^{-1}$ for a current increase to 120%, which corresponds to less than 1% output-power loss for an operation time of 200 h. Furthermore, the electroluminescence inspection of the fundamental emission did not reveal any dark-line defects being indicative for strong aging. Hence, this resembles a situation at a very early stage of gradual degradation, which is usually associated with a creation and/or accumulation of point defects (cf. section 2.4). Apparently, at this stage the emitters are less affected than their edges possibly through the specific geometry of the strain.

Summary

In this section, a case study was presented that aimed on both the analysis of early stages of laser diode degradation and on the qualification of the earlier found DL-defect-related IR luminescence (measured by NIR imaging) from the GaAs substrate as a degradation probe. Both spatially resolving techniques LBIC scanning and NIR imaging exhibited similar degradation signatures for red-emitting high-power laser bars that were operated for only 200 h. LBIC scanning showed a slightly asymmetric decrease in signal with the maximum nearly in center of the bar, whereas NIR imaging showed almost the inverse behavior, that is an increase with its maximum near center. A much stronger correlation was found for these degradation signatures with the packaging-induced strain than with the bulk temperature. Surprisingly, the most intense decrease of the LBIC was observed at the edges of the emitter stripes, peaking slightly outside, a fact not seen in similar single emitters before. This indicates an interplay of the average bar-inherent packaging-induced strain and local strain fields, caused for instance by the fabrication of the emitter metallizations. Such mechanism proved responsible for the creation and/or accumulation of point defects, which are seen as the microscopic origin of the observed defect signatures.

5.5.4 Chapter Conclusions

A typical application for thermography is the analysis of the transient thermal behavior of high-power laser bars. The ms-range temporal resolution allowed for extraction of the dominant thermal time constants, which are to a large extend defined by the heat sink and the cooling setup. The simultaneous detection of the temperature transient at different locations enabled for an assignment of the time constants to parts of the laser device. The application of synchronous undersampling lock-in thermography allowed even for visualization of the heat flows within the semiconductor chip on a sub-ms-time scale. Detection from the side of the laser device indicated a substantial heating of the front facet.

In a first reliability study, thermography was applied as a screening tool in order to detect, beside temperature distributions, hot-spots in high-power cm-bars. Hot-spot statistics indicated correlations with the applied packaging technology and showed a reduction in frequency with the technological step from soft to hard solder. Surprisingly, the shape of the hot-spot distribution did neither follow the temperature nor the packaging-induced strain distributions, which suggested the importance of failure causes acquired during operation.

In a second case study, thermography was applied to monitor red-emitting high-power AlGaInP laser diodes during COD. The analyzed cw-operating devices exhibited a pronounced overshoot in temperature that was tightly spatially and temporally confined. Simultaneously recorded optical near-fields strongly indicated a correlation between a high optical density at the front facet and COD occurrence, thereby supporting the existence of a critical facet temperature as precondition for COD occurrence. The developed methodology is versatile and potentially applicable to a wide class of semiconductor lasers.

In the last part, an additional IR emission from GaAs-based semiconductor lasers and its application as a probe for laser degradation was analyzed. The origin of the non-thermal IR emission (NIR emission) was found in band-to-band and band-to-DL-defect transitions inside the GaAs substrate. Integral and spatially resolved emission spectra suggested these associations and indicated that they are photoexcited by the spontaneously emitted radiation from the gain material. In a second part, the increase of such DL-defect-related IR luminescence was found to be indicative for laser degradation. Application of the thermography setup allowed for its measurement in parallel to the device temperature. Comparison with LBIC and micro-PL-scanning indicated a stronger correlation of the degradation with the packaging-induced strain than with the bulk temperature.

Chapter 6

Conclusions

This thesis is devoted to the thermography of semiconductor lasers. It covered many aspects that can be divided into three principal parts: experimental determination of thermal emission from semiconductors and semiconductor lasers, discussion of the methodology for thermography of semiconductor lasers, and application of thermography as analytical tool for semiconductor laser studies.

Thermography relies on the detection of thermal radiation according to Planck's law. In the case of real materials like semiconductors, this fundamental relation needs to be modified by the emittance of the radiation source. A spectrally resolved measurement and analysis of the thermal emission from bulk GaAs semiconductors and GaAs-based semiconductor lasers near room temperature provided the materials-related foundation of the thermography of semiconductor lasers. In the course of that study the semiconductor lasers were found semitransparent for the thermal radiation and an enhancement of the emittance of the laser structures over bulk semiconductor material was found, being a result of laser specific components.

Methodological aspects of the thermography of semiconductor lasers were discussed in a next part. The measurement strategy is determined by the composite signal from the omnipresent thermal radiation, making difference measurements and temperature calibration procedures necessary. The infrared-camera approach allows for the determination of temperature distributions in single chip broad-area laser diodes and laser arrays in both the transient and the steady-state regime. The issues arising from the semiconductor materials properties were discussed, and, in particular, the effect of thermal radiation propagating inside the semitransparent laser cavity is analyzed for the case of highly spatially resolved thermography, in conjunction with the effects from diffraction limited imaging. It became evident that thermographically determined temperature distributions can be approximated by a collection of heat sources, including the gain material and all passive regions, where its thermal radiation propagates through the laser diode according to geometrical optics. In this context thermography evolves into a robust technique for the detection of complete temperature distributions, even in large devices.

A major technological challenge is the improvement in the reliability of high-power semiconductor lasers. A first step is the careful analysis of the thermal performance of such devices since large amounts of excess heat are produced during high-power operation, and of the degradation behavior of state-of-the-art devices.

Specific applications demand for different heat-sink technologies. The characterization of the transient thermal behavior of high-power laser arrays via spatially resolved measurements of the dominant thermal time constants revealed that on a 10-ms to 10-s-time scale the heat sink determines the device behavior. On a sub-ms-time scale the heat spreads from the active region across the substrate, which was visualized through application of lock-in thermography with simultaneously high spatial and thermal resolution.

The distinction of the origins of the thermal time constants helped to isolate hot-spot signatures that are regarded to be indicative for device degradation of high-power bars during the turn-on. Such hot-spots were demonstrated to correlate with the packaging technology and, to some degree, with defects at the front facet, but neither with temperature nor strain, which points to failure causes acquired during operation.

The output power of high-power devices is fundamentally limited by the COD, an abrupt degradation process that occurs under high load. The spatio-temporally resolved analysis of this process, with help of its thermal and optical near-field characteristics, was developed and supported the existence of a critical facet temperature triggering the catastrophic process and the relevance of reabsorption at the front facet.

The thermal IR camera allows for imaging in a shorter-wavelength range ($\lambda < 3\ \mu$m) in parallel with standard thermography ($\lambda > 3\ \mu$m). There additional non-thermal infrared emission from GaAs-based semiconductor lasers was identified as band-to-band and band-to-DL-defect transitions that are photoexcited by the spontaneous radiation from the gain material. Such spectral component was found to correlate with gradual device degradation of high-power laser bars due to increasing defect concentrations, which correlated much stronger with packaging-induced strain than with the bulk temperature.

The establishment of thermography as analytical tool for laser diode characterization enriches the spectrum of available techniques. Applied in concert, these techniques help to better understand the operation of semiconductor lasers and to find novel solutions that overcome the present limitations and eventually lead to more reliable, durable, high-power devices. Several important issues need to be addressed in future, or are already under way. The efficiency of electrical-to-optical power conversion, for instance, is a key parameter that needs to be improved, for example by using novel waveguides, by optimization of interfaces and doping profiles, by exploiting novel gain materials, or by recycling the spontaneous radiation for the lasing process (cf. section 5.4). The matter of more efficient cooling is vital for both the durability and the applicability of high-power devices. Tremendous effort is spent towards optimization of conductive and convective cooling (cf. section 5.1) and replacing the classical In solder on Cu heat sinks by harder AuSn solder on strain-reducing CuW heat sinks, on the cost of a higher thermal resistance (cf. section 5.2). Application of novel (nano) materials may lead to a more efficient heat removal as well as the exploitation of novel cooling strategies such as cooling from more than one side. The laser facets are another big issue since they limit the extractable optical power density (cf. section 5.3). Different approaches that necessarily involve surface chemistry and band-structure engineering may lead to more robust facets (cf. section 2.4). Alternatively, novel waveguide concepts like tapered resonators or photonic crystals, or novel gain materials like QDs may lower the optical power density at the facets and reduce filamentation. Another improvements can be expected from optimization of the processing and fabrication of laser devices. For instance, avoiding (local) mechanical strain through optimized metal-contact semiconductor interfaces or passivating trenches should reduce stress-mediated degradation (cf. section 5.5).

Bibliography

[1] J. Neukum. Laser diodes: pump up the power. *Nature Photonics*, 1: 385, 2007.

[2] F. Bachmann. *High-Power Diode Lasers, Technology and Applications*, volume 128 of *Springer Series in Optical Sciences*, chapter Diode Laser Systems, pages 215–284. Springer Science+Business Media, LLC, 2007.

[3] D. Petring, R. Polzin, and M. Becker. *High-Power Diode Lasers, Technology and Applications*, volume 128 of *Springer Series in Optical Sciences*, chapter Applications, pages 285–533. Springer Science+Business Media, LLC, 2007.

[4] U. Brauch, P. Loosen, and H. Opower. *High-Power Diode Lasers, Fundamentals, Technology, Applications*, volume 78 of *Topics Appl. Phys.*, chapter High-Power Diode Lasers for Direct Applications, pages 303–369. Springer Verlag, Berlin Heidelberg, 2000.

[5] D. Lorenzen, M. Schröder, J. Meusel, P. Hennig, H. König, M. Philippens, J. Sebastian, and R. Hülsewede. Comparative performance studies of indium and gold-tin packaged diode laser bars. *Proc. SPIE*, 6104 (1):610404, 2006.

[6] H. Li, T. Towe, I. Chyr, D. Brown, T. Nguyen, F. Reinhardt, X. Jin, R. Srinivasan, M. Berube, T. Truchan, R. Bullock, and J. Harrison. Near 1 kW of continuous-wave power from a single high-efficiency diode-laser bar. *IEEE Phot. Tech. Lett.*, pages 960–962, 2007.

[7] O.J.F. Martin, G.-L. Bona, and P. Wolf. Thermal behavior of visible AlGaInP-GaInP ridge laser diodes. *IEEE J. Quant. Electr.*, 28(11): 2582–2588, Nov 1992.

[8] J. S. Yu, A. Evans, J. David, L. Doris, S. Slivken, and M. Razeghi. Cavity-length effects of high-temperature high-power continuous-wave

characteristics in quantum-cascade lasers. *Appl. Phys. Lett.*, 83(25): 5136–5138, 2003.

[9] A. Knigge, G. Erbert, J. Jonsson, W. Pittroff, SR. taske, B. Sumpf, M. Weyers, and G. Trankle. Passively cooled 940 nm laser bars with 73% wall-plug efficiency at 70 W and 25°C. *Electron Lett.*, 41(5):250–251, 2005.

[10] M. Kanskar, T. Earles, T.J. Goodnough, E. Stiers, D. Botez, and L.J. Mawst. 73% cw power conversion efficiency at 50 W from 970 nm diode laser bars. *Electronics Letters*, 41(5):245–247, 2005.

[11] P. Crump, H. Wenzel, G. Erbert, P. Ressel, M. Zorn, F. Bugge, S. Einfeldt, R. Staske, U. Zeimer, A. Pietrzak, and G. Trankle. Passively Cooled TM Polarized 808-nm Laser Bars With 70% Power Conversion at 80-W and 55-W Peak Power per 100- μm Stripe Width. *IEEE Photon. Technol. Lett.*, 20(16):1378–1380, 2008.

[12] 2008. http://www.briolas.de.

[13] 2008. http://www.briolas.de/trust_detail.html.

[14] 2008. http://www.ist-brighter.eu/.

[15] 2008. http://www.darpa.mil/mto/programs/sheds/.

[16] F. Sibille. Infrared detection and imaging. *Rep. Prog. Phys.*, 49:1197–1242, 1986.

[17] G. Gaussorgues. *Infrared thermography.* Chapman and Hall, London, 1994.

[18] O. Breitenstein and M. Langenkamp. *Lock-in Thermography: Basics and Use for Functional Diagnostics of Electronic Components.* Springer, Berlin, 2003.

[19] H. Kaplan. *Practical applications of infrared thermal sensing and imaging equipment, 3rd ed.* SPIE Press, Bellingham, WA, USA, 2007.

[20] T. Kobayashi, T. Kawakami, and Y. Furukawa. Thermal diagnosis of dark lines in degraded GaAs-AlGaAs double-heterostructure lasers. *Jpn. J. Appl. Phys.*, 14(4):508, 1975.

[21] T. Kobayashi, Y. Seki, and Y. Furukawa. Optical absorption at dark lines in degraded double-heterostructure lasers. *Jpn. J. Appl. Phys.*, 14(4):516, 1975.

[22] T. Kobayashi and Y. Furukawa. Temperature distributions in the GaAs-AlGaAs double-heterostructure laser below and above threshold current. *Jpn. J. Appl. Phys.*, 14(12):1981, 1975.

[23] M. Passlack, C. G. Bethea, W. S. Hobson, John Lopata, E. F. Schubert, G. J. Zydzik, D. T. Nichols, J. F. de Jong, U. K. Chakrabarti, and N. K. Dutta. Infrared microscopy studies on high-power InGaAs-GaAs-InGaP lasers with Ga_2O_3 facet coatings. *IEEE J. Sel. Top. Quant. Elec.*, 1(2):110, 1995.

[24] W. Fang, C. G. Bethea, Y. K. Chen, and S. L. Chuang. Longitudinal spatial inhomogeneities in high-power semiconductor lasers. *IEEE J. Sel. Top. Quant. Elec.*, 1(2):117, 1995.

[25] V. K. Malyutenko. Mapping of current and heat flows in IR light emitting devices and lasers. *Proc. SPIE*, 4648(1):43, 2002.

[26] J. Troger, M. Schwarz, and A. Jakubowicz. Measurement systems for the investigation of soldering quality in high-power diode laser bars. *J. Lightwave Techn.*, 23(11):3889–3892, 2005.

[27] B. L. Meadows, F. Amzajerdian, N. R. Baker, V. Sudesh, and U. N. Singh et al. Thermal characteristics of high-power, long pulse width, quasi-cw laser diode arrays. *Proc. SPIE*, 5336(1):203, 2004.

[28] A. Kozlowska, M. Latoszek, Jens W. Tomm, F. Weik, T. Elsaesser, M. Zbroszczyk, M. Bugajski, B. Spellenberg, and M. Bassler. Analysis of thermal images from diode lasers: Temperature profiling and reliability screening. *Appl. Phys. Lett.*, 86(20):203503, 2005.

[29] A. Kozlowska, P. Wawrzyniak, J. W. Tomm, F. Weik, and T. Elsaesser. Deep level emission from high-power diode laser bars detected by multispectral infrared imaging. *Appl. Phys. Lett.*, 87:153503, 2005.

[30] A. Kozlowska, P. Wawrzyniak, A. Malag, M. Teodorczyk, J. W. Tomm, and F. Weik. Reliability screening of diode lasers by multispectral infrared imaging. *J. Appl. Phys.*, 99(5):053101, 2006.

[31] A. Kozlowska. Infrared imaging of semiconductor lasers. *Semicond. Sci. Technol.*, 22:R27, 2007.

[32] M. Planck. Über eine Verbesserung der Wienschen Spektralgleichung. *Verhandl. Dtsch. phys. Ges.*, 2:202–204, 1900.

[33] M. Planck. Zur Theorie des Gesetzes der Energieverteilung im Normalspektrum. *Verhandl. Dtsch. phys. Ges.*, 2:237–245, 1900.

[34] M. Planck. Über das Gesetz der Energieverteilung im Normalspektrum. *Ann. Phys.*, 4(3):553–563, 1901.

[35] J. Faist, F. Capasso, D. L. Sivco, C. Sirtori, A. L. Hutchinson, and A. Y. Cho. Quantum cascade laser. *Science*, 264:553–556, 1994.

[36] D.F. Welch. A brief history of high-power semiconductor lasers. *IEEE J. Sel. Top. Quant. Elec.*, 6(6):1470–1477, 2000.

[37] J. Piprek. *Semiconductor Optoelectronic Devices, Introduction to Physics and Simulation*. Academic Press, Amsterdam, 1999.

[38] B. Saleh and M. C. Teich. *Fundamentals of photonics*. John Wiley and Sons, Inc., Hoboken, New Jersey, 2007.

[39] B. Mroziewicz, M. Bugajski, and W. Nakwaski. *Physics of Semiconductor Lasers*. North-Holland, Amsterdam, 1991.

[40] T. Numai. *Fundamentals of Semiconductor Lasers*, volume 93 of *Springer Series in Optical Sciences*. Springer-Verlag, New York, Inc., 2004.

[41] S. M. Sze and K. K. Ng. *Physics of Semiconductor Devices*. John Wiley & Sons, Inc., Hoboken, New Jersey, 2007.

[42] L. A. Coldren and S. W. Corzine. *Diode Lasers and Photonic Integrated Circuits*. John Wiley and Sons, New York, 1995.

[43] I. Vurgaftman, J. R. Meyer, and L. R. Ram-Mohan. Band parameters for III-V compound semiconductors and their alloys. *J. Appl. Phys.*, 89(11):5815–5875, 2001.

[44] C. Cohen-Tannoudji, B. Diu, and F. Laloë. *Quantenmechanik*. Walter de Gruyter, Berlin, 1999.

[45] G. Zhang. Influence of strain on lasing performances of Al-free strained-layer Ga(In)As(P)-GaInAsP-GaInP quantum-well lasers emitting at $0.78 < \lambda < 1.1\mu$m. *IEEE J. Sel. Top. Quant. Elec.*, 1(2):183–188, 1995.

[46] E. Yablonovitch and E.O. Kane. Band structure engineering of semiconductor lasers for optical communications. *J. Lightwave Technol.*, 6 (8):1292–1299, 1988.

[47] J. Mukherjee and J. G. McInerney. Electrothermal analysis of cw high-power broad-area laser diodes: A comparison between 2-d and 3-d modeling. *IEEE J. Sel. Top. Quant. Elec.*, 13(5):1180–1187, 2007.

[48] S. Adachi. *GaAs and Related Materials.* World Scientific, Singapore, 1994.

[49] M. Ziegler, F. Weik, J. W. Tomm, T. Elsaesser, W. Nakwaski, R. P. Sarzała, D. Lorenzen, J. Meusel, and A. Kozlowska. Transient thermal properties of high-power diode laser bars. *Appl. Phys. Lett.*, 89(26):263506, 2006.

[50] J. LeClech, M. Ziegler, J. Mukherjee, J. W. Tomm, T. Elsaesser, J.-P. Landesman, B. Corbett, J. G. Mclnerney, J. P. Reithmaier, S. Deubert, A. Forchel, W. Nakwaski, and R. P. Sarzała. Microthermography of diode lasers: The impact of light propagation on image formation. *J. Appl. Phys.*, 105(1):014502, 2009.

[51] M. Ziegler. *Charakterisierung und Eigenschaften von* $In_xGa_{1-x}As$*-*$In_yAl_{1-y}As$ *Quantenkaskadenlasern.* Diplomarbeit, Humboldt-Universität zu Berlin, 2004.

[52] M. Weyers, A. Bhattacharya, F. Bugge, and A. Knauer. *High-Power Diode Lasers, Fundamentals, Technology, Applications*, volume 78 of *Topics Appl. Phys.*, chapter Epitaxy of High-Power Diode Laser Structures, pages 83–120. Springer Verlag, Berlin Heidelberg, 2000.

[53] M. Behringer. *High-Power Diode Lasers, Technology and Applications*, volume 128 of *Springer Series in Optical Sciences*, chapter High-Power Diode Laser Technology and Characteristics, pages 5–74. Springer Science+Business Media, LLC, 2007.

[54] G. Erbert, A. Bärwolff, J. Sebastian, and J. W. Tomm. *High-Power Diode Lasers, Fundamentals, Technology, Applications*, volume 78 of *Topics Appl. Phys.*, chapter High-Power Broad-Area Diode Lasers and Laser Bars, pages 173–223. Springer Verlag, Berlin Heidelberg, 2000.

[55] P. Loosen. *High-Power Diode Lasers, Fundamentals, Technology, Applications*, volume 78 of *Topics Appl. Phys.*, chapter Cooling and Packaging of High-Power Diode Lasers, pages 289–301. Springer Verlag, Berlin Heidelberg, 2000.

[56] K. Boucke. *High-Power Diode Lasers, Technology and Applications*, volume 128 of *Springer Series in Optical Sciences*, chapter Packaging

of Diode Laser Bars, pages 75–120. Springer Science+Business Media, LLC, 2007.

[57] P. Unger. *High-Power Diode Lasers, Fundamentals, Technology, Applications*, volume 78 of *Topics Appl. Phys.*, chapter Introduction to Power Diode Lasers, pages 1–54. Springer Verlag, Berlin Heidelberg, 2000.

[58] O. Ueda. *Reliability and Degradation of III-V Optical Devices.* Artech House, Boston, 1996.

[59] P. Y. Yu and M. Cardona. *Fundamentals of Semiconductors.* Springer-Verlag, Berlin Heidelberg New York, Third edition, 2002.

[60] N. W. Ashcroft and N. D. Mermin. *Solid state physics.* Harcourt College Publishers, 1976.

[61] C. Kittel. *Introduction To Solid State Physics.* John Wiley and Sons, Inc., New York, 7th edition, 1996.

[62] A. Jakubowicz. Material and fabrication-related limitations to high-power operation of GaAs/AlGaAs and InGaAs/AlGaAs laser diodes. *Mater. Sci. Eng. B*, B44(1-3):359–363, 1997.

[63] J. W. Tomm and J. Jimenez, editors. *Quantum-Well Laser Array Packaging: Nanoscale Packaging Techniques.* The McGraw-Hill Companies, New York, 2007.

[64] J. Jimenez. Laser diode reliability: crystal defects and degradation modes. *C. R. Physique*, 4(6):663–673, 2003.

[65] M. Fukuda. *Reliability and Degradation of Semiconductors Lasers and LEDs.* Artech House, Boston, 1991.

[66] C. Basaran, S. Li, and M. F. Abdulhamid. Thermomigration induced degradation in solder alloys. *J. Appl. Phys.*, 103(12):123520, 2008.

[67] X. Liu, R. W. Davis, L. C. Hughes, M. H. Rasmussen, R. Bhat, C.-E. Zah, and J. Stradling. A study on the reliability of indium solder die bonding of high power semiconductor lasers. *J. Appl. Phys.*, 100(1): 013104, 2006.

[68] G. J. van Gurp, P. J. de Waard, and F. J. du Chatenier. Thermomigration in indium films. *Appl. Phys. Lett.*, 45(10):1054–1056, 1984.

[69] G. J. van Gurp, P. J. de Waard, and F. J. du Chatenier. Thermomigration in indium and indium alloy films. *J. Appl. Phys.*, 58(2):728–735, 1985.

[70] D. R. Campell and H.B. Huntington. Thermomigration and electromigration in zirconium. *Phys. Rev.*, 179(3):601–611, 1969.

[71] K. Fujiwara, H. Imai, T. Fujiwara, K. Hori, and M. Takusagawa. Analysis of deterioration in In solder for GaAlAs DH lasers. *Appl. Phys. Lett.*, 35(11):861–863, 1979.

[72] R.G. Waters. Diode laser degradation mechanisms: A review. *Prog. Quantum Electron.*, 15(3):153–174, 1991.

[73] P. G. Eliseev. Optical strength of semiconductor laser materials. *Prog. Quantum Electron.*, 20(1):1–82, 1996.

[74] W. Nakwaski. Thermal conductivity of binary, ternary, and quaternary III-V compounds. *J. Appl. Phys.*, 64:159, 1988.

[75] J. W. Matthews and A. E. Blakeslee. Defects in epitaxial multilayers, I. Misfit dislocations. *J. Cryst. Growth*, 27:118–125, 1974.

[76] M. Ziegler, T. Q. Tien, S. Schwirzke-Schaaf, J. W. Tomm, B. Sumpf, G. Erbert, M. Oudart, and J. Nagle. Gradual degradation of red-emitting high-power diode laser bars. *Appl. Phys. Lett.*, 90(17):171113, 2007.

[77] J. W. Tomm, T. Q. Tien, M. Ziegler, F. Weik, B. Sumpf, M. Zorn, U. Zeimer, and G. Erbert. Degradation behavior and thermal properties of red (650 nm) high-power diode single emitters and laser bars. *Proc. SPIE*, 6456:645606, 2007.

[78] J. W. Tomm, M. Ziegler, M. Oudart, J. Nagle, and J. Jimenez. Gradual degradation of GaAs-based quantum well lasers, creation of defects, and generation of compressive strain. *Phys. Stat. Sol. (c)*, page In press, 2009.

[79] C. H. Henry, P. M. Petroff, R. A. Logan, and F. R. Meritt. Catastrophic damage of $\mathrm{Al}_x\mathrm{Ga}_{1-x}$ double-heterostructure laser material. *J. Appl. Phys.*, 50(5):3721–3732, 1979.

[80] W. C. Tang, H. J. Rosen, P. Vettiger, and D. J. Webb. Raman microprobe study of the time development of AlGaAs single quantum

well laser facet temperature on route to catastrophic breakdown. *Appl. Phys. Lett.*, 58(6):557–559, 1991.

[81] H. Fujii, Y. Ueno, and K. Endo. Effect of thermal resistivity on the catastrophic optical damage density of AIGalnP laser diodes. *Appl. Phys. Lett.*, 62(17):2114–2115, 1993.

[82] R. E. Mallard and R. Clayton. EBIC and TEM analysis of catastrophic optical damage in high power GaAlAs/GaInAs lasers. *Proc. SPIE*, 3004:145, 1997.

[83] C. W. Snyder, J. W. Lee, R. Hull, and R. A. Logan. Catastrophic degradation lines at the facet of InGaAsP/InP lasers investigated by transmission electron microscopy. *Appl. Phys. Lett.*, 67(4):488, 1995.

[84] M. Bou Sanayeh, A. Jaeger, W. Schmid, S. Tautz, P. Brick, K. Streubel, and G. Bacher. Investigation of dark line defects induced by catastrophic optical damage in broad-area AlGaInP laser diodes. *Appl. Phys. Lett.*, 89(10):101111, 2006.

[85] K. H. Park, J. K. Lee, D. H. Jang, H. S. Cho, C. S. Park, K. E. Pyun, J. Y. Jeong, S. Nahm, and J. Jeong. Characterization of catastrophic optical damage in Al-free InGaAs/InGaP 0.98 μm high-power lasers. *Appl. Phys. Lett.*, 73(18):2567–2569, 1998.

[86] T. S. Yeoh, J. A. Chaney, M. S. Leung, N. A. Ives, Z. D. Feinberg, J. G. Ho, and J. Wen. Three-dimensional failure analysis of high power semiconductor laser diodes operated in vacuum. *J. of Appl. Phys.*, 102 (12):123104, 2007.

[87] S.N.G. Chu, S. Nakahara, M.E. Twigg, L.A. Koszi, E.J. Flynn, A.K. Chin, B.P. Seeger, and Jr. W.D. Johnston. Defect mechanisms in degradation of $1.2-\mu$m wavelength channeled-substrate buried heterostructure lasers. *J. Appl. Phys.*, 63(3):611, 1988.

[88] M. Levinshtein, S. Rumyantsev, and M. Shur, editors. *Handbook series on semiconductor parameters.* World Scientific Publishing Co. Pte. Ltd., Singapore, 2000.

[89] F. A. Houle, D. L. Neiman, W. C. Tang, and H. J. Rosen. Chemical changes accompanying facet degradation of AlGaAs quantum well lasers. *J. Appl. Phys.*, 72(9):3884–3896, 1992.

[90] A. Chavan, R. Radionova, G.W. Charache, R.J. Menna, H. Schluter, and J.L. Hostetler. Comparison of facet temperature and degradation of unpumped and passivated facets of Al-free 940-nm lasers using photoluminescence. *IEEE J. Quant. Electr.*, 41(5):630–635, 2005.

[91] M. Fukuda and K. Takahei. Optically enhanced oxidation of III-V compound semiconductors. *J. Appl. Phys.*, 57(1):129–134, 1985.

[92] T. Schoedl, U.T. Schwarz, V. Kümmler, M. Furitsch, A. Leber, A. Miler, A. Lell, and V. Härle. Facet degradation of GaN heterostructure laser diodes. *J. Appl. Phys.*, 97(12):123102, 2005.

[93] H. Brugger and P. W. Epperlein. Mapping of local temperatures on mirrors of GaAs/AlGaAs laser diodes. *Appl. Phys. Lett.*, 56(11):1049–1051, 1990.

[94] M. Ziegler, V. Talalaev, J. W. Tomm, T. Elsaesser, P. Ressel, B. Sumpf, and G. Erbert. Surface recombination and facet heating in high-power diode lasers. *Appl. Phys. Lett.*, 92(20):203506, 2008.

[95] L. W. Tu, E. F. Schubert, M. Hong, and G. J. Zydzik. In-vacuum cleaving and coating of semiconductor laser facets using thin silicon and a dielectric. *J. Appl. Phys.*, 80(11):6448–6451, 1996.

[96] J. H. Marsh. Quantum well intermixing. *Semicond. Sci. Technol.*, 8 (6):1136–1155, 1993.

[97] C.L. Walker, A.C. Bryce, and J.H. Marsh. Improved catastrophic optical damage level from laser with nonabsorbing mirrors. *IEEE Photon. Technol. Lett.*, 14(10):1394–1396, 2002.

[98] F. Rinner, J. Rogg, M. T. Kelemen, M. Mikulla, G. Weimann, J. W. Tomm, E. Thamm, and R. Poprawe. Facet temperature reduction by a current blocking layer at the front facets of high-power InGaAs/AlGaAs lasers. *J. Appl. Phys.*, 93(3):1848–1850, 2003.

[99] D. Botez. Design considerations and analytical approximations for high continuous-wave power, broad-waveguide diode lasers. *Appl. Phys. Lett.*, 74(21):3102–3104, 1999.

[100] A. Schmitt, M. Behringer, G. Herrmann, M. Philippens, J. Heerlein, and J. Luft. High-brightness highly-reliable InGaAlAs/GaAs laser bars with reduced fill factor and 60% efficiency. *Proc. SPIE*, 4973:1–9, 2003.

[101] M. Behringer, S. Tautz, W. Pammer, K. Friepes, U. Steegmueller, M. Philippens, J. Maric, and H. Koenig. Highly reliable and efficient laser bars and cost efficient packaging. *Proc. SPIE*, 5711(1):12–20, 2005.

[102] F. Bugge, A. Knauer, S. Gramlich, I. Rechenberg, G. Beister, J. Sebastian, H. Wenzel, G. Erbert, and M. Weyers. MOVPE growth of AlGaAs/GaInP diode lasers. *J. Electron. Mater.*, 29(1):57, 2000.

[103] W. Pittroff, G. Erbert, G. Beister, F. Bugge, A. Klein, A. Knauer, J. Maege, P. Ressel, J. Sebastian, R. Staske, and G. Traenkle. Mounting of high power laser diodes on boron nitride heat sinks using an optimized Au/Sn metallurgy. *Advanced Packaging, IEEE Transactions on*, 24(4):434–441, 2001.

[104] M. Zorn, H. Wenzel, U. Zeimer, B. Sumpf, G. Erbert, and M. Weyers. High-power red laser diodes grown by MOVPE. *J. Cryst. Growth*, 298: 667–671, 2007.

[105] B. Corbett, P. Lambkin, J. O'Callaghan, S. Deubert, W. Kaiser, J.P. Reithmaier, and A. Forchel. Modal analysis of large spot size, low output beam divergence quantum-dot lasers. *IEEE Photon. Technol. Lett.*, 19(12):916–918, 2007.

[106] W. Heisenberg. 50 Jahre Quantentheorie. *Naturwissenschaften*, 38(3): 49–55, 1950.

[107] W. Nolting. *Grundkurs Theoretische Physik, 5 Quantenmechanik, Teil 1:Grundlagen.* Friedr. Vieweg und Sohn Verlagsgesellschaft mbH, Braunschweig/Wiesbaden, 1997.

[108] R. Siegel and J. R. Howell. *Thermal Radiation Heat Transfer, 4. ed.* Taylor and Francis, New York, 2002.

[109] A. Einstein. Über einen die Erzeugung und Verwandlung des Lichtes betreffenden heuristischen Gesichtspunkt. *Ann. Phys.*, 17:132–148, 1905.

[110] A. Einstein. Zur Theorie der Lichterzeugung und Lichtabsorption. *Ann. Phys.*, 20:199–206, 1906.

[111] A. Einstein. Die Plancksche Theorie der Strahlung und die Theorie der spezifischen Wärme. *Ann. Phys.*, 22:180–190, 1907.

[112] A. Einstein. Zur Quantentheorie der Strahlung. *Physik Z.*, 18:121–128, 1917.

[113] M. A. Weinstein. On the validity of Kirchhoff's law for a freely radiating body. *Am. J. Phys.*, 28:123, 1960.

[114] D. G. Burkhard, J. V. S. Lochhead, and C. M. Penchina. On the validity of Kirchhoff's law in a nonequilibrium environment. *Am. J. Phys.*, 40:1794, 1972.

[115] W. Eckhardt. Kirchhoff-Planck law for freely radiating bodies and fluctuation-dissipation theorem. *Physica*, 128A:467–485, 1984.

[116] A. Resnick, C. Persons, and G. Lindquist. Polarized emissivity and Kirchhoff's law. *Appl. Opt.*, 38(8):1384–1387, 1999.

[117] W. C. Snyder, Z. Wan, and X. Li. Thermodynamic constraints on reflectance reciprocity and Kirchhoff's law. *Appl. Opt.*, 37(16):3464–3470, 1998.

[118] P. Würfel. The chemical potential of radiation. *J. Phys. C: Solid State Phys.*, 15:3967–3985, 1982.

[119] M. Kuball, A. Sarua, H. Ji, M.J. Uren, R.S. Balmer, and T. Martin. Integrated Raman - IR thermography on AlGaN/GaN transistors. *Microwave Symposium Digest, 2006. IEEE MTT-S International*, pages 1339–1342, 2006. ISSN 0149-645X.

[120] 2008. http://www.aim-ir.com/.

[121] 2008. http://www.thermosensorik.de.

[122] 2008. http://www.ircam.de.

[123] 2008. http://www.flir.com.

[124] C. C. Williams and H. K. Wickramasinghe. Scanning thermal profiler. *Appl. Phys. Lett.*, 49(23):1587–1589, 1986.

[125] U. F. Wischnath, J. Welker, M. Munzel, and A. Kittel. The near-field scanning thermal microscope. *Review of Scientific Instruments*, 79(7): 073708, 2008.

[126] H. I. Abdelkader, H. H. Hausien, and J. D. Martin. Temperature rise and thermal rise-time measurements of a semiconductor laser diode. *Rev. Sci. Instrum.*, 63(3):2004–2007, 1992.

[127] B. G. Cohen, W. B. Snow, and A. R. Tretola. GaAs p-n junction diodes for wide range thermometry. *Rev. Sci. Instrum.*, 34(10):1091–1093, 1963.

[128] Y. P. Varshni. Temperature dependence of the energy gap in semiconductors. *Physica*, 34:149–154, 1967.

[129] J. W. Tomm, M. Ziegler, T. Q. Tien, F. Weik, P. Hennig, J. Meusel, H. Kissel, G. Seibold, J. Biesenbach, G. Groenninger, G. Herrmann, and U. Strauß. Screening of high power laser diode bars in terms of stresses and thermal profiles. *Proc. SPIE*, 6876:687619, 2008.

[130] M. L. Biermann, S. Duran, K. Peterson, A. Gerhardt, J. W. Tomm, A. Bercha, and W. Trzeciakowski. Spectroscopic method of strain analysis in semiconductor quantum-well devices. *J. Appl. Phys.*, 96(8): 4056–4065, 2004.

[131] A. Gerhardt, F. Weik, T. QuocTran, J. W. Tomm, T. Elsaesser, J. Biesenbach, H. Müntz, G. Seibold, and M. L. Biermann. Device deformation during low-frequency pulsed operation of high-power diode bars. *Appl. Phys. Lett.*, 84(18):3525–3527, 2004.

[132] W.W. Chow and S.W. Koch. *Semiconductor-Laser Fundamentals, Physics of the Gain Materials.* Springer, Berlin, 1999.

[133] C. H. Henry, R. A. Logan, and K. A. Bertness. Spectral dependence of the change in refractive index due to carrier injection in GaAs lasers. *J. Appl. Phys.*, 52(7):4457–4461, 1981.

[134] N. K. Dutta, N. A. Olsson, and W. T. Tsang. Carrier induced refractive index change in AlGaAs quantum well lasers. *Appl. Phys. Lett.*, 45(8): 836–837, 1984.

[135] A. Olsson and C. L. Tang. Injected-carrier induced refractive-index change in semiconductor lasers. *Appl. Phys. Lett.*, 39(1):24–26, 1981.

[136] A. J. Bennett, R. D. Clayton, and J. M. Xu. Above-threshold longitudinal profiling of carrier nonpinning and spatial modulation in asymmetric cavity lasers. *J. Appl. Phys.*, 83(7):3784–3788, 1998.

[137] C. G. Bethea. Spatially imaged inhomogeneous spontaneous emission spectra of high power in InGaAsP/InP Fabry-Perot lasers. *Applied Physics Letters*, 67(2):182–184, 1995.

[138] F. Rinner, J. Rogg, P. Friedmann, M. Mikulla, G. Weimann, and R. Poprawe. Longitudinal carrier density measurement of high power broad area laser diodes. *Appl. Phys. Lett.*, 80(1):19–21, 2002.

[139] S. Todoroki, M. Sawai, and K. Aiki. Temperature distribution along the striped active region in high-power GaAlAs visible lasers. *J. Appl. Phys.*, 58(3):1124–1128, 1985.

[140] P. W. Epperlein, G. L. Bona, and P. Roentgen. Local mirror temperatures of red-emitting (Al)GaInP quantum-well laser diodes by Raman scattering and reflectance modulation measurements. *Appl. Phys. Lett.*, 60(6):680–682, 1992.

[141] T. J. Ochalski, D. Pierścińska, K. Pierściński, M. Bugajski, J. W. Tomm, T. Grunske, and A. Kozlowska. Complementary thermoreflectance and micro-Raman analysis of facet temperatures of diode lasers. *Appl. Phys. Lett.*, 89(7):071104, 2006.

[142] D. Wawer, T. J. Ochalski, T. Piwonski, A. Wojcik-Jedlinska, M. Bugajski, and H. Page. Spatially resolved thermoreflectance study of facet temperature in quantum cascade lasers. *Phys. Stat. Sol. (a)*, 202(7): 1227–1232, 2005.

[143] D. C. Hall, L. Goldberg, and D. Mehuys. Technique for lateral temperature profiling in optoelectronic devices using a photoluminescence microprobe. *Appl. Phys. Lett.*, 61(4):384–386, 1992.

[144] J. M. Rommel, P. Gavrilovic, and F. P. Dabkowski. Photoluminescence measurement of the facet temperature of 1 W gain-guided AlGaAs/GaAs laser diodes. *J. Appl. Phys.*, 80(11):6547–6549, 1996.

[145] D. P. Bour, D. W. Treat, R. L. Thornton, R. S. Geels, and D. F. Welch. Drift leakage current in AlGaInP quantum-well lasers. *IEEE J. Quant. Electr.*, 29(5):1337, 1993.

[146] S. A. Wood, P. M. Smowton, C. H. Molloy, P. Blood, D. J. Somerford, and C. C. Button. Direct monitoring of thermally activated leakage current in AlGaInP laser diodes. *Appl. Phys. Lett.*, 74(17):2540–2542, 1999.

[147] Jr. H. C. Casey, D. D. Sell, and K. W. Wecht. Concentration dependence of the absorption coefficient for n- and p - type GaAs between 1.3 and 1.6 eV. *J. Appl. Phys.*, 46(1):250–257, 1975.

[148] D. E. Aspnes, S. M. Kelso, R. A. Logan, and R. Bhat. Optical properties of $Al_xGa_{1-x}As$. *Journal of Applied Physics*, 60(2):754–767, 1986.

[149] W. C. Tang, H. J. Rosen, P. Vettiger, and D. J. Webb. Comparison of the facet heating behavior between AlGaAs single quantum-well lasers and double-heterojunction lasers. *Appl. Phys. Lett.*, 60(9):1043–1045, 1992.

[150] S. Perkowitz. *Optical characterization of semiconductors, infrared, raman and photoluminscence spectroscopy.* Academic Press, London, 1993.

[151] V. Saptari. *Fourier-transform spectroscopy instrumentation engineering.* SPIE Press, Bellingham, WA, USA, 1993.

[152] H. Schneider and K. v. Klitzing. Thermionic emission and Gaussian transport of holes in a $GaAs/Al_xGa_{1-x}As$ multiple-quantum-well structure. *Phys. Rev. B*, 38(9):6160–6165, 1988.

[153] J. Nelson, M. Paxman, K.W.J. Barnham, J.S. Roberts, and C. Button. Steady-state carrier escape from single quantum wells. *IEEE J. Quant. Electr.*, 29(6):1460–1468, 1993.

[154] R.G. Ispasoiu, A.M. Fox, and D. Botez. Carrier transport mechanisms in high-power InGaAs-InGaAsP-InGaP strained quantum-well lasers. *IEEE J. Quant. Electr.*, 36(7):858–863, 2000.

[155] K.H. Herrmann, J.W. Tomm, and H. Al-Otaibi. Temperature dependent carrier escape from quantum well states in GaAs/GaAlAs graded index laser structures. *Semicond. Sci. Technol.*, 14(3):293–297, 1999.

[156] C. Ropers, Tran Quoc Tien, C. Lienau, J. W. Tomm, P. Brick, N. Linder, B. Mayer, M. Müller, Sönke Tautz, and Wolfgang Schmid. Observation of deep level defects within the waveguide of red-emitting high-power diode lasers. *Appl. Phys. Lett.*, 88(13):133513, 2006.

[157] M. Born and E. Wolf, editors. *Principles of optics.* Cambridge University Press, Cambridge, 7th edition, 1999.

[158] D. W. Pohl, W. Denk, and M. Lanz. Optical stethoscopy: Image recording with resolution lambda/20. *Appl. Phys. Lett.*, 44(7):651–653, 1984.

[159] A. Lewis, M. Isaacson, A. Harootunian, and A. Murray. Development of a 500 Å spatial resolution light microscope. I. Light is efficiently transmitted through $\lambda/16$ diameter apertures. *Ultramicroscopy*, 13: 227–231, 1984.

[160] U. Dürig, D. W. Pohl, and F. Rohner. Near-field optical-scanning microscopy. *J. Appl. Phys.*, 59(10):3318–3327, 1986.

[161] E. Betzig and J. K. Trautman. Near-field optics - microscopy, spectroscopy, and surface modification beyond the diffraction limit. *Science*, 257(5067):189–195, 1992.

[162] D. Courjon and C. Bainier. Near field microscopy and near field optics. *Rep. Prog. Phys.*, 57:989–1028, 1994.

[163] C. Girard. Near fields in nanostructures. *Rep. Prog. Phys.*, 68(8): 1883–1933, 2005.

[164] G. Binnig, H. Rohrer, Ch. Gerber, and E. Weibel. Surface studies by scanning tunneling microscopy. *Phys. Rev. Lett.*, 49(1):57–61, 1982.

[165] J. Kim and K. Song. Recent progress of nano-technology with NSOM. *Micron*, 38:409–426, 2007.

[166] 2008. Private communication with R. Pomraenke.

[167] A. Richter, G. Behme, M. Sueptitz, C. Lienau, T. Elsaesser, M. Ramsteiner, R. Noetzel, and K. Ploog. Real-space transfer and trapping of carriers into single GaAs quantum wires studied by near-field optical spectroscopy. *Phys. Rev. Lett.*, 79:2145, 1997.

[168] C. Lienau. Ultrafast near-field spectroscopy of single semiconductor quantum dots. *Phil. Trans. Roy. Soc. A*, 362:861, 2004.

[169] S. K. Buratto, J. W. P. Hsu, J. K. Trautman, E. Betzig, R. B. Bylsma, C. C. Bahr, and M. J. Cardillo. Imaging InGaAsP quantum-well lasers using near-field scanning optical microscopy. *J. Appl. Phys.*, 76(12): 7720–7725, 1994.

[170] C. Lienau, A. Richter, and T. Elsaesser. Light-induced expansion of fiber tips in near-field scanning optical microscopy. *Appl. Phys. Lett.*, 69:325, 1996.

[171] J. Lohrengel, R. Todtenhaupt, and M. Ragab. Bestimmung des gerichteten spektralen Emissionsgrades von Feststoffen im Wellenlängenbereich von $2,5\ \mu$m bis $45\ \mu$m bei Temperaturen zwischen 80°C und 350°C. *Waerme- Stoffuebertrag.*, 28:321, 1993.

[172] J. Lohrengel and R. Todtenhaupt. Wärmeleitfähigkeit, Gesamtemissionsgrade und spektrale Emissionsgrade der Beschichtung Nextel-Velvet-Coating 811-21 (RAL 900 15 tiefschwarz matt). *PTB Mitteilungen*, 106:259, 1996.

[173] 2008. Private communication with C. Monte.

[174] J. Hollandt, R. Friedrich, B. Gutschwager, D. R. Taubert, and J. Hartmann. High-accuracy radiation thermometry at the National Metrology Institute of Germany, the PTB. *High Temperatures - High Pressures*, 35/36(4):379–415, 2003/2004.

[175] M. Ziegler, J. W. Tomm, T. Elsaesser, G. Erbert, F. Bugge, W. Nakwaski, and Robert P. Sarzała. Visualization of heat flows in high-power diode lasers by lock-in thermography. *Appl. Phys. Lett.*, 92 (10):103513, 2008.

[176] M. Ziegler, R. Pomraenke, M. Felger, J. W. Tomm, C. Lienau, M. Bou Sanayeh, A. Gomez-Iglesias, M. Reufer, F. Bugge, and G. Erbert. Infrared emission from the substrate of GaAs-based semiconductor lasers. *Appl. Phys. Lett.*, 93(4):041101, 2008.

[177] D. Weber. Low-temperature, directional, spectral emissivity of translucent solids. *J. Opt. Soc. Am.*, 50(8):808–810, 1960.

[178] S. C. Jain, S. K. Agarwal, W. N. Borle, and S. Tata. Total emissivity of silicon at high temperatures. *Journal of Physics D: Applied Physics*, 4:1207–1209, 1971.

[179] P. J. Timans. The experimental determination of the temperature dependence of the total emissivity of GaAs using a new temperature measurement technique. *J. Appl. Phys.*, 72(2):660–670, 1992.

[180] P. J. Timans. Emissivity of silicon at elevated temperatures. *J. Appl. Phys.*, 74(10):6353–6364, 1993.

[181] D. F. Takeuti, P. J. Timans, and H. Ahmed. Emissivity of B-implanted and annealed silicon. *Appl. Phys. Lett.*, 67(15):2206–2208, 1995.

[182] H. Rogne, P. J. Timans, and H. Ahmed. Infrared absorption in silicon at elevated temperatures. *Appl. Phys. Lett.*, 69(15):2190–2192, 1996.

[183] N. M. Ravindra, B. Sopori, O. H. Gokce, S. X. Cheng, A. Shenoy, L. Jin, S. Abedrabbo, W. Chen, and Y. Zhang. Emissivity measurements and modeling of silicon-related materials: An overview. *Int. J. Thermophysics*, 22(5):1593–1611, 2001.

[184] M. Ohtsuka and R. E. Bedford. Measurement of size-of-source effects in an optical pyrometer. *Measurement*, 7(1):2, 1989.

[185] P. Bloembergen. On the correction for the size-of-source effect corrupted by background radiation. *Proc. TEMPMEKO '99*, page 607, 1999.

[186] G. Machin and M. Ibrahim. Size of source effect and temperature uncertainty: I - high temperature systems. *Proc. TEMPMEKO '99*, page 681, 1999.

[187] G. Machin and M. Ibrahim. Size of source effect and temperature uncertainty: II - low temperature systems. *Proc. TEMPMEKO '99*, page 687, 1999.

[188] S. Kasap and P. Capper, editors. *Springer handbook of electronic and photonic materials.* Springer, New York, 2006.

[189] H. B. Briggs and R. C. Fletcher. Absorption of infrared light by free carriers in germanium. *Phys. Rev.*, 91(6):1342–1346, 1953.

[190] H. Y. Fan, W. Spitzer, and R. J. Collins. Infrared absorption in n-type germanium. *Phys. Rev.*, 101(2):566–572, 1956.

[191] W. G. Spitzer and J. M. Whelan. Infrared absorption and electron effective mass in n-type gallium arsenide. *Phys. Rev.*, 114(1):59–63, 1959.

[192] A. S. Jordan. Determination of the total emittance of n-type GaAs with application to Czochralski growth. *J. Appl. Phys.*, 51:2218, 1980.

[193] R. Braunstein and E. O. Kane. The valence band structure of the III-V compounds. *J. Phys. Chem. Solids*, 23:1423–1431, 1962.

[194] E. J. Mayer, A. Lohner, M. Woerner, and T. Elsaesser. Infrared absorption spectra of photoexcited holes in undoped GaAs. *Phys. Rev. B*, 46(3):1878–1881, 1992.

[195] W. Songprakob, R. Zallen, W. K. Liu, and K. L. Bacher. Infrared studies of hole-plasmon excitations in heavily-doped p-type MBE-grown GaAs:C. *Phys. Rev. B*, 62(7):4501–4510, 2000.

[196] W. Songprakob, R. Zallen, D. V. Tsu, and W. K. Liu. Intervalenceband and plasmon optical absorption in heavily doped GaAs:C. *J. Appl. Phys.*, 91:171–177, 2002.

[197] D. M. Szmyd, P. Porro, A. Majerfeld, and S. Lagomarsino. Heavily doped GaAs:Se. I. Photoluminescence determination of the electron effective mass. *J. Appl. Phys.*, 68(5):2367–2375, 1990.

[198] H. R. Chandrasekhar and A. K. Ramdas. Nonparabolicity of the conduction band and the coupled plasmon-phonon modes in n-GaAs. *Phys. Rev. B*, 21(4):1511–1515, 1980.

[199] M. Ziegler, J. W. Tomm, F. Weik, T. Elsaesser, C. Monte, J. Hollandt, H. Kissel, G. Seibold, and J. Biesenbach. Accurate determination of absolute temperatures of GaAs based high-power diode lasers. *Proc. SPIE*, 6876:68761A, 2008.

[200] J. W. Tomm, F. Weik, R. Glatthaar, U. Vetter, J. Nurnus, A. Lambrecht, B. Spellenberg, M. Bassler, M. Behringer, and J. Luft. A novel light-emitting structure for the 3- to 5-μ m spectral range. *Proc. SPIE*, 5722:319–326, 2005.

[201] A. Kozlowska, M. Ziegler, J. W. Tomm, R. P. Sarzała, and W. Nakwaski. Thermal imaging of actively cooled high-power laser bars. *Mixed Design of Integrated Circuits and Systems, 2007. MIXDES '07*, pages 396–400, 2007.

[202] T. Kitamoto, Y. Inoue, M. Yamada, and T. Kawase. Optical measurement of carrier concentration profile in n-type semiconducting GaAs substrate. *Phys. Stat. Sol. (a)*, 204(4):1002–1007, 2007.

[203] R. P. Sarzała and W. Nakwaski. An appreciation of usability of the finite element method for the thermal analysis of stripe-geometry diode lasers. *J. Therm. Anal.*, 36:1171, 1990.

[204] R. P. Sarzała and W. Nakwaski. Thermal analysis of oxide-isolated stripe diode lasers. *J. Therm. Anal.*, 38:1447, 1992.

[205] R. P. Sarzała and W. Nakwaski. Finite-element thermal model for buried-heterostructure diode lasers. *Opt. Quantum Electron.*, 26:87, 1994.

[206] M. Voss, C. Lier, U. Menzel, A. Bärwolff, and T. Elsaesser. Time-resolved emission studies of GaAs/AlGaAs laser diode arrays on different heat sinks. *J. Appl. Phys.*, 79(2):1170–1172, 1996.

[207] R. Puchert, A. Barwolff, M. Voss, U. Menzel, J. W. Tomm, and J. Luft. Transient thermal behavior of high power diode laser arrays. *Components and Packaging Technologies, IEEE Transactions on*, 23(1):95–100, 2000.

[208] A. Gourevitch, B. Laikhtman, D. Westerfeld, D. Donetsky, G. Belenky, C. W. Trussell, Z. Shellenbarger, H. An, and R. U. Martinelli. Transient thermal analysis of InGaAsP-InP high-power diode laser arrays with different fill factors. *J. Appl. Phys.*, 97(8):084503, 2005.

[209] F. P. Incropera, D. P. DeWitt, T. L. Bergman, and A. S. Lavine. *Introduction to Heat Transfer, 5th ed.* John Wiley and Sons, New York, 2006.

[210] T. Hayakawa. Facet temperature distribution in broad stripe high power laser diodes. *Appl. Phys. Lett.*, 75(10):1467–1469, 1999.

[211] F. P. Dabkowski, A. K. Chin, P. Gavrilovic, S. Alie, and D. M. Beyea. Temperature profile along the cavity axis of high power quantum well lasers during operation. *Appl. Phys. Lett.*, 64(1):13–15, 1994.

[212] J. Le Clech. Micro-thermographie infrarouge et modelisation numerique de diodes laser a semi-conducteurs : impact de la propagation des rayons lumineux infrarouges sur la formation d'images. Master's thesis, Faculte des Sciences de l'Universite de Nantes, sept. 2008.

[213] J. L. Hostetler, C.-L. Jiang, V. Negoita, T. Vethake, R. Roff, A. Shroff, T. Li, C. Miester, U. Bonna, G. Charache, H. Schlüter, and F. Dorsch. Thermal and strain characteristics of high-power 940 nm laser arrays mounted with AuSn and In solders. *Proc. SPIE*, 6456(1):645602, 2007.

[214] H. Kissel, G. Seibold, J. Biesenbach, G. Groenninger, G. Herrmann, and U. Strauß. A comprehensive reliability study of high-power 808 nm laser diodes mounted with AuSn and indium. *Proc. SPIE*, 6876: 687618, 2008.

[215] T. Q. Tien, A. Gerhardt, S. Schwirzke-Schaaf, J. W. Tomm, H. Müntz, J. Biesenbach, M. Oudart, J. Nagle, and M. L. Biermann. Relaxation of packaging-induced strains in AlGaAs-based high-power diode laser arrays. *Appl. Phys. Lett.*, 86(10):101911, 2005.

[216] H.X. Li, I. Chyr, X. Jin, F. Reinhardt, T. Towe, D. Brown, T. Nguyen, M. Berube, T. Truchan, D. Hu, R. Miller, R. Srinivasan, T. Crum, E. Wolak, R. Bullock, J. Mott, and J. Harrison. >700 W continuous-wave output power from single laser diode bar. *Electronics Letters*, 43 (1):27–28, 2007.

[217] H.X. Li, I. Chyr, D. Brown, F. Reinhardt, O. Romero, C.-H. Chen, R. Miller, K. Kuppuswamy, X. Jin, T. Ngugen, T. Towe, T. Crum, C. Mitchell, T. Truchan, R. Bullock, E. Wolak, J. Mott, and J. Harrison. Next-generation high-power, high-efficiency diode lasers at spectra-physics. *Proc. SPIE*, 6824:68240S, 2007.

[218] 2008. Private communication with H. Kissel.

[219] K Mizuishi. Some aspects of bonding-solder deterioration observed in long-lived semiconductor lasers: Solder migration and whisker growth. *J. Appl. Phys.*, 55(2):289–295, 1984.

[220] S. Bull, J. W. Tomm, M. Oudart, J. Nagle, C. Scholz, K. Boucke, I. Harrison, and E. C. Larkins. By-emitter degradation analysis of high-power laser bars. *Journal of Applied Physics*, 98(6):063101, 2005.

[221] R. Xia, E. C. Larkins, I. Harrison, S. R. A. Dods, A. V. Andrianov, J. Morgan, and J. P. Landesman. The effect of mounting-induced strain and defect on the properties of AlGaAs 808 nm LDs. *Synthetic Metals*, 127:255–259, Jul 2002.

[222] R. Xia, E. C. Larkins, I. Harrison, S. R. A. Dods, A. V. Andrianov, J. Morgan, and J. P. Landesman. Mounting-induced strain threshold for the degradation of high-power AlGaAs laser bars. *Photonics Technology Letters, IEEE*, 14(7):893–895, Jul 2002.

[223] P. W. Epperlein. Micro-temperature measurements on semiconductor laser mirrors by reflectance modulation: A newly developed technique for laser characterization. *Jpn. J. Appl. Phys.*, 32(12A):5514–5522, 1993.

[224] B. W. Hakki and F. R. Nash. Catastrophic failure in GaAs double-heterostructure injection lasers. *J. Appl. Phys.*, 45(9):3907–3912, 1974.

[225] O. Ueda, K. Wakao, S. Komiya, A. Yamaguchi, S. Isozumi, and I. Umebu. Catastrophic degradation of InGaAsP/InGaP double-heterostructure lasers grown on (001) GaAs substrates by liquid-phase epitaxy. *J. Appl. Phys.*, 58(11):3996–4002, 1985.

[226] M. Bou Sanayeh, P. Brick, W. Schmid, B. Mayer, M. Müller, M. Reufer, K. Streubel, J. W. Tomm, and G. Bacher. Temperature-power dependence of catastrophic optical damage in AlGaInP laser diodes. *Appl. Phys. Lett.*, 91(4):041115, 2007.

[227] M. Bou Sanayeh, P. Brick, W. Schmid, B. Mayer, M. Müller, M. Reufer, K. Streubel, M. Ziegler, J. W. Tomm, and G. Bacher. The physics of catastrophic optical damage in high-power AlGaInP laser diodes. *Proc. SPIE*, 6997:699703, 2008.

[228] M. Bou Sanayeh, P. Brick, W. Schmid, B. Mayer, M. Müller, M. Reufer, K. Streubel, S. Schwirzke-Schaaf, J. W. Tomm, A. Danilewsky, and G. Bacher. Defect investigation and temperature analysis of high-power AlGaInP laser diodes during catastrophic optical damage. *J. Mater. Sci.: Mater Electron*, 91:S155, 2008.

[229] J. Stohs, D.J. Bossert, D.J. Gallant, and S.R.J. Brueck. Gain, refractive index change, and linewidth enhancement factor in broad-area GaAs and InGaAs quantum-well lasers. *IEEE J. Quant. Electr.*, 37(11):1449–1459, 2001.

[230] P. M. Smowton, E. J. Pearce, H. C. Schneider, W. W. Chow, and M. Hopkinson. Filamentation and linewidth enhancement factor in ingaas quantum dot lasers. *Appl. Phys. Lett.*, 81(17):3251–3253, 2002.

[231] D. H. Newman, R. F. Godfrey, A. R. Goodwin, and D. F. Lovelace. Enhanced localized degradation and anomalous emission spectra of Ga[sub 1 - x]Al[sub x]As double heterostructure lasers induced by fabrication processes. *Appl. Phys. Lett.*, 29(6):353–355, 1976.

[232] U. Imai, K. Isozumi, and M. Takusagawa. Deep level associated with the slow degradation of GaAlAs DH laser diodes. *Appl. Phys. Lett.*, 33 (4):330, 1978.

[233] S. Metz. Deep center luminescence (1.02 eV) in GaAs/(GaAl)As epitaxial layers and double-heterostructure lasers. *Appl. Phys. Lett.*, 33 (2):198–200, 1978.

[234] A. Hayat, P. Ginzburg, and M. Orenstein. Observation of two-photon emission from semiconductors. *Nat Photon*, 2(4):238, 2008.

[235] R. L. Hartman and L. A. Koszi. Characterization of (Al,Ga)As injection lasers using the luminescence emitted from the substrate. *J. Appl. Phys.*, 49(12):5731–5744, 1978.

[236] J. P. van der Ziel and R. L. Hartman. Deep-level luminescence in $Al_xGa_{1-x}As$ double-heterostructure lasers. *Appl. Phys. Lett.*, 34(8): 520–522, 1979.

[237] S. M. Abbott. Measurement of spatial distribution of long-wavelength radiation from GaAlAs injection lasers. *Appl. Phys. Lett.*, 34(11):766–768, 1979.

[238] T. Q. Tien, F. Weik, J. W. Tomm, B. Sumpf, M. Zorn, U. Zeimer, and G. Erbert. Thermal properties and degradation behavior of red-emitting high-power diode lasers. *Appl. Phys. Lett.*, 89(18):181112, 2006.

[239] T. L. Paoli. Reduction in the rate of increase of spontaneous emission from double-heterostructure injection lasers at threshold. *Appl. Phys. Let.*, 21(3):101–102, 1972.

[240] A. Maaßdorf, S. Gramlich, E. Richter, F. Brunner, M. Weyers, G. Tränkle, J. W. Tomm, Y. I. Mazur, D. Nickel, V. Malyarchuk, T. Günther, Ch. Lienau, A. Bärwolff, and T. Elsaesser. Minority-carrier kinetics in heavily doped GaAs:C studied by transient photoluminescence. *J. Appl. Phys.*, 91(8):5072–5078, 2002.

[241] F. M. Vorobkalo, D. Glinchuk, and A. V. Prokhorovich. The characteristics of the 0.93 to 1.0 eV luminescence bands in GaAs. *Phys. stat. sol. (a)*, 7(135):1170–1172, 1971.

[242] R. Enrique Viturro, Michael R. Melloch, and Jerry M. Woodall. Optical emission properties of semi-insulating GaAs grown at low temperatures by molecular beam epitaxy. *Appl. Phys. Lett.*, 60(24):3007–3009, 1992.

[243] J.L. Pan, J.E. Mcmanis, M. Gupta, M.P. Young, and J.M. Woodall. Novel deep centers for high-performance optical materials. *Appl. Phys. A*, 90:105, 2008.

[244] J. L. Pan, J. E. Mcmanis, T. Osadchy, L. Grober, J. M. Woodall, and P. J. Kindlmann. Gallium arsenide deep-level optical emitter for fibre optics. *Nature Materials*, 2:375, 2003.

[245] Jr. H. C. Casey, B. I. Miller, and E. Pinkas. Variation of minority-carrier diffusion length with carrier concentration in GaAs liquid-phase epitaxial layers. *J. Appl. Phys.*, 44(3):1281–1287, 1973.

[246] C.-M. Wu and E. S. Yang. Physical mechanisms of carrier leakage in DH injection lasers. *J. Appl. Phys.*, 49(6):3114–3117, 1978.

[247] F. Stern and J.M. Woodall. Photon recycling in semiconductor lasers. *J. Appl. Phys.*, 45(9):3904–3906, 1974.

[248] P. Asbeck. Self-absorption effects on the radiative lifetime in GaAs-GaAlAs double heterostructures. *J. Appl. Phys.*, 48(2):820–822, 1977.

[249] J.P. Bergman, C. Hallin, and E. Janzen. Temperature and doping dependence of the photon recycling effect in GaAs-GaAlAs heterostructures. *J. Appl. Phys.*, 77(9):4611–4615, 1995.

[250] D. Pierscinska, A. Kozlowska, K. Pierscinski, M. Bugajski, J. W. Tomm, M. Ziegler, and F. Weik. Thermal processes in high-power laser bars investigated by spatially resolved thermoreflectance. *J. Mater. Sci.: Mater Electron*, 19:S150, 2008.

[251] M. Ziegler, J. W. Tomm, T. Elsaesser, C. Matthiesen, M. Bou Sanayeh, and P. Brick. Real-time thermal imaging of catastrophic optical damage in red-emitting high-power diode lasers. *Appl. Phys. Lett.*, 92(10): 103514, 2008.

[252] D. Masanotti, F. Causa, F. Weik, M. Ziegler, and J. W. Tomm. Analysis of mechanical strain and temperature profiling in high-brightness parabolic bow-tie laser arrays. *Proc. SPIE*, 6368:63680Y, 2006.

[253] I. C. Noyan, P.-C. Wang, S. K. Kaldor, and J. L. Jordan-Sweet. Deformation field in single-crystal fields semiconductor substrates caused by metallization features. *Appl. Phys. Lett.*, 74(16):2352–2354, 1999.

[254] J. W. Tomm, T. Q. Tien, and D. T. Cassidy. Spectroscopic strain measurement methodology: Degree-of-polarization photoluminescence versus photocurrent spectroscopy. *Appl. Phys. Lett.*, 88(13):133504, 2006.

Appendix

A. Emittance of Semiconductors

This Appendix derives an expression for the emittance of the semitransparent semiconductor samples of section 3.1. The used subscripts S, H, N, E, D, and BB denote contributions from the sample, the sample holder, the Nextel reference area behind the sample, the enclosure, the detector, and the blackbody-reference radiator.

Starting with the measurement of the sample in the sample holder, the corresponding FTIR signal is given by

$$\begin{aligned} S_\mathrm{S}(\nu, T_\mathrm{S}, T_\mathrm{H}, T_\mathrm{N}, T_\mathrm{E}, T_\mathrm{D}) = s_\mathrm{D}(\nu)\Omega F\Big[&A\epsilon_\mathrm{S}(\nu)L_\mathrm{BB}(\nu, T_\mathrm{S}) \\ &+ (1-A)\epsilon_\mathrm{H}(\nu)L_\mathrm{BB}(\nu, T_\mathrm{H}) \\ &+ A\widetilde{\tau}_\mathrm{S}(\nu)\epsilon_\mathrm{N}(\nu)L_\mathrm{BB}(\nu, T_\mathrm{N}) \\ &+ \{A\widetilde{\varrho}_\mathrm{S}(\nu) + (1-A)\widetilde{\varrho}_\mathrm{H}(\nu)\}\epsilon_\mathrm{E}L_\mathrm{BB}(\nu, T_\mathrm{E}) \\ &- \epsilon_\mathrm{D}L_\mathrm{BB}(\nu, T_\mathrm{D})\Big] . \end{aligned} \tag{1}$$

For the sample holder without sample the signal is

$$\begin{aligned} S_\mathrm{H}(\nu, T_\mathrm{H}, T_\mathrm{N}, T_\mathrm{E}, T_\mathrm{D}) = s_\mathrm{D}(\nu)\Omega F\Big[&A\epsilon_\mathrm{N}(\nu)L_\mathrm{BB}(\nu, T_\mathrm{N}) \\ &+ (1-A)\epsilon_\mathrm{H}(\nu)L_\mathrm{BB}(\nu, T_\mathrm{H}) \\ &+ \{A\widetilde{\varrho}_\mathrm{N}(\nu) + (1-A)\widetilde{\varrho}_\mathrm{H}(\nu)\}\epsilon_\mathrm{E}L_\mathrm{BB}(\nu, T_\mathrm{E}) \\ &- \epsilon_\mathrm{D}L_\mathrm{BB}(\nu, T_\mathrm{D})\Big] . \end{aligned} \tag{2}$$

The temperatures of the enclosure T_E and the detector T_D are kept constant during the measurements and, thus, are omitted in the following equations for S. Their emittances ϵ_E and ϵ_D were determined in independent measurements to be 0.97, independent of the wavelength.[173]

The net signal from the sample is given by

$$\begin{aligned} S_\mathrm{S}(\nu, T_\mathrm{S}, T_\mathrm{H}, T_\mathrm{N}) - S_\mathrm{H}(\nu, T_\mathrm{H}, T_\mathrm{N}) = {} & A s_\mathrm{D}(\nu) \Omega F \Big[\epsilon_\mathrm{S}(\nu) L_\mathrm{BB}(\nu, T_\mathrm{S}) \\ & + \{\widetilde{\tau}_\mathrm{S}(\nu) - 1\} \epsilon_\mathrm{N}(\nu) L_\mathrm{BB}(\nu, T_\mathrm{N}) \\ & + \{\widetilde{\varrho}_\mathrm{S}(\nu) - \widetilde{\varrho}_\mathrm{N}(\nu)\} \epsilon_\mathrm{E} L_\mathrm{BB}(\nu, T_\mathrm{E}) \Big] . \end{aligned} \tag{3}$$

The emittance $\epsilon_\mathrm{N}(\nu)$ and the reflectance $\widetilde{\varrho}_\mathrm{N}(\nu)$ of the reference area behind the semiconductor are related by $\widetilde{\varrho}_\mathrm{N}(\nu) = 1 - \epsilon_\mathrm{N}(\nu)$. $\epsilon_\mathrm{N}(\nu)$ is determined in an independent experiment without the sample and the sample holder where the measured signal is given by

$$\begin{aligned} S_\mathrm{N}(\nu, T_\mathrm{N}) = {} & s_\mathrm{D}(\nu) \Omega F \Big[\epsilon_\mathrm{N}(\nu) L_\mathrm{BB}(\nu, T_\mathrm{N}) \\ & + \widetilde{\varrho}_\mathrm{N}(\nu) \epsilon_\mathrm{E} L_\mathrm{BB}(\nu, T_\mathrm{E}) - \epsilon_\mathrm{D} L_\mathrm{BB}(\nu, T_\mathrm{D}) \Big] . \end{aligned} \tag{4}$$

The signal gained from a blackbody-reference radiator with emittance of 0.9997 - in the following replaced by a value of 1 - is given by

$$S_\mathrm{BB}(\nu, T_\mathrm{BB}) = s_\mathrm{D}(\nu) \Omega F \Big[L_\mathrm{BB}(\nu, T_\mathrm{BB}) - \epsilon_\mathrm{D} L_\mathrm{BB}(\nu, T_\mathrm{D}) \Big] . \tag{5}$$

Resolving the ratio of $S_\mathrm{N}(\nu, T_\mathrm{N}) / S_\mathrm{BB}(\nu, T_\mathrm{BB})$ for the emittance $\epsilon_\mathrm{N}(\nu)$ yields

$$\begin{aligned} \epsilon_\mathrm{N}(\nu) = {} & \frac{S_\mathrm{N}(\nu, T_\mathrm{N})}{S_\mathrm{BB}(\nu, T_\mathrm{BB})} \times \frac{L_\mathrm{BB}(\nu, T_\mathrm{BB}) - \epsilon_\mathrm{D} L_\mathrm{BB}(\nu, T_\mathrm{D})}{L_\mathrm{BB}(\nu, T_\mathrm{N}) - \epsilon_\mathrm{E} L_\mathrm{BB}(\nu, T_\mathrm{E})} \\ & + \frac{\epsilon_\mathrm{D} L_\mathrm{BB}(\nu, T_\mathrm{D}) - \epsilon_\mathrm{E} L_\mathrm{BB}(\nu, T_\mathrm{E})}{L_\mathrm{BB}(\nu, T_\mathrm{N}) - \epsilon_\mathrm{E} L_\mathrm{BB}(\nu, T_\mathrm{E})} . \end{aligned} \tag{6}$$

As a next step, the quantity A of Eq. (3), the sample-related fraction of the area seen by the detector, is determined in a series of measurements without the sample. There the temperature of the reference area is varied from T_N to T'_N while all other temperatures are kept constant. Consequently, the difference signal yields

$$\begin{aligned} S_\mathrm{H}(\nu, T_\mathrm{H}, T_\mathrm{N}) - S_\mathrm{H}(\nu, T_\mathrm{H}, T'_\mathrm{N}) = {} & A s_\mathrm{D}(\nu) \Omega F \epsilon_\mathrm{N}(\nu) \\ & \times \left[L_\mathrm{BB}(\nu, T_\mathrm{N}) - L_\mathrm{BB}(\nu, T'_\mathrm{N}) \right] , \end{aligned} \tag{7}$$

from which A is derived as:

$$A = \frac{S_\mathrm{H}(\nu, T_\mathrm{H}, T_\mathrm{N}) - S_\mathrm{H}(\nu, T_\mathrm{H}, T'_\mathrm{N})}{s_\mathrm{D}(\nu) \Omega F \epsilon_\mathrm{N}(\nu) \left[L_\mathrm{BB}(\nu, T_\mathrm{N}) - L_\mathrm{BB}(\nu, T'_\mathrm{N}) \right]} . \tag{8}$$

Analogously, measurements with the sample yield the signal difference

$$\begin{aligned} S_\mathrm{S}(\nu, T_\mathrm{S}, T_\mathrm{H}, T_\mathrm{N}) - S_\mathrm{S}(\nu, T_\mathrm{S}, T_\mathrm{H}, T'_\mathrm{N}) = {} & \widetilde{\tau}_\mathrm{S}(\nu) A s_\mathrm{D}(\nu) \Omega F \epsilon_\mathrm{N}(\nu) \\ & \times \left[L_\mathrm{BB}(\nu, T_\mathrm{N}) - L_\mathrm{BB}(\nu, T'_\mathrm{N}) \right] \\ = {} & \widetilde{\tau}_\mathrm{S}(\nu) \left[S_\mathrm{H}(\nu, T_\mathrm{H}, T_\mathrm{N}) - S_\mathrm{H}(\nu, T_\mathrm{H}, T'_\mathrm{N}) \right] \end{aligned} \tag{9}$$

from which the transmittance of the sample is found as a function of four measured signals

$$\widetilde{\tau}_{\mathrm{S}}(\nu) = \frac{S_{\mathrm{S}}(\nu, T_{\mathrm{S}}, T_{\mathrm{H}}, T_{\mathrm{N}}) - S_{\mathrm{S}}(\nu, T_{\mathrm{S}}, T_{\mathrm{H}}, T'_{\mathrm{N}})}{S_{\mathrm{H}}(\nu, T_{\mathrm{H}}, T_{\mathrm{N}}) - S_{\mathrm{H}}(\nu, T_{\mathrm{H}}, T'_{\mathrm{N}})} \,. \tag{10}$$

As a final result, the sample emittance is found from rearranging Eq. (3) and inserting Eq. (8) as

$$\begin{aligned} \epsilon_{\mathrm{S}}(\nu) = {} & \frac{\epsilon_{\mathrm{N}}(\nu)}{L_{\mathrm{BB}}(\nu, T_{\mathrm{S}}) - L_{\mathrm{BB}}(\nu, T_{\mathrm{E}})} \\ & \times \left\{ \frac{S_{\mathrm{S}}(\nu, T_{\mathrm{S}}, T_{\mathrm{H}}, T_{\mathrm{N}}) - S_{\mathrm{H}}(\nu, T_{\mathrm{H}}, T_{\mathrm{N}})}{S_{\mathrm{H}}(\nu, T_{\mathrm{H}}, T_{\mathrm{N}}) - S_{\mathrm{H}}(\nu, T_{\mathrm{H}}, T'_{\mathrm{N}})} \left[L_{\mathrm{BB}}(\nu, T_{\mathrm{N}}) - L_{\mathrm{BB}}(\nu, T'_{\mathrm{N}}) \right] \right. \\ & \left. - L_{\mathrm{BB}}(\nu, T_{\mathrm{N}}) [\widetilde{\tau}_{\mathrm{S}}(\nu) - 1] - L_{\mathrm{BB}}(\nu, T_{\mathrm{E}}) \left[1 - \frac{\widetilde{\tau}_{\mathrm{S}}(\nu)}{\epsilon_{\mathrm{N}}(\nu)} \right] \right\} . \end{aligned} \tag{11}$$

B. Quantitative Lock-In Correlation

This Appendix provides points in time corresponding to a certain transient situation measured by synchronous undersampling lock-in thermography in section 4.2.3. Such points are used for comparison with data from a transient FEM simulation in section 4.3.1.

A minimal number of frames is necessary for high temporal resolution in lock-in thermography. The present setup provides four frames correlated with a rectangular correlation function. The summation in Eq. (4.9) for the case $\tau_{\mathrm{PW}} \sim 2\,\mathrm{IT}$ is approximately an integral over time leading to one image essentially averaged over the whole pulse (with weighting function K).

In order to compare such an image with FEM-simulation data, the corresponding point in time for the simulation needs to be specified. Thus, the mentioned correlation is simulated by summing the product of the FEM data for the active layer and the correlation function over a single pulse according to Eq. (4.9) (compare representative results in Fig. 1). As a result, the FEM data corresponding to 15 μs and 11 ms after turn on of the laser current describes best the transient thermal situation as measured by the lock-in experiment with 110 μs and 69 ms long pulses, respectively.

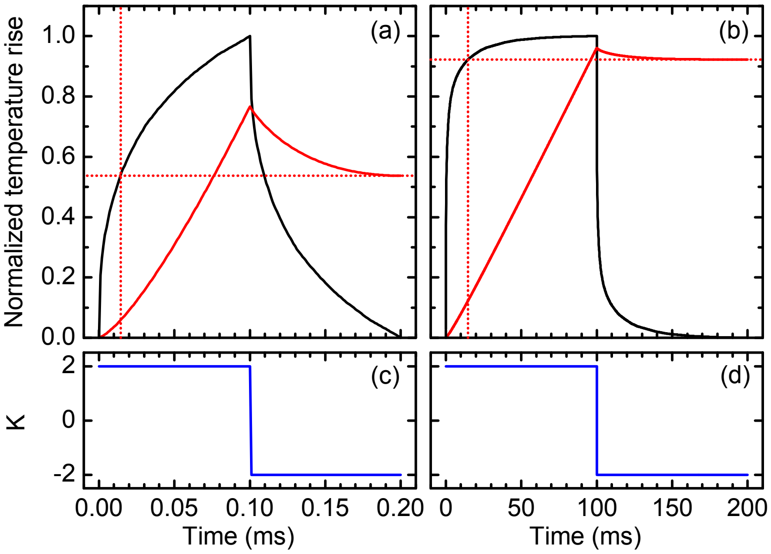

Figure 1: **(a,b)** Normalized temperature rise (solid black lines) of the active region at the device center, obtained from FEM simulations and the cumulative sum (solid red line) given by its correlation with rectangular correlation functions displayed in **(c,d)**. Pulse widths of **(a)** 100 μs and **(b)** of 100 ms are used. Dotted horizontal lines mark the sums. Dotted vertical lines mark the points in time that correspond to the measured lock-in magnitudes: 14 μs for (a) and 15 ms for (b).

C. Lumped Capacitance Method

This Appendix provides a derivation of the lumped capacitance method for a ladder of n capacitances. Starting with Eq. (5.1) from section 5.1

$$P_{\mathrm{i}}(t) = m_{\mathrm{i}} C_{\mathrm{i}} \frac{\partial T_{\mathrm{i}}(t)}{\partial t} = P_{\mathrm{i-1 \to i}}(t) - P_{\mathrm{i \to i+1}}(t) = P_{\mathrm{i-1 \to i}}(t) - \frac{T_{\mathrm{i}}(t) - T_{\mathrm{i+1}}(t)}{R_{\mathrm{th,i \to i+1}}} \, . \tag{12}$$

The solution to this equation is given by

$$T_{\mathrm{i}}(t) = T_{\mathrm{i+1}}(t) + P_{\mathrm{i-1 \to i}}(t) R_{\mathrm{th,i \to i+1}} \left(1 - e^{-t/\tau_{\mathrm{i}}}\right) \, . \tag{13}$$

where the time constant is defined as $\tau_i = R_{\mathrm{th,i \to i+1}} m_{\mathrm{i}} C_{\mathrm{i}}$. Hence, the temperature evolution of every stage is bound to its neighboring stages until the last stage at a fixed temperature (e.g., the heat sink) $T_{\mathrm{n}}(t) = T_{\mathrm{n}}$.

From such recursive expressions one derives the temperature of the first stage as

$$T_1(t) = T_n + \sum_{\mathrm{i}=1}^{n-1} P_{\mathrm{i-1 \to i}}(t) R_{\mathrm{th,i \to i+1}} \left(1 - e^{-t/\tau_{\mathrm{i}}}\right) \tag{14}$$

and of the retarded $P_{\mathrm{gen}} = P_{0 \to 1}$ as

$$P_{\mathrm{i-1 \to i}}(t) = P_{\mathrm{gen}} \prod_{\mathrm{j}=1}^{\mathrm{i}-1} \left(1 - e^{-t/\tau_{\mathrm{j}}}\right) \, . \tag{15}$$

This expression can be further simplified in case of a limited number of sufficiently well separated thermal time constants, i.e., $\tau_{\mathrm{i-1}} \ll \tau_{\mathrm{i}}$. Then the impact of the preceding stage as the heat source for the subsequent stage can be regarded as instantaneous, that is

$$P_{\mathrm{i-1 \to i}}(t) \left(1 - e^{-t/\tau_{\mathrm{i}}}\right) = P_{\mathrm{gen}} \prod_{\mathrm{j}=1}^{\mathrm{i}} \left(1 - e^{-t/\tau_{\mathrm{j}}}\right) \approx P_{\mathrm{gen}} \left(1 - e^{-t/\tau_{\mathrm{i}}}\right) \, . \tag{16}$$

Finally, inserting Eq. (16) into Eq. (14) and introducing $T_{\mathrm{i}}^{*} = P_{\mathrm{gen}} R_{\mathrm{th,i \to i+1}}$ yields a simplified formula for the evolution of the temperature increase of an n-staged system as a sum of exponential temperature increases:

$$\Delta T_1(t) = T_1(t) - T_{\mathrm{n}} = \sum_{\mathrm{i}=1}^{\mathrm{n}-1} T_{\mathrm{i}}^{*} \left(1 - e^{-t/\tau_{\mathrm{i}}}\right) \, . \tag{17}$$

D. Correlation of Hot-Spots with Facet Damages

This Appendix provides an overview of representative examples for the correlation of hot-spots measured in the MIR and NIR spectral range with front-facet damages or anomalies obtained from micrographs (100× magnification). The occurrence of hot-spots or anomalies in Figs. 2-6 is indicated by arrows. Table 1 lists the observed cases and gives the frequency of observation relative to the number of hot-spots. The visual inspection of the front has only been performed if a hot-spot was observed.

Table 1: Correlation of hot-spots detected in the MIR and NIR spectral range with front facet damages observed with a microscope. ● means observed, ○ not observed.

Case	Relative probability	MIR hot-spot	NIR hot-spot	Facet damage
1	0.43	○	●	○
2	0.30	●	○	●
3	0.12	●	●	●
4	0.10	●	○	○
5	0.04	●	●	○
6	0.01	○	●	●

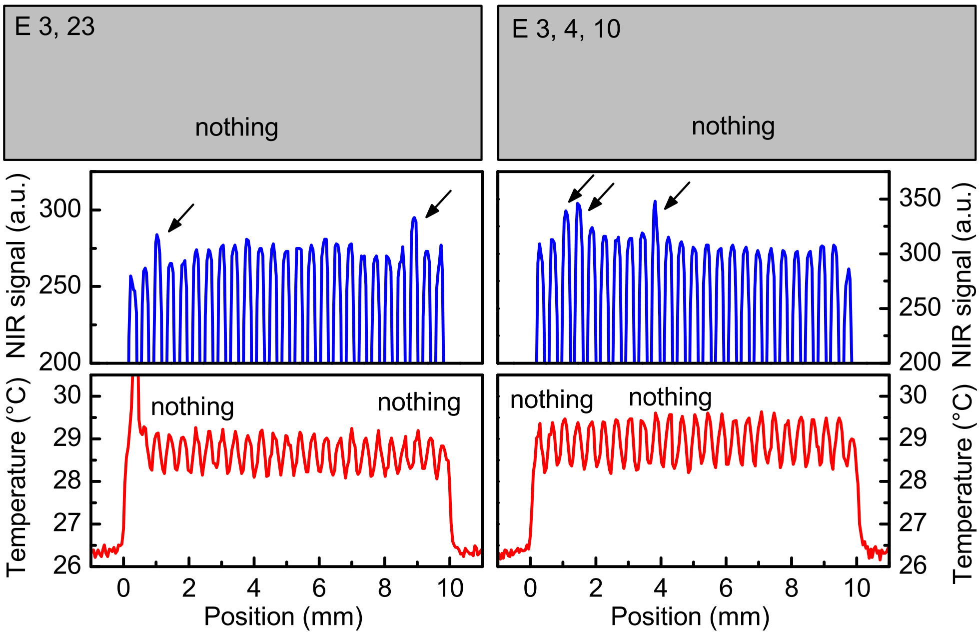

Figure 2: Case 1: NIR hot-spot and no facet anomaly/damage.

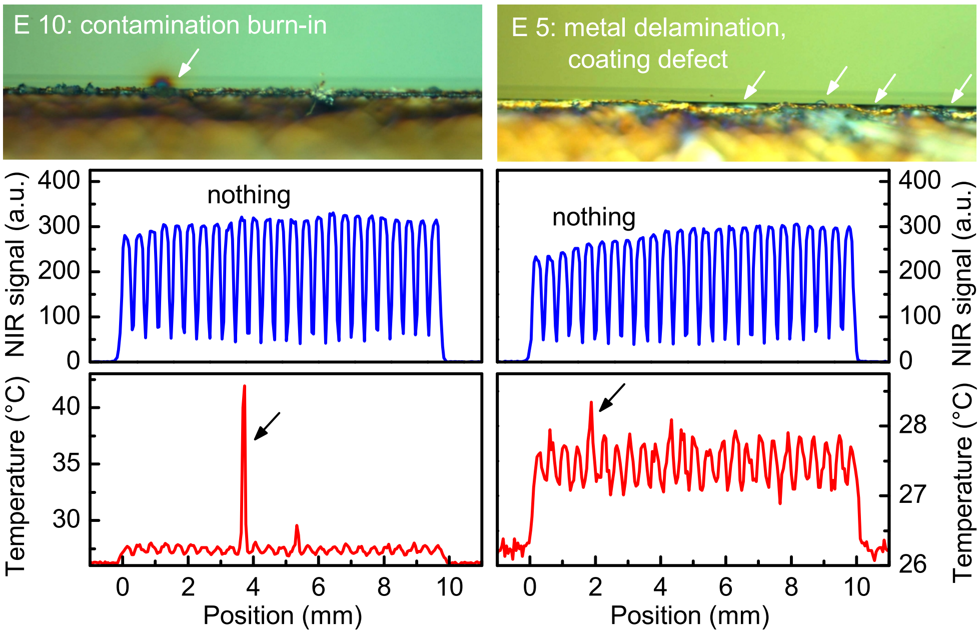

Figure 3: Case 2: MIR hot-spot and facet anomaly/damage.

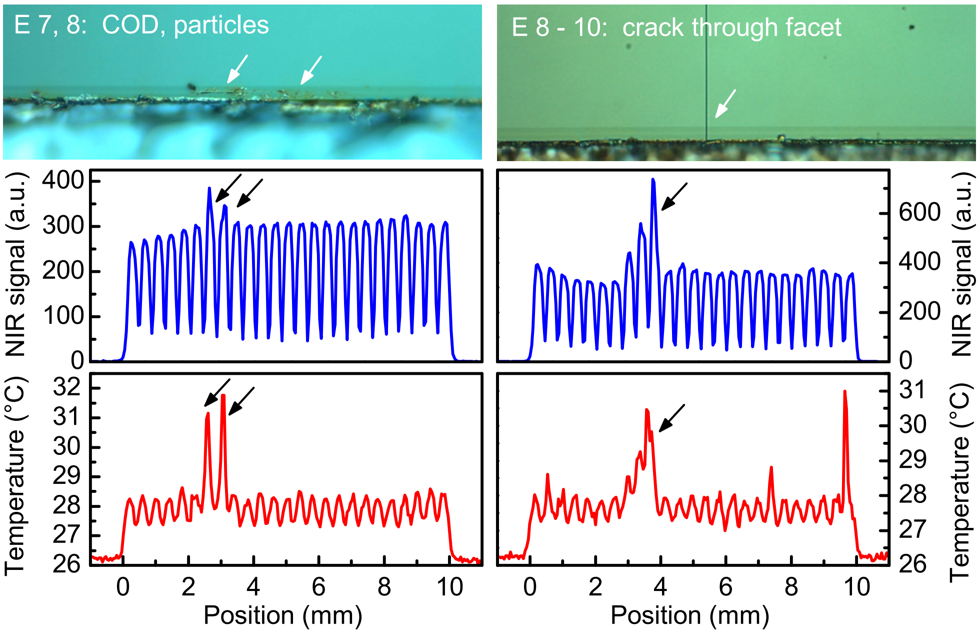

Figure 4: Case 3: NIR hot-spot and MIR hot-spot and facet anomaly/damage.

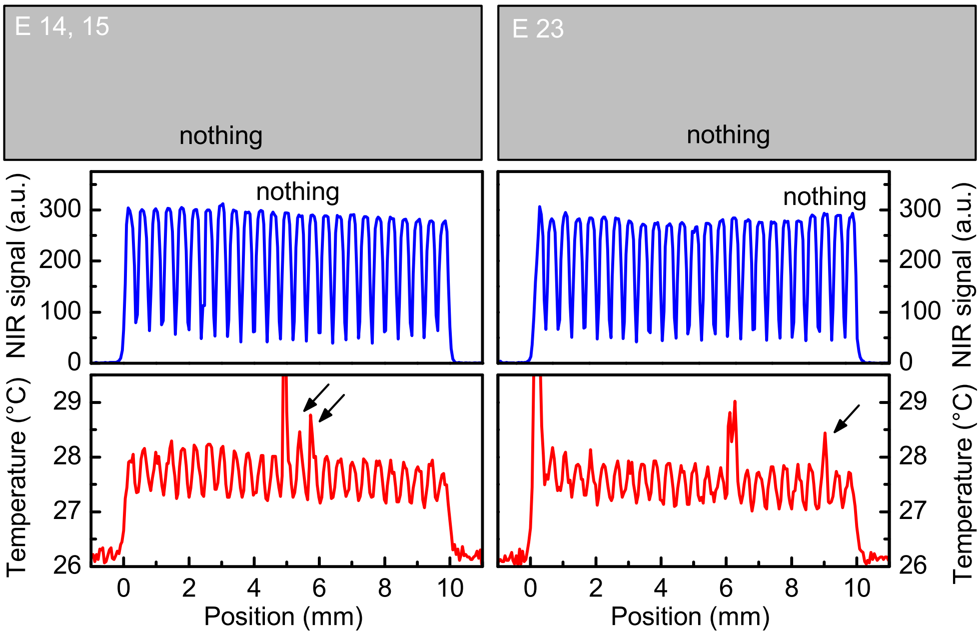

Figure 5: Case 4: MIR hot-spot and no facet anomaly/damage.

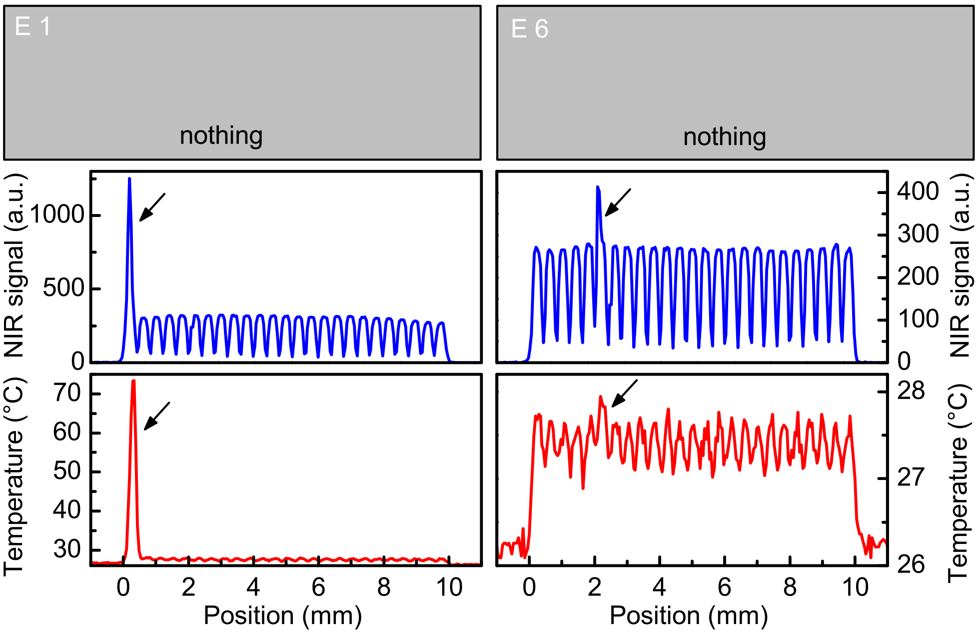

Figure 6: Case 5: NIR hot-spot and MIR hot-spot and no facet anomaly/damage.

E. Spatial Model for IR Substrate Emission

The model for the red-emitting laser in Fig. 5.20(b) should be compared to the measured spatio-spectral characteristic in Fig. 5.20(a). The two-staged photon recycling leading to B3 is modeled as a spatial convolution of the QW excitation (QW), the intermediate interband excitation (B2), and the decay of the DL luminescence (B3) with distance d from the QW. The spatial characteristic of the normalized intensity (analogous to assuming complete energy transfer) can be approximated by the following expression

$$A_{\mathrm{B3}}(d,\nu) = e^{-\alpha(\nu)d}\left(1 - e^{-\alpha(\nu_{\mathrm{B2}})d}\right)\left(1 - e^{-\alpha(\nu_{\mathrm{QW}})d}\right) . \tag{18}$$

Here, the exciting contributions (QW, B2) are characterized by effective absorption coefficients $\alpha(\nu_{\mathrm{B2}}) = 300\ \mathrm{cm}^{-1}$ and $\alpha(\nu_{\mathrm{QW}}) = 35000\ \mathrm{cm}^{-1}$ according to average photon energies $h\nu_{\mathrm{QW}} = 1.91$ eV and $h\nu_{\mathrm{B2}} = 1.41$. The $\alpha(h\nu)$ are taken from Ref. 147 for $N = 2 \times 10^{18}\ \mathrm{cm}^{-3}$.

For each point of the 60 μm scan along x [Fig. 5.19(b)] above the laser surface this relation needs to be integrated along the whole resonator length taking into account partial transmittance at the GaAs/air interface. The domain of integration is the angle ϕ_{i} (where $\sin\phi_{\mathrm{i}} = x/d$) formed by the rays starting along the resonator axis and escaping out the front facet and the surface normal at this exit point. For a single pass through the substrate the characteristic of B3 is approximated by:

$$L(x,\nu)_{\mathrm{B3}} = \int_{\phi_{\min}(x)}^{\phi_{\max}(x)} T(\phi_{\mathrm{i}}, n_{\mathrm{i}}, n_{\mathrm{e}}) A_{\mathrm{B3}}(x, \phi_{\mathrm{i}}, \nu) d\phi_{\mathrm{i}} , \tag{19}$$

with the transmittance averaged over perpendicularly and normally polarized emission powers given by Fresnel's formulae:

$$T(\phi_{\mathrm{i}}, n_{\mathrm{i}}, n_{\mathrm{e}}) = 2n_{\mathrm{i}}^2 \cos\phi_{\mathrm{e}} \cos^2\phi_{\mathrm{i}}[(n_{\mathrm{i}}\cos\phi_{\mathrm{i}} + \cos\phi_{\mathrm{e}})^{-2} + (n_{\mathrm{i}}\cos\phi_{\mathrm{e}} + \cos\phi_{\mathrm{i}})^{-2}]. \tag{20}$$

The angle in air ($n_{\mathrm{e}} = 1$) is $\cos\phi_{\mathrm{e}} = \sqrt{1 - (n_{\mathrm{i}}\sin\phi_{\mathrm{i}})^2}$, given by the refractive index of GaAs $n_{\mathrm{i}} = 3.5$. The integration limits $\phi_{\min}(x) = \arctan(x/l_y)$ and $\phi_{\max}(x) = \arcsin(1/n_{\mathrm{i}}) \approx 17°$ in Eq. (19) are given for each position (x) by the cavity length ($l_y = 1.2$ mm) and the total angle for internal reflection[1] [TIR in Fig. 5.19(b)].

$L(x,\nu)_{\mathrm{B3}}$ [Eq. (19)] is normalized for each wavelength taking into account the spectral dependence of the absorption coefficient and plotted in Fig. 5.20(b).

---

[1] Since in the long-range line scans the tip was held $d \sim 4\ \mu\mathrm{m} > \lambda$ above the laser facet, i.e., outside the near-field, total internal reflection must be taken into account.

F. Abbreviations and Symbols

Abbreviations

0D-3D	zero-dimensional - three-dimensional
AR	Anti-reflection
BA	Broad area
CB	Conduction band
CCD	Charge-coupled device
COD	Catastrophic optical damage
CTE	Coefficient of thermal expansion
cw	Continuous wave
DL	Deep level
DTGS	Deuterated Tri-Glycine Sulfate
FCA	Free-carrier absorption
FEM	Finite element method
FTIR	Fourier-transform infrared
HR	High-reflection
IR	Infrared
LBIC	Laser-beam-induced current
MIR	Mid-infrared
MOVPE	Metal-organic vapor phase epitaxy
NF	Near-field
NIR	Near-infrared
NSOM	Near-field scanning optical microscopy
PCS	Photocurrent spectroscopy
PL	Photoluminescence
QD, QW	Quantum dot, quantum well
VB	Valence band
WPE	Wall-plug efficiency

Abbreviations for semiconductor alloys

HgCdTe	$\mathrm{Hg}_{1-x}\mathrm{Cd}_x\mathrm{Te}$
AlGaAs	$\mathrm{Al_xGa_{1-x}As}$
AlGaInAs	$\mathrm{Al_xGa_yIn_{1-x-y}As}$
AlGaInP	$\mathrm{Al_xGa_yIn_{1-x-y}P}$
AlInP	$\mathrm{Al_xIn_{1-x}P}$
GaInP	$\mathrm{Ga_xIn_{1-x}P}$
GaAsP	$\mathrm{GaAs_xP_{1-x}}$

List of Symbols

This is a list of the symbols for the text. Some symbols that are used in only a local development are not included here. In addition, typical units of the symbols are indicated.

$\widetilde{a}$	Absorbance, nondimensional
c	Speed of light in vacuum, m s^{-1}
C	Specific heat, J kg^{-1} K^{-1}
e	Elementary charge, C
E	Energy, J or eV
E_{g}	Band gap Energy, eV
F_{e}	Quasi Fermi energy for electrons, eV
F_{h}	Quasi Fermi energy for holes, eV
h	Planck's constant, J s
$\hbar$	Reduced Planck's constant, J s
I	Intensity, W m^{-2}
I	Injection current, A
I_{th}	Threshold current, A
k	Boltzmann constant, J K^{-1}
k	Wave vector, m^{-1}
L	Radiance, W m^{-2} sr^{-1} s
m_{e}	Electron mass, kg
m_c^*	Electron effective mass in the CB, kg
n	Real refractive index, nondimensional
N	Electron or hole concentration, cm^{-3}
P	Power, W
P_{out}	Optical output power, W
R	Reflectance, nondimensional
R_{th}	Thermal resistance, K W^{-1}
s_{D}	Detector responsivity, arb.u.
S	Signal, arb.u.
t	Time, s
T	Temperature, K or °C
U	Voltage, V

Greek Symbols

α	Absorption coefficient, cm^{-1}
ε	Complex dielectric function, nondimensional
ε_0	Vacuum permittivity, $\mathrm{F\ m}^{-1}$
ε_∞	High frequency dielectric constant, nondimensional
ϵ	Emittance, nondimensional
λ	Wavelength, nm or μm
λ_T	Thermal conductivity, $\mathrm{W\ m}^{-1}\ \mathrm{K}^{-1}$
ν	(Photon) frequency, eV/h
π	Circular constant, nondimensional
$\widetilde{\varrho}$	Reflectance, nondimensional
σ	Stefan-Boltzmann constant, $\mathrm{W\ m}^{-2}\ \mathrm{K}^{-4}$
σ	Absorption cross-section, cm^2
τ	Time constant or period, s
τ	Transmissivity, nondimensional
$\widetilde{\tau}$	Transmittance, nondimensional
$\mathit{\Phi}_\nu$	Spectral radiant power, W s
Ω	Solid angle, sr

Publications

Publications Related to this Thesis

1. M. Ziegler, J. W. Tomm, D. Reeber, T. Elsaesser, U. Zeimer, H. E. Larsen, P. M. Petersen, and P. E. Andersen, "Catastrophic optical mirror damage in diode lasers monitored during single-pulse operation," *Appl. Phys. Lett.*, 94(19), 191101, 2009.

2. J. W. Tomm, M. Ziegler, V. Talalaev, C. Matthiesen, T. Elsaesser, M. Bou Sanayeh, P. Brick, H. Koenig, M. Reufer, "New approaches towards the understanding of the catastrophic optical damage process in in-plane diode lasers," *Proc. SPIE*, 72300V, 2009.

3. J. Mukherjee, M. Ziegler, J. LeClech, J. W. Tomm, B. Corbett, J. G. Mclnerney, J. P. Reithmaier, S. Deubert, A. Forchel, "Bulk temperature mapping of broad area quantum dot lasers: modeling and micro-thermographic analysis," *Proc. SPIE*, 72300W, 2009.

4. J. W. Tomm, M. Ziegler, M. Oudart, J. Nagle, and J. Jimenez, "Gradual degradation of GaAs-based quantum well lasers, creation of defects, and generation of compressive strain," *Phys. Stat. Sol. (c)*, In press, 2009.

5. J. LeClech, M. Ziegler, J. Mukherjee, J. W. Tomm, T. Elsaesser, J.-P. Landesman, B. Corbett, J. G. Mclnerney, J. P. Reithmaier, S. Deubert, A. Forchel, W. Nakwaski, and R. P. Sarzała, "Micro-thermography of diode lasers: The impact of light propagation on image formation," *J. Appl. Phys.*, 105(1), 014502, 2009.

6. M. Ziegler, R. Pomraenke, M. Felger, J. W. Tomm, C. Lienau, M. Bou Sanayeh, A. Gomez-Iglesias, M. Reufer, F. Bugge, G. Erbert, "Infrared emission from the substrate of GaAs-based semiconductor lasers," *Appl. Phys. Lett.*, 93(4), 041101, 2008.

7. M. Ziegler, J. W. Tomm, T. Elsaesser, C. Monte, J. Hollandt, H. Kissel, and J. Biesenbach, "Cavity-enhanced thermal emission from semiconductor lasers," *J. Appl. Phys.*, 103(10), 104508, 2008.

8. M. Ziegler, V. Talalaev, J. W. Tomm, T. Elsaesser, P. Ressel, B. Sumpf, and G. Erbert, "Surface recombination and facet heating in high-power diode lasers," *Appl. Phys. Lett.*, 92(20), 203506, 2008.

9. M. Bou Sanayeh, P. Brick, W. Schmid, B. Mayer, M. Müller, M. Reufer, K. Streubel, M. Ziegler, J. W. Tomm, and G. Bacher, "The physics of catastrophic optical damage in high-power AlGaInP laser diodes," *Proc. SPIE*, 6997, 699703, 2008.

10. M. Ziegler, J. W. Tomm, T. Elsaesser, C. Matthiesen, M. Bou Sanayeh, and P. Brick, "Real-time thermal imaging of catastrophic optical damage in red-emitting high-power diode lasers," *Appl. Phys. Lett.*, 92(10), 103514, 2008.

11. M. Ziegler, J. W. Tomm, T. Elsaesser, G. Erbert, F. Bugge, W. Nakwaski, and Robert P. Sarzała, "Visualization of heat flows in high-power diode lasers by lock-in thermography," *Appl. Phys. Lett.*, 92(10), 103513, 2008.

12. D. Pierscinska, A. Kozlowska, K. Pierscinski, M. Bugajski, J. W. Tomm, M. Ziegler, and F. Weik, "Thermal processes in high-power laser bars investigated by spatially resolved thermoreflectance," *J. Mater. Sci.*, 19, S150, 2008.

13. M. Ziegler, J. W. Tomm, F. Weik, T. Elsaesser, C. Monte, J. Hollandt, H. Kissel, G. Seibold, and J. Biesenbach, "Accurate determination of absolute temperatures of GaAs based high-power diode lasers," *Proc. SPIE*, 6876, 68761A, 2008.

14. J. W. Tomm, M. Ziegler, T. Q. Tien, F. Weik, P. Hennig, J. Meusel, H. Kissel, G. Seibold, J. Biesenbach, G. Groenninger, G. Herrmann, and U. Strauß, "Screening of high power laser diode bars in terms of stresses and thermal profiles," *Proc. SPIE*, 6876, 687619, 2008.

15. A. Kozlowska, M. Ziegler, J. W. Tomm, R. P. Sarzała, and W. Nakwaski, "Thermal imaging of actively cooled high-power laser bars," *Mixed Design of Integrated Circuits and Systems, 2007, MIXDES'07*, pages 396–400, 2007.

16. M. Ziegler, T. Q. Tien, S. Schwirzke-Schaaf, J. W. Tomm, B. Sumpf, G. Erbert, M. Oudart, and J. Nagle, "Gradual degradation of red-emitting high-power diode laser bars," *Appl. Phys. Lett.*, 90(17), 171113, 2007.

17. J. W. Tomm, T. Q. Tien, M. Ziegler, F. Weik, B. Sumpf, M. Zorn, U. Zeimer, and G. Erbert, "Degradation behavior and thermal properties of red (650 nm) high-power diode single emitters and laser bars," *Proc. SPIE*, 6456(1), 645606, 2007.

18. M. Ziegler, F. Weik, J. W. Tomm, T. Elsaesser, W. Nakwaski, R. P. Sarzała, D. Lorenzen, J. Meusel, and A. Kozlowska, "Transient thermal properties of high-power diode laser bars," *Appl. Phys. Lett.*, 89(26), 263506, 2006.

19. D. Masanotti, F. Causa, F. Weick, M. Ziegler, and J. W. Tomm, "Analysis of mechanical strain and temperature profiling in high-brightness parabolic bow-tie laser arrays," *Proc. SPIE*, 6368, 63680Y, 2006.

Other Publications

1. M. Wienold, M. P. Semtsiv, I. Bayrakli, W. T. Masselink, M. Ziegler, K. Kennedy, and R. Hogg, "Optical and thermal characteristics of narrow-ridge quantum-cascade lasers," *J. Appl. Phys.*, 103(8), 083113, 2008.

2. W. T. Masselink, M. P. Semtsiv, S. Dressler, M. Ziegler, and M. Wienold, "Physics, growth, and performance of (In,Ga)As-AlP/InP quantum-cascade lasers emitting at $\lambda < 4\mu$m," *Phys. Stat. Sol. (a)*, 244(8), 2906, 2007.

3. M. P. Semtsiv, S. Dressler, U. Müller, S. Knigge, M. Ziegler, and W. T. Masselink, "Proton-implanted shallow-ridge quantum-cascade laser," *IEEE J. Quant. Electr.*, 42(5), 490, 2006.

4. M. P. Semtsiv, M. Ziegler, W. T. Masselink, N. Georgiev, T. Dekorsy, and M. Helm, "Near-infrared intersubband transitions in InGaAs–AlAs–InAlAs double quantum wells," *J. Appl. Phys.*, 97(11), 113538, 2005.

5. W. T. Masselink, M. P. Semtsiv, S. Dressler, M. Ziegler, N. Georgiev, T. Dekorsy, and M. Helm, "High-power short-wavelength quantum cascade lasers," *Proc. SPIE*,5738, 13, 2005.

6. O. Drachenko, J. Galibert, J. Leotin, J. W. Tomm, M. P. Semtsiv, M. Ziegler, S. Dressler, U. Müller, and W. T. Masselink, "Electron-optical-phonon interaction in the $In_{0.73}Ga_{0.27}As$-AlAs intersubband laser," *Appl. Phys. Lett.*, 87(7), 072104, 2005.

7. M. P. Semtsiv, M. Ziegler, S. Dreßler, W. T. Masselink, N. Georgiev, T. Dekorsy, and M. Helm, "Strain-compensated AlAs/(In,Ga)As heterostructures for short-wavelength intersubband absorption and laser emission," *J. Cryst. Growth*, 278, 526, 2005.

8. M. P. Semtsiv, M. Ziegler, S. Dressler, W. T. Masselink, N. Georgiev, T. Dekorsy, and M. Helm, "Above room temperature operation of short wavelength (λ=3.8 μm) strain-compensated $In_{0.73}Ga_{0.27}As$-AlAs quantum-cascade lasers," *Appl. Phys. Lett.*, 85(9), 1478, 2004.

Conference Contributions and Talks Related to this Thesis

1. J. W. Tomm, M. Ziegler, V. Talalaev, C. Matthiesen, T. Elsaesser, M. Bou Sanayeh, P. Brick, H. Koenig, M. Reufer"New approaches towards the understanding of the catastrophic optical damage process in in-plane diode lasers," Photonics West, San Jose, CA, USA, Jan. 28, 2009.

2. J. Mukherjee, M. Ziegler, J. LeClech, J. W. Tomm, B. Corbett, J. G. Mclnerney, J. P. Reithmaier, S. Deubert, A. Forchel."Bulk temperature mapping of broad area quantum dot lasers: modeling and micro-thermographic analysis," Photonics West, San Jose, CA, USA, Jan. 28, 2009.

3. J. W. Tomm, M. Ziegler, M. Oudart, J. Nagle, and J. Jimenez, "Gradual degradation of GaAs-based quantum well lasers, creation of defects, and generation of compressive strain," EDS2008, Poitiers, France, Sept. 17, 2008.

4. M. Ziegler, J. W. Tomm, T. Elsaesser, C. Matthiesen, M. Bou Sanayeh, and P. Brick, "Catastrophic optical damage in high-power diode lasers monitored by real-time imaging," CLEO, San Jose, CA, USA, May 8, 2008.

5. M. Bou Sanayeh, P. Brick, W. Schmid, B. Mayer, M. Müller, M. Reufer, K. Streubel, M. Ziegler, J. W. Tomm, and G. Bacher, "The physics

of catastrophic optical damage in high-power AlGaInP laser diodes," Photonics Europe, Strasbourg, France, Apr. 07, 2008.

6. M. Bou Sanayeh, P. Brick, M. Reufer, B. Mayer, M. Müller, W. Schmid, M. Ziegler, J. W. Tomm, and G. Bacher, "Influence of low-absorption laser facets on catastrophic optical damage in AlGaInP lasers," DPG - spring meeting of the Division Condensed Matter, Berlin, Feb. 27, 2008.

7. J. W. Tomm, M. Ziegler, T. Q. Tien, F. Weik, P. Hennig, J. Meusel, H. Kissel, G. Seibold, J. Biesenbach, G. Groenninger, G. Herrmann, and U. Strauß, "Screening of high power laser diode bars in terms of stresses and thermal profiles," Photonics West, San Jose, CA, USA, Jan. 22, 2008.

8. M. Ziegler, J. W. Tomm, F. Weik, T. Elsaesser, C. Monte, J. Hollandt, H. Kissel, G. Seibold, and J. Biesenbach, "Accurate determination of absolute temperatures of GaAs based high-power diode lasers," Photonics West, San Jose, CA, USA, Jan. 22, 2008.

9. D. Pierscinska, A. Kozlowska, K. Pierscinski, M. Bugajski, J. W. Tomm, M. Ziegler, and F. Weik, "Thermal processes in high-power laser bars investigated by spatially resolved thermoreflectance," DRIP 12, Berlin, Germany, Sept. 09, 2007.

10. M. Ziegler, F. Weik, J. W. Tomm, T. Elsaesser, and R. P. Sarzał a, and W. Nakwaski, "Transient thermal properties of high-power diode laser bars," CLEO, Baltimore, MD, USA, May 09, 2007.

11. M. Ziegler, F. Weik, J. W. Tomm, W. Nakwaski, and R. P. Sarzala, "Transient thermal properties of high-power laser-diode arrays," IR-Kolloquium, Fraunhofer IAF, Freiburg, March 28, 2007.

12. J. W. Tomm, T. Q. Tien, M. Ziegler, F. Weik, B. Sumpf, M. Zorn, U. Zeimer, and G. Erbert, "Degradation behavior and thermal properties of red (650 nm) high-power diode single emitters and laser bars," Photonics West, San Jose, CA, USA, Jan. 22, 2007.

13. D. Masanotti, F. Causa, F. Weik, M. Ziegler, and J. W. Tomm, "Analysis of mechanical strain and temperature profiling in high-brightness parabolic bow-tie laser arrays," Optics East, Boston, MA, USA, Oct. 01, 2006.

14. A. Kozlowska, R. Kozlowski, M. Kozubal, P. Kaminski, A. Malag, P. Wawrzyniak, J. W. Tomm, and M. Ziegler, "Microthermographic investigations of aging processes in diode lasers," Optics East, Boston, MA, USA, Oct. 01, 2006.

15. M. Ziegler, F. Weik, and J. W. Tomm, "Multi-spectral infrared imaging of high-power diode lasers," DPG - spring meeting of the Division Condensed Matter and EPS - 21st General Conference of the Condensed Matter Division, Dresden, March 28, 2006.

16. M. Ziegler, F. Weik, A. Kozlowska, and J. W. Tomm, "Deep level emission from high-power diode laser bars detected by multi-spectral infrared imaging," Laser-Optik-Berlin, March 24, 2006.

Acknowledgment - Danksagung

An dieser Stelle möchte ich mich bei all denjenigen bedanken, die mich während der Zeit meiner Promotion unterstützt haben.

Zunächst möchte ich besonders Herrn Prof. Dr. Thomas Elsässer für die Betreuung dieser Arbeit danken, für die zielführenden Diskussionen und die Zusammenarbeit bei zahlreichen Publikationen.

Die freundschaftliche Anleitung in der Arbeitsgruppe Optoelektronische Bauelemente durch Dr. Jens W. Tomm beinhaltete nicht nur die klare, effiziente und fundierte wissenschaftliche Betreuung durch tägliche Gespräche, sondern vor allem auch die vertrauensvolle Einbindung in alle Belange der Projekt-, Publikations-, und Konferenztätigkeit und die Motivation und Freiheit bei der Verfolgung eigener Ideen. Für Alles meinen allerherzlichsten Dank.

Sandy Schwirzke-Schaaf und Tobias Grunske möchte ich danken für die konstante unschätzbare Unterstützung in allen Belangen der Laborarbeit und für die freundschaftliche Zusammenarbeit.

Dr. Vadim Talalaev, Dr. Fritz Weik und Dr. Tien Quoc Tran danke ich für die vielfältige, exzellente, experimentelle Unterstützung.

PD. Dr. Günter Steinmeyer und den zahlreichen Kollegen der Abteilung C2 danke ich vielmals für das äußerst angenehme Arbeitsklima; es hat immer Spaß gemacht hier zu arbeiten. Weiterhin bedanke ich mich bei den netten Damen und Herren des Sekretariats und der Werkstatt für den exzellenten organisatorischen und feinmechanischen Support.

Numerous colleagues from Germany and from abroad supported essentially to this work in many ways (i.e., publications, samples, joint experiments, etc.). Those I'd like to acknowledge and thank. I am deeply indebted to: Dr. G. Erbert, Dr. B. Sumpf, Dr. F. Bugge, Dr. U. Zeimer *et al.* from the Ferdinand-Braun-Institut für Höchstfrequenztechnik, Berlin; Dr. C. Monte, Dr. J. Hollandt *et al.* from the Physikalisch-Technische Bundesanstalt, Berlin; R. Pomraenke, Prof. Dr. C. Lienau, Dr. P. Vasa *et al.* from the Carl von Ossietzky Universität, Oldenburg; Dr. A. Kozlowska from the Institute of Electron Technology, Warsaw; Prof. Dr. W. Nakwaski, Dr. R. P. Sarzała *et al.* from the Technical University of Łódź; Dr. U. Strauss, G. Grönninger, Dr. M. Bou Sanayeh, Dr. P. Brick, Dr. M. Reufer *et al.* from OSRAM OS, Regensburg; Dr. H. Kissel, Dr. J. Biesenbach *et al.* from DILAS, Mainz-Hechtsheim; Dr. P. Hennig, Dr. D. Lorenzen, Dr. J. Meusel *et al.* from JENOPTIK Laserdiode, Jena; J. Mukherjee *et al.* from Tyndall Institute, Cork; Dr. M. Oudart, Dr. J. Nagle *et al.* from Alcatel Thales III-V lab and Thales Research and Technology, Palaiseau. In connection with those I'd like to gratefully acknowledge the technical and financial support through the projects WWW.BRIGHTER.EU, TRUST, and BRILASI.

I'd like to express my gratitude to Prof. Dr. Ignacio Esquivias Moscardo, Dr. Jose Manuel Garcia Tijero and colleagues for hosting, supporting, and cordially receiving me during my stay at the Universidad Politécnica de Madrid.

A number of individuals that essentially provided to this work during their internship or their master thesis I'd like to acknowledge: David Reeber, Julien Le Clech, Clemens Matthiesen, and Sabrina Metz.

Weiterhin möchte ich mich vielmals bei Prof. Dr. Joachim Wagner und Prof. Dr. W. Ted Masselink für die Begutachtung dieser Arbeit bedanken.

Meiner Familie und meinen Freunden danke ich für Ihre Unterstützung und Ihr Verständnis dafür, daß ich nicht so viel Zeit mit Ihnen verbringen konnte wie ich es mir gewünscht hätte.

Von unschätzbarem Wert für mich ist die Liebe und Unterstützung meiner Frau Anja und meiner beiden Söhne Leonard und Konrad. Während der Promotion gaben sie mir konsequenten Rückhalt und brachten viel Verständnis für lange Arbeitstage auf. Ihre Erdung fernab der Physik hat mich stark gemacht. Dafür den allergrößten Dank!

Selbständigkeitserklärung

Hiermit erkläre ich, die vorliegende Dissertation selbständig und nur unter Verwendung der angegebenen Literatur und Hilfsmittel angefertigt zu haben.

Mathias Ziegler
Berlin, 24. Februar 2009